

Horn Antennas and Dual-Polarized Circuits in Substrate Integrated Waveguide (SIW) Technology

THÈSE N° 6421 (2014)

PRÉSENTÉE LE 14 NOVEMBRE 2014

À LA FACULTÉ DES SCIENCES ET TECHNIQUES DE L'INGÉNIEUR
LABORATOIRE D'ÉLECTROMAGNÉTISME ET ACOUSTIQUE
PROGRAMME DOCTORAL EN GÉNIE ÉLECTRIQUE

ÉCOLE POLYTECHNIQUE FÉDÉRALE DE LAUSANNE

POUR L'OBTENTION DU GRADE DE DOCTEUR ÈS SCIENCES

PAR

Marc ESQUIUS MOROTE

acceptée sur proposition du jury:

Prof. C. N. Jones, président du jury
Prof. J. R. Mosig, directeur de thèse
Prof. L. Jofre Roca, rapporteur
Prof. F. Rachidi-Haeri, rapporteur
Prof. K. Wu, rapporteur



ÉCOLE POLYTECHNIQUE
FÉDÉRALE DE LAUSANNE

Suisse
2014

*But still try, for who knows what is possible?
I am no poet, but if you think for yourselves, as I proceed,
the facts will form a poem in your minds.*

— Michael Faraday,
the father of that enlarged science of electromagnetism

A la meva dona, als meus pares i a la meva germana, que sempre
m'han recolzat i encoratjat en totes les decisions que he pres...

Abstract

The Substrate Integrated Waveguide (SIW) technology is a very promising candidate to provide widespread commercial solutions for modern communications systems. Its main advantage is the possibility to integrate passive/active components and antennas in the same substrate by using standard manufacturing processes, such as the Printed Circuits Board (PCB) processing technique.

Nevertheless, the production of low-cost SIW devices is inherently linked to commercially available substrates and fabrication methods. In particular, these constraints usually limit (a) the frequency range of operation of certain SIW antennas and (b) the possibility of creating multimode structures dealing with orthogonal polarizations. The motivation of this PhD thesis is to overcome these two limitations by proposing innovative SIW components based on PCBs in order to favour the compatibility with existing systems and to lower their cost. Hence, the usage of the SIW technology would be extended towards new applications and scenarios.

One type of antenna strongly affected by the limitation (a) is the H-plane SIW horn antenna. While standard horns are employed in many applications and in a wide range of frequencies, their counterparts in SIW technology are restricted to the Ka-band and above. At lower frequencies, commercial substrates are electrically thin and the performances of these end-fire antennas severely diminish. To solve this problem, a novel low-profile SIW horn antenna has been designed to be used at the Ku-band and below, while offering wideband characteristics. In addition, the horn shape has been further optimized to reduce the antenna footprint for a given directivity.

In order to overcome the limitation (b), a substrate integrated guide able to simultaneously carry orthogonally polarized modes has been developed: the so called Extended Substrate Integrated Waveguide (ESIW). An ESIW dual-polarized system composed of an Orthomode Transducer (OMT) feeding a dual-polarized horn antenna has been designed and experimentally verified.

The overall combination of concepts and ideas proposed in this thesis opens the door towards new SIW components that can increase the capacity, robustness and compactness of modern communication systems.

Keywords: Substrate Integrated Waveguide (SIW), Substrate Integrated Circuits (SICs), horn antennas, end-fire radiation, low-profile, Unmanned Airborne Vehicles (UAV), orthogonal modes, dual-polarization, Orthomode Transducer (OMT).

Résumé

La technologie *Substrate Integrated Waveguide* (SIW) — littéralement "guide d'onde intégré au substrat" — est une technologie très prometteuse pour fournir des solutions commerciales aux futurs systèmes de communications. Son principal avantage est la possibilité d'intégrer des composants passifs/actifs et des antennes dans le même substrat en utilisant des procédés de fabrication standard, tels que les circuits imprimés ou PCBs (Printed Circuits Boards).

Cependant, la production de composants SIW à bas coût est intrinsèquement liée aux substrats disponibles sur le marché et aux méthodes de fabrication. En particulier, ces contraintes limitent (a) les fréquences de fonctionnement de certaines antennes SIW et (b) la possibilité de créer des dispositifs ayant des polarisations orthogonales. La motivation de cette thèse de doctorat est de dépasser ces deux limitations en proposant des composants SIW basés sur des procédés PCB pour qu'ils soient compatibles avec les systèmes déjà existants et pour réduire leurs coûts de production. Une telle solution permettrait d'élargir l'utilisation de la technologie SIW vers de nouvelles applications et scénarios.

Une antenne fortement influencée par la limitation (a) est l'antenne cornet SIW. Tandis que les cornets standards sont utilisées dans de nombreuses applications et bandes de fréquences, son homologue en technologie SIW est limité à la bande Ka et au-dessus. Aux fréquences plus basses, les substrats disponibles sont électriquement minces et les performances de ces antennes se détériorent sévèrement. Pour résoudre ce problème, une nouvelle antenne cornet SIW donc totalement intégrée au substrat a été conçue pour être utilisée dans la bande Ku et au-dessous avec des propriétés large bande. De plus, la forme du cornet a été optimisée pour réduire la taille de l'antenne par rapport à la directivité souhaitée.

Pour surmonter la limitation (b), un guide d'onde intégré capable de transporter plusieurs modes polarisés orthogonalement a été aussi proposé et appelé *Extended Substrate Integrated Waveguide* (ESIW). Un système ESIW avec deux entrées à polarisation orthogonale composé d'un Orthomode Transducer (OMT) alimentant une antenne cornet a été conçu et vérifié expérimentalement.

La panoplie complète de concepts et idées proposés dans cette thèse ouvre la voie à de nouveaux dispositifs SIW qui peuvent augmenter la capacité, la fiabilité et la compacité des systèmes modernes de communication.

Mots clefs : Substrate Integrated Waveguide (SIW), Substrate Integrated Circuits (SICs), antenne intégrée au substrat, antenne cornet, rayonnement end-fire, Unmanned Airborne Vehicles (UAV), double-polarisation, modes orthogonaux, Orthomode Transducer (OMT).

Kurzfassung

Substrat-integrierte-Wellenleiter-Technologie (engl. SIW-Technology) ist ein vielversprechendes Konzept, das weitverbreitete kommerzielle Lösungen für moderne Kommunikationssysteme anbietet. Ihr größter Vorteil liegt darin, daß sich mit standardisierten Fertigungsprozessen (z. B. gedruckte Leiterplattentechnologie) sowohl passive als auch aktive Komponenten und Antennen auf dem gleichen Substrat integrieren lassen.

Die Produktion von kostengünstigen SIW-Bauelementen hängt jedoch unmittelbar mit den kommerziell verfügbaren Substraten und Herstellungsverfahren zusammen. Dies schränkt insbesondere (a) den Frequenzbereich, in welchem solche SIW Antennen arbeiten können, und (b) die Entwicklung von mehrmodigen Strukturen für die Übertragung von orthogonal polarisierten Signalen ein. Ziel dieser Dissertation ist es, Wege aufzuzeigen, wie diese Einschränkungen durch den Einsatz von innovativen SIW-Komponenten überwunden werden können. Diese sollen dabei auf der Leiterplattentechnologie aufbauen, sowohl um die Kompatibilität mit bereits existierenden Systemen zu garantieren als auch die Herstellungskosten gering zu halten und damit den Weg für neue Anwendungen der SIW-Technologie zu ebnen.

Hauptsächlich betroffen von der ersten Einschränkung sind H-Ebenen SIW-Hornstrahler. Während gewöhnliche Hornstrahler in vielen Anwendungen zu finden sind und über einen großen Frequenzbereich funktionieren, ist die SIW-Variante auf das Ka-Band und darüber beschränkt. Bei niedrigeren Frequenzen sind die handelsüblichen Substrate sehr dünn und die Leistung dieser Art von Längsstrahlerantennen nimmt drastisch ab. Um dieses Problem zu lösen, wurde ein neuartiger, flacher und breitbandiger SIW-Hornstrahler konzipiert, der für das Ku-Band und darunter geeignet ist. Darüberhinaus wurde die Form des Hornstrahlers optimiert, um eine möglichst geringe Größe bei gegebenem Richtfaktor zu erreichen.

Um die zweite Einschränkung zu überwinden, wurde ein im Substrat integrierter Wellenleiter entwickelt, der sogenannte Extended SIW (ESIW), der gleichzeitig mehrere orthogonal polarisierte Moden übertragen kann. Basierend auf diesem Konzept wurde eine Polarisationsweiche (engl. Orthomode Transducer), die zur Einspeisung eines SIW-Hornstrahlers mit dualer Polarisation geeignet ist, entwickelt und experimentell überprüft.

Die Kombination der in dieser Dissertation vorgestellten Konzepte und Ideen öffnet die Tür für die Entwicklung von neuen SIW-Bauelementen, die das Leistungsvermögen, die Robustheit und die Kompaktheit moderner Kommunikationssysteme erhöhen können.

Schlagnworte : Substrate Integrated Waveguide (SIW), Substrate Integrated Circuits (SICs), Hornstrahler, Längsstrahler, Unmanned Airborne Vehicles (UAV), orthogonale Moden, duale Polarisation, Orthomode Transducer (OMT).

Resum

La tecnologia *Substrate Integrated Waveguide* (SIW) —literalment "guia d'ona integrada al substrat"— és una tecnologia molt prometedora per proporcionar solucions comercials per als futurs sistemes de comunicació. El seu principal avantatge és la possibilitat d'integrar components passius/actius i antenes en el mateix substrat i utilitzant processos de fabricació estàndard, com per als circuits impresos o PCBs (Printed Circuits Boards).

Tanmateix, la producció de components SIW a baix cost està intrínscament lligada als substrats disponibles al mercat i als mètodes de fabricació. En particular, aquestes restriccions limiten (a) les freqüències de funcionament de certes antenes SIW i (b) la possibilitat de crear dispositius multi-mode amb polaritzacions ortogonals. La motivació d'aquesta tesi doctoral és de superar aquestes dues limitacions proposant components SIW basats en processos PCB perquè siguin compatibles amb sistemes ja existents i per reduir els seus costos de producció. D'aquesta manera, la utilització de la tecnologia SIW podria estendre's cap a noves aplicacions i escenaris.

Una antena fortament afectada per la limitació (a) és l'antena botzina SIW. Mentre les botzines estàndard s'utilitzen en nombroses aplicacions i bandes de freqüència, el seu homòleg en tecnologia SIW està limitat a la banda Ka i per sobre. A freqüències més baixes, els substrats disponibles són elèctricament fins i les propietats d'aquestes antenes es deterioren dràsticament. Per resoldre aquest problema, un nou disseny per a antenes botzina SIW ha estat proposat per tal de ser utilitzat a la banda Ku i per sota conservant bones propietats de banda ampla. A més a més, la forma de la botzina ha estat optimitzada per tal de reduir el tamany de l'antena donada una certa directivitat.

Per sobrepassar la limitació (b), una guia d'ona integrada capaç de transportar diversos modes polaritzats ortogonalment ha estat desenvolupada : la *Extended Substrate Integrated Waveguide* (ESIW). Un sistema basat en aquesta nova guia ESIW i compost d'un Orthomode Transducer (OMT) alimentant una antena botzina de doble polarització ha estat dissenyat i verificat experimentalment.

El conjunt d'idees i conceptes proposats en aquesta tesi obre les portes a nous dispositius SIW que poden augmentar la capacitat, fiabilitat i compacitat dels sistemes de comunicació moderns.

Paraules clau : Substrate Integrated Waveguide (SIW), Substrate Integrated Circuits (SICs), antena integrada al substrat, antenes botzina, radiació end-fire, Unmanned Airborne Vehicles (UAV), doble polarització, modes ortogonals, Orthomode Transducer (OMT).

Resumen

La tecnología *Substrate Integrated Waveguide* (SIW) —literalmente "guía de onda integrada en sustrato"— es una tecnología muy prometedora para proporcionar soluciones comerciales para los futuros sistemas de comunicación. Su principal ventaja es la posibilidad de integrar componentes pasivos/activos y antenas en el mismo sustrato y utilizando procesos de fabricación estándar, como para los circuitos impresos o PCBs (Printed Circuits Boards).

Sin embargo, la producción de componentes SIW de bajo coste depende intrínsecamente de los sustratos disponibles en el mercado y de los métodos de fabricación. En particular, estas restricciones limitan (a) las frecuencias de funcionamiento de ciertas antenas SIW y (b) la posibilidad de crear dispositivos multi-modo con polarizaciones ortogonales. La motivación de esta tesis doctoral es de superar estas dos limitaciones proponiendo componentes SIW basados en procesos PCB para que sean compatibles con sistemas ya existentes y para reducir sus costes de producción. De esta manera, la utilización de la tecnología SIW podría extenderse hacia nuevas aplicaciones y escenarios.

Una antena fuertemente afectada por la limitación (a) es la antena de bocina SIW. Mientras las bocinas estándar se utilizan en numerosas aplicaciones y bandas de frecuencia, su homólogo en tecnología SIW está limitado a la banda Ka y por encima. A frecuencias más bajas, los sustratos disponibles son eléctricamente finos y las propiedades de estas antenas se deterioran drásticamente. Para solventar este problema, un nuevo diseño para antenas de bocina SIW se ha propuesto, el cual puede ser utilizado en la banda Ku y por debajo conservando buenas propiedades de banda ancha. Además, la forma de la bocina se ha optimizado con el fin de reducir el tamaño de la antena dada una cierta directividad.

Para superar la limitación (b), una guía de onda integrada capaz de transportar distintos modos polarizados ortogonalmente ha sido desarrollada : la *Extended Substrate Integrated Waveguide* (ESIW). Un sistema basado en esta nueva guía ESIW y compuesto de un Orthomode Transducer (OMT) alimentando una antena de bocina de doble polarización se ha diseñado y verificado experimentalmente.

El conjunto de ideas y conceptos propuestos en esta tesis abre las puertas hacia nuevos dispositivos SIW que pueden aumentar la capacidad, fiabilidad y compacidad de los sistemas de comunicación modernos.

Palabras clave : Substrate Integrated Waveguide (SIW), Substrate Integrated Circuits (SICs), antena integrada en sustrato, antenas de bocina, radiación end-fire, Unmanned Airborne Vehicles (UAV), doble polarización, modos ortogonales, Orthomode Transducer (OMT).

Acknowledgements

This thesis became possible thanks to all the discussions, contributions, advices, etc. of all the colleagues and friends from the Laboratory of Electromagnetics and Acoustics (LEMA). First of all, I would like to deeply thank my thesis director, Prof. Juan R. Mosig, whose advices and guidance from the scientific and personal point of view made this journey a really nice and fruitful experience. His positive and encouraging attitude along with his trust and freedom during these years of work led to very interesting and new cross-fertilizing ideas.

I am also very thankful to Benjamin Fuchs who helped me since the beginning to set this thesis in the right course and kept doing it despite the distance. His suggestions and willingness to discuss new (and often crazy) ideas defined the character of this thesis. The latter also goes for Michael Mattes, who I would like to thank for his unconditional help either concerning the different modes in a waveguide or the most optimum way to water the plants. I would also like to acknowledge the members of my thesis jury Prof. Ke Wu, Prof. Lluís Jofre Roca, Prof. Farhad Rachidi-Haeri and Prof. Colin Jones for having examined my work and provided constructive comments. My particular gratitude goes to Lluís for convincing me to explore the world of electromagnetism and antennas.

The achievements in this thesis wouldn't be neither possible without the extensive expertises of Jean-François Zürcher when it came to building and measuring any kind of device. Thanks, together with Philippe Vosseler and Manuel Leitons, for providing me with the best solutions in the manufacturing processes of my prototypes. Daily life at LEMA (and in Switzerland in general) became also much easier thanks to the advices and discussions with Prof. Anja Skrivervik, Eulalia Durussel and Mercedes Quintas. Good morning stops at the ELB 030 always solve any practical issues or just help you to start the day fresh, *muchas gracias*.

The excellent family atmosphere at LEMA also played a key role in this PhD journey. Starting with my first Italian office mates, Francesco and Madda, until Eduardo and Anton, with whom I could have any kind of esoteric discussion just to have a break. Also the nice field trips with my armasuisse-buddy Jovanche (either in Thun or in Sat), the salsa dances with María and Joana, the conspirational coffees with Sebas and Eduardo, the reverberating laughs at the ELB 032 with Hamed, Michele and Hussein, the mystic debates with Edén, the Greek parties with Yiannis, Apo, Yiannis Jr., and the many coffee breaks and lake barbecues with Carlos, Gabriele,

Tomislav, Santi, Baptist, Pedro, Przemek, Mina, Fred, Roberto, Rafal, Nuno, Erio, Marco, Dani and Pietro. Many thanks as well to all the others friends in Lausanne and abroad for all the countless hikings, skiing weekends and random trips!

Finally, I would like to thank my family who has been always supporting me in all the decisions I have taken, from close or from far away, giving me strength to go on, *moltes gracies*. Of course, these incredible years wouldn't have been possible without my wife, Sarah, who have been always by my side, encouraged me and pushed me towards the right direction. To all of you I dedicate this thesis.

A handwritten signature in blue ink, appearing to be 'M. S. M.', located on the right side of the page.

Contents

Acronyms and Abbreviations	xxi
List of Symbols	xxiii
1 Introduction	1
1.1 Motivations and Context of the Work	1
1.2 The Initial Challenge: A Direction Finding System	3
1.2.1 The Direction Finding Antenna Requirements	3
1.3 Outline and Original Contributions	6
1.4 Additional Research Performed During the Thesis	10
2 Substrate Integrated Waveguide (SIW) Antennas and Systems	13
2.1 The SIW Concept	13
2.2 Overview on SIW Antennas, Systems and Applications	15
2.3 DF Antenna Selection	16
2.4 Conclusions	20
3 Thin and Compact H-plane SIW Horn Antenna	21
3.1 Principle of Operation of H-plane SIW Horns	22
3.2 Matching Improvements	23
3.2.1 Coupled Resonator Model	25
3.2.2 Transmission Line Model	28
3.2.3 Design Guidelines	31
3.2.4 Experimental Results	32
3.3 Radiation Improvements	35
3.3.1 Validation of the Array Analogy	36

3.3.2	Simultaneous FTBR and Matching Improvement	38
3.4	Surface Reduction	40
3.4.1	Improvements in the Conventional Horn Performances	41
3.4.2	Proposed Horn Shape	42
3.4.3	Compact Horn vs. Conventional Horn	45
3.5	Prototype Design and Measurements	45
3.5.1	SIW Horn Design Steps	45
3.5.2	Feeding System	47
3.5.3	Measurements	47
3.6	Conclusions	50
4	Low-profile Azimuth Direction Finding System	53
4.1	Interconnection SIW Horn Antennas - MMICs	54
4.1.1	Type of Transition	54
4.1.2	Preliminary SIW Horn Array Prototype	55
4.2	RF Electronics	58
4.2.1	RF Output	61
4.2.2	Interferences and Shielding	63
4.2.3	Parasitic Oscillations	64
4.3	DC Electronics	66
4.4	Experimental Results	69
4.4.1	Manufacturing Process	69
4.4.2	Measurements	71
4.5	System Interaction with Airborne Platforms	75
4.6	Conclusions	77
5	Extended Substrate Integrated Waveguide (ESIW)	79
5.1	Analysis and Design of the ESIW	81
5.1.1	Maximum Frequency of Operation	82
5.1.2	Cut-off Frequency of the TE_{01} Mode	82
5.1.3	Bandgap Effects	85
5.1.4	Loss Mechanisms	87
5.2	Slotline Feeding for the TE_{01} Mode	89
5.3	ESIW Prototype and Measurements	91
5.4	Conclusions	93

6	Dual-Polarized System based on the ESIW	95
6.1	Substrate Integrated Orthomode Transducer (OMT)	95
6.1.1	OMT Design Strategy	97
6.1.2	Excitation of the TE_{10} and TE_{01} Modes	99
6.1.3	Complete OMT Performances	102
6.2	Dual-Polarized Substrate Integrated Horn Antenna	104
6.2.1	The H-plane Horn Antenna	104
6.2.2	The E-plane Horn Antenna	105
6.2.3	Dual-Polarized Horn Antenna Design	107
6.3	Experimental Results	108
6.4	Conclusions	113
7	Conclusions and Perspectives	115
A	Comparison between TE and LSE/LSM Modes	119
B	Graphene-based Reconfigurable Leaky-Wave Antennas	123
B.1	Introduction	123
B.2	Tunability of Graphene Conductivity	125
B.3	Sinusoidally-Modulated Reactance Surfaces	125
B.4	Periodically Modulated Graphene LWA	126
B.4.1	Proposed Structure	126
B.4.2	Design Strategy	128
B.5	Design Example	129
B.6	Practical Considerations	132
B.7	Conclusions	134
	Bibliography	135
	CV	149
	List of Publications	151

Acronyms and Abbreviations

ADC	Analog-to-Digital Converter
BFN	Beam Forming Network
CR	Coupled Resonator
DF	Direction Finding
DoA	Direction of Arrival
EBG	Electromagnetic Band-Gap
ESIW	Extended Substrate Integrated Waveguide
FTBR	Front-to-Back Ratio
GaAs	Gallium Arsenide
HFSS	High Frequency Structure Simulator
HPBW	Half Power BeamWidth
IC	Integrated Circuit
IEEE	Institute of Electrical and Electronics Engineers
IL	Insertion Loss
LD	Logarithmic Detector
LED	Light-Emitting Diode
LSE	Longitudinal Section Electric
LSM	Longitudinal Section Magnetic
LTCC	Low-Temperature Co-fired Ceramic
LWA	Leaky-Wave Antenna
MCU	MicroController Unit
MMIC	Monolithic Microwave Integrated Circuits
MSL	MicroStrip Line
NRD	Non-Radiative Dielectric

Acronyms and Abbreviations

OMT	OrthoMode Transducer
PCB	Printed Circuit Board
PIC	Peripheral Interface Controller
QFN	Quad Flat No-leads
RF	Radio Frequency
RL	Return Loss
RWG	Rectangular WaveGuide
SIC	Substrate Integrated Circuit
SINRD	Substrate Integrated Non-Radiative Dielectric
SIW	Substrate Integrated Waveguide
SMD	Surface Mounted Device
SP4T	Single Pole 4 Through
SPDT	Single Pole Double Through
SWA	Surface Wave Antenna
TE	Transverse Electric
TEM	Transverse ElectroMagnetic
TEN	Transverse Equivalent Network
TM	Transverse Magnetic
TL	Transmission Line
TRE	Transverse Resonance Equation
UAV	Unmanned Aerial Vehicle

List of Symbols

α	Attenuation constant
α_c	Attenuation constant due to conductor losses
α_d	Attenuation constant due to dielectric losses
α_{rad}	Attenuation constant due to radiation losses or leakage factor
β	Phase constant
c	Speed of light in free space
ϵ_0	Permittivity in vacuum
ϵ_r	Relative permittivity
f_0	Central frequency of operation
f_c	Cut-off frequency
f_h	Maximum frequency of operation
γ	Complex propagation constant
λ_0	Free space wavelength
λ_c	Cut-off wavelength
λ_g	Guided wavelength
k_0	Wavenumber in free space
σ	Conductivity
S_{ij}	Scattering parameter associated to input port i and output port j
$\tan \delta$	Dielectric loss tangent

1 Introduction

1.1 Motivations and Context of the Work

The interest in wireless components and systems has greatly increased in the recent years. As a result, current services extensively use the frequencies lying at the X-band and below, making this part of the spectrum overcrowded and reaching its maximum throughput. The exponential growth of users and applications indicates then the need to migrate towards the Ku-band and above, where the large portion of spectrum available becomes really attractive to deploy new high throughput applications. Examples of upcoming services located at these higher frequency bands are in-flight connectivity in commercial airplanes (Ku/Ka-band), satellite broadcasting reception in vehicles (Ku/Ka-band), high data-rate indoor communications (V-band), automotive radars (W-band) and the new generation of wireless mobile networks (ongoing research from Ka- to V-band).

The deployment of these services is, however, subject to several challenges. Wireless links at these frequencies do not only suffer from strong propagation losses, but also the material losses severely deteriorate the system performances. In particular, the conductor loss significantly increases because the copper thickness in printed circuits becomes close to the dimensions of the skin depth. A classic and well-mastered approach to overcome this problem is to use hollow metallic waveguides which offer, among other features, unrivalled efficiency and high power handling capabilities. Nevertheless, they are also heavy, bulky and expensive to manufacture. The latter is particularly true at higher frequencies where the tolerances in the machining and the assembling processes become really strict, usually requiring additional tuning mechanisms to adjust the performances after the manufacturing process. Therefore, due to their high cost and complexity, metallic waveguide components are not suitable for widespread solutions and they are mainly used in high-performance systems, such as for space or military applications.

Antennas and microwave components used at lower frequencies typically rely on planar designs, mostly realised with the Printed Circuit Board (PCB) processing technique. This mature technology leads to, not only low-cost designs, but also the possibility to easily integrate them with common electronic components. However, these planar designs are by nature not fully shielded, thus subject to radiation, cross-talk and packaging problems. These drawbacks—added to the potentially high conductor losses— make this technology not feasible to implement high frequency complex structures, such as large feeding networks. It is then obvious that a large performance gap exists between components based on metallic waveguides and the ones based on PCBs.

A very promising candidate to fill this gap and to provide widespread commercial solutions is the Substrate Integrated Waveguide (SIW) technology or, more in general, the Substrate Integrated Circuit (SIC) architecture. This technology allows building high performance, low-cost and reliable waveguide-like components using planar processing techniques, such as the PCB or the Low-Temperature Co-fired Ceramic (LTCC). In SIW technology, the top and bottom metallizations of the substrate act as the top and bottom horizontal walls of the waveguide, while the vertical walls are synthesized by drilling and metallizing vias through the substrate. Many types of antennas and other microwave devices typically built using metallic waveguides can be implemented in SIW technology. Importantly, they are able to preserve most of the advantages of standard waveguides (e.g., low conductor losses, low cross-talk, medium-high power handling capabilities) while keeping the ones of the planar technology (e.g. low-cost, light weight, easy integration).

Despite the strong potential of this technology, the feasibility of creating low-cost SIW components is inherently linked to commercially available substrates and manufacturing processes. These constraints typically limit (a) the frequency range of operation of certain SIW antennas and (b) the possibility of creating waveguides dealing with orthogonal polarizations. The first limitation originates from the fact that commercial substrates are electrically thin at the Ku-band and below, which introduces a great challenge in preserving the good electromagnetic properties of some antennas when implemented in SIW technology (specially for antennas radiating at the end-fire direction). The second limitation is due to the discontinuities—or gaps—between the metallized vias defining the vertical walls, which hinders the implementation of dual-polarized waveguide components requiring the simultaneous use of vertically and horizontally polarized modes, such as orthomode transducers for antenna feed chains.

The motivation of this PhD thesis is to overcome these two limitations by proposing innovative SIW components boasting the above functionalities but still based on PCBs in order to favour the compatibility with existing systems and to lower the cost. Hence, the usage of the SIW technology would be extended towards new applications and scenarios helping to establish this technology as the best option for future commercial solutions.

1.2 The Initial Challenge: A Direction Finding System

This PhD thesis was carried out in the framework of a research project awarded by armasuisse, whose main objective was to create an azimuth Direction Finding (DF) system for Unmanned Aerial Vehicles (UAVs) working at the Ku-band¹. The research topics and original contributions of this thesis mainly concern the electromagnetic aspects of this problem and the new original antennas motivated by this initial challenge. Nevertheless, it must be pointed out that a fully operational DF system has been provided to armasuisse by using off-the-shelf electronic components.

1.2.1 The Direction Finding Antenna Requirements

When incorporating communication systems in airborne vehicles, the reduction of the drag and power consumption caused by the antennas is a must. To this end, the antenna system should be low-profile and light weight. This calls for a printed antenna technology ideally compatible with standard PCB processing techniques to further reduce the cost.

This problematic is well-known in the design of flush-mounted antenna system for commercial/military airplanes which can be used, for instance, to provide satellite communications. In this case, the antenna elements mainly radiate at broadside covering a portion of the upper semi-sphere. They can also be arranged in an array configuration to obtain beam scanning capabilities. In the proposed DF system, however, a planar antenna array must cover the 360° of the azimuthal plane, which indicates the need for a circular array of *end-fire antennas*. The difference between these two types of antenna systems is illustrated in Fig. 1.1.

The purpose of a DF system is to estimate the Direction of Arrival (DoA) of an incoming signal. In our case, the DF algorithm will be based on a beam-switching antenna architecture to reduce both cost and complexity [1, 2]. A beam-switching antenna is an antenna array that can form a set of predefined beams. Each antenna creates a sectoral radiation pattern and, by switching between them, the 360° of the azimuthal plane are covered. A common number of antennas that allows for a trade-off between array size and accuracy is eight [3–5]. While, of course, the use of more antennas increases the precision of the DoA estimation, the complexity (and cost) of the system rapidly increases. Therefore, each antenna of the circular array must generate a stable Half Power Beamwidth (HPBW) of 45° (= 360°/8) over the whole frequency band. In this kind of multibeam applications, an overlapping between adjacent beams of 3 ~ 5 dB and a *mutual coupling* between array elements below -30 dB are typically desired [6, 7].

¹Project *Conformal Multifunction Antenna System* contract Nr 041-18, Science and Technology Federal Department of Defense, Civil Protection and Sport (DDPS), armasuisse.

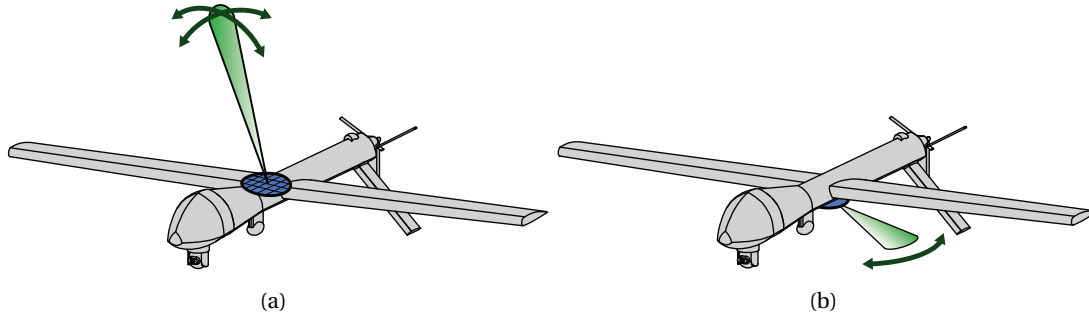


Fig. 1.1: Illustrative examples of flush-mounted antenna systems on an UAV: (a) Broadside radiating elements covering a portion of the upper semi-sphere and (b) end-fire radiating elements covering the azimuthal plane (our case of interest).

The frequency range of operation of the DF system is at the Ku-band, specifically between 14.62 – 15.35 GHz (5% *bandwidth*), which is reserved for military use in Switzerland [8]. At this frequency range, the thicknesses of commonly available substrates are about $\lambda_0/8 - \lambda_0/12$, where λ_0 is a free space wavelength at the central frequency of operation $f_0 = 15$ GHz. Moreover, in order to guarantee a good signal quality even when using the system near the ground, antennas with *vertical polarization* are required.

Fig. 1.2 shows the schematic view of the 8-element DF circular array and its possible mounting in a conventional light UAV. One can see that, apart from the overlapping between adjacent beams, the beam overlapping between opposite antennas (such as 3 and 7) could be as well a source of problems. High back radiation levels may lead to wrong signal detections meaning large errors in the DoA estimation. In our scenario, the reduction of unwanted back radiation is an important challenge and became one of the key points in this work. The figure of merit used to measure this characteristic is the Front-to-Back Ratio (FTBR) which gives the difference in dB between the front and back radiation level. In general, a *FTBR of at least 15 dB* is required to guarantee the proper behaviour of the DF system [6, 7].

In order to cover a sufficient distance range with a reasonable amount of power, the antennas should be directive. In a receiving antenna, the directivity describes how well an antenna converts radio waves arriving from a specified direction into electrical power. In our case, each antenna needs to be selective in the azimuthal plane (*H-plane HPBW* $\simeq 45^\circ$) and receive any signal from the elevation plane (*E-plane HPBW* $\simeq 180^\circ$). This corresponds to an eighth of a sphere, meaning a maximum theoretical directivity of 9 dB. Taking into account that this value cannot be reached in practice as well as the presence of different loss mechanisms, the final requirement was set to achieve a *gain higher than 6 dBi*.

The electronic subsystem responsible to control the antennas and to compute the DoA is placed in the middle of the circular array. It is then also shown in Fig. 1.2 that a transition to

interconnect these antennas with commercial electronic components must be designed. A summary of the DF antenna requirements is presented in Tab. 1.1.

The fundamental requirements of the DF system—to be low-profile, light weight and low-cost— together with the aforementioned advantages of the SIW technology led to the choice of this technology as the best option to implement a DF array based on SIW horn antennas. These end-fire SIW antennas suffer from the previously mentioned frequency limitation (a) and triggered the first research line *A* of this thesis (this point is explained in more detail in the antenna selection process of Chapter 2). The organization followed throughout the thesis in order to fulfil this research line as well as the second one *B*—the development of dual-polarized substrate integrated systems—is described in the next section.

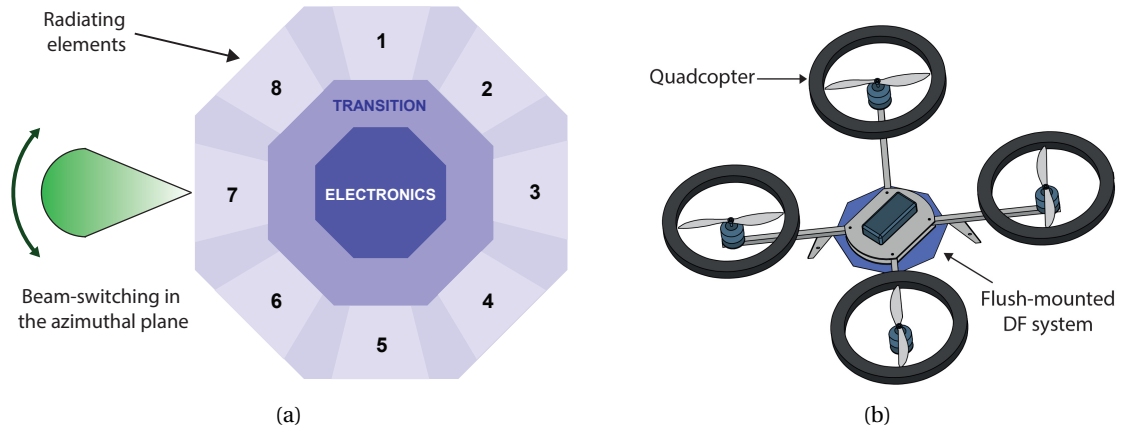


Fig. 1.2: (a) Schematic view of the 8-element azimuth DF system and (b) its possible use in a conventional light UAV. The *transition* region indicates the need to design a structure to interconnect the antennas with the electronic components.

Central frequency of operation f_0	15 GHz
Height or thickness	$\approx \lambda_0/10$
Polarization	vertical
Bandwidth	5%
H-plane HPBW	$\approx 45^\circ$
E-plane HPBW	$\approx 180^\circ$
FTBR	> 15 dB
Gain	> 6 dBi
Mutual coupling	< -30 dB

Tab. 1.1: Requirements of the single end-fire antenna element of DF array.

1.3 Outline and Original Contributions

The first research line *A* of this thesis is tackled in Chapters 2, 3 and 4 through the implementation of the previously described DF system. Chapters 5 and 6 follow the second research line *B* by proposing a substrate integrated guide able to transport orthogonally polarized modes and a complete dual-polarized system based on it. The connections between the different chapters and the two research lines are illustrated in Fig. 1.3. The specific topics covered by each chapter and their original contributions are detailed in the following sections.

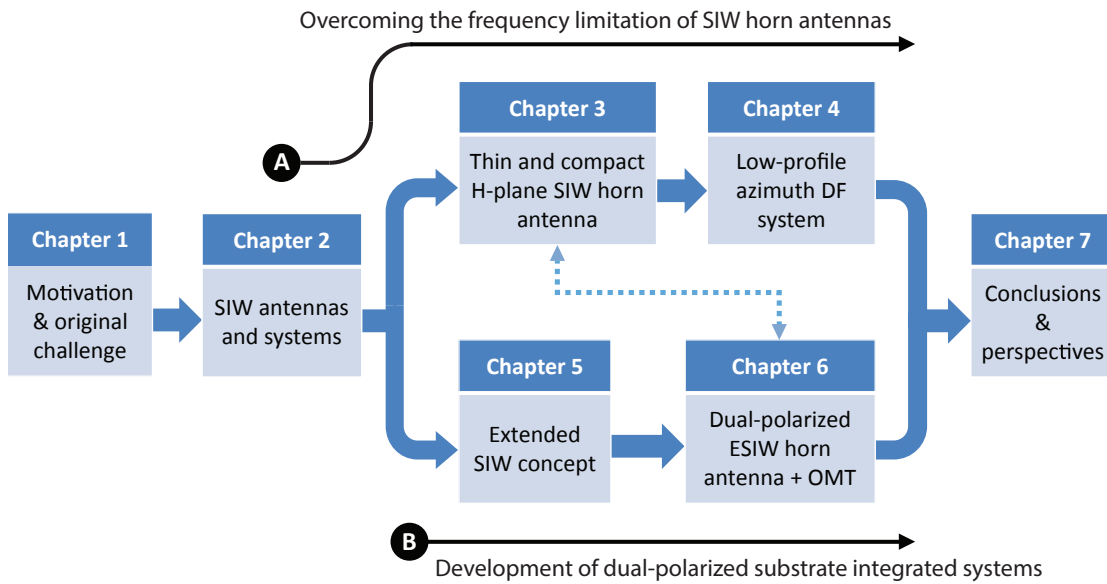


Fig. 1.3: Connection between the different chapters and the two research lines *A* and *B* of this thesis.

Chapter 2 - Substrate Integrated Waveguide (SIW) Antennas and Systems

Description: The basis of the SIW technology are briefly recalled and a state-of-the-art on SIW antennas and RF systems is provided. This overview serves to emphasize the advantages of this technology, its practical limitations and to identify the possible candidates for the DF antenna array. A trade-off analysis between these candidates is performed, leading to the selection of the most promising one: the H-plane SIW horn antenna (see Fig. 1.4).

Original contributions: The concepts and results discussed in this chapter are not new. Nevertheless, a thorough and detailed literature review on the scenarios of usage and applications of different SIW antennas, specifically made for this thesis, allowed us to conduct a fast selection process according to the given specifications.

Chapter 3 - Thin and Compact H-plane SIW Horn Antenna

Description: Although SIW horn antennas offer very attractive properties for our DF system, their practical fabrication at the Ku-band turned out to be very challenging, leading to poor performances in terms of matching and radiation. In this chapter, a rigorous study on the characteristics of H-plane SIW horn antennas is first conducted, bringing to light the reasons behind these problems. Integrated solutions to overcome these problems are proposed and combined, defining a novel design for H-plane SIW horn antennas able to widely fulfil the project requirements (see Fig. 1.4).

Original contributions: A printed transition to improve the matching of SIW horns is first developed and tested. This structure is then further studied to simultaneously improve the radiation performances. Simplified models based on transmission line and array theory are derived to provide quick design rules and predict the SIW horn characteristics. On top of these improvements, the horn taper is modified to obtain a more uniform aperture field distribution thus reducing the required size for a given directivity. The combination of all these concepts results into a practical single-layer PCB design for H-plane SIW horn antennas which has been referred and even adopted by other research groups.

Chapter 4 - Low-profile Azimuth Direction Finding System

Description: The design and manufacturing of a complete DF system based on the previous SIW horns is presented. As first step, the interconnection between these antennas and commercial Monolithic Microwave Integrated Circuits (MMICs) is studied. Then, the selection and implementation of both RF and DC electronics needed to control the antennas and to compute the DoA are described. In addition, common problems encountered with high frequency electronics are addressed, such as the need for a shielding structure and the reduction of parasitic oscillations appearing in amplifiers stages. Finally, experimental results are provided and the future placement of the system in a conventional UAV platform is discussed (see Fig. 1.4). This chapter closes the first research line *A* of this thesis.

Original contributions: A robust transition to interconnect SIW horn antennas with MMICs is proposed. While no novelty resides in the electronic subsystem and in the DF algorithm, this is the first time that such a low-profile SIW-based system working in the azimuthal plane is proposed. This aims to prove the viability of using the SIW technology in scenarios where it is not typically considered, although its main advantages in terms of low-cost and ease of manufacture still hold true.

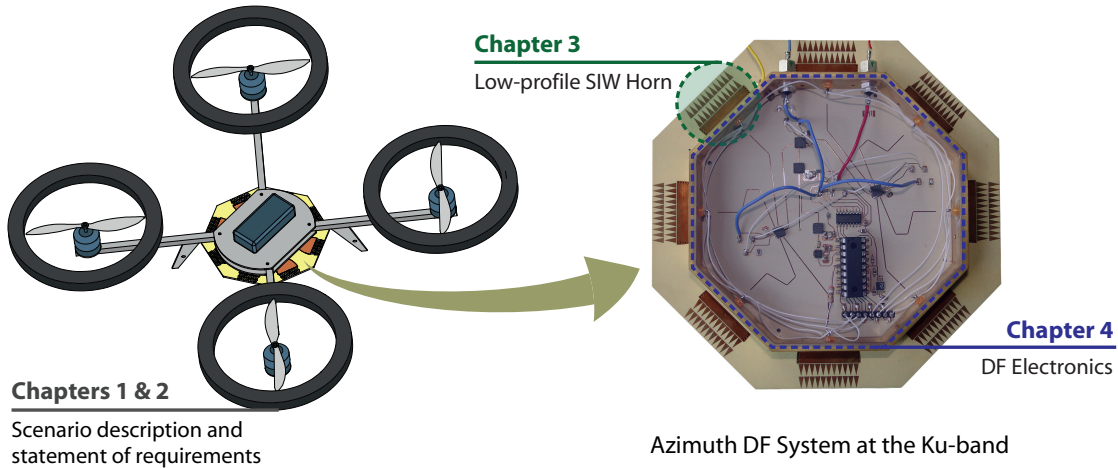


Fig. 1.4: Contributions of the chapters of this thesis to the low-profile direction finding system.

Chapter 5 - Extended Substrate Integrated Waveguide (ESIW)

Description: The characteristics of different substrate integrated guides are compared and combined to design a new guide able to carry orthogonally polarized modes. This guide, named as Extended Substrate Integrated Waveguide (ESIW), offers the same properties as standard SIWs concerning vertically polarized TE_{m0} modes, plus the additional capability of supporting horizontally polarized TE_{0n} modes (see Fig. 1.5). A rigorous analysis on the propagation characteristics and loss mechanisms of the TE_{01} mode in the ESIW is provided and experimentally verified.

Original contributions: This is, to our best knowledge, the first time that a dual-polarized substrate integrated guide with robust control over the different modes is presented. The impact of the different ESIW geometrical parameters on the propagation characteristics is studied both through the use of the Transverse Equivalent Network (TEN) representation and full-wave simulations. Importantly, a planar excitation scheme for the horizontally polarized TE_{01} mode is also designed for measurement purposes as well as to make this guide compatible with other SICs.

Chapter 6 - Dual-Polarized System based on the ESIW

Description: A substrate integrated Orthomode Transducer (OMT) based on the ESIW concept is first implemented. This is a key component typically needed in antenna feed chains used for dual-polarized communication systems. The complete structure, including the excitation schemes for both orthogonal TE_{10} and TE_{01} modes, requires only 2 layers of substrate. This OMT is then used to feed a dual-polarized horn antenna (see Fig. 1.5). Experimental results

prove the feasibility of creating dual-polarized substrate integrated systems and, therefore, fulfilling the second research line *B* of this thesis.

Original contributions: A methodology to easily design an OMT using only 2 layers of substrate is explained. Physical insight into the influence of the OMT dimensions on the different figures of merit (isolation, cross-coupling, etc.) is provided. This allows one to establish a relationship between electromagnetic performances and manufacturing complexity in order to adapt the OMT design according to the given specifications. A strategy to create a dual-polarized substrate integrated horn antenna offering similar performances for both orthogonal TE_{10} and TE_{01} modes is also proposed.

Chapter 7 - Conclusions and Perspectives

This last section summarizes the work done during this PhD thesis emphasizing the most important conclusions and original contributions. Future research lines are drawn concerning the different topics covered throughout the thesis.

The original contributions of this thesis have been validated and disseminated via several publications in scientific journals and presentations in conferences. The link between thesis chapters and publications is summarized in Tab. 1.2. The complete list of publications can be found at the end of this document, in page 151.

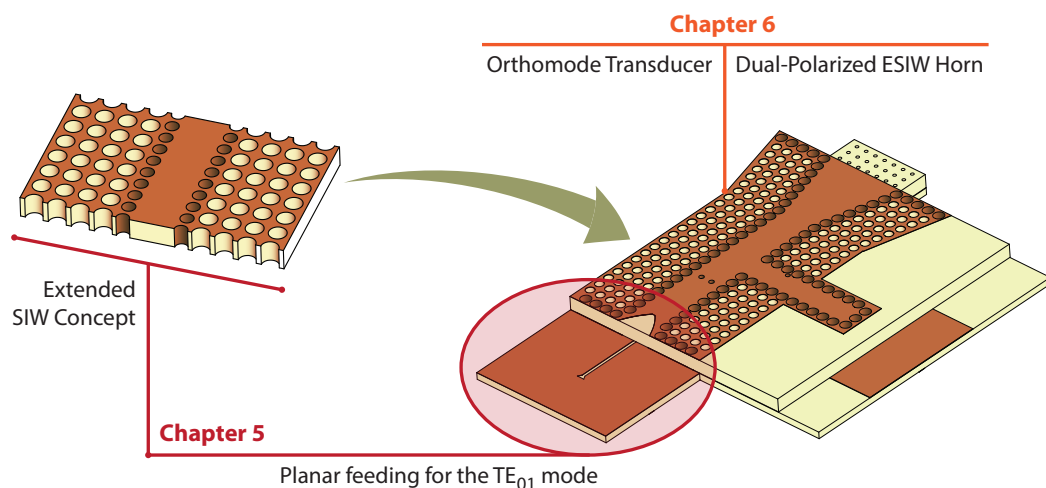


Fig. 1.5: Contributions of the chapters of this thesis to the dual-polarized substrate integrated system.

Chapter	Topic	Publications
3	Printed transition to improve the matching of SIW horn antennas	[9, 10]
	Printed transition to simultaneously improve the matching and radiation of SIW horns	[11]
	Novel thin and compact design for H-plane SIW horn antennas with improved performances	[12, 13]
4	Interconnection between SIW horn antennas and MMICs	[14]
	Low-profile DF system based on SIW horns and commercial electronic components	[15, 16]
5	The ESIW concept: a new guide for dual-polarized SICs	[17]
	Planar excitation scheme for the TE ₀₁ mode	[17]
6	Substrate integrated OMT	[18, 19]
	Dual-polarized substrate integrated horn antenna	[19]

Tab. 1.2: Link between the thesis chapters, topics and publications.

1.4 Additional Research Performed During the Thesis

As previously mentioned, the main activity during the PhD years was the fulfilment of the armasuisse project providing the financial support. Nevertheless, several additional activities frequently leading to fruitful interactions and cross-fertilizations are worth mentioning.

A collaboration with the Adaptive MicroNanoWave Systems - LEMA/Nanolab group was established in the field of Leaky-Wave Antenna (LWA). Its aim was the theoretical design of a graphene-based reconfigurable LWA to operate at the THz region and the work was presented in a conference paper [20] and in two journal papers [21, 22]. Nevertheless, since this work significantly differs from the main topics of the thesis, it has not been included in its main body but summarized in Appendix B.

In addition, in the course of this PhD thesis, three Master Theses were also supervised:

- "Metasurfing Leaky-Wave Antennas", Ioannis Iliopoulos, *School of Engineering (EPFL) and School of Electrical and Computer Engineering (AuTh, Greece)*, April 2013.
- "Numerical Study of Leaky Wave Antennas in SIW Technology", Mina Bjelogrić, *School of Engineering (EPFL)*, July 2013.
- "Steerable Beam Antenna for Industrial Sensing Applications", Nevena Saponjic, *School of Engineering (EPFL) and ABB-Switzerland*, July 2014.

The first one concerned the design of periodic LWAs based on metasurfaces and was in-line with the collaboration with the Adaptive MicroNanoWave Systems - LEMA/Nanolab group.

The second one also dealt with LWAs, but targeted a numerical study of SIW-based LWAs allowing for a fast modelling of these structures using equivalent circuits and transmission lines models. The objective of the third project was to build a complete demonstrator of a small phased array antenna at the C-band.

Finally, several contributions on writing technical proposals (mainly for the European Space Agency (ESA)) and pre-studies for new research projects were also carried out. In particular, the topics treated were: (1) miniaturised multi-function antenna system for nano-satellites, (2) cost effective antenna feed chains based on additive manufacturing, (3) Active Electronically Scanned Arrays (AESAs) and (4) Wireless Power Transfer (WPT).

2 Substrate Integrated Waveguide (SIW) Antennas and Systems

The original seed for the research described in this thesis was the challenge posed by the armasuisse project, whose main objective was to create an azimuth Direction Finding (DF) system for UAVs working at the Ku-band. The fundamental requirements of this system were to be low-profile, light weight and low-cost. To this end, the Substrate Integrated Waveguide (SIW) technology was chosen to implement the DF antenna array.

The bases of the SIW technology are recalled in Section 2.1. A literature review on different SIW antenna topologies is presented in Section 2.2 along with their common applications and frequency range of operation. After this general overview and taking into account the requirements stated in Section 1.2, the possible candidates for the DF antenna array are analysed in Section 2.3 and the most promising one is chosen.

2.1 The SIW Concept

The substrate integrated waveguide concept was first proposed in [23] and since then gave rise to a broad range of planar and non-planar circuits integrated within one or multiple substrate layers. The most significant feature of this technology is the possibility to integrate all the components on the same substrate, including passive components (filters, couplers, etc.), active elements (oscillators, amplifiers, etc.) as well as antennas [24–29]. In particular, [29] provides a recent and quite complete survey of the possibilities of this technology.

In SIW technology, the top and bottom metallizations of the substrate act as the top and bottom horizontal walls of the waveguide, while the vertical walls are synthesized by drilling and metallizing vias through the substrate. A representation of an SIW is shown in Fig. 2.1(a). These waveguides can largely preserve the well-known advantages of conventional rectangular metallic waveguides while keeping the advantages of microstrip lines, such as low profile, small volume and light weight. Therefore, common waveguide devices can be implemented

in a planar form and at low-cost by using standard processing techniques such as the PCB or the Low-Temperature Co-fired Ceramic (LTCC) [28–30].

The planar waveguide strictly referred as SIW (as the one in Fig. 2.1(a)) allow only the propagation of TE_{m0} modes, where the sub-index m refers to the direction parallel to the substrate plane. The electric field component of these modes is perpendicular to the substrate plane and parallel to the metallized vias. A sketch of the fundamental TE_{10} modes in an SIW is shown in Fig. 2.1(b). In order to carry other types of modes, alternative waveguide topologies can be also synthesis in a planar form, such as the Non-Radiative Dielectric (NRD) guide [31]. In this case, the concept of integrating waveguide components within a dielectric substrate is more generally referred as Substrate Integrated Circuits (SICs) which lead to the possibility of conceiving complete Systems-on-Substrate (SoS) [23]. This topic is treated in more detail from Chapter 5 on, whereas Chapters 2, 3 and 4 exclusively deal with SIWs and, therefore, with TE_{m0} modes.

The SIW technology also provides the advantages of high density component integration, low-profile and light weight. These aspects make it attractive for implementing flush-mounted antenna systems for vehicles. Then, the antenna system barely affects the vehicle aerodynamic and aesthetic profiles minimizing the drag. The combination of all these characteristics is the reason why this technology was chosen as the most suitable for the envisioned DF system as well as the cornerstone of this PhD thesis.

Many different types of antennas and complete communication systems based on the SIW technology can be found in the literature. In the following section, a selection of various kind of SIW-based structures are described in order to illustrate the potentialities of this technology.

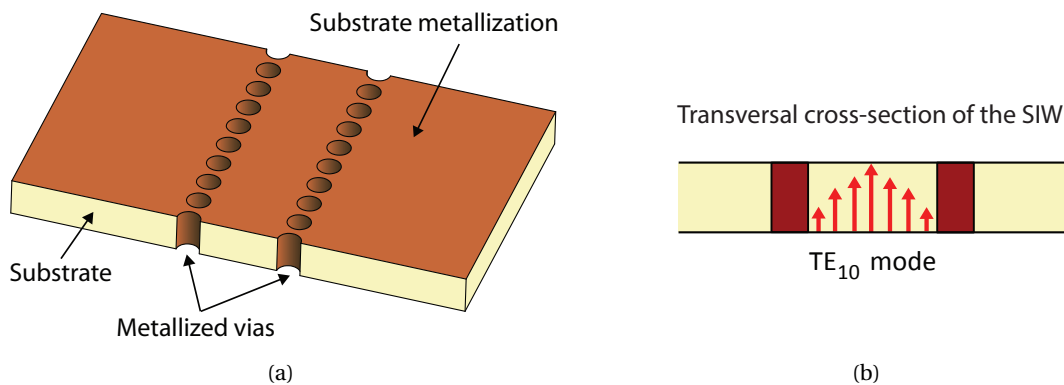


Fig. 2.1: (a) Substrate Integrated Waveguide (SIW) topology and (b) sketch of the electric field distribution of its fundamental TE_{10} mode. Metal is represented in brown, dielectric substrate in beige and the electric field in red.

2.2 Overview on SIW Antennas, Systems and Applications

The SIW concept opened the door to the use of many types of antennas which before were not considered for commercial applications due to its manufacturing complexity and/or high cost. Good examples are the slotted-waveguide antennas [32–42], horn antennas [9–13, 43–49], leaky-wave antennas [50–54] and cavity-backed antennas (patches, slots, etc.) [55–58]. A part from these antenna topologies which are fully implemented using SIWs, the performances of already existing printed antennas can be also improved by combining them with SIWs. For instance, more robust and complex feeding networks have been designed for tapered slots [59–62], printed yagi-udas [63–65] and even rod antennas [66–68]. The aims of the latter designs are typically to reduce the mutual coupling, to improve the polarization purity and/or to ease the system packaging.

Within the previous examples, one can find single radiators, 1D or 2D arrays with their corresponding Beam Forming Network (BFN) as well as complete RF subsystems. Many attention has been paid to the SIW slot antennas due to their attractive applications and their practical fabrication in a wide range of frequencies. Complete RF transceivers including several SIW components (such as mixers, power dividers, filters, phase shifters, etc.) and their interconnection with Surface Mounted Devices (SMD) have been reported for radar applications at 24 GHz [32, 33] or for high-data rate transmissions at 60 GHz [34, 35]. Other RF subsystems based on SIW slot antennas can be found at lower frequencies such as at the X-band [36] and at much higher frequencies for future applications at the sub-THz band [37]. The detailed design of SIW slot arrays has been also extensively studied for monopulse-tracking DF applications [38, 39], Ka-band multibeam satellite communications [40, 41] and even MIMO systems [42]. Some of these examples are shown in Fig. 2.2.

While SIW slot antennas can be used in a broad range of frequencies, other SIW antennas are of more interest beyond the Ku-band (particularly in the mm-wave region), since the thicknesses

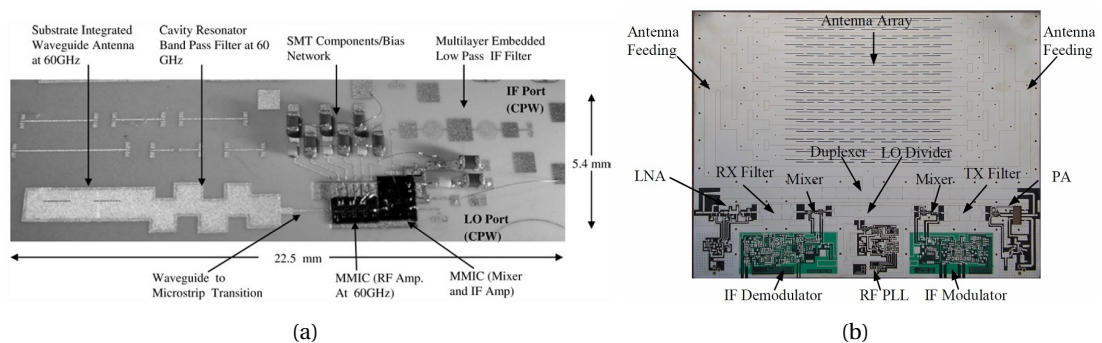


Fig. 2.2: Examples of communication systems based on SIW slot antennas: (a) 60-GHz multi-chip module receiver [34] and (b) X-band transceiver [36].

of commercial substrates limit their proper implementation at lower frequencies. This is mainly the case of cavity-backed antennas, SIW horn antennas and Leaky-Wave Antennas (LWA). Cavity-backed antennas have been used for implementing phased-arrays at the Ku/Ka-band thanks to their high degree of integration and reduction of the mutual coupling [58, 69]. The stable beam pattern, wide bandwidth and end-fire radiation of the SIW horns make them really attractive for communications systems requiring high density packaging, e.g., for high-data rate transmissions at the 60 GHz unlicensed band [47–49] (see Fig. 2.3(a)). Although the dispersive nature of LWA is not usually a wanted property in many commercial applications, some designs have been also proposed for multibeam scenarios [51] and for automotive radars at 77 GHz [52] (see Fig. 2.3(b)).

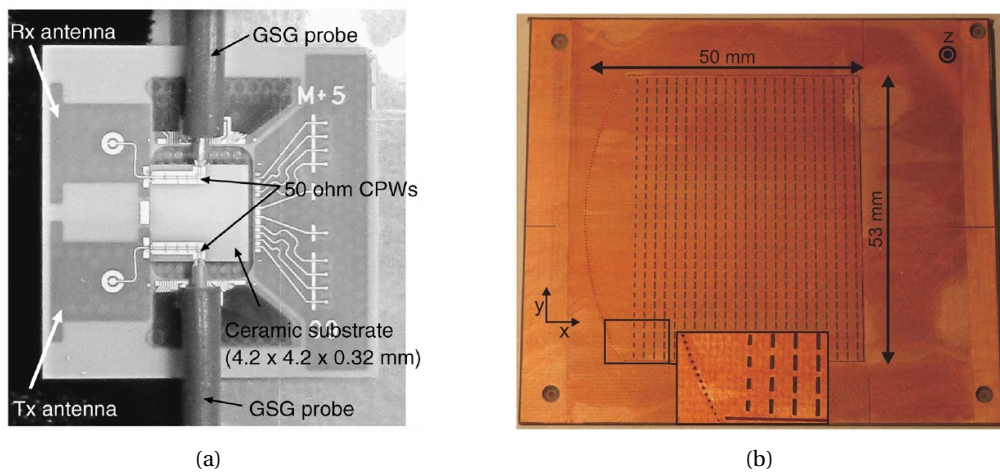


Fig. 2.3: Examples of communication systems based on (a) H-plane apertures for high-data rate transmissions at 60 GHz [47] and (b) LWA for automotive radars at 77 GHz [52].

2.3 DF Antenna Selection

The previous overview provides a snapshot on types of antennas and systems that can (and could) be built in SIW technology. Keeping these concepts in mind, as well as the requirements of Section 1.2, the possible antenna topologies to be used as basic element in the DF array are here discussed.

First of all, a planar array able to cover the 360° of the azimuthal plane implies the need for end-fire radiating elements with focusing capabilities. At the same time, it is also desirable to build all 8 antennas in a single layer of substrate, thus reducing both cost and time in the manufacturing process. These specifications narrow down the possible antenna candidates to the following: Tapered Slot Antennas (TSA), printed Yagi-Uda antennas, H-plane SIW horn antennas and end-fire Surface-Wave Antennas (SWA).

Low-profile DF systems based on TSAs (or Vivaldis) and planar Yagi-Udas have been already proposed [5, 70], where they also achieve full azimuthal coverage by using an 8-element beam-switching array (see Fig. 2.4(a)). However, in addition to a medium-low FTBR (< 10 dB) and a high mutual coupling (> -15 dB) the antennas are horizontally polarized. Some trials to use these types of antennas in vertically polarized systems result in structures that are complex to manufacture and mechanically weak. An example can be found in [71], where a Rotman lens is used to implement a planar BFN, but then TSAs are connected to it in a perpendicular manner (see Fig. 2.4(b)). In our case, this approach loses the most important advantages of the SIW technology namely low-profile and ease of manufacture.

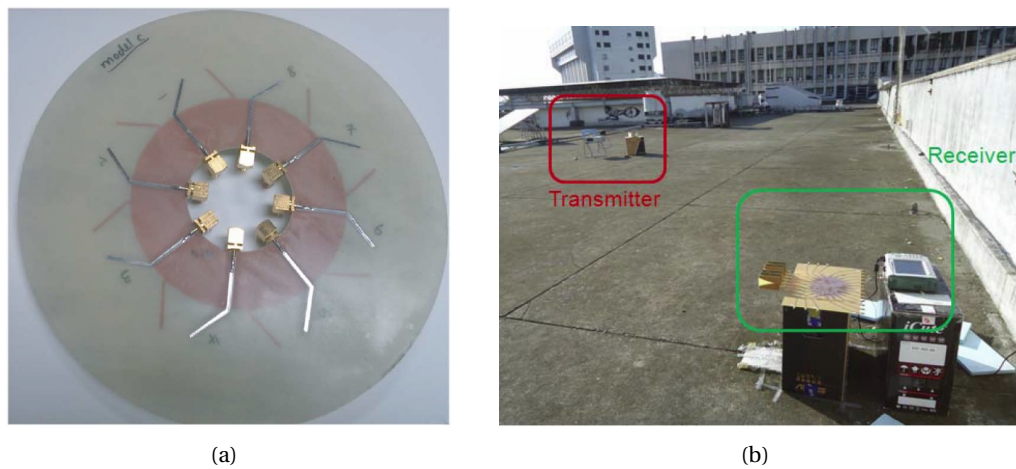


Fig. 2.4: Examples of DF systems based on TSAs: (a) Horizontally polarized system based on an 8-element circular array [5] and (b) vertically polarized system based on a Rotman BFN [71].

After the previous observation, the two remaining antenna candidates are the H-plane SIW horn antenna and the end-fire SWA. An H-plane SIW horn is created as a standard H-plane horn, i.e., by flaring the SIW dimensions parallel to the H-field while keeping the other dimension (substrate thickness) constant [43, 72]. Thus, the radiation is focused in the H-plane and, as the flare angle is increased, the H-plane beamwidth becomes narrower up to a given flare. An illustrative example of how to mimic a conventional horn antenna with SIW technology is shown in Fig. 2.5.

When referring to an end-fire SWA, one means an antenna based on the excitation of TM vertically polarized surface-waves along a dielectric slab, which propagate until its edge to finally radiate by diffraction [73, 74]. The radiation properties can then be controlled by properly shaping the edge of the slab (similarly to a lens) as shown in Fig. 2.6. These both antenna topologies fulfil the most important requirements of our DF system: They are vertically polarized, offer focusing capabilities and all 8 array elements can be built in a single layer of substrate.

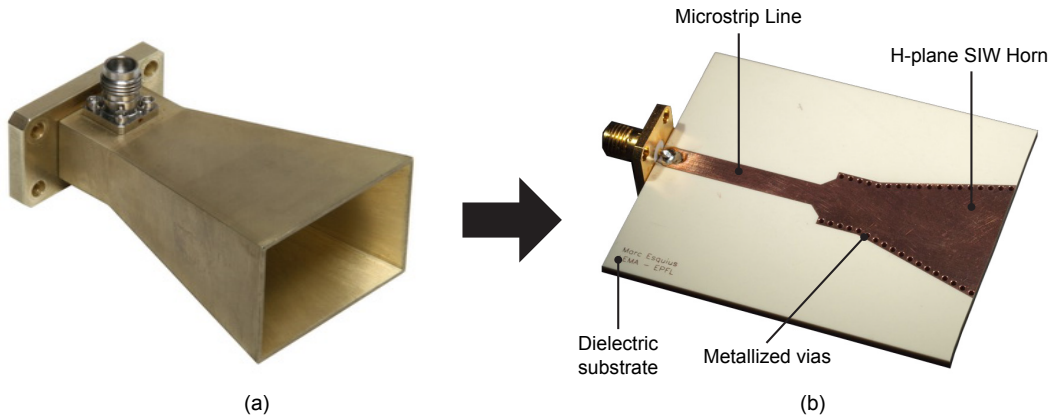


Fig. 2.5: (a) Conventional horn antenna and (b) its counterpart in SIW technology.

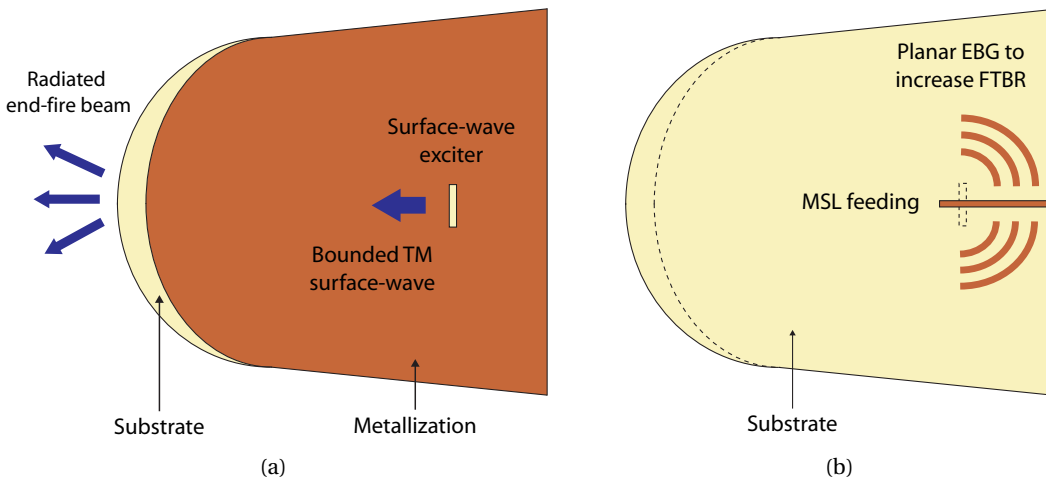


Fig. 2.6: (a) Top and (b) bottom view of an end-fire Surface-Wave Antenna (SWA) example.

It must be pointed out that other printed antennas such as higher-order mode patch antennas (e.g., with the TM_{21} mode) may also radiate vertically polarized waves at the substrate edge [75, 76]. However, they radiate in an omnidirectional manner and the possible strategies to focus the radiation would require bulky non-printed elements.

In order to choose the most appropriate antenna, the rest of the electromagnetic requirements must be analysed in more detail. Concerning SIW horn antennas, a stable HPBW of 45° can be easily achieved: Clear and simple design rules are provided even in the case of dielectric loaded horn antennas like SIW horns [72]. In addition, their practically enclosed structure guarantees a low mutual coupling between adjacent array elements as well as good control over the radiated beam.

The main drawback of H-plane SIW horns is that both the matching and the FTBR are linked to the substrate thickness h and they deteriorate as h decreases. This is a well known problem

and, commonly used solutions such as the use of dielectric lenses are not efficient when $h < \lambda_0/6$. As explained in Section 1.2, the required substrate thickness h in our DF system is around $\lambda_0/10$ which would yield a poor and narrow matching ($< 2\%$) as well as low FTBR (< 5 dB). This degradation of performances is the main drawback on the use of H-plane SIW horn antennas in our DF array.

Regarding end-fire SWAs, they are typically used to generate narrow pencil-beams because less directive beams may suffer from a high side-lobe level due to undesired diffractions at the substrate's edge [77, 78]. Wider beams may be obtained, but a specific design should address the reduction of the side-lobes. The thickness h of the substrate must be chosen not only to support the propagation of TM surface-waves, but also to provide a good coupling between these and the surface-waves exciter (see Fig. 2.6(a)). Following the considerations and design rules of [79], one can see that antennas of thickness $h \simeq \lambda_0/10$ and 10% bandwidth can be created by properly designing the surface-wave exciter. Moreover, a medium-high FTBR ($\simeq 10$ dB) can be obtained by including planar Electromagnetic Band-Gap (EBG) structures (see Fig. 2.6(b)) to attenuate the surface-waves travelling towards undesired directions [77].

The stability and robustness of an SWA, however, strongly depend on the efficient control of all surface-waves. The inability of properly guiding some of the surface-waves may greatly increase the mutual coupling between array elements and/or even damage the future electronic components. In order to control them, a considerable amount of surface is usually needed meaning that a single antenna could be several wavelengths in size [77, 78]. For the same reason, it might be also difficult to achieve the required values of directivity/gain.

A summary of the electromagnetic performances of H-plane SIW horns and end-fire SWAs is presented in Tab. 2.1. Preliminary designs using full-wave electromagnetic solvers¹ were conducted in both antenna types to verify their expected performances as well as to identify potential drawbacks. On the one hand, SWAs revealed not to be suitable for our purposes due to difficulties in obtaining a stable radiation pattern and in controlling all surface-waves. This fact, added to the semi-opened structure of this antenna, led to the appearance of nulls in the elevation plane pattern (E-plane), thus not completely covering the required E-plane HPBW of 180° . On the other hand, despite the aforementioned drawbacks of the H-plane SIW horn, this one proved to be the most robust and reliable solution.

The matching and radiation problems of H-plane SIW horn antennas are studied in detail in the next chapter. This further study induced the design of a fully printed transition to solve these problems and to finally obtain an SIW horn which widely fulfils all the DF system requirements.

¹All the simulated results presented throughout this thesis have been obtained with the commercial full-wave electromagnetic solver Ansys HFSS v14.

Characteristics	H-plane SIW Horn	End-fire SWA
Vertical Polarization	✓	✓
Bandwidth > 5%	X	✓
H-plane HPBW $\approx 45^\circ$	✓	~
E-plane HPBW $\approx 180^\circ$	✓	X
FTBR > 15 dB	X	~
Gain > 6 dBi	✓	~
Mutual Coupling < -30 dB	✓	X
Surface size	✓	~

Tab. 2.1: Performances of the two antenna candidates considering a substrate of thickness $\lambda_0/10$ and the specifications stated in Section 1.2.

2.4 Conclusions

The SIW technology have been chosen as the best option to implement the DF antenna array thanks to its excellent characteristics in terms of low-profile, light weight and low-cost. The basis of the SIW technology have been briefly recalled and a literature review on SIW antennas and RF systems has been performed. This allowed us to classify the main SIW antenna topologies according to their electromagnetic properties and to their possible applications. This study also served to show the potentialities of this technology as well as its practical limitations.

After a preliminary evaluation of the different antenna candidates, the H-plane SIW horn antenna has been chosen as the best option to construct the DF array. Nevertheless, the practical implementation of this antenna at the Ku-band and below turns out to be very challenging, leading to poor performances in terms of matching and radiation. The next chapter is devoted to study in detail the reasons behind these problems and to propose a printed solution to simultaneously solve them both.

3 Thin and Compact H-plane SIW Horn Antenna

The H-plane SIW horn antenna is the most commonly used antenna in planar systems requiring vertically polarized signals radiated at the end-fire direction [9–13, 43–49]. However, as mentioned in the previous chapter, the thicknesses of commercially available substrates restrict its use at the Ka-band and above. This is because the H-plane SIW horn performances diminish significantly when the substrate thickness h is much smaller than the free space wavelength λ_0 .

This degradation of performances is frequently encountered at frequencies lower than 20 GHz. At this frequency range, most commonly available substrates are thinner than $\lambda_0/6$ and the mismatch between the antenna aperture and the air results in poor matching and unwanted back radiation. Furthermore, existing thicker substrates ($h > 2.5$ mm) are not preferred for manufacturing SIW components because the via-hole metallization is challenging and eventually flawed.

Aiming to use the H-plane SIW horn as basic element in our DF array, an integrated solution to extend its use below 20 GHz is here presented. First, the characteristics and principles of operation of this antenna are explained in Section 3.1. This first study illustrates and brings to light the reasons behind the aforementioned problems. To tackle these problems, a fully printed solution is developed in Section 3.2 to improve the matching and in Section 3.3 to improve the radiation of H-plane SIW horns. On top of these improvements, the horn taper is further optimized in Section 3.4 to reduce the needed aperture size for a given directivity.

The combination of all these concepts defines a new family of SIW horn antennas with really attractive properties to be used in commercial applications at the Ku-band and below. In Section 3.5, guidelines to easily design these horns are provided and applied to manufacture a prototype which validates the theoretical results.

3.1 Principle of Operation of H-plane SIW Horns

A schematic view of a H-plane SIW horn antenna is shown in Fig. 3.1. H-plane horn antennas are created by flaring the dimension of a rectangular waveguide parallel to the H-field, while keeping the perpendicular dimension constant. Thus, the radiation is focused in the H-plane and, as the flare angle is increased, the H-plane beamwidth becomes narrower up to a given flare. Beyond that point, the pattern starts to broaden, due essentially to the phase error across the aperture of the horn [80].

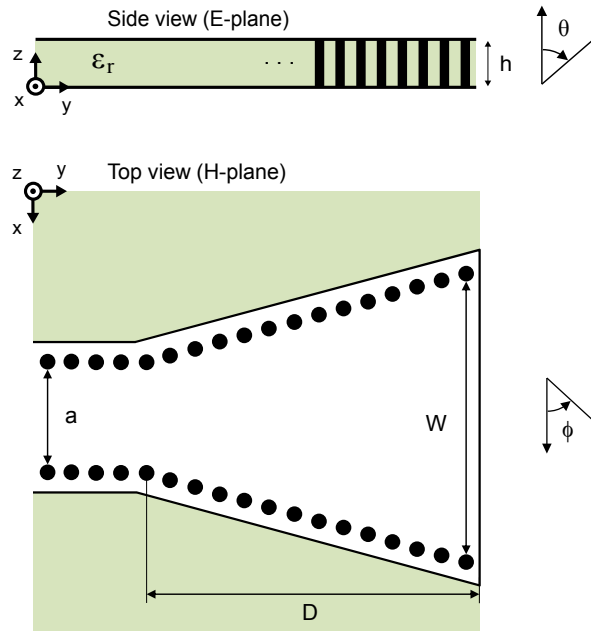


Fig. 3.1: Side and top view of a H-plane SIW horn. Metal is represented in white, the dielectric substrate in grey and the metallized via holes in black.

To ensure the single mode excitation of a H-plane SIW horn, the equivalent width of the feeding waveguide¹ a_{eq} should be $\lambda_0/(2\sqrt{\epsilon_r}) < a_{eq} < \lambda_0/\sqrt{\epsilon_r}$ and the height h (in this case the substrate thickness) smaller than $\lambda_0/(2\sqrt{\epsilon_r})$, where λ_0 is a wavelength in free space. Therefore, following this trend, h could be as small as desired. However, when the dielectric slab becomes thinner, the mismatch between the horn aperture and the air increases which yields a poor matching and bandwidth.

The design rules for SIW H-plane horn antennas follow the same principles as for conventional horns. Hence, the same strategies to improve their performances can be used. However, the constraints associated with the SIW technology make some solutions more feasible than others. A common way to improve the horn performances and to reduce its dimensions is

¹The equivalent width a_{eq} is the width of the equivalent waveguide created between the SIW vias. Several approximate expressions to compute a_{eq} according to the vias dimensions can be found in [29].

to place a lens over the horn aperture. Usually, dielectric lenses are used since metal-plate lenses introduce a polarizing effect and their edges cause diffraction [72]. In the case of SIW horns, this solution is easy to implement because the lens can be created by extending the same dielectric slab where the horn is built [44, 45]. These horns are known as lens-corrected horns [72], where the lens focuses the radiation frontwards increasing the Front-to-Back Ratio (FTBR) and reducing the phase error. This solution provides good performances in terms of matching and FTBR as reported in [45]. Nevertheless, for substrates of small thicknesses (generally speaking $h < \lambda_0/6$), such solutions are not feasible because the effect of the lens becomes negligible.

To illustrate these limitations, the performances of a lens-corrected SIW horn antenna with different thickness are compared in Fig. 3.2. The horn is designed to work at 16.5 GHz in a substrate of $\epsilon_r = 4.5$ that is extended 18 mm after the horn aperture to create the lens. According to the notations in Fig. 3.1, the dimensions of the horn are [mm]: $W = 28$, $D = 20$ and $a = 9$. It can be seen in Fig. 3.2(a) that, with a $h = \lambda_0/4 = 4.7$ mm, a -10 dB bandwidth of 10% is achieved around 16.5 GHz. However, as h decreases, the bandwidth is greatly reduced until the point that, at $h = \lambda_0/12 = 1.5$ mm, the $|S_{11}|$ is practically flat presenting only poor narrow resonances.

From the radiation point of view (see Fig. 3.2(b)), the effect of the lens also becomes less relevant as h is reduced: The beamwidth is increased (i.e., no phase correction) and the FTBR is decreased (i.e., no focusing). As expected, for a $h = \lambda_0/12$ the SIW horn radiation resembles the one of a slot antenna with a low FTBR. Notice that ϕ -angles are defined in such a way that the horn front direction is $\phi = 90^\circ$ and the back direction $\phi = 270^\circ$. The phase error is not a major problem because it can be solved by increasing the horn H-plane dimensions. However, the FTBR remains an important issue since the E-plane dimension h cannot be increased.

Another possible solution which aims to improve the radiation performances of end-fire SIW antennas has been presented in [47]. In this case, the antenna directivity is increased by placing two parasitic elements after the horn aperture which focus the radiation at the E-plane, similarly to a Yagi-Uda antenna. Nevertheless, a substrate of $h \simeq \lambda_0/5$ is used and, if h is reduced, the radiation and matching performances degrade akin to the previous example.

In the next section, the matching problems of SIW horns are studied in more detail and a printed solution to create low-profile SIW horns with more than a 10% bandwidth is proposed.

3.2 Matching Improvements

So far, the only known integrated solution to improve the performances of SIW horn antennas is the use of a dielectric lens. Of course, other solutions based on non-printed elements have

been also proposed [46, 81], but they result in complicated and expensive building procedures not suitable for mass production. In this section, a printed transition is proposed to improve the matching of SIW horns, even when built in substrates thinner than $\lambda_0/10$. The transition is etched on the same dielectric slab as the antenna which keeps the advantages of both compactness and integration of the SIW technology. A sectoral H-plane SIW horn with the proposed transition is represented in Fig. 3.3.

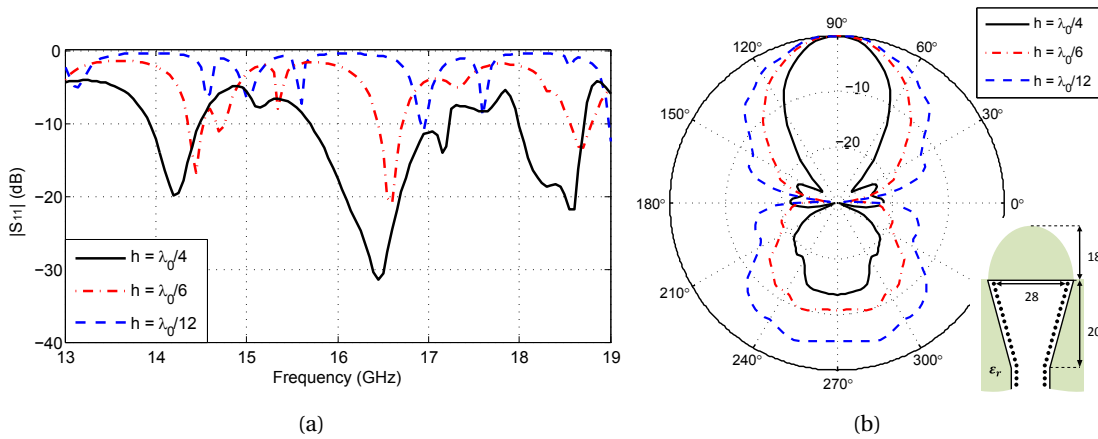


Fig. 3.2: Comparison of a lens-corrected SIW horn antenna with different thickness. (a) Reflection coefficient and (b) normalized radiation patterns (H-plane) at 16 GHz. The dimensions of the horn are in *mm* and $\epsilon_r = 4.5$.

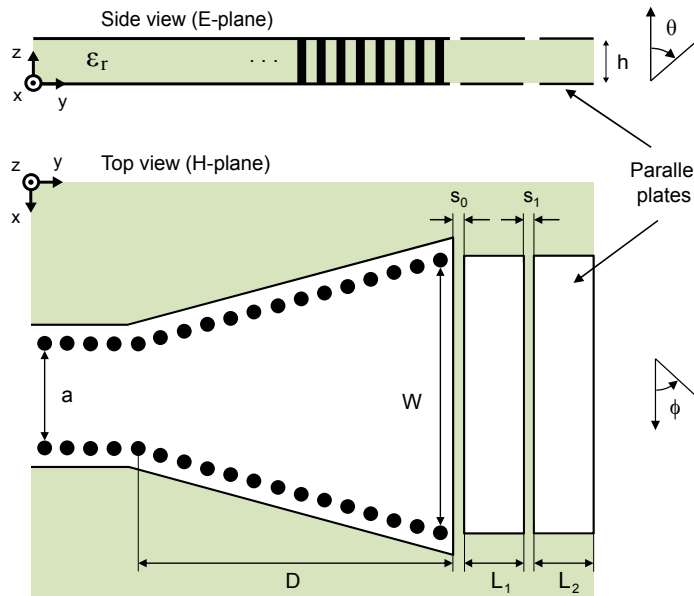


Fig. 3.3: Side and top view of the proposed H-plane SIW horn with a 2-block printed transition. Metal is represented in white, the dielectric substrate in grey and the metallized via holes in black.

A simplified Coupled Resonator (CR) model to explain and predict the behaviour of this transition is derived in Section 3.2.1. For more quantitative information about the reflection coefficient $|S_{11}|$, a Transmission Line (TL) model is developed in Section 3.2.2. Design guidelines are given in Section 3.2.3 and applied to manufacture a prototype with different transitions in Section 3.2.3.

3.2.1 Coupled Resonator Model

The degradation of the reflection coefficient seen in Fig. 3.2(a) is due to the mismatch at the antenna-air interface and does not depend on the feeding system. To smooth the impedance gap between the horn aperture and the air, a transition is placed after the horn aperture. This transition can be seen as a concatenation of blocks, each one being a parallel plate waveguide of length L_i separated by gaps of width s_i .

The proposed printed transition can be studied as a 2D structure where the width (x direction) is assumed to be infinite (see Fig. 3.4). To explain its working principle, the transition can be seen as a concatenation of blocks acting as resonators, each one being a parallel plate waveguide separated by gaps. The resonant frequency $f r_1$ of one stand-alone block is:

$$f r_1 = \frac{c}{2L_{eq}\sqrt{\epsilon_r}} \quad (3.1)$$

where L_{eq} is an equivalent length that is larger than L to consider the effect of the fringing field. According to [82], L_{eq} can be estimated by $L(1 + 0.7h/L)$.

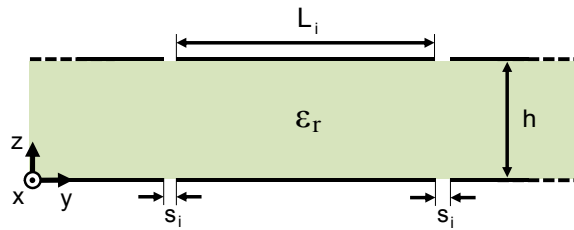


Fig. 3.4: Cutting view of the printed transition structure with the associated notations.

When two or more blocks are separated by a distance s_i , charges build up on the ends of the metallic plates, generating a capacitance which produces a shift in their resonant frequency $f r_1$. The physical explanation of this shift is that the coupling effect enhances and reduces the capability of a single block to store charge [83]. Thus, in the case of two blocks, a frequency higher ($f r_{2+}$) and a frequency lower ($f r_{2-}$) than $f r_1$ are generated.

In the theory of coupled resonators, a coupling factor k_2 is used to calculate $f r_{2\pm}$. This factor is defined as the ratio between the capacitance generated by the coupling effect C_C and the capacitance of the original structure C_0 . Therefore, the new resonant frequencies can be

calculated as follows:

$$fr_{2\pm} = \frac{fr_1}{\sqrt{1 \mp k_2}}. \quad (3.2)$$

Note that the presented structure differs from coupled microstrip resonators since there is no ground plane, i.e., there is a discontinuity (gap) at the ground plane. The presence of this gap slightly modifies the procedure used in the coupled resonators theory for calculating fr_{i-} [83]. Actually, in this case, the gap enhances even more the capability to store charge of a single resonator. Therefore, the fr_{i-} generated by the proposed structure are lower than the model predictions. However, in Section 3.2.2 it is shown that the frequencies fr_{i-} are of less interest than the fr_{i+} .

Let us now describe how to find the coupling factor k_i , i.e., C_C and C_0 , in the case of a structure of 2, 3 and N blocks.

Two Block Structure

When two blocks are concatenated, the capacitances C_S generated by the gaps at the top and bottom faces contribute to the coupling effect. Therefore, since both gaps are in series, C_C equals $C_S/2$. Hereinafter we consider for simplicity that the gaps are $s_0 = s_1 = s$.

The capacitance per unit of length C_S can be obtained using the conformal mapping technique [84]. Thus, provided that $s/h \ll 1$, C_S is given as follows:

$$C_S(L_1, L_2) = \varepsilon_0(\varepsilon_r + 1) \frac{K(\sqrt{1 - p^2(L_1, L_2)})}{K(p(L_1, L_2))} \quad (3.3)$$

with

$$p(L_1, L_2) = \sqrt{\frac{1 + L_1/s + L_2/s}{(1 + L_1/s)(1 + L_2/s)}}$$

where $K()$ is the complete elliptic integral of the first kind. The lengths of the metallic plates at each side of the slot are noted as L_1 and L_2 . In the current case, two equal blocks are concatenated meaning that $L_1 = L_2 = L$.

Concerning the capacitance of the original structure C_0 , its value is twice the capacitance between the two metallic parallel plates of one block, $2C_P$. The fringing fields effect must be considered to obtain an accurate result for C_P . This effect is only relevant at the exterior faces while it can be neglected at the junction between blocks. Following the approach presented in [85], the capacitance per unit of length C_P can be estimated by:

$$C_P \simeq \frac{\varepsilon_0 \varepsilon_r L}{h} \left(1 + \frac{h}{\pi L} \ln \left(\frac{\pi L}{h} \right) \right). \quad (3.4)$$

Finally, the coupling factor for the case of 2 blocks is calculated as:

$$k_2 = \frac{C_C}{C_0} = \frac{1}{2} \frac{C_S(L, L)}{2C_P}. \quad (3.5)$$

N Block Structure

Several aspects should be taken into account when more than 2 blocks are concatenated. As an example, a structure of 3 blocks is now considered. A sketch of the electric field in the upper part of this structure is presented in Fig. 3.5, where it can be seen that now the central metallic plate contributes to generate two capacitances.

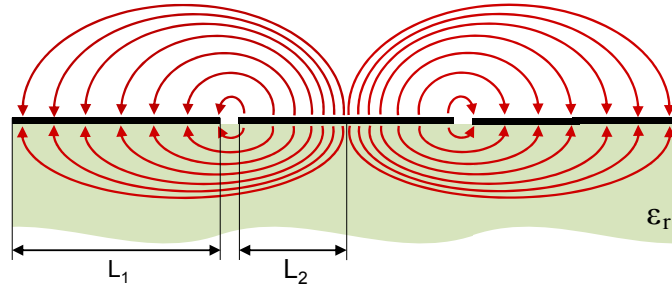


Fig. 3.5: Representation of the electric field distribution in the half upper part of a 3 block transition.

In order to obtain the coupling capacitance C_C , the new values for the different C_S can be calculated by applying again the conformal mapping technique. Nevertheless, for $s/L \ll 1$, a good approximation for the capacitance of each gap is to apply (3.3) with $L_1 = L$ and $L_2 = L/2$ as illustrated in Fig. 3.5. This approach can be also followed in the case of more blocks. It provides a physical insight on the behavior of the structure without the need to use the specific conformal mapping transformation in each scenario.

Regarding the calculation of C_0 , the exterior blocks in a 3 block structure are under the same conditions as the ones of a 2 block structure. Thus, their capacitance value is also C_P . However, the middle block has no exterior faces meaning that its capacitance is calculated neglecting the fringing fields effect. Therefore, its per unit length value is $C_{P0} = \epsilon_0 \epsilon_r L/h$.

From the previous reasoning, the coupling factor k_3 for the case of 3 blocks is:

$$k_3 = \frac{C_C}{C_0} = \frac{1}{2} \frac{2C_S(L, L/2)}{2C_P + C_{P0}}. \quad (3.6)$$

The same reasoning can be extended to N blocks by adapting the values of C_S and C_P for each gap or parallel plate structure, respectively. The general expression of the coupling factor k_N

where $N \geq 3$ is:

$$k_N = \frac{1}{2} \frac{2C_S(L, L/2) + (N-3)C_S(L/2, L/2)}{2C_P + (N-2)C_{P0}}. \quad (3.7)$$

The intermediate frequencies that appear between the lowest and highest frequency are also obtained following the theory of coupled resonators [83]. However, it will be explained in Section 3.2.3 that it is not convenient in practise to design a more than 3 block transition.

CR Model vs Full-Wave Simulations

To validate the CR model, the resonant frequencies of a printed transition composed of 1, 2 and 3 block are also computed using HFSS. The resonances above f_{r1} are predicted with a very good accuracy (relative error < 2%) as shown in Tab. 3.1. As expected, the resonances below f_{r1} are less well estimated ($\sim 6\%$).

Number of blocks	Full-wave (GHz)	CR model (GHz)
1	17.95	18.03
2	15.75	16.61
	19.50	19.89
3	15.25	16.21
	17.20	18.03
	20.40	20.63

Tab. 3.1: Resonant frequencies for different transitions ($L = 3.8$ mm, $h = 1.5$ mm, $s = 0.15$ mm, $\epsilon_r = 2.94$)

This CR model allows for a quick prediction of the resonant frequencies of the proposed transition. When quantitative information about the $|S_{11}|$ is required, more aspects need to be considered: source and load impedances, propagating modes, radiation losses, etc. To this end, a Transmission Line (TL) model is proposed in the next section.

3.2.2 Transmission Line Model

A TL model is proposed to compute the $|S_{11}|$ of a horn loaded with the printed transition. The transition is also decomposed into blocks, now taking into account the width W in the x direction defining a 3D problem. Each block is formed by a slot, modeled as a capacitance C_S in parallel with a radiation resistance R_{rad} , and a parallel plate waveguide, defined by its characteristic impedance Z_{pp} and propagation velocity v_{pp} . These blocks are then cascaded to model the full transition.

Note that the TL model of one block is asymmetric (see Fig. 3.6(a)). This has been chosen to accurately represent the transition structure which starts after the horn aperture with a gap

and ends with a parallel plate open-ended termination.

The antenna (horn) is modeled as a generator with an equivalent impedance Z_A . Finally, a load Z_{air} connected at the end of the TL model represents the outer boundary of the transition, i.e., the open-ended termination of the last parallel plate waveguide (see Fig. 3.6(b)).

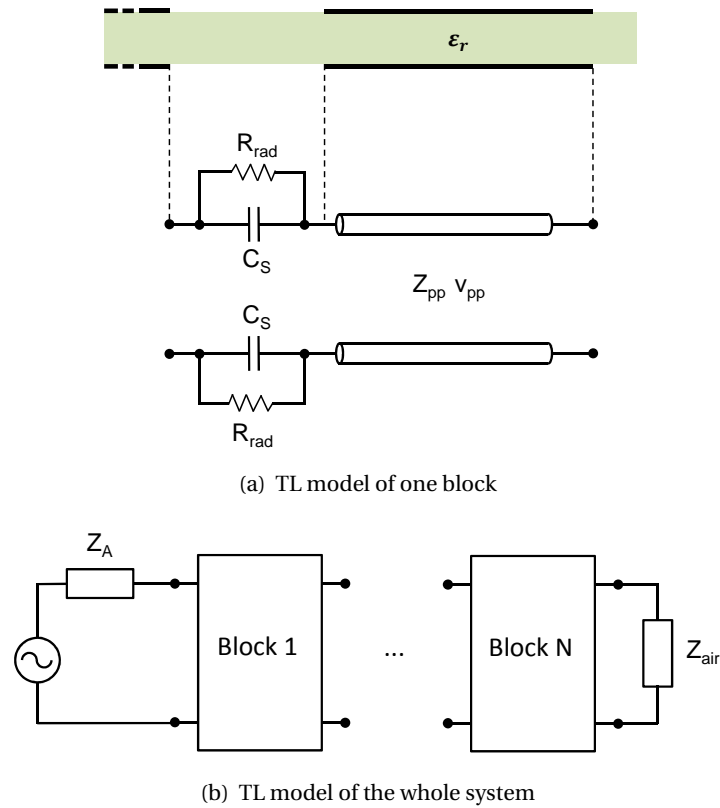


Fig. 3.6: Transmission Line model of the system: antenna, transition, air.

Block's Parameters

One block is completely defined by four parameters: C_S , R_{rad} , Z_{pp} and v_{pp} .

The different values of C_S are obtained using (3.3) with W as length dimension. For more accurate results, the substrate thickness h is also considered when using the conformal mapping technique [86].

The electric field distribution across the slot is nearly uniform. Therefore, the radiated power can be computed as the one of a uniform distribution aperture and, by assuming that the

voltage between plates is $V = |E_0|s$, the radiation resistance R_{rad} is given as follows:

$$R_{rad} = \frac{|E_0|^2 s^2}{\oint_S W_{av} dS} \quad (3.8)$$

where W_{av} is the average power density of a uniform distribution aperture [80].

It is assumed that the main propagating mode in the parallel plates waveguide is the TEM mode. Therefore the following expressions are used:

$$Z_{pp} = \sqrt{\frac{L_{pp}}{C_{pp}}} \quad (3.9)$$

$$v_{pp} = \frac{1}{\sqrt{\epsilon_{rpp}\epsilon_0\mu_0}} \quad (3.10)$$

where L_{pp} and C_{pp} are the inductance and capacitance in a TEM parallel plates waveguide and ϵ_{rpp} is the effective relative permittivity between the rectangular parallel plates.

To obtain more accurate results, the values for C_{pp} and ϵ_{rpp} are computed taking into account the effect of the fringing fields. The expression of C_{pp} depends on the position of the block following the same reasoning described for C_p in Eq. (3.4). Using the quasi-static approximation and figures presented in [87], ϵ_{rpp} is computed as the quotient between the capacitance of the parallel plates filled with a dielectric substrate and filled with air.

Antenna and Air Parameters

A good approximation of the horn impedance where only the TE_{10} mode propagates is given by:

$$Z_A = \frac{k_{wg}\eta_{wg}}{\beta_{wg}} \frac{h}{W} \quad (3.11)$$

where k_{wg} is the wavenumber, η_{wg} the wave impedance and β_{wg} the propagation constant of the waveguide [88].

The open-ended termination of the last parallel plate waveguide is modeled with an air impedance Z_{air} computed as:

$$Z_{air} = \frac{1}{W(g_s + jb_s)} \quad (3.12)$$

The real part of the air admittance Wg_s represents the radiation effect while the imaginary part Wb_s models the stored energy. Their expressions can be found in Chapter 10.2 of [89].

TL model vs Full-Wave Simulations

A transition composed of several blocks is placed in front of a long horn in order to minimize the amplitude and phase error at the aperture. A commercial substrate Rogers RO 4350 ($\epsilon_r = 3.66$, $h = 1.524$ mm) is considered and the different dimensions [mm]: $L = 3.6$, $s = 0.2$, $W = 20$, $D = 50$. With these parameters, f_{r_1} is equal to 16.8 GHz (from Eq. (3.1)).

The $|S_{11}|$ comparison between HFSS simulations and the TL model for a transition of 2 and 3 blocks is presented in Fig. 3.7. In both cases, a good agreement is achieved concerning the position and level of the resonances. Therefore, it is clearly demonstrated that fast and accurate preliminary results can be obtained using the TL model before performing final full-wave simulations.

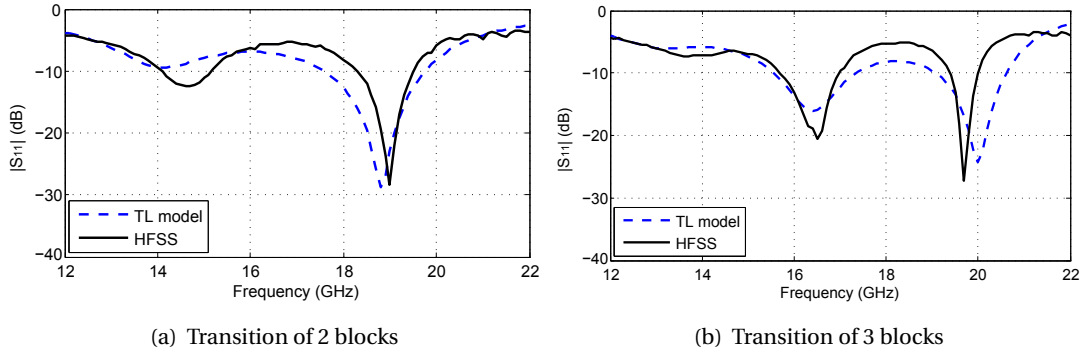


Fig. 3.7: $|S_{11}|$ comparison between HFSS and the TL model for an SIW horn with different transitions.

As pointed out in Section 3.2.1, the low resonances $f_{r_{i-}}$ are due to the enhancement in the storage capability thanks to the coupling effect. It can be seen that, in general, these resonances present a poor matching being of less interest than the ones above $f_{r_{i+}}$.

3.2.3 Design Guidelines

The steps to design an SIW horn with the proposed transition are the following:

1. With a given substrate (h and ϵ_r), the horn dimensions are chosen (D , W , and a) to excite only the TE_{10} mode and to obtain an acceptable quadratic phase error at the horn aperture [80].
2. The number of blocks (N) is chosen depending on the desired number of frequency bands. Then, Eqs. (3.1)-(3.2) are used to compute the initial dimensions of the printed transition (L and s). Afterwards, the TL model of Section 3.2.2 is applied to further tune these dimensions.

According to the CR model described in Section 3.2.1, it is in principle possible to design a transition working at any desired frequency. However, the following trends should be kept in mind when it comes to choose the values of L , s , h and ϵ_r :

- Increasing the ratio h/L improves the matching and bandwidth but other modes might be excited.
- Reducing the ratio s/L diminishes the radiation losses, but also the bandwidth is reduced.
- Increasing the value of ϵ_r increases even more the antenna-air mismatch.

A reasonable trade-off is the following: $0.25 < h/L < 0.5$, $0.03 < s/L < 0.06$, $\epsilon_r < 5$. The accuracy of the two proposed models is good when the transition dimensions are within these boundaries. Considering the transition as a transformer between the antenna and the air impedances, a recommended starting point is to set to $L = 0.4\lambda_0/\sqrt{\epsilon_r}$.

Regarding the choice of the number of blocks, it is not recommended to use more than 3. Adding more blocks increases indeed the radiation losses which leads to narrower and poorer resonances. To illustrate this effect, a transition of 5 blocks is placed in front of the SIW horn used for the comparison in Fig. 3.7. The simulated $|S_{11}|$ results with HFSS and the TL model are plotted in Fig. 3.8. As expected, even with the use of 5 blocks, only 3 narrow working frequency bands (relative bandwidth around 5% at -10 dB) are obtained.

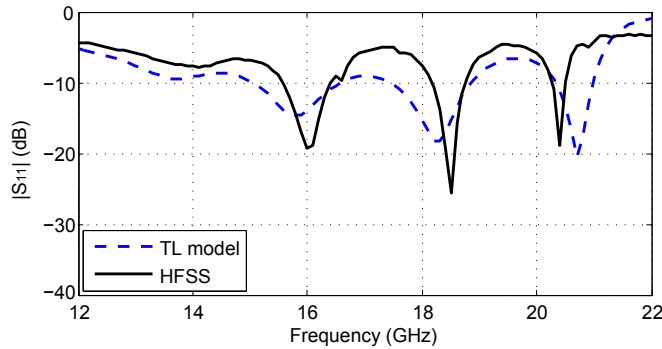


Fig. 3.8: $|S_{11}|$ comparison between HFSS and the TL model for an SIW horn with a 5 block transition.

3.2.4 Experimental Results

A H-plane SIW horn antenna with the proposed printed transition was built to validate the matching improvements as well as the proposed simplified models. Using a commercial substrate Rogers TMM3 ($\epsilon_r = 3.27$, $h = 1.91$ mm), this antenna alone presents a poor matching ($|S_{11}| > -10$ dB) at the Ku-band (between 12 and 18 GHz) as shown in Fig. 3.10(a). Therefore,

the proposed transition is implemented to match the SIW horn at different frequencies at this band.

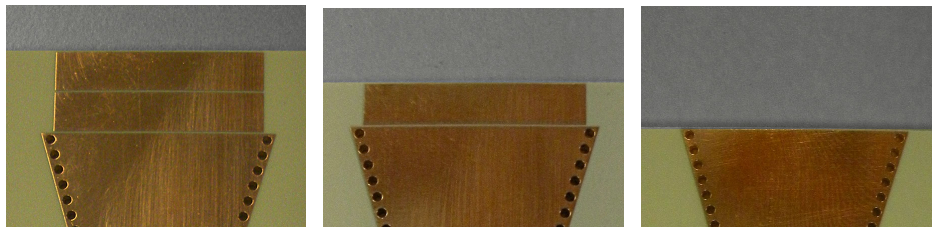
Following the steps described in Section 3.2.3, the dimensions of the prototype are [mm]: $a = 9$, $D = 22$, $W = 22$, $L = 4.3$, $s = 0.2$. In order to keep the radiation losses reasonably low, according to [29], the separation between vias and the via diameter were chosen to be 1.7 mm and 1 mm respectively. To feed the SIW horn with a microstrip line, a tapered microstrip-to-SIW transition was designed as described in [90].

The initial SIW horn prototype with a 3 block transition is shown in Fig. 3.9(a). As explained in the CR model, the same horn can work at different frequency bands depending on the number of blocks placed after its aperture. In order to prove it, a diamond saw was used to cut one by one the exterior blocks of the transition. Thus, as shown in Fig. 3.9, the same SIW horn with 3, 2, 1 and no block transition could be measured by manufacturing only one prototype.

The $|S_{11}|$ comparison between the results predicted by the CR model, the TL model, HFSS and measurements are presented in Fig. 3.10(b)-3.10(d). Clear working bands are obtained according to the different number of blocks: 14.7 GHz for 1 block, 12.2 and 16 GHz for 2 blocks,



(a) Original prototype with a 3 block transition



(b) 2 block transition

(c) 1 block transition

(d) No transition

Fig. 3.9: H-plane SIW horn prototype with a transition of different number of blocks.

14.4 and 17.3 GHz for 3 blocks. As expected from Section 3.2.2, the lowest resonant frequency obtained with a 3 block transition has a poor matching being of less interest.

The measured and simulated positions of the resonant frequencies are in good agreement with the predictions of both proposed models. The measured bandwidths at -10 dB are narrower than predicted by the TL model, but bands with a 10% relative bandwidth are obtained. Furthermore, a 4.5% -10 dB bandwidth is obtained with a two block transition at 12.2 GHz. At this frequency, the substrate thickness is thinner than $\lambda_0/12$. To obtain similar matching performances by using dielectric lenses as proposed in [44, 45], a substrate thickness of around $\lambda_0/5$ would be required. This means a 4 mm thick substrate instead of the 1.91 mm one used.

Here concludes all the theory concerning the use of the printed transition to improve the matching of SIW horn antennas. The characteristics of this transition from the radiation point of view are studied in the next section.

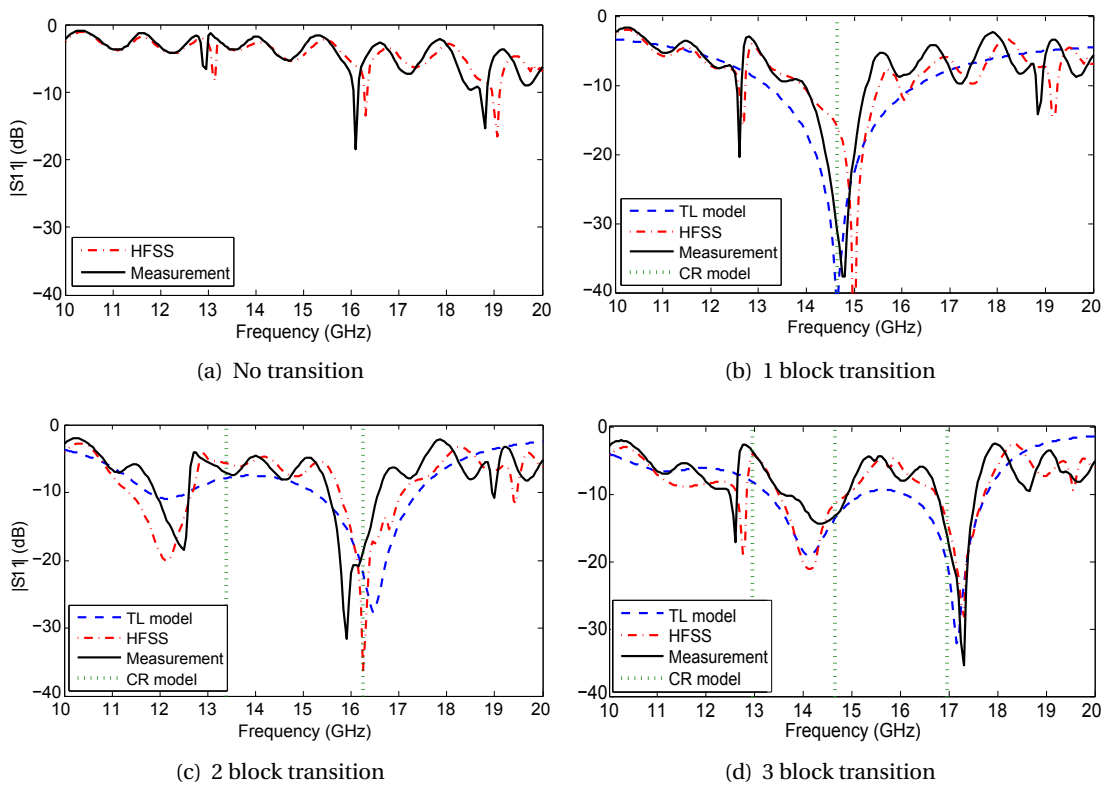


Fig. 3.10: $|S_{11}|$ of the SIW horn prototype with a transition of different number of blocks. Results for: Coupled Resonator (CR) model, TL model, HFSS and measurement.

3.3 Radiation Improvements

It is known that the radiation of a H-plane horn antenna mainly comes from the edges of the aperture that are parallel to the H-plane. In the case of the SIW horn with a 2 block transition represented in Fig. 3.3, there are three apertures in the XZ plane contributing to the radiation: E_0 , E_1 and E_2 (see Fig. 3.11). These apertures can be seen as radiating elements of a series-fed array along the y axis. Then, by properly choosing the amplitudes and phases of these elements, the radiation pattern and consequently the FTBR of the SIW horn can be increased.

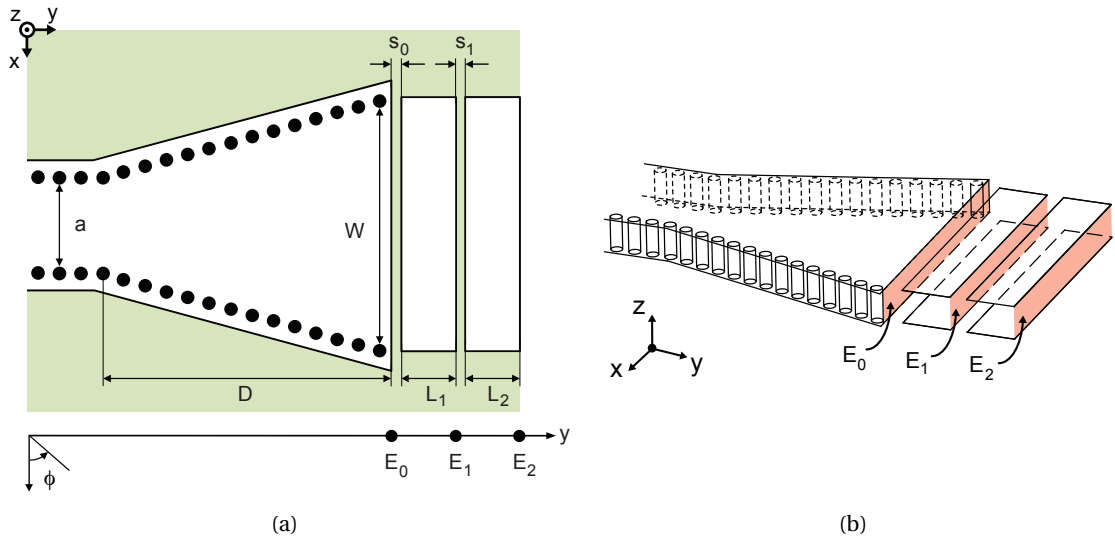


Fig. 3.11: (a) Top and (b) 3D view of the proposed H-plane SIW horn with a 2-block printed transition showing the associated radiating apertures (in red).

The gap s_i affects the amplitudes A_i and A_{i+1} of the elements E_i and E_{i+1} : When s_i becomes larger, E_i radiates better, i.e., A_i increases, but less energy arrives to the next element, i.e., A_{i+1} decreases. There is a trade-off between no radiation (small s_i) and energy leakage (large s_i). For instance, in our case, if s_0 is too big then $A_0 \gg A_1, A_2$ and the antenna radiation will mainly depend on the element E_0 . Another extreme case would be when s_0 and s_1 are too small making then $A_0, A_1 \ll A_2$ hence being E_2 the only radiating element.

The phase difference $\alpha_{i,i+1}$ between two adjacent elements E_i and E_{i+1} is controlled by the length L_{i+1} that separates both elements. Indeed, $\alpha_{i,i+1} \simeq \beta_{pp} L_{i+1}$ where $\beta_{pp} = 2\pi \sqrt{\epsilon_{rpp}} / \lambda_0$ is the propagation constant of the parallel plate waveguide. An accurate value for the effective permittivity ϵ_{rpp} can be obtained by using the quasi-static approximation and figures presented in [87] (same value used in the TL model of Section 3.2.2).

The radiation pattern $f(\phi)$ of the SIW horn of Fig. 3.11 can then be expressed using standard

array theory as:

$$f(\phi) \simeq A_0 g(\phi) + A_1 e^{j\alpha_{01}} g(\phi) e^{-j\frac{2\pi}{\lambda_0} L_1 \sin(\phi)} + A_2 e^{j(\alpha_{01} + \alpha_{12})} g(\phi) e^{-j\frac{2\pi}{\lambda_0} (L_1 + L_2) \sin(\phi)} \quad (3.13)$$

where $g(\phi)$ denotes the radiation pattern of one element and it has been assumed that $L_i \gg s_i$.

Let us discuss the choice of s_i that controls A_i and A_{i+1} . It is explained in Section 3.2.3 that at least one gap s_i should be much smaller than λ_0 to have a good matching at one resonant frequency. At the same time, two elements are required to have an array and thus to improve the FTBR. Therefore, since the SIW horn of Fig. 3.11 has 2 gaps, one can choose the gap s_0 to be much smaller than λ_0 for matching purposes (which also implies $A_0 \ll A_1, A_2$) and then use the gap s_1 to control A_1 and A_2 as desired. Hence, the radiation pattern is mainly defined by the elements E_1 and E_2 .

Regarding the value of L_i , for the sake of simplicity, the same strip length is chosen for both blocks, i.e., $L_1 = L_2 = L$, which yields $\alpha_{01} = \alpha_{12} = \alpha$. The effect of L in the matching performances will be discussed in Section 3.3.2.

In this case, the radiation pattern $f(\phi)$ of the SIW horn with a 2 block transition becomes:

$$f(\phi) \simeq (A_1 + A_2 e^{j\alpha} e^{-j\frac{2\pi L}{\lambda_0} \sin(\phi)}) g(\phi). \quad (3.14)$$

Then, assuming that s_1 has been chosen such as $A_1 \simeq A_2$, the relation found to minimize $f(-\pi/2)$ and that also maximizes the FTBR is:

$$2\pi L / \lambda_0 + \beta_{pp} L = (2n + 1)\pi, \text{ with } n \in \mathbb{Z}. \quad (3.15)$$

Finally, the shortest length L that fulfills (3.15) thus maximizing the FTBR of the SIW horn at the frequency f_{FTBR} is:

$$L = \frac{c}{2f_{FTBR}(1 + \sqrt{\epsilon_{rpp}})} \quad (3.16)$$

where c denotes the speed of light in free space.

3.3.1 Validation of the Array Analogy

To validate the array analogy, a transition of 2 blocks is used to improve the FTBR of a H-plane SIW horn at $f_{FTBR} = 17$ GHz. The substrate used is Rogers TMM 4 ($h = 1.524$ mm, $\epsilon_r = 4.5$) and the horn dimensions are [mm]: $W = 30, D = 70, a = 7$.

The first step is to find the strip length L that allows to maximize the FTBR. To do so, a value

for ϵ_{rpp} of 3.83 is found with the quasi-static approximation of [87] and a length $L = 3$ mm is obtained using (3.16).

Secondly, full-wave simulations are needed to find the right value of s_1 that makes $A_1 \simeq A_2$. Notice that there will be always a difference between A_1 and A_2 due to radiation losses and, therefore, the back radiation can be greatly attenuated but not completely canceled. Using a reasonable 15% difference between both amplitudes (similarly to the radiation losses of a microstrip gap discontinuity [91]) a FTBR of 20.6 dB is predicted with (3.14).

To illustrate the effect and importance of the gap s_1 , the simulated H-plane radiation patterns of different SIW horn configurations are shown in Fig. 3.12. In particular, a conventional SIW horn and a 2 block transition SIW horn ($L = 3$ mm, $s_0 \ll \lambda_0$) with different s_1 (0.1 mm and 0.8 mm) are compared. As expected, a poor FTBR is achieved when no transition is used (0.8 dB) and when $s_1 \ll \lambda_0$, i.e., equal to 0.1 mm (4.6 dB). But for an optimized s_1 value of 0.8 mm, an excellent FTBR of 19.2 dB is obtained in accordance with the predictions of our approximate array model.

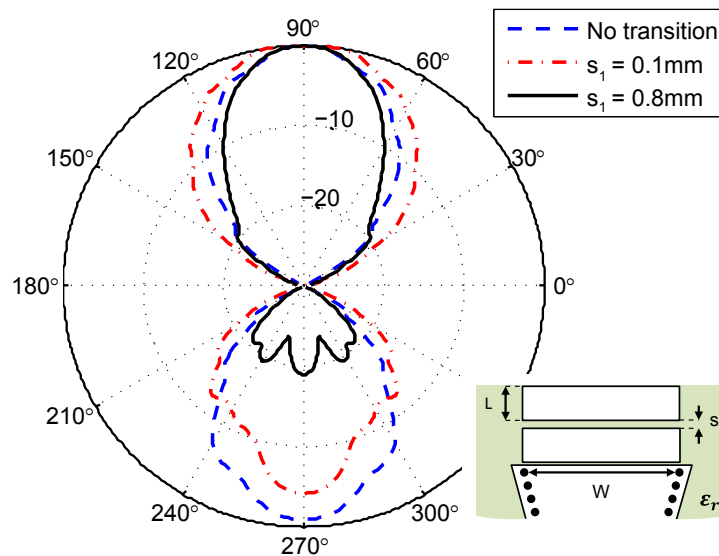


Fig. 3.12: Simulated normalized radiation pattern (H-plane) at 17 GHz of an SIW horn with and without transition for different s_1 values. The relative permittivity is $\epsilon_r = 4.5$ and the horn dimensions are [mm]: $W = 30, D = 70, a = 7$.

The described procedure allows therefore to design the transition (L and s_1) in order to obtain a high FTBR. Of course, this procedure will be of real interest provided that the SIW horn can be well matched for the same transition and at the same frequency. This important point is investigated in the next section.

3.3.2 Simultaneous FTBR and Matching Improvement

The conditions to achieve simultaneously a good $|S_{11}|$ and a good FTBR are in general not compatible. This means that the frequency for which the SIW horn is well matched, f_{match} , and the one for which the FTBR is high, f_{FTBR} , are different. In this case with a 2 block transition f_{match} corresponds to the highest resonant frequency $f_{r_{2+}}$ (from Eq. (3.2)).

To illustrate this lack of compatibility, let us consider the following practical example, where a substrate of $h = 1.91$ mm and $\epsilon_r = 3.27$ is used to implement a 15 GHz SIW horn of dimensions [mm]: $W = 32.5, D = 35, a = 8$. On one side, the condition to maximize the FTBR (3.16) gives an initial value for L of 3.8 mm. After full-wave simulations, the optimum values of $L = 3.9$ mm and $s_1 = 0.7$ mm are found. On the other hand, by applying these dimensions in (3.2), a f_{match} of 17.2 GHz is predicted. To make $f_{match} = f_{FTBR} = 15$ GHz, a length L of 4.55 mm would be required, but this length would deteriorate the FTBR below 10 dB.

To confirm and quantify this lack of compatibility, the values of f_{FTBR} and f_{match} are plotted in Fig. 3.13 as a function of the strip length L . A 10% window around both frequencies has been considered to take into account the bandwidth of the improvements. It is shown that, for a given transition, the frequency bands for f_{FTBR} and f_{match} do not overlap.

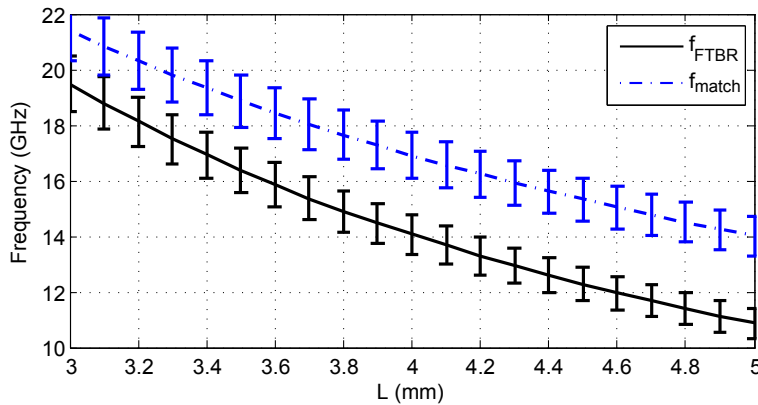


Fig. 3.13: f_{FTBR} and f_{match} as a function of L of an SIW horn with a 2 block transition. The SIW horn parameters are $W = 32.5$ mm, $D = 35$ mm, $a = 8$ mm and $\epsilon_r = 3.27$.

Printed Transition with Gratings

By analyzing the expressions in (3.2) and (3.16), it can be seen that the effective permittivity of the parallel plate waveguide ϵ_{rpp} has a greater effect on the value of f_{FTBR} than on that of f_{match} . Therefore, a way to simultaneously achieve both improvements, i.e., $f_{FTBR} \approx f_{match}$, is to decrease the value of ϵ_{rpp} . To do so, the parallel plate structure composing each transition block must be modified. Instead of using full metallic strips of width W , a grating is introduced

along the transversal direction x .

A possible grating transition with a rectangular pattern is shown in Fig. 3.14, where p defines the grating periodicity and g the separation between gratings. Obviously, as g increases, the value of ϵ_{rpp} decreases. However, the value of g should remain reasonably small to avoid undesired radiation. Hence, it is recommended that $g < p/2$ and $p < W/10$.

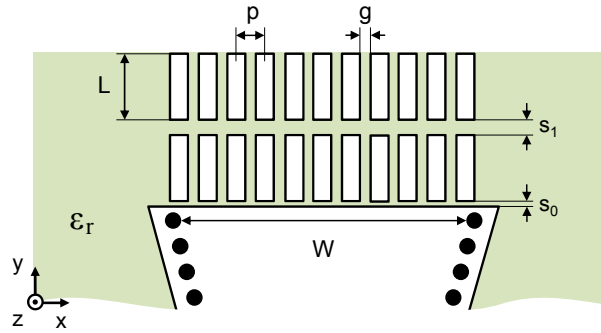


Fig. 3.14: Top view of a H-plane SIW horn with a 2 blocks rectangular grating transition with the associated notations.

The presented rectangular gratings are applied to the previous 15 GHz SIW horn. Three versions of a 2 block transition with gaps of $s_0 = 0.2$ mm and $s_1 = 0.7$ mm are compared to show the advantages of the gratings:

- *SIW horn A*: Transition optimized for FTBR ($L = 3.9$ mm)
- *SIW horn B*: Transition optimized for $|S_{11}|$ ($L = 4.55$ mm)
- *SIW horn C*: Transition with gratings optimized for both FTBR and $|S_{11}|$ ($L = 4.55$ mm, $p = 2.6$ mm, $g = 1.2$ mm)

The procedure to determine the values of p and g for SIW horn C consists in transforming gradually the full metallic strip into gratings. Thus, one can decrease the effective permittivity ϵ_{rpp} until reaching the desired value that makes $f_{FTBR} \approx f_{match}$. Full wave simulations are needed to obtain the exact dimensions of p and g .

The simulated radiation patterns and the $|S_{11}|$ are plotted in Fig. 3.15(a)-3.15(b), respectively. As expected from Eq. (3.16), a high FTBR is achieved with horn A (18.6 dB) and a low one with horn B (8 dB). Concerning the $|S_{11}|$, horn B is well matched at 15 GHz, but horn A is not. Horn C has the same strip length as horn B but gratings are introduced across the strips. As expected, the FTBR is greatly increased (15.4 dB) while the resonant frequency is slightly shifted but still well matched at 15 GHz. Therefore, the only horn which simultaneously presents a good $|S_{11}|$ and a good FTBR is the one with a grating transition, horn C.

Discussion on the Gratings Shape

In addition to the effect on the FTBR, the gratings also introduce other small changes in the radiation performances. Indeed, the metallic surface at the aperture is no more continuous and the amplitude distribution becomes less uniform. Hence, as it can be appreciated in Fig. 3.15(a), a slightly wider beamwidth is obtained when a grated transition is used. This effect could be controlled by using non-uniform gratings to further modify the field or current distribution.

The matching characteristics are also affected by the fact of not having a continuous metallic surface. In this case, the currents at the blocks' edges can follow slightly different paths, thus increasing the operational bandwidth. In Fig. 3.15(b), the horn with a grated transition, horn C, achieves a -10 dB bandwidth of 10.4% while exactly the same horn with a fully metallic transition, horn B, obtains only a 6%.

In order to further increase the bandwidth of this grated transition, the shape of the gratings can be tapered defining thus triangular gratings. Then, each block radiates along the taper instead of only at the edges of the parallel plates improving the matching as well as the FTBR bandwidth. For this reason, triangular gratings were chosen as the best option for the final manufactured prototype in Section 3.5.

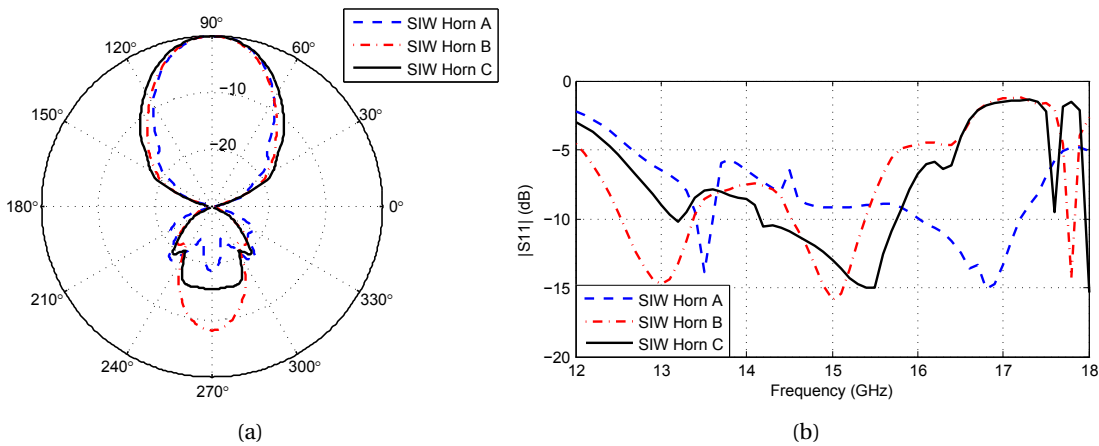


Fig. 3.15: Simulation results for the SIW horns A, B and C. (a) Normalized radiation patterns (H-plane) at 15 GHz. (b) Reflection coefficient.

3.4 Surface Reduction

A printed transition to improve both the $|S_{11}|$ and FTBR of SIW horn antennas has been presented in sections 3.2-3.3. In this section, a way to design a horn more compact than conventional ones is proposed. The aim is to properly shape the horn taper to reduce both the

length D and the aperture width W required for a given directivity. Such taper can then be easily implemented thanks to the flexibility provided by the SIW technology.

3.4.1 Improvements in the Conventional Horn Performances

The structure of a conventional horn usually includes a monomode waveguide before the beginning of the taper (see Fig. 3.1). This waveguide is designed to only allow the propagation of the fundamental mode TE_{10} . This determines the distribution of the electric field E_{AP} at the horn aperture which is proportional to $\cos(\pi x/W)$. Then, if the cross sectional area increases with a linear flare angle along x , an spherical phase error $\delta(x)$ does appear [80]:

$$\delta(x) = \frac{x^2}{2D} \left(\frac{W-a}{W} \right). \quad (3.17)$$

In order to reduce the width of the horn aperture W , keeping the same directivity, the phase error $\delta(x)$ must be reduced and the field distribution E_{AP} must become more uniform.

On the one hand, a common way to decrease $\delta(x)$ is to minimize the flare angle at the aperture. Thus, the horn radiates similarly to an open-ended waveguide which does not present spherical error. This concept is used, for instance, in the design of profiled horns [72].

On the other hand, a more uniform E_{AP} can be generated by properly combining the TE_{10} and TE_{30} modes. In presence of both modes, the field distribution E_{AP} is proportional to a linear combination of the two modes:

$$E_{AP}(x) \propto \cos(\pi x/W) - \rho e^{j\psi} \cos(\pi 3x/W) \quad (3.18)$$

where ρ defines the ratio between the amplitudes of the TE_{30} and the TE_{10} , and ψ their phase difference. A similar TE mode combination strategy to increase the horn aperture efficiency is used in the case of step-horns [92–94]. In particular, it is demonstrated in [94] that TM modes should not exist to achieve a maximum aperture efficiency. This requirement perfectly suits our case since SIW do not support the propagation of TM modes.

In order for the proposed E_{AP} to be more uniform than a cosine function, it must strictly increase between $-W/2$ and 0 and decrease between 0 and $W/2$. This is obtained by applying the following operations:

$$\frac{\partial E_{AP}(x)}{\partial x} \geq 0, \text{ for } -W/2 \leq x \leq 0 \quad (3.19)$$

$$\frac{\partial E_{AP}(x)}{\partial x} \leq 0, \text{ for } 0 \leq x \leq W/2 \quad (3.20)$$

which provide the optimum values $\rho = 1/9$ and $\psi = 0$. It is clearly shown in Fig. 3.16 that the combination $TE_{10} + 1/9 TE_{30}$ generates a more uniform distribution than the TE_{10} alone.

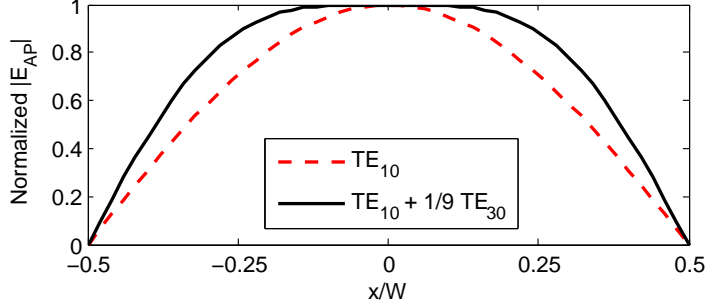


Fig. 3.16: Comparison between TE_{10} mode distribution and the distribution obtained with a proper combination of the TE_{10} and TE_{30} modes.

3.4.2 Proposed Horn Shape

Several aspects must be considered in practice to fulfil the previous conditions for E_{AP} and $\delta(x)$. First, to excite both modes, TE_{10} and TE_{30} , a coaxial probe or a multilayer transition should be used, rather than a monomode waveguide. Secondly, the taper should change smoothly to minimize reflections. A possible taper that satisfies these requirements is the one following a superelliptical function:

$$\left(\frac{y}{D}\right)^u + \left(\frac{x}{W/2}\right)^u = 1, \text{ with } u \geq 2. \quad (3.21)$$

The superelliptical function has been chosen since it inherently defines a 90° angle with respect to the aperture which helps to minimize the flare angle thus decreasing $\delta(x)$. However, other shapes could provide satisfactory results provided that the procedure described in the next section is followed.

The proposed superelliptical horn is presented in Fig. 3.17. The aperture width W is fixed by the desired beamwidth and the distance D_F should be around $\lambda_g/4$ for matching purposes, where $\lambda_g = \lambda_0/\sqrt{\epsilon_r}$ is a guided wavelength. The taper width, equal to the TE_{30} cut off wavelength, is noted as W_A . Therefore, from the feeding point to $y = D_A$, the TE_{30} mode is attenuated defining the value of ρ . Then, from $y = D_A$ to $y = D$, the TE_{30} mode can propagate affecting the value of ψ .

To simultaneously fulfil the conditions of $\rho = 1/9$ and $\psi = 0$, the taper shape can be modified by changing the parameters D and u in (3.21). A way to find these optimum values is to monitor the TE_{10} and TE_{30} modes between the feeding point and the horn aperture.

A practical design example

For a horn of parameters $W = 30$ mm, $D_F = 3.07$ mm and $\epsilon_r = 2.33$, the amplitude ratio ρ and phase difference ψ are plotted in Fig. 3.18 as a function of D and for different values of u . It is shown that by changing D and u , different combinations of ρ and ψ are obtained. In this case, the optimal values are $D = 28.5$ mm and $u = 2$.

To illustrate the importance of achieving the right ρ and ψ values, the electric field distribution inside two different horns is plotted in Fig. 3.19. The optimal case previously found is shown

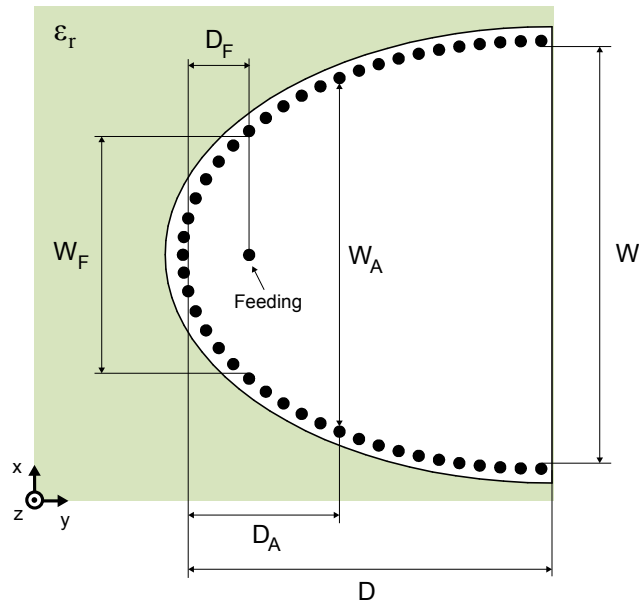


Fig. 3.17: Proposed superelliptical horn taper with the associated notations.

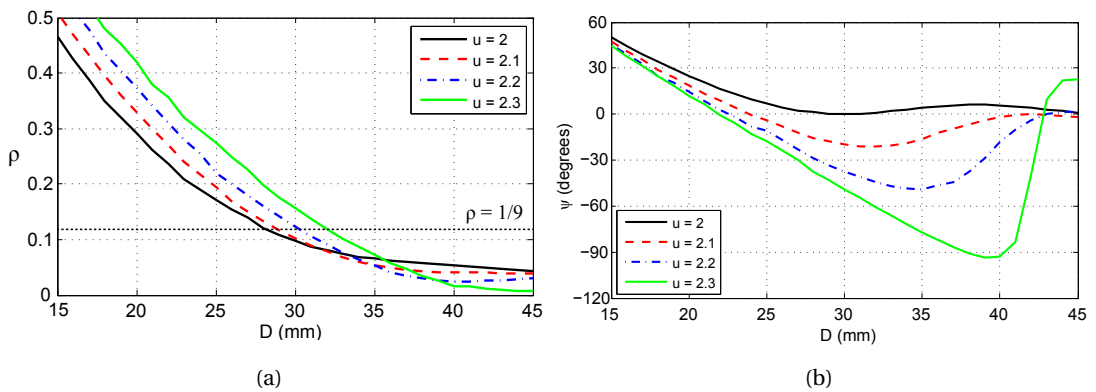


Fig. 3.18: Results at 16 GHz for a superelliptical SIW horn with $W = 30$ mm, $D_F = 3.07$ mm and $\epsilon_r = 2.33$. (a) Amplitude ratio ρ and (b) phase difference ψ as a function of D and for different values of u .

in Fig. 3.19(a) where the wavefronts along the horn present a shape as in Fig. 3.16 and they are in phase. Let us now assume that D is reduced while keeping the same W . In this case, in order to achieve $\psi \simeq 0$, the combination $D = 22$ mm and $u = 2.2$ can be chosen (see Fig. 3.18). However, now ρ equals 0.3 making the contribution of the TE_{30} stronger which creates two maximums in the wavefront front as shown in Fig. 3.19(b).

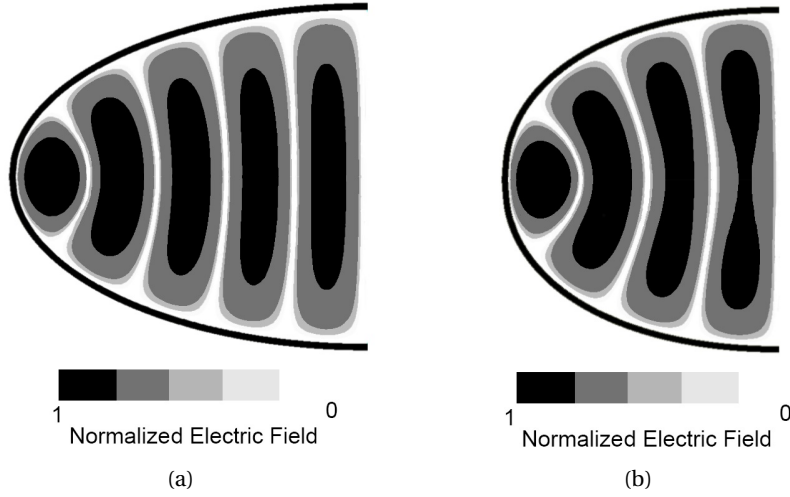


Fig. 3.19: Electric field distribution at 16 GHz inside a superelliptical horn with $W = 30$ mm, $D_F = 3.07$ mm and $\epsilon_r = 2.33$. (a) $D = 28.5$ mm and $u = 2$. (b) $D = 22$ mm and $u = 2.2$.

Discussion on the proposed shape

The strategy to successfully combine the TE_{10} and TE_{30} modes is conditioned by the aperture width W and the substrate permittivity ϵ_r . First of all, the dominant mode TE_{10} must not be attenuated along the taper. To ensure this, the taper width at the feeding position W_F (see Fig. 3.17) must be wider than the cut off wavelength of the TE_{10} mode:

$$W_F = W \sqrt{1 - \left(\frac{D - D_F}{D}\right)^2} > \frac{\lambda_0}{2\sqrt{\epsilon_r}} \quad (3.22)$$

$$W > \frac{\lambda_0}{2\sqrt{\epsilon_r} \sqrt{1 - \left(\frac{D - D_F}{D}\right)^2}}. \quad (3.23)$$

Secondly, to properly combine both modes, the TE_{30} mode must arrive at the aperture as a propagating mode. Hence, the aperture width W must be wider than the cut off wavelength of the TE_{30} mode:

$$W > \frac{3\lambda_0}{2\sqrt{\epsilon_r}}. \quad (3.24)$$

By comparing Eqs. (3.23) and (3.24), it can be seen that (3.24) is always the most restrictive condition for lengths D shorter than $4.4 \lambda_g$, which includes most practical cases.

3.4.3 Compact Horn vs. Conventional Horn

In order to illustrate the compactness of the proposed horn with respect to a conventional one, let us see the size requirements for a given ε_r as a function of the desired HPBW. The parameters of the compact horn in Fig. 3.19(a) are $D = 28.5$ mm, $W = 30$ mm and $\varepsilon_r = 2.33$ generating a pattern with HPBW = 37.5° .

To obtain the same radiation performances (HPBW = 37.5°) with a linear horn, a width $W = 33$ mm (instead of 30 mm for the compact horn) is required even when assuming that the phase error at the aperture $\delta(x)$ is negligible. Therefore, in this example, the fact of combining the TE₁₀ and TE₃₀ modes reduces the horn width in a 9%.

When using a linear taper instead of a profiled one, the horn length must be considerably increased to also achieve a negligible $\delta(x)$ [72]. In this case, a linear horn of $D = 54$ mm is required being the compact horn 47% shorter.

To sum up, for the given HPBW and ε_r , the use of a superelliptical horn instead of a linear conventional horn halves the antenna surface (52% of surface reduction).

3.5 Prototype Design and Measurements

A H-plane SIW horn antenna using the triangular grating transition and the superelliptical taper was built to validate the proposed concepts (see Fig. 3.20). Design steps to determine the SIW horn parameters and the feeding system are provided along with measurements.

3.5.1 SIW Horn Design Steps

A central frequency $f_0 = 15$ GHz was selected for our prototype. The substrate used is a Rogers TMM3 with $\varepsilon_r = 3.27$ and $h = 1.91$ mm ($< \lambda_0/10$). The working frequency band is defined by the following requirements: $|S_{11}| < -10$ dB, FTBR > 15 dB and H-plane HPBW $\approx 45^\circ$. The steps to design the SIW horn are the following:

- *Compact Taper*

1. Given the HPBW, the horn aperture width W is calculated assuming an E_{AP} as in (3.18) with $\rho = 1/9$ and $\psi = 0$.

2. The conditions (3.23) and (3.24) are checked to verify that the proposed superelliptical taper can be applied for the given ϵ_r and W . If not, a substrate with a higher permittivity must be chosen.
3. Knowing W , the procedure described in Section 3.4.2 is followed to determine the optimum values for D and u .

• *Printed Transition*

1. To simultaneously improve the FTBR and the $|S_{11}|$ at a given central frequency f_0 , a printed transition of 2 blocks is used.
2. To obtain $f_{FTBR} = f_0$, the strip length L is found using (3.16). Simulations are needed to find the right value for s_1 as well as to optimize the value of L .
3. The values of L and s_1 are applied in (3.2) to check if also $f_{match} = f_0$.
4. If $f_{match} \neq f_{FTBR} = f_0$, the grating design presented in Section 3.3.2 is applied.

After following these design steps, the geometrical parameters fully defining our antenna (Fig. 3.20) are given in Tab. 3.2. According to [29], the separation between via holes was chosen to be 1.1 mm for a hole diameter of 0.6 mm to keep the SIW radiation losses reasonably low.

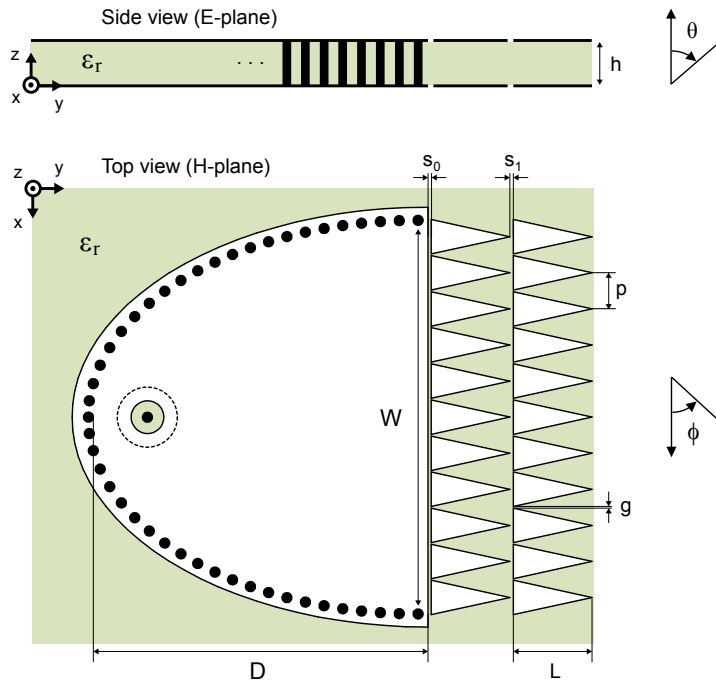


Fig. 3.20: Side and top view of the proposed thin and compact SIW horn. Metal is represented in white, the dielectric substrate in grey and the metallized via holes in black.

3.5.2 Feeding System

A coaxial probe placed at the beginning of the taper was used as feeding system. A coaxial-to-SIW transition with electric coupling was chosen (see Fig. 3.21) since, in the case of thin substrates, this type of transition offers better performances than the magnetic one [95]. Thus, a ring-slot of width $(d_{R2} - d_{R1})/2$ was inserted between the current probe and the top copper layer. The circle of diameter d_C denotes the opening at the bottom copper layer where the connector is placed.

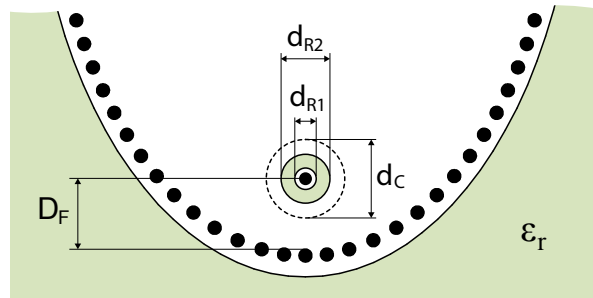


Fig. 3.21: Coaxial-to-SIW transition with the associated notations.

In this feeding structure, the dimensions d_{R1} , d_{R2} and d_C strongly depend on the type of connector. In our case, the connector used was a 22 SMA-50-0-6/111NE and, after an optimization process, the following values were found [mm]: $d_{R1} = 0.8$, $d_{R2} = 2$, $d_C = 3.6$, $D_F = 3.35$.

3.5.3 Measurements

The manufactured prototype is shown in Fig. 3.22. Its overall dimensions are $[\lambda_0]$: $1.56 \times 1.26 \times 0.094$. The H- and E- plane radiation patterns for different frequencies are shown in Fig. 3.25. Full-wave simulations and measurements are in good agreement and a FTBR above 15 dB is achieved between 14.2 and 15.4 GHz. Low levels of the cross-polarization component below -20 dB are also obtained.

At the same frequency range where the FTBR is greatly improved (14.2-15.4 GHz), a matching better than -10 dB is also obtained (see Fig. 3.23). Furthermore, the -10 dB bandwidth of the antenna extends from 14.1 to 16.6 GHz defining a relative 16% bandwidth.

Compact Taper [mm]			Triangular Grating Transition [mm]				
W	D	u	L	s_0	s_1	p	g
24	20.45	2	4.8	0.2	0.2	2.2	0.15

Tab. 3.2: Geometrical parameters of the SIW Horn Prototype.

The addition of the proposed transition does not affect the typical behavior of horn antennas in terms of beamwidth. Indeed, the HPBW of the manufactured prototype only slightly changes from 46° to 43° as the electrical length of the aperture increases with the frequency. The simulated and measured gain of the antenna as a function of the frequency is plotted in Fig. 3.24 showing an average measured gain of of 7.1 dBi.

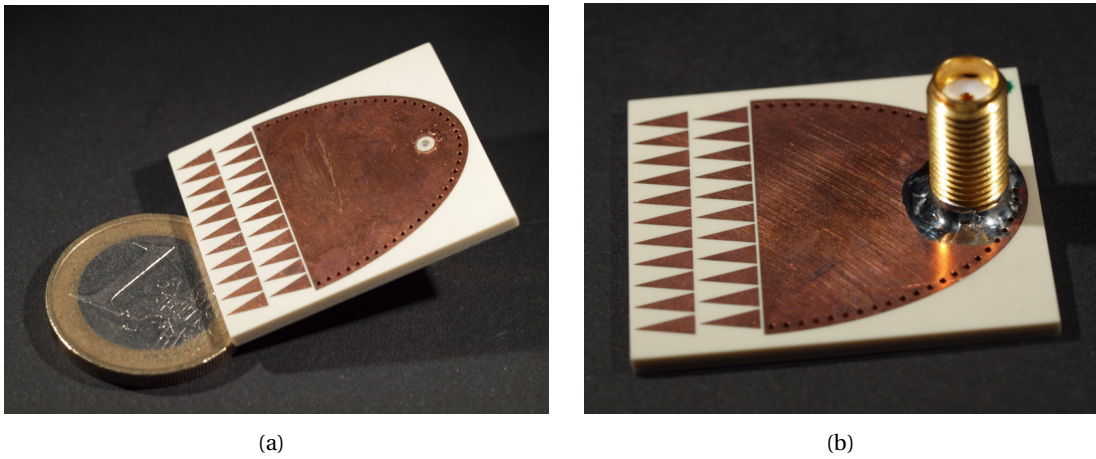


Fig. 3.22: (a) Top view and (b) bottom view of the manufactured prototype of an SIW horn antenna with a triangular grated transition and a superelliptical taper. Overall dimensions $[\lambda_0]$: 1.56 x 1.26 x 0.094.

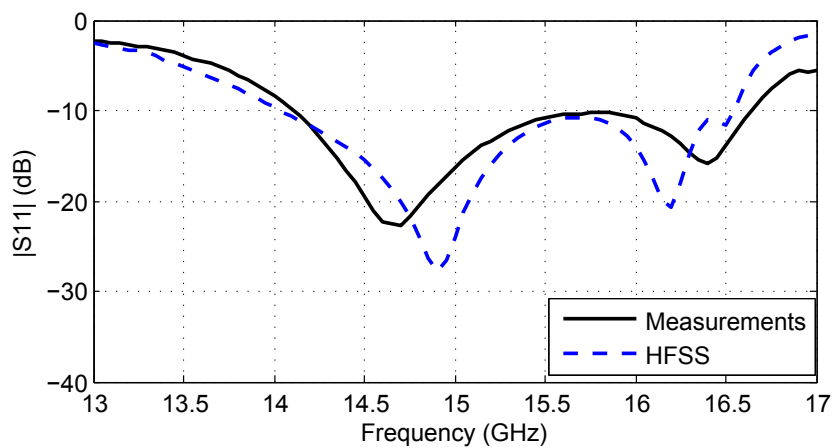


Fig. 3.23: Simulated and measured $|S_{11}|$ of the manufactured prototype.

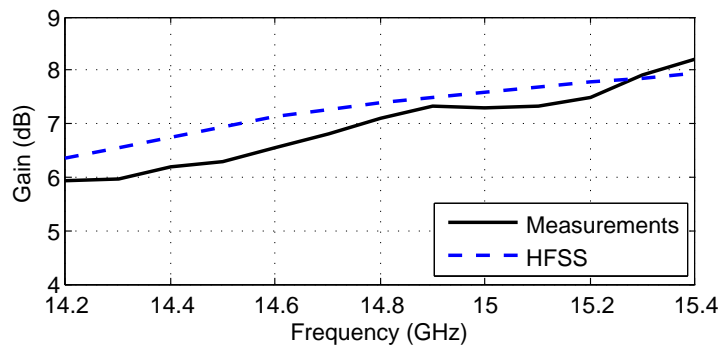


Fig. 3.24: End-fire simulated and measured gain of the SIW horn prototype in the frequency range of interest.

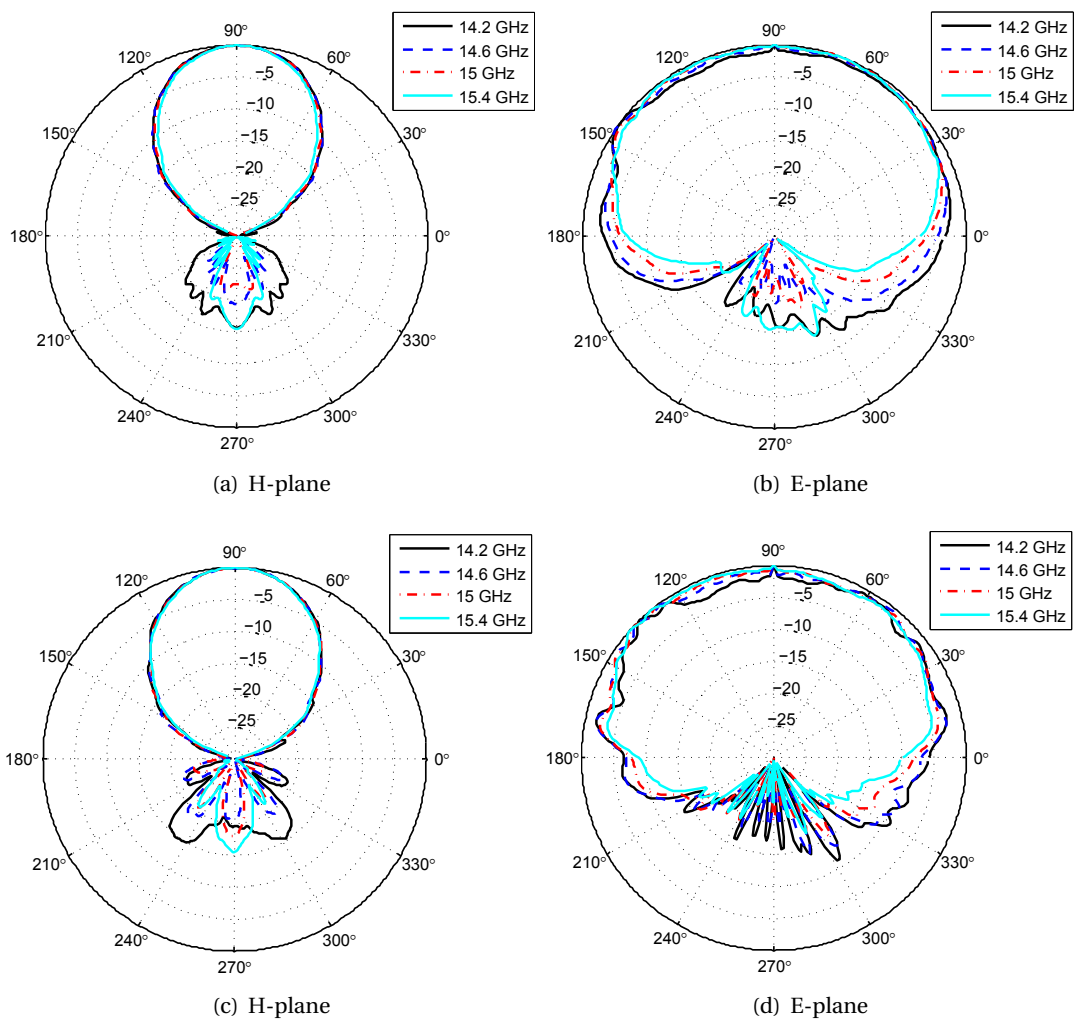


Fig. 3.25: (a)-(b) Simulated and (c)-(d) measured radiation patterns of the SIW horn prototype.

3.6 Conclusions

The SIW technology offers very interesting possibilities to build H-plane horn antennas. However, the thickness of the SIW substrate is limited both by the reduced availability of thick substrates and by practical constraints in the technologies used to drill metallized via-holes. In general, good SIW performances call for substrates of at least $\lambda_0/6$ thick and, with the current available substrates, this puts around 20 GHz the lower frequency where SIW horns can be properly used. When SIW horns are built in thinner substrates, not only a strong mismatch between the antenna aperture and the air appears, but also the resulting antenna behaves like a slot antenna with a FTBR ratio near to unity. Thus, despite its promising features, standard H-plane SIW horns are not suitable for our DF array working at 15 GHz.

In this chapter, an innovative structure has been developed to simultaneously overcome these two problems of thin H-plane SIW horns. This structure can be seen as metallic gratings integrated in the same substrate as the horn antenna. By modelling these gratings with a combination of transmission line and array theories, simple analytical design rules have been developed to characterize the needed geometry according to the desired performances in terms of matchings, FTBR or both.

The proposed SIW horn antenna has been further optimized by reducing its required dimensions for a given directivity. This is obtained by modifying the classic linear taper of the horn into a superelliptical taper to properly combine different TE modes in order to generate a more uniform electric field distribution at the aperture. Here, the inherent flexibility of the SIW technology is exploited to implement the desired taper shape.

The different concepts introduced in this chapter to improve the performances of H-plane SIW horn antennas are summarized in Tab. 3.3. As a conclusive demonstration, a prototype has been designed following the proposed guidelines and built in a commercial substrate thinner than $\lambda_0/10$. Despite this miniaturization, it exhibits excellent electromagnetic properties: In the design frequency band (14.2-15.4 GHz), the matching is better than -10 dB and the radiation pattern remains reasonably constant with a HPBW of 45° and a FTBR higher than 15 dB. In addition, an average value of 7.1 dBi for the gain is obtained.

In summary, the excellent performances of this prototype together with its simple and low-cost fabrication (only one layer of substrate), pave the way for a new family of SIW horns with a working range extended towards the Ku-band and below. In the next chapter, a circular array of these SIW horns is used to implement the complete DF system.

Type of H-plane SIW horn antenna						
	Standard	Transition for matching	Transition for FTBR	Transition with Rectangular Gratings	Transition with Triangular Gratings	Superelliptical taper
Bandwidth for $S_{11} < -10$ dB	< 2%	~ 8%	< 2%	~ 10%	~ 15%	~ 15%
FTBR	< 5 dB	< 5 dB	> 15 dB	> 15 dB	> 15 dB	> 15 dB
Surface reduction for a given directivity	-	-	-	-	-	up to 50%*
Respective section	3.1	3.2	3.3	3.3.2	3.3.2 and 3.5	3.4 and 3.5

*Note that the surface reduction depends on the substrate permittivity ϵ_r , but increasing ϵ_r do not necessarily decreases the antenna size because the phase error at the aperture also increases requiring then to lengthen the horn (see Section 3.4.2).

Tab. 3.3: Performance evolution of the SIW horn antennas proposed throughout Chapter 3 (always considering a substrate of thickness $h = \lambda_0 / 10$).

4 Low-profile Azimuth Direction Finding System

Mobile Direction Finding (DF) systems covering the azimuthal plane are used, for instance, in navigation, rescue operations, location of illegal/interfering transmitters, etc. and can be also included in terrestrial or aerial vehicles to improve the inter-vehicle communications. Many commercial products of such systems are available since decades [96–98], most of them conceived to be mounted on terrestrial vehicles. While these systems may offer really high performances (wide frequency range of operation, high accuracies, etc.), they are voluminous and heavy, not convenient to be used on light aircrafts. The latter is particularly true in the case of UAVs, where the reduction of weight and drag are extremely important, as explained in detail in Section 1.2.

In this chapter, a beam-switching DF system based on a circular array of the previous SIW horn antennas is proposed. Hence, the complete system would be low-profile and light weight suitable to be flush-mounted on UAVs. To this end, the interconnection between these horns and commercial MMICs is first studied in Section 4.1. Then, the electronic system needed to control the antennas is divided in two parts: the RF part (Section 4.2) and the DC part (Section 4.3). The RF part is mainly responsible to select the signal coming from the desired antenna and to convert it to a proportional DC voltage to be later treated by a MicroController Unit (MCU). In this section, common problems encountered with high frequency electronics such as the need for a shielding structure and parasitic oscillations are also addressed. The core of the DC part is the MCU, which must be programmed in order to generate the control loop and to compute the Direction of Arrival (DoA) estimation. A functional block diagram of the electronic part is shown in Fig. 4.1.

The different steps in the manufacturing process of the complete DF prototype are detailed in Section 4.4 along with experimental results. The interaction of this system with a conventional UAV platform is finally studied in Section 4.5.

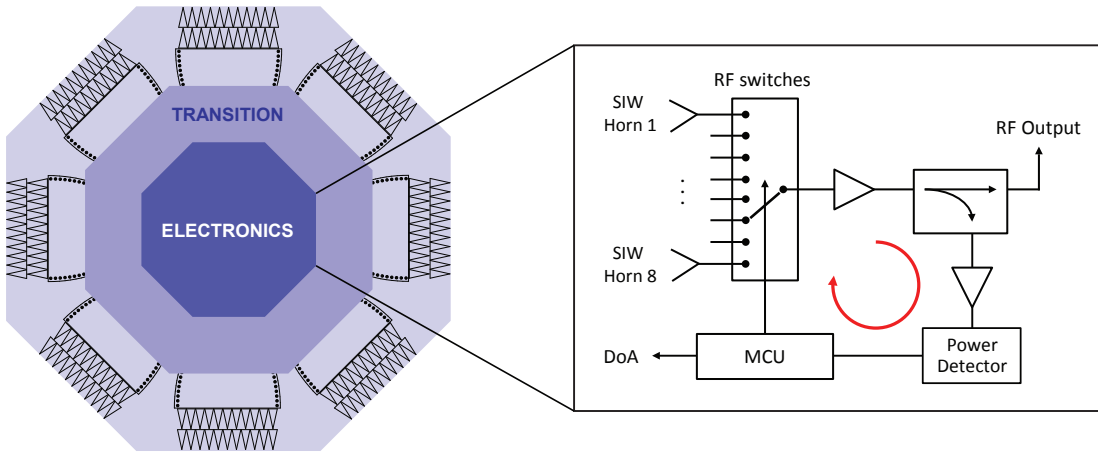


Fig. 4.1: Functional block diagram of the DF electronic part.

4.1 Interconnection SIW Horn Antennas - MMICs

Planar transmission lines, such as Microstrip Lines (MSL) and coplanar waveguides are favorable to the integration of microwave systems. More specifically, MSLs are the most viable option when encapsulated MMICs are used. Thus, a transition SIW-MSL must be designed to create a fully integrated system.

4.1.1 Type of Transition

The whole system is designed to work at the Ku-band and specifically at the central frequency $f_0 = 15$ GHz. Then, in order to choose the most suitable type of transition, the substrate needed to implement the antennas (SIW substrate) must be compared with the one required for the electronics (MSL substrate). On the one hand, the type of SIW horn antenna described in Chapter 3 requires a low permittivity substrate commonly available with a maximum thickness of around 2 mm (such as the 1.91 mm Rogers TMM3 used in Section 3.5). On the other hand, thin and high permittivity substrates are preferred to place electronic components since their connectivity with MSLs is more convenient and they allow for a higher degree of integration. Moreover, encapsulated electronic components usually present a 50Ω input pin of width 0.3-0.4 mm. Thus, a 0.38 mm Rogers TMM10 ($\epsilon_{r2} = 9.56$) was chosen on which a 50Ω MSL has a width $M_W = 0.38$ mm.

Due to the large difference between the thickness of both substrates, a vertical transition must be chosen for both electromagnetic and mechanical constraints. Several SIW-MSL vertical transitions offering similar performances have been proposed in the literature. They are mainly based on probe feeding [99–101] and slot coupling [101, 102]. However, the slot coupling transition eases the assembling process and it is more robust to tolerances. Thus,

in our case, a slot in the common metal plane between the MSL and SIW was opened for the energy to couple between these two structures (see Fig. 4.2). T_W defines the slot width, T_L the slot length and M_S the microstrip stub.

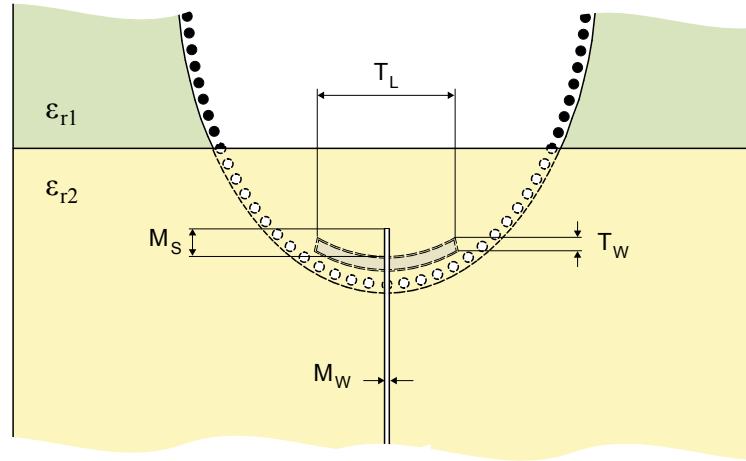


Fig. 4.2: Top view of the slot coupling transition between the SIW horn antenna and a MSL.

In a slot coupling transition, the forward and backward travelling waves of the electric field excited by the slot within the waveguide are in opposite direction, i.e., the slot must be opened as close as possible to the shortest end of the SIW for a maximum power transfer [101]. In order to match the impedance of the MSL with the input conductance seen at the center of the slot, all the stubs departing from this point should be roughly a quarter guided wavelength at the central frequency of operation, i.e., $T_L/2 \simeq \lambda_{g(SIW)}/4$ and $M_S \simeq \lambda_{g(MSL)}/4$. In addition, a similar procedure as described in Section 3.4.2 must be followed to further optimize the dimensions for a proper combination of the TE_{10} and TE_{30} modes within the horn.

Despite the large differences in the relative permittivity and thickness between both substrates, this transition offers a good wideband behaviour. The detailed dimensions and performances of the SIW horn antenna fed by this MSL transition are presented in the next section, along with the antenna array configuration and measurements.

4.1.2 Preliminary SIW Horn Array Prototype

A three-element SIW horn antenna array was manufactured to test the antenna performances when fed by the previous multilayer transition. The measurements extracted from this prototype are then directly used to design the complete circular array of 8 elements. In practice, one element of the complete array will have the same behavior as the central one in this 3-element prototype since its performances are mainly affected by the adjacent horns.

Each SIW horn has the same dimensions as the one in Section 3.5 and, after an optimization

process, the SIW-MSL transition dimensions were chosen as [mm]: $T_W = 0.6$, $T_L = 8.1$ and $M_S = 1.7$. Finally, in order to obtain an overlapping between adjacent beams at around -3 dB, the horns are placed on a circle of 52 mm radius with a 45° separation. The layered view of the structure is shown in Fig. 4.3 and a picture of the prototype in Fig. 4.4. In this case, instead of MMICs, three SMA connectors were placed after the MSLs to accurately measure the antenna performances.

The simulated and measured S parameters are plotted in Fig. 4.5. All three SIW horns present a reflection coefficient below -10 dB over a 20% bandwidth (between 14.2 and 17.5 GHz). Thanks to the practically enclosed structure of an SIW horn antenna and a good design of the multilayer transition, the mutual coupling between horns is practically negligible. Indeed, the measured values of $|S_{12}|$ and $|S_{23}|$ are below -40 dB over the whole frequency range.

The measured H-plane radiation patterns of the three SIW horns at f_0 are superimposed in Fig. 4.6. Despite their low-profile, the horns are able to considerably focus the energy frontwards achieving a front-to-back ratio above 15 dB. The -3 dB beam overlapping required for beam-switching applications can also be observed. The efficiency of the central horn is 85% with a realized gain of 5.6 dBi. Moreover, a cross-polarization level below -20 dB was also measured.

After the validation of the electromagnetic performances of the SIW horn antenna array, the electronic system can be designed.

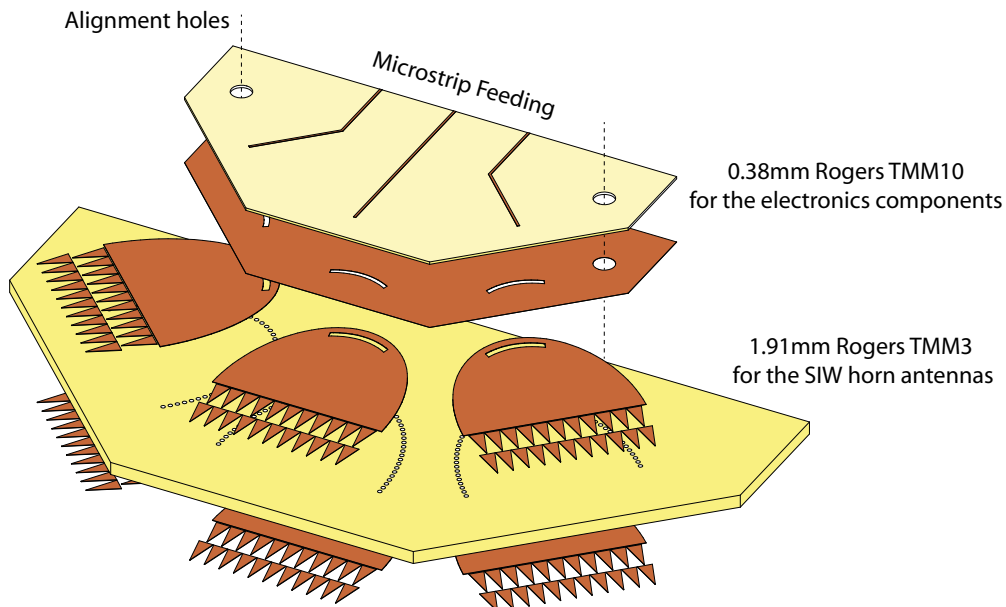


Fig. 4.3: Layered view of a 3-element SIW horn antenna array fed by MSLs for interconnection with electronic components.

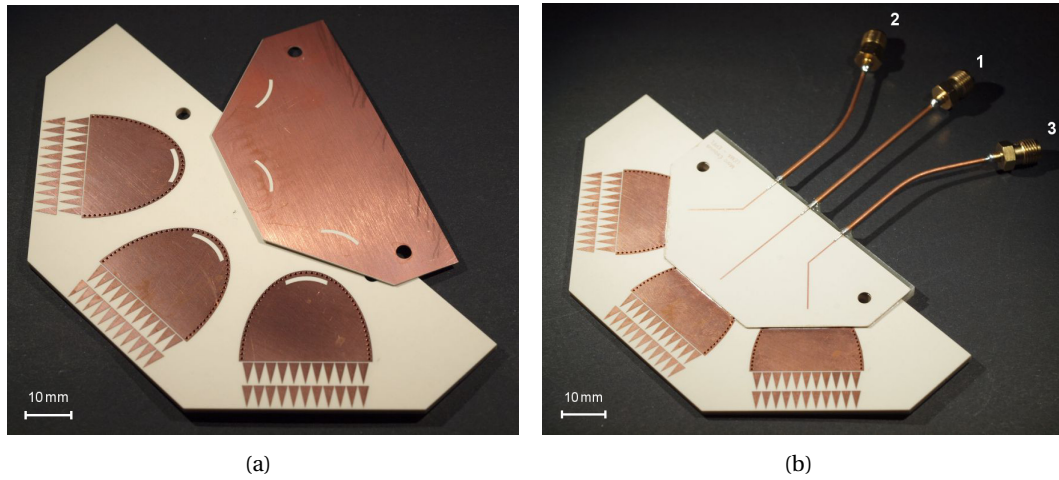
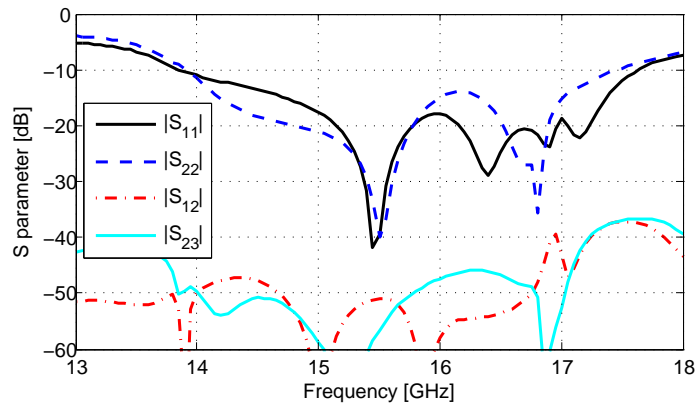
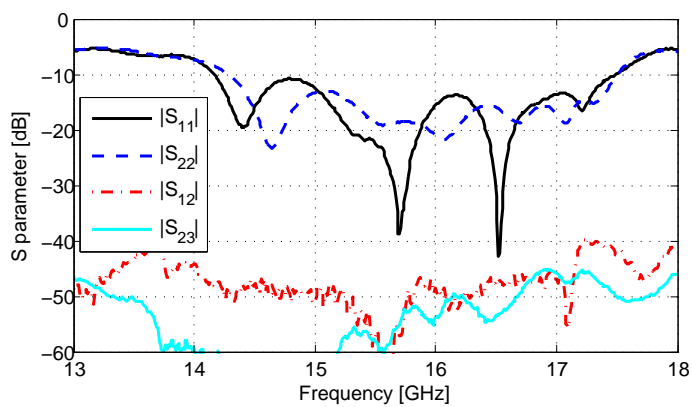


Fig. 4.4: 3-element SIW horn antenna array fed by MSLs for interconnection with MMICs. (a) Pre-assembly picture and (b) final configuration with SMA connectors for measurements.



(a)



(b)

Fig. 4.5: S parameters of the 3-element SIW horn antenna prototype. (a) Simulated and (b) Measured.

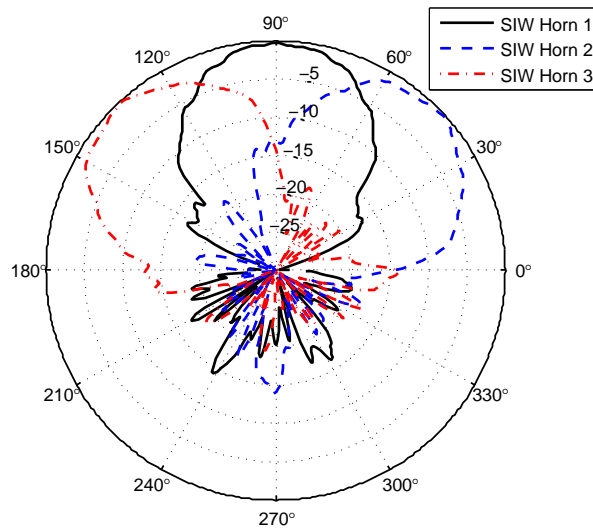


Fig. 4.6: Superposition of the measured H-plane radiation patterns at 15 GHz of the three SIW horns.

4.2 RF Electronics

In this section, the MMICs used to implement a beam-switching antenna system are described. A beam-switching antenna is an antenna array that can form a set of predefined beams. Once a beam is selected using switches, its received signal is downconverted and then processed by a MCU (Section 4.2). Although this type of systems is not as flexible as an adaptive array, its main advantage is simplicity and, therefore, low cost. All processing is done in the RF domain so that only one signal has to be downconverted: This is a significant price-wise advantage since the circuits for downconversion are among the most expensive ones in today's wireless systems (this is particularly true when working at mm-wave frequencies). Moreover, it is important to mention that the performances offered by a beam-switching system are usually enough for many common applications [1, 2]. Hereinafter, the design and prototyping of a receiving system are presented.

The first components needed to choose between the different antennas are RF switches. At the frequency range of our application, commercial switches in ceramic/plastic packages are only available in SP4T or SPDT formats. Therefore, in order to switch between the 8 antennas, two SP4T switches and one SPDT switch are needed. In practice, three HMC641LC4 SP4T switches from Hittite Microwave Corporation [103] were used for both operations. These are GaAs MMIC non-reflective switches working from DC up to 20 GHz. The functional diagram of a switch is shown in Fig. 4.7(a). Differently from other switches, the HMC641LC4 offers an on board binary decoder circuit which reduces the number of required logic control lines from four to two, CTLA and CTLB. It is controlled with 0/-5 V logic and consumes much less than a pin diode based solutions (typically around 2 mA).

Once the desired antenna is selected, the signal is split with a directional coupler: The main part is destined to the system RF output and a small part is used for the control loop. In order to convert the latter RF signal into a proportional DC voltage, a Logarithmic Detector (LD) is used as power detector. For this task, the HMC948LP3E from Hittite was chosen. This LD works between 1 and 23 GHz and is based on a chain of amplifiers that successively move into saturation creating an approximation of the logarithmic function. The functional diagram of the LD is shown in Fig. 4.7(b). The HMC948LP3E provides a nominal logarithmic slope of +14.2 mV/dB. At our frequency range of operation, the RF input dynamic range of the LD goes from -52 to 5 dBm, delivering a DC voltage between 0.95 and 1.75 V, respectively. This component is fed at +3.3 V and consumes around 90 mA.

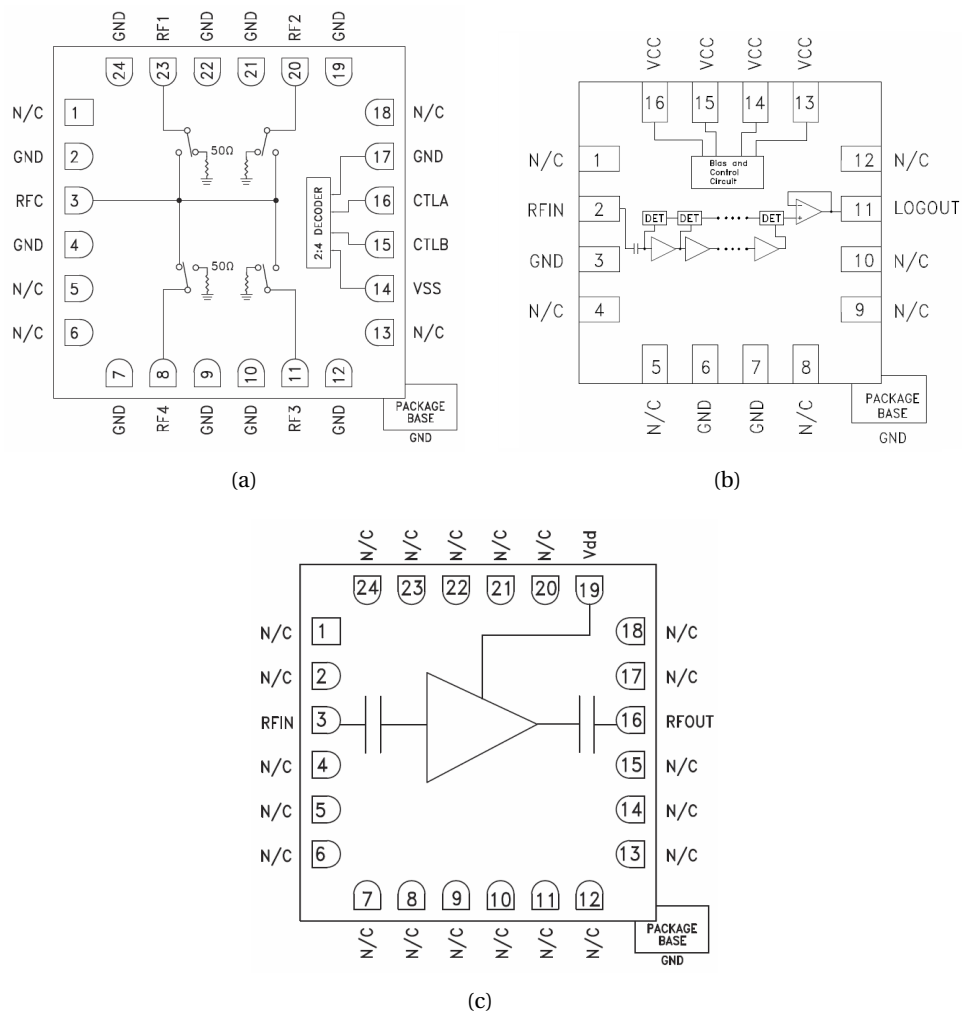


Fig. 4.7: Functional diagram of the HMC641LC4 SP4T switch (a), the HMC948LP3E logarithmic detector (b) and the HMC383LC4 medium power amplifier (c).

A link budget under certain test condition must be done to properly design the system. This defines the needed number of amplifiers and their placement. The block diagram of the RF part until the last SPDT switch is shown in Fig. 4.8 along with typical scenario specifications. Then, the RF power level after the SPDT switch is given by:

$$P_{SPDT} = P_{Tx} + G_{Tx} - 20 \log_{10} \left(\frac{4\pi d}{\lambda_0} \right) + G_{Rx} - IL_{\mu strips} - IL_{switches} \quad (4.1)$$

where $IL_{\mu strips}$ accounts for the dielectric and conductor loss of the microstrip lines and $IL_{switches}$ is the insertion loss of the switches. Considering the central working frequency $f_0 = 15$ GHz and the values given in Fig. 4.8, the RF power level after the SPDT switch is expected to be between -65 and -29 dBm. At this point, an 8 dB directional coupler is used to split the RF signal between the system RF output and LD input. Thus, in order to guarantee a sufficient signal level after the directional coupler, a RF amplifier is placed after the SPDT switch. The amplifier chosen is the GaAs phemet MMIC medium power amplifier HMC383LC4 from Hittite. It provides a gain $G_A = 15$ dB and +18 dBm of saturated power from a single +5 V supply. The functional diagram is shown in Fig. 4.7(c). As expected, this component is the most demanding in terms of power consumption and might consume up to 135 mA.

Finally, in order to well work in the linear range of the LD, a second 15 dB amplifier is used after the direction coupler. Thus, an input RF signal level between -43 and -7 dBm is guaranteed, which corresponds to an output DC signal varying from 1.1 to 1.6 V. The complete RF block diagram for any antenna is shown in Fig. 4.9.

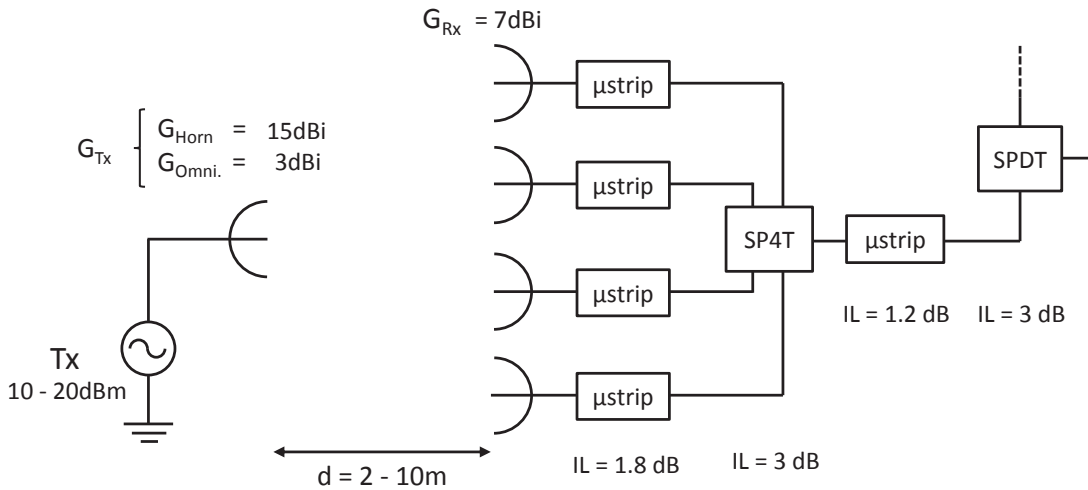


Fig. 4.8: Block diagram of the system until the SPDT switch with the scenario specifications.

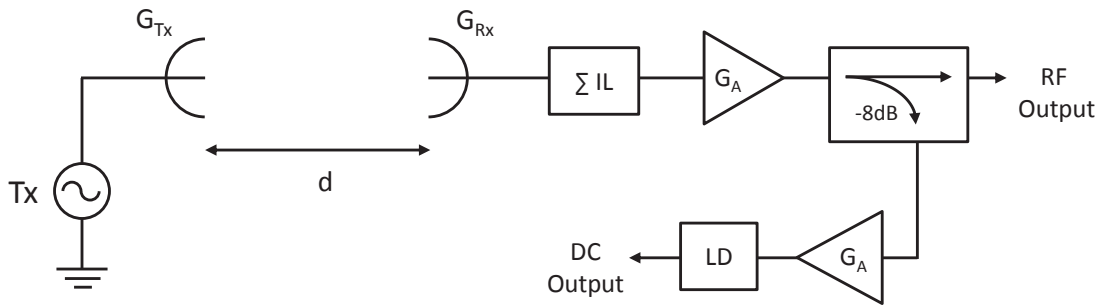


Fig. 4.9: Complete RF block diagram for any antenna.

A schematic view of the placement and interconnection of the different RF components is shown in Fig. 4.10. The decoupling capacitors and feeding voltages for each component are also shown, where $V_{DD} = 5\text{ V}$ and $V_{EE} = -5\text{ V}$. The output of the logarithmic detector DC_LD_OUTPUT corresponds to the input of the DC part and the control signals $CTRL_1$, $CTRL_2$ and $CTRL_3$ are generated by the MCU (see Section 4.3). An array of metallized vias enclosing all the electronics was also foreseen for shielding purposes (see Section 4.2.2).

4.2.1 RF Output

The main functionality of the system is to read an incoming signal and compute its DoA. The directional coupler used to split this signal between the control loop and the RF output is a simple 8 dB coupled-line coupler (see Fig. 4.11). This coupler has a gap between lines of 0.5 mm and a coupling section length of 6.65 mm. Note that the $50\ \Omega$ load was omitted since the coupler can only be used in one direction (for receiving).

The RF signal at the through output of the coupler is extracted using a 23 SMA-50 connector. For this purpose, a multilayer transition must be designed between the MSL on the 0.38 mm TMM10 substrate and the SMA connector, going through the 1.91 mm TMM3 substrate. First of all, in order to create a smooth impedance variation between the connector and the TMM3 substrate, a cylinder of diameter $d_C = 2.4\text{ mm}$ is created in the TMM3 substrate by drilling metallized vias of diameter $d_v = 0.8\text{ mm}$ (see Fig. 4.11), which defines a $50\ \Omega$ guiding structure. Then, the inner pin of the coaxial cable goes through both substrates and is connected to the $50\ \Omega$ MSL.

The simulated values for the reflection coefficient $|S_{11}|$, the attenuation $|S_{12}|$ and the coupling $|S_{13}|$ of the whole structure of Fig. 4.11 are presented in Fig. 4.12. The values of the different parameters over the band of interest (14.62 – 15.35 GHz) are: $|S_{11}| < 18\text{ dB}$, $|S_{12}| > 1.5\text{ dB}$ and the coupling $|S_{13}|$ varies between -9 and -7.5 dB.

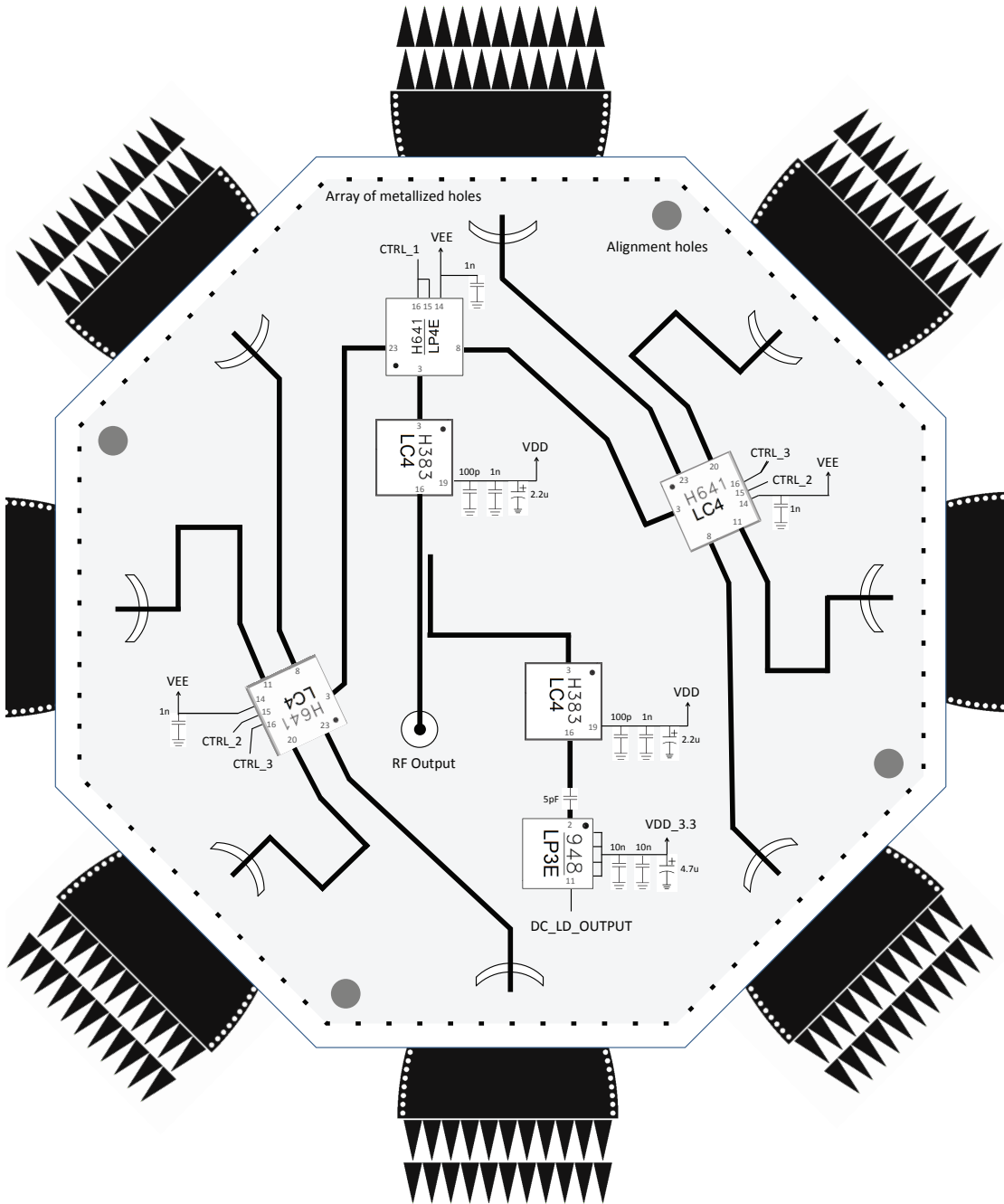


Fig. 4.10: Schematic view of the placement and interconnection of the different RF components. The decoupling capacitors and feeding voltages for each component are also shown, where $V_{DD} = 5\text{ V}$ and $V_{EE} = -5\text{ V}$. The output of the logarithmic detector DC_LD_OUTPUT corresponds to the input of the DC part and the control signals $CTRL_1$, $CTRL_2$ and $CTRL_3$ are generated by the microcontroller unit (see Section 4.3). An array of metallized vias enclosing all the electronics is also foreseen for shielding purposes (see Section 4.2.2). Note that the left and right SIW horn antennas are not entirely shown due to space reasons.

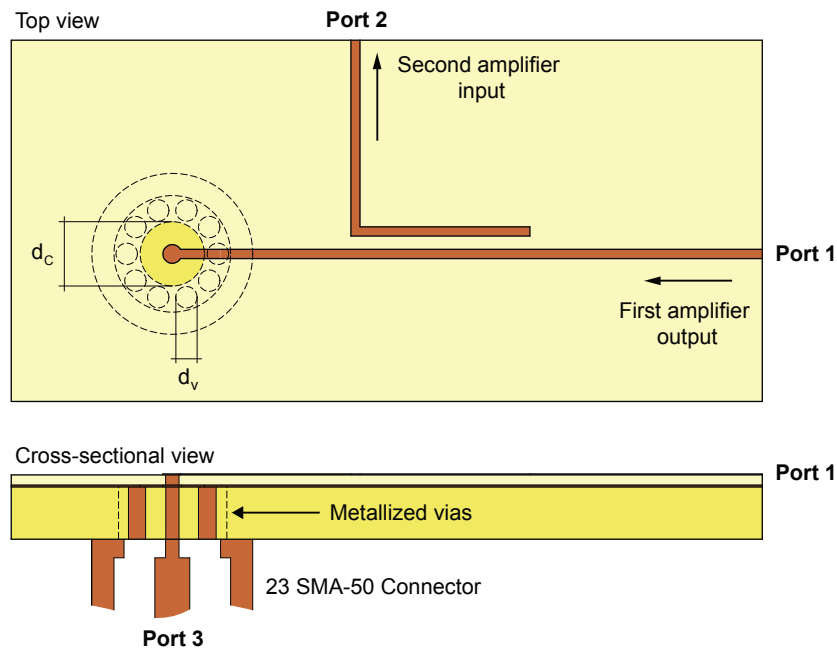


Fig. 4.11: Top and cross-sectional view of the coupled-line coupler with the RF output.

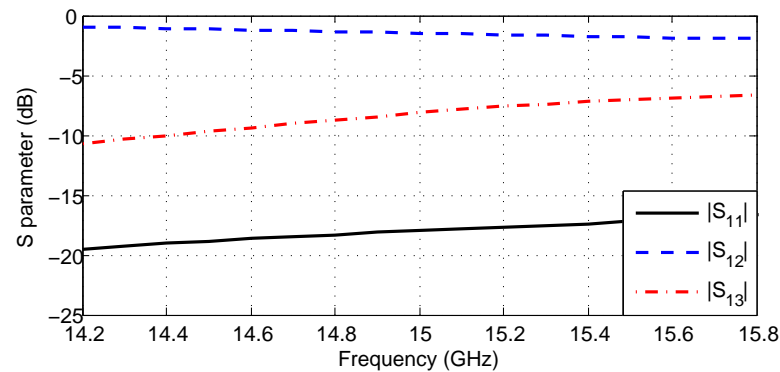


Fig. 4.12: Simulated S parameter of the coupled-line coupler with the RF output.

4.2.2 Interferences and Shielding

The proposed system has been conceived as a receiving antenna system for DF operations. It is then extremely important to protect the RF electronics part from external interferences using a shielding structure. Without any shielding, the incoming high frequency signal can easily couple to the transmission and/or feeding lines generating interferences which could blind the complete system and even damage some sensitive components.

The shielding structure is composed of a brass wall enclosing all the electronics and a copper cover. An array of metallized vias must be previously done in the TMM10 substrate (see Fig. 4.10) in order to connect the brass wall to the system ground. The wall and the copper cover

are then mechanically and electrically connected using M2 screws.

In order to feed the components with two external feeding lines of 5 and -5 V, two feed-through connectors are used. In addition, as detailed later in Section 4.3, a LED diode is placed in front of each antenna to indicate which one is receiving the highest signal level. In this case, 3mm-diameter holes must be drilled through the brass wall. It is important to point out that undesired signals might also go through these holes. Taking into account the permittivity of the LED plastic ($\epsilon_r \approx 3$), a 15 GHz signal passing through the hole would be attenuated around 20 dB, which could yield system malfunctioning. As a safety measure, shielding screens can be soldered in front of each hole, which protect from RF signals but allow to see through.

4.2.3 Parasitic Oscillations

A typical problem that arises when designing RF circuits is the parasitic oscillations happening in an amplifier stage. Parasitic oscillation is an undesirable oscillation caused by feedback and it is one of the fundamental issues addressed by control theory [104]. This phenomena is undesirable for several reasons: The oscillations may radiate from the circuit, waste power or cause undesirable heating.

Parasitic oscillation in an amplifier stage occurs when part of the output energy is coupled into the input, with the correct phase and amplitude to provide positive feedback at some frequency. If there is one frequency where the feedback is positive and the coupling is approximately $1/G_A$, the system will oscillate at that frequency. A circuit that is oscillating will not amplify linearly, so desired signals passing through the stage will be distorted. This is unacceptable in our system because the module placed after one amplifier is a power detector.

The amplifiers previously used provide a gain $G_A \approx 15$ dB in a wide frequency range between 12 and 30 GHz. Thus, a coupling between the input and the output of around -15 dB is enough for the amplifier to oscillate. This level of coupling can easily happen due to the combination of high frequency signals and components packaging. Indeed, component packaging is a major issue in microwave circuits as frequencies go higher [105]. The so-called cavity-resonance is a well known problem concerning the packaging of many microwave circuits and, in our case, couples energy between the input and the output ports of the amplifiers.

The HMC383LC4 amplifiers of our system are encapsulated in a $4 \times 4 \times 1$ mm³ alumina package. When these components are fed with standard MSLs, the package properties are such that the coupling $|S_{12}|$ between the lines is higher than -15 dB in the main part of the frequency range of operation. The $|S_{11}|$ and $|S_{12}|$ of two MSLs connected to a HMC383LC4 amplifier are shown in Fig. 4.13. It can be seen that, from around 19 GHz on, $|S_{12}| > -15$ dB and the amplifier will likely work in oscillating mode. This phenomena was observed using a probe

connected to the spectrum analyser and feeding only the amplifiers, which exhibited a similar oscillating behaviour with resonance peaks at 22.4 and 24 GHz.

It must be pointed out that this problem is strictly due to the coupling through the package and, therefore, its electrical properties should be changed in order to mitigate it. Common solutions applied at lower frequencies (such as grounding the surroundings of the microstrip lines to reduce parasitic radiation) do not apply here. Under these conditions, using microwave-absorbent material has proven to be very effective at damping the resonance [106]. When absorbers are attached to the component package, the energy primarily resides in them due to their high values for permittivity and permeability (as well as losses) hence, reducing the $|S_{12}|$.

The scenario of Fig. 4.13 was resimulated by introducing different absorbent material from ECCOSORB [107] to try to reduce the package coupling. The results are shown in Fig. 4.14 and the electromagnetic properties of the absorbers in Tab. 4.1. Since these results are based on extrapolations provided by the manufacturer, several empirical tests were also carried out with the spectrum analyser. As expected from the simulations, magnetic materials were performing the best in our measurements and, in particular, the ECCOSORB GDS-U was the only one able to completely cancel the oscillating behaviour of the amplifier over the whole band.

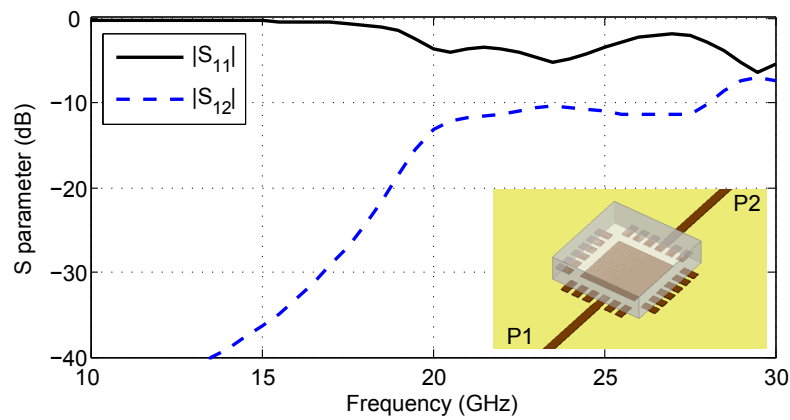


Fig. 4.13: S parameter of a HMC383LC4 amplifier in a ceramic package fed by two microstrip lines.

Absorber	Thickness (mm)	Relative Permittivity	Relative Permeability
ECCOSORB FGM-U-40	1	30 - j	1 - j1.2
ECCOSORB MCS-U	1	38 - j0.95	1 - j
ECCOSORB GDS-U	0.76	14 - j0.55	1 - j1.05
ECCOSORB LS-26	3	3 - j7	1

Tab. 4.1: Absorbers used in our tests and their estimated electrical properties around 20 GHz.

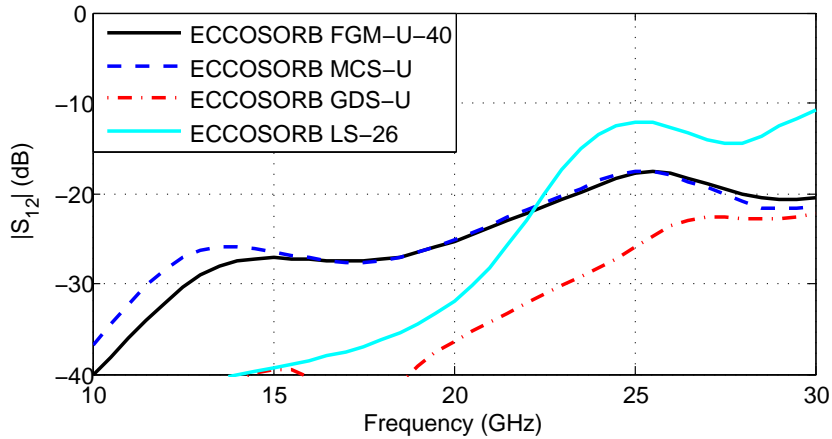


Fig. 4.14: $|S_{12}|$ of a HMC383LC4 amplifier in a ceramic package with different absorbers on top and fed by two microstrip lines.

4.3 DC Electronics

The purpose of the DC part is to define the control loop of the system and to store the LD output value corresponding to each antenna in order to compute the DoA estimation. The core of this part is the PIC16F88 used as Microcontroller Unit (MCU). This well established and low cost PIC presents several advantages with respect to the widely used PIC16F84A, such as an internal 10-bit Analog-to-Digital Converter (ADC) which, in our case, is needed to convert the LD analog output into a digital signal. Its functional diagram is shown in Fig. 4.15(a).

First of all, the signals $CTRL_1$, $CTRL_2$ and $CTRL_3$ are generated to control the SP4T switches and to select the desired antenna, as shown in Fig. 4.10. However, these switches work with a 0/-5 V logic while the PIC offers output levels between 0/+5 V. To convert the logic level, the analog triple 2-channel multiplexer MC14053BD is used (see Fig. 4.15(b)). The PIC digital outputs RA0, RA1 and RA2 are connected to the multiplexer control inputs A, B and C, respectively. These control pins are used to assign the desired values to the multiplexer outputs X,Y,Z. In our case, X0, Y0 and Z0 are connected to ground and X1, Y1 and Z1 to -5 V. Therefore, the multiplexer outputs X, Y and Z vary between 0 and -5 V and can be directly used as the control signals $CTRL_3$, $CTRL_2$ and $CTRL_1$, respectively.

In order to read the LD analog output, the RA4 pin of the PIC is configured as the input of the internal ADC. The default reference voltages of 0 and 5 V are kept. Since the LD provides a nominal logarithmic slope of 14.2 mV/dB, a theoretical 0.34 dB precision can be achieved. Although this precision could be increased by changing the ADC reference voltages, it is shown later that the accuracy of the system is limited by the number of output bits that PIC provides.

The PIC must be programmed to periodically change the control signals $CTRL_1$, $CTRL_2$ and

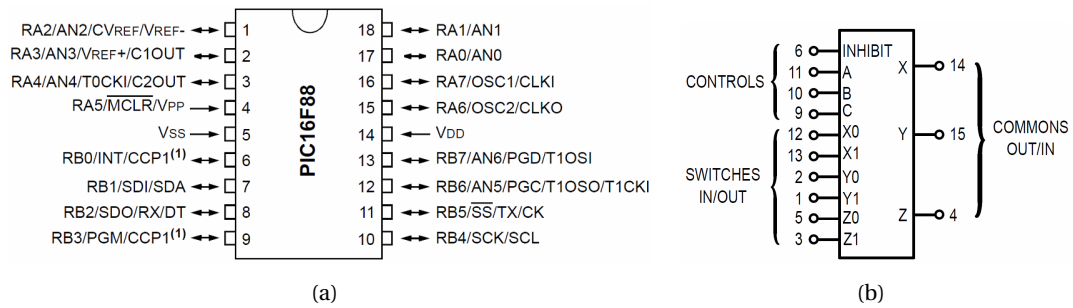


Fig. 4.15: (a) Functional diagram of the PIC16F88 and (b) of the MC14053BD.

CTRL_3 in order to scan the signals received by the different antennas. As a first demonstrator, each output RB pin of the PIC is connected to a LED diode placed in front of each antenna, which is used to indicate the one receiving the highest signal. As explained in Section 4.3, the RB pins can also be used to code the DoA value for a more accurate DF information.

Finally, the low dropout voltage regulator LT1962 is used to obtain a stable +3.3 V signal to feed the LD. The schematic and routing of the DC part was done with Altium Designer and is shown in Fig. 4.16.

DF Algorithm

As previously explained, the task of the PIC are to sample the signals received from the different antennas and to compute the DoA estimation. Setting the PIC internal oscillator to 4 MHz allows to read the signal of one antenna in 60 ms. This means that the DoA can be updated approximately every half second. Then, all 8 pins of PORTB (RB0-7) are used to codify the angle of arrival leading to a maximum accuracy of $360/2^8 \approx 1.4^\circ$.

To illustrate the functionality of the whole system, a simple amplitude comparison technique is used as DF algorithm. First, the signal level received by all 8 antennas is sampled in order to identify the two antennas receiving the highest power. Then, the difference ΔR in the received power between these two antennas is determined and, by knowing the antenna radiation patterns, the angle of arrival ϕ_0 is computed. For simplicity, it is assumed that only one signal is being received at a time.

As an example, let us consider that the antennas pointing at $\phi = 0^\circ$ and $\phi = 45^\circ$ are the ones receiving the highest signals, respectively. Using the measured patterns of Fig. 4.6, the difference ΔR in dB is shown in Fig. 4.17 as a function of the receiving angle ϕ_0 and for different frequencies. As expected, the highest difference corresponds to a signal coming from $\phi_0 = 0^\circ$ and, the minimum, to around $\phi_0 \approx 21^\circ$ where the patterns overlap. Averaging the response

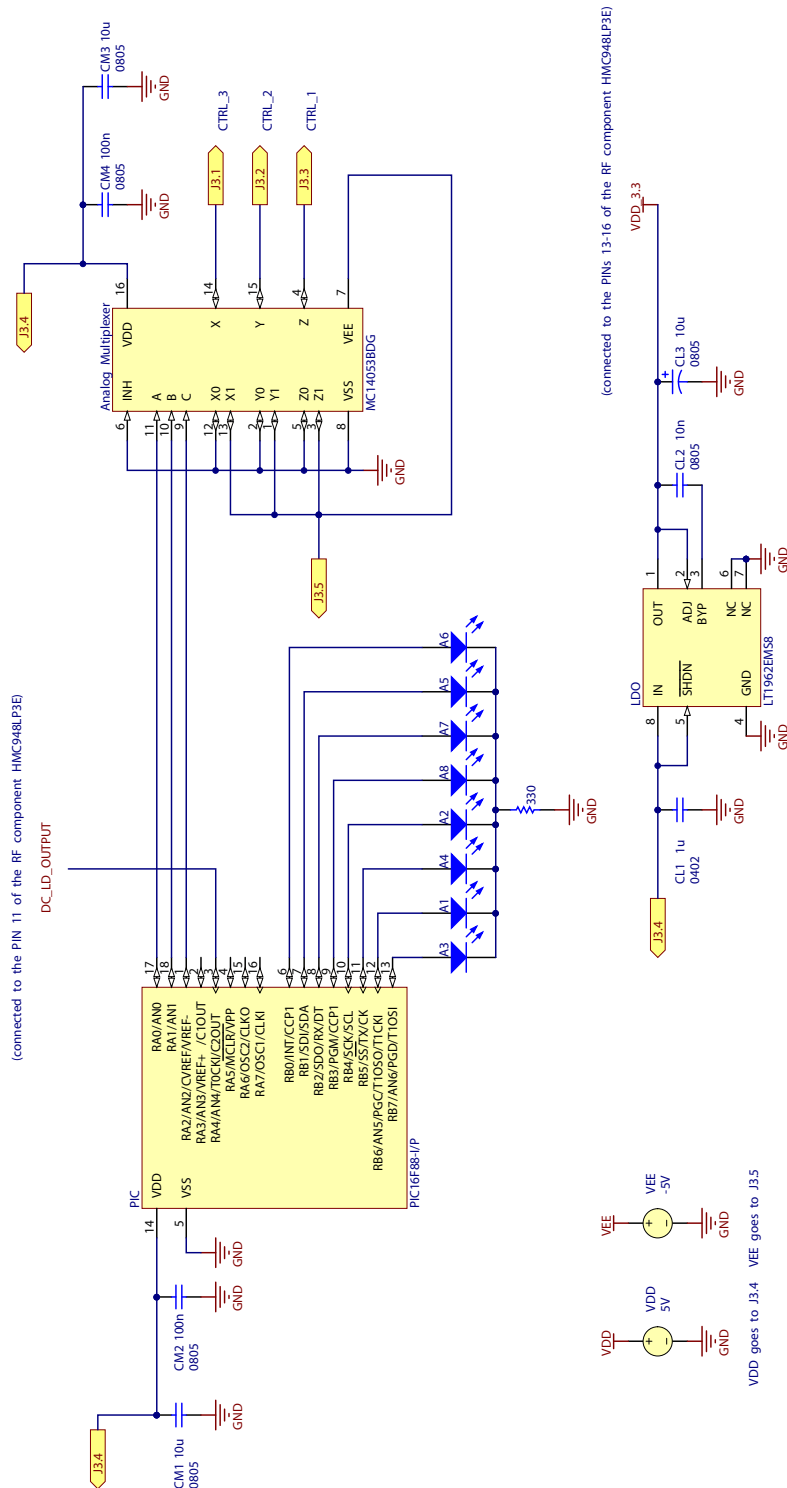


Fig. 4.16: Schematic view of the DC part. The low dropout voltage regulator LT1962 is used to obtain a stable 3.3 V signal to feed the logarithmic detector HMC948LP3E.

between the different frequencies, the relation between ϕ_0 and ΔR can be linearised as:

$$\phi_0 = 21 - 1.75\Delta R. \quad (4.2)$$

It can be seen in Fig. 4.17 that ΔR leads to different values of ϕ_0 depending on the frequency of operation, which limits the accuracy of the systems. According to Fig. 4.17 and Eq. (4.2), the maximum error in the value of ϕ_0 is $\pm 2.5^\circ$ within our range of interest (between 14.6 and 15.4 GHz).

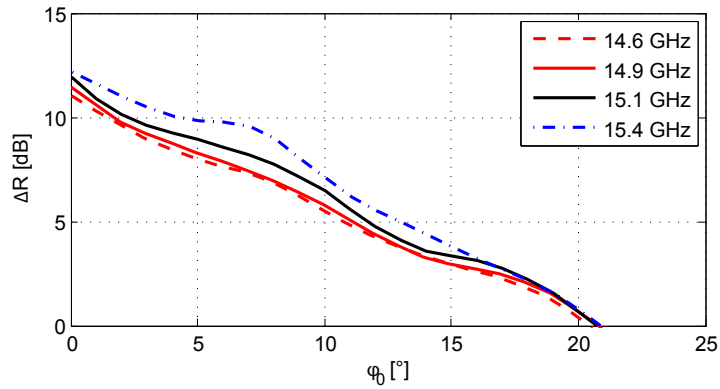


Fig. 4.17: Amplitude difference ΔR between the radiation patterns of two adjacent antennas as a function of the receiving angle ϕ_0 and for different frequencies.

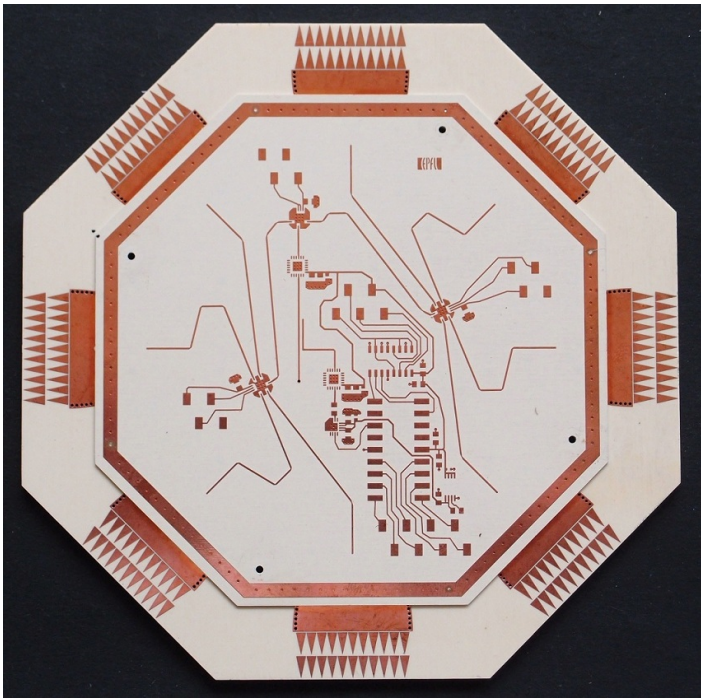
A minimum threshold for the received signal level is also required before estimating the DoA. Otherwise, even if there is no transmitting antenna, a meaningless value of ϕ_0 could be provided due to the system noise. According to the previous scenario specifications of Section 4.2, a threshold of 1.1 V is set at the input of the LD.

4.4 Experimental Results

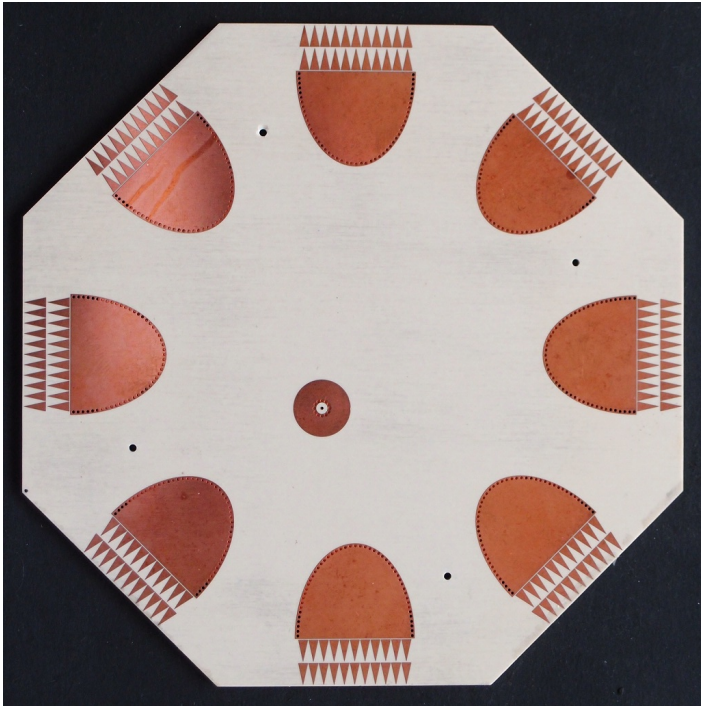
4.4.1 Manufacturing Process

The complete DF antenna array was based on the prototype of Section 4.1.2. All the dimensions for the antennas, the feeding transition and the substrates are the same. In order to easily accommodate all the required RF and DC components, the radius of the array was set to 9 cm.

The RF design and masks were created with Ansys Designer following the scheme of Fig. 4.10. The routing for the DC part (Fig. 4.16) was done with the help of Mr. Peter Brühlmeier from the ACI workshop at the EPFL. Once the antennas were built in the TMM3 substrate and the mask for the electronics etched in the TMM10, they were glued with conductive epoxy. The result is shown in Fig. 4.18.



(a)



(b)

Fig. 4.18: (a) Top and (b) bottom picture of the two substrates after the gluing process.

The next step was to solder the electronic components. The quantity and characteristics of all required components are summarized in Tab. 4.2. First of all, the MMICs must be placed. These components are encapsulated in QFN plastic or ceramic packages and must be soldered in a special hot air station following a certain temperature profile which rises until 230°C. This task was performed with the help of Mr. André Badertscher from the EPFL ACI workshop. Due to the high temperature exposition in the hot air station, the cooper was slightly oxidized and had to be properly cleaned before continuing with the soldering. The rest of the DC components, connectors and wires were soldered under microscope and the final result (including the 3mm-thick brass wall for the shielding) is shown in Fig. 4.20.

Component name	Quantity	Description	Package Type
HMC641LC4	3	SP4T RF switch	LP4 QFN
HMC383LC4	2	15 dB RF Amplifier	LP4 QFN
HMC948LP3E	1	Logarithmic Detector	LP3 QFN
PIC16F88-I/P	1	16bit PIC microcontroller	18-Lead PDIP
DIL 18 SMD M	1	Socket for the PIC	"
LT1962EMS8-3.3	1	LDO regulator (3.3V output)	MS8
MC14053BDG	1	Analogic Multiplexer	CASE 751B-05
SMD Capacitor	3	10 μF	0805
	1	4.7 μF	0603
	2	2.2 μF	0603
	1	1 μF	0402
	2	100 nF	0805
	3	10 nF	0805
	5	1 nF	0805
	2	100 pF	0805
	1	5 pF	0805
Resistor	1	330 Ω	ceramic
LED	8	Yellow LED	3 mm

Tab. 4.2: List of required components for the complete DF system.

Finally, the copper cover for the shielding structure was done by etching a 200 μm copper foil and bending it accordingly as shown in Fig. 4.21(a). More absorbent material was also glued at the sealing of the cover to avoid possible cavity resonances within the shielding structure [105]. The complete prototype is shown in Fig. 4.21(b).

4.4.2 Measurements

As a first testing set-up, the DF system was placed in the LEMA anechoic chamber (see Fig. 4.19). The emitter antenna was a medium gain ridged horn antenna ($G_t \approx 10$ dBi) placed at 2.4 m from the DF system. Under these conditions, the minimum signal strength that the DF

system was able to detect was -8 dBm (≈ 0.15 mW), which is in very good agreement with the link budget expectations from Section 4.2. This means that an UAV equipped with this system could detect a transmitting signal of 24 dBm (which is a typical transmission power level of a mobile phone) at a distance of 100 m.

For accurate DoA estimation, a system calibration was also performed. Although the MSLs coming from each antenna were designed of the same length (same losses), the insertion losses of the SP4T switches were slightly different for each port. To account for this difference, the signal strength received by each antenna under the same conditions was measured at the RF output and the difference compensated later by post-processing in the PIC.

The sensitivity of the system is mainly limited by the sensitivity of the logarithmic detector. For a reliable DoA estimation, a signal strength of at least -65 dBm is required at the antenna level. Then, by using the amplitude comparison algorithm, the maximum DoA error is of $\pm 2.5^\circ$ between 14.6 and 15.4 GHz. The system consumes around 300 mA (the major part is due to the amplifiers and the logarithmic detector) and its total weight is 220 g (including the shielding structure). Note that the total weight could be significantly reduced by using aluminium instead of brass for the shielding structure.

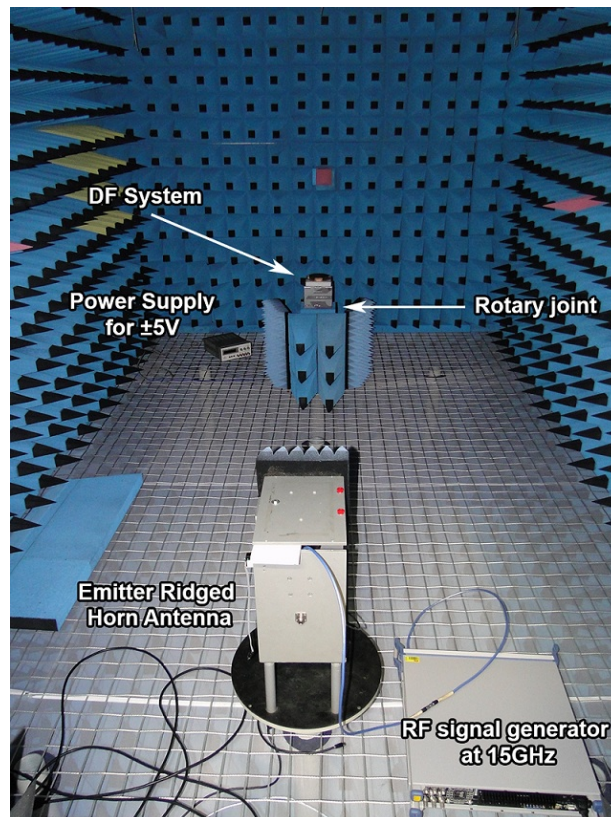


Fig. 4.19: DF system testing set-up in the LEMA anechoic chamber.

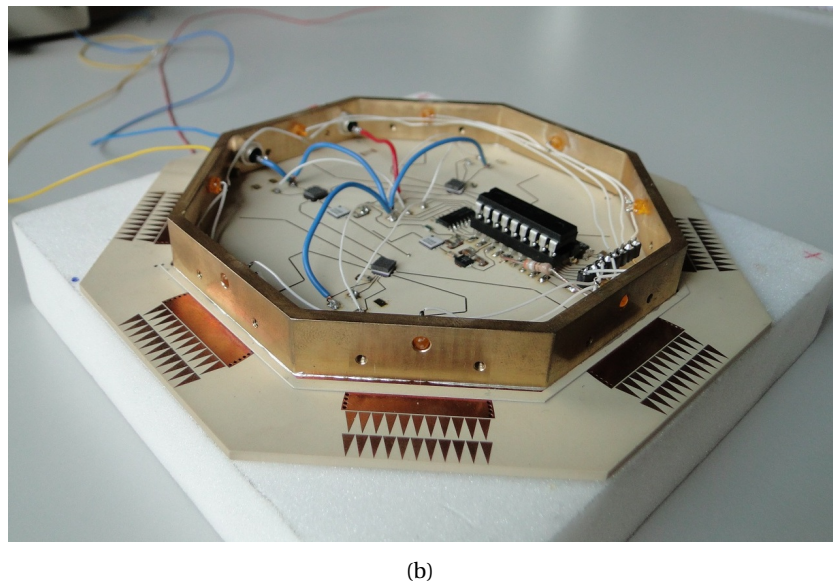
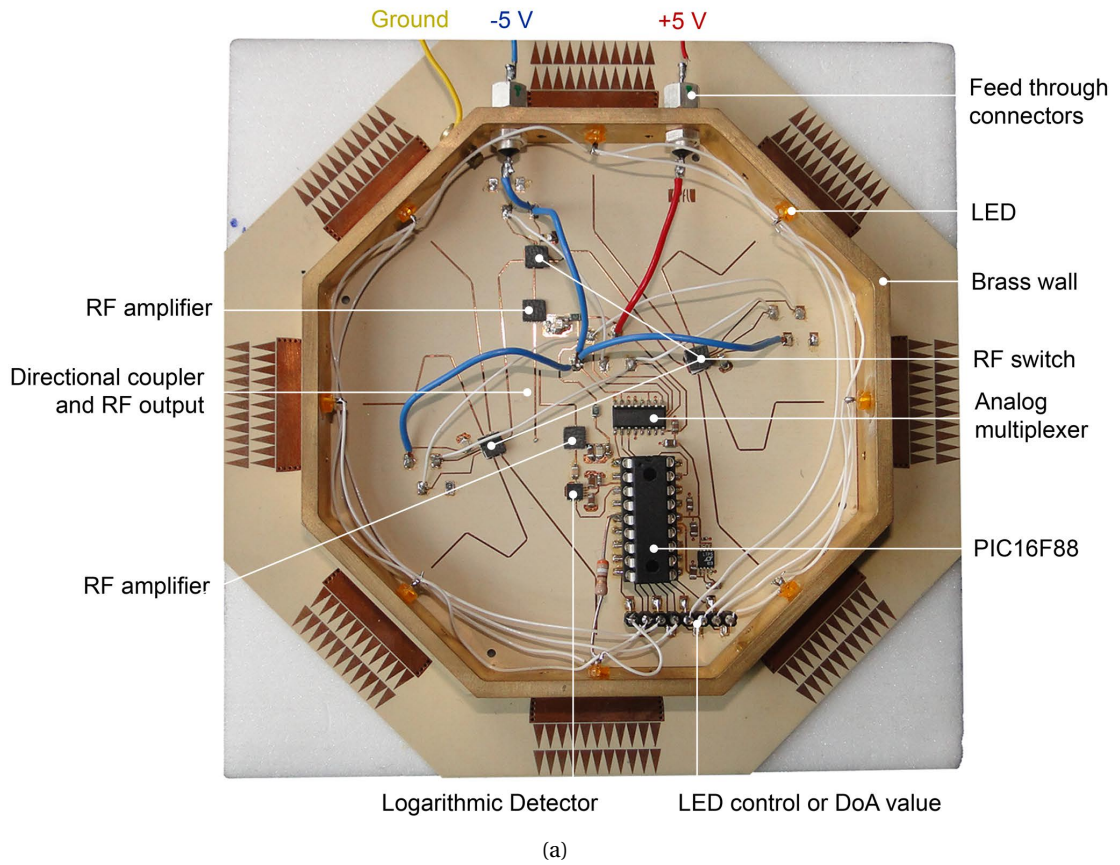
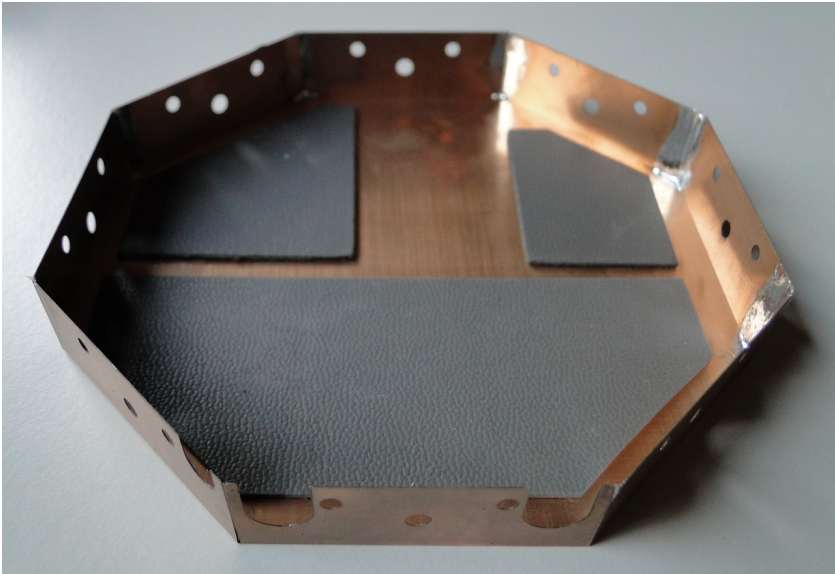
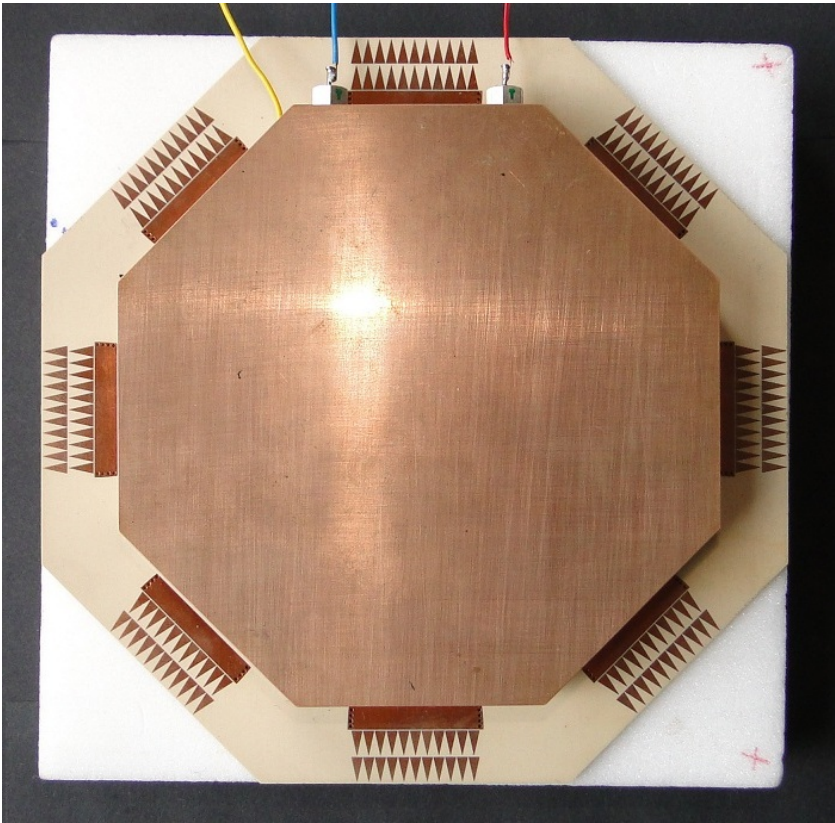


Fig. 4.20: (a) Top and (b) isometric view of the final DF prototype without cover.



(a)



(b)

Fig. 4.21: (a) Copper cover with absorbent material and (b) top view of the final DF prototype.

4.5 System Interaction with Airborne Platforms

A possible scenario for the usage of the presented DF system is in UAV such as drones or quadcopters, where the reduction of the weight and the drag are key points. Furthermore, although the system has been demonstrated for a simple receiving DF application, the whole antenna array and part of the electronics could be directly used to implement more ambitious applications requiring high-data rate transmissions at the Ku-band.

As an example, the performances of the proposed system are evaluated when mounted on a commercial quadcopter whose typical weight is more than 3 kg. These quadcopters are usually designed to carry high definition cameras or other devices weighting more than 500 g, being thus our DF system of weight 220 g well within their capabilities. A 3D model¹ of a quadcopter including the DF system is shown in Fig. 4.22(a).

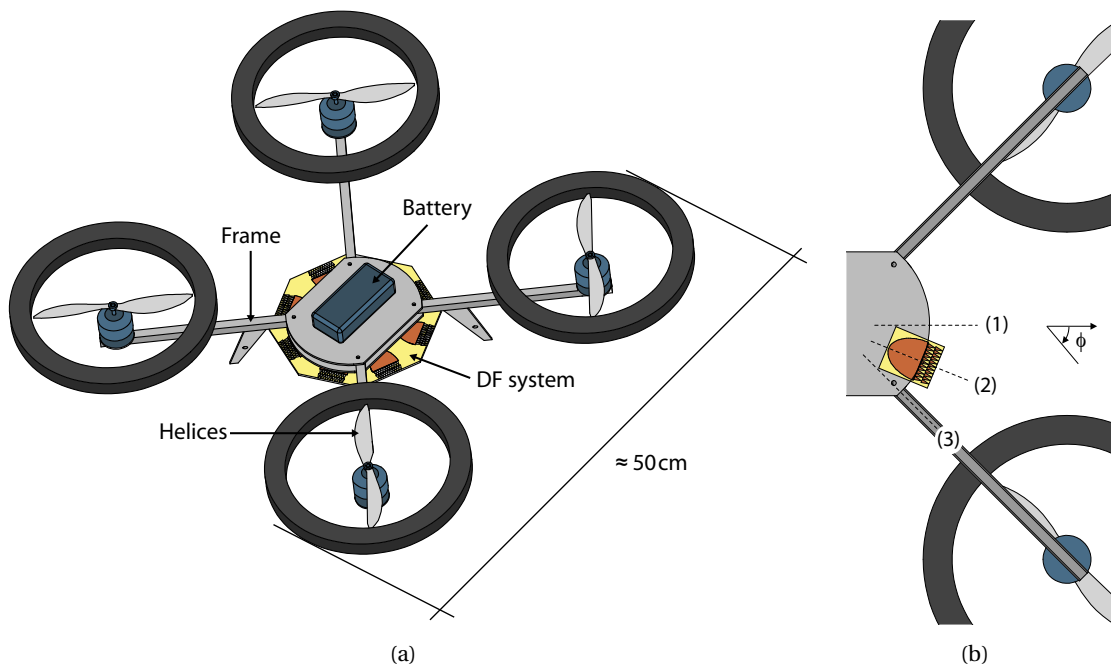


Fig. 4.22: (a) Quadcopter 3D model with the DF system. (b) Detailed view of the possible placement of a single SIW horn on the quadcopter platform.

In order to find the optimum placement of the system, its RF performances including the complete quadcopter structure must be studied. To tackle this electrically large problem, the integral equation solver of Ansys HFSS v14 was used for simulations. The main parts of the quadcopter are here listed with their approximate relative permittivity ϵ_r at the Ku-band:

¹The 3D model used was downloaded from the GRABCAD community (grabcad.com)

- Frame: carbon or glass fiber ($\epsilon_r \approx 3.5$)
- Helices: hard plastic ($\epsilon_r \approx 3$)
- Rotor engine and batteries: metal-based
- Other supporting structures: foam-based ($\epsilon_r \approx 1.3$)

The performances of a single SIW horn antennas in three different position (shown in Fig. 4.22(b)) are first computed. The H-plane radiation patterns at 15 GHz of the horn are shown in Fig. 4.23. As expected, its performances in position (1) do not significantly differ from the ones of the SIW horn alone. However, if the 8 element array is placed such that one antenna is in (1), the adjacent antenna would be in (3), i.e., aligned with the supporting frame of the helices. The latter position, not only degrades the HPBW and FTBR (see Fig. 4.23(a)), but also dramatically increases the cross-polar component (see Fig. 4.23(b)). As a trade-off to accommodate all the elements, the horns are placed in position (2) which barely affects the H-plane pattern and the cross-polar components still remains below -20 dB.

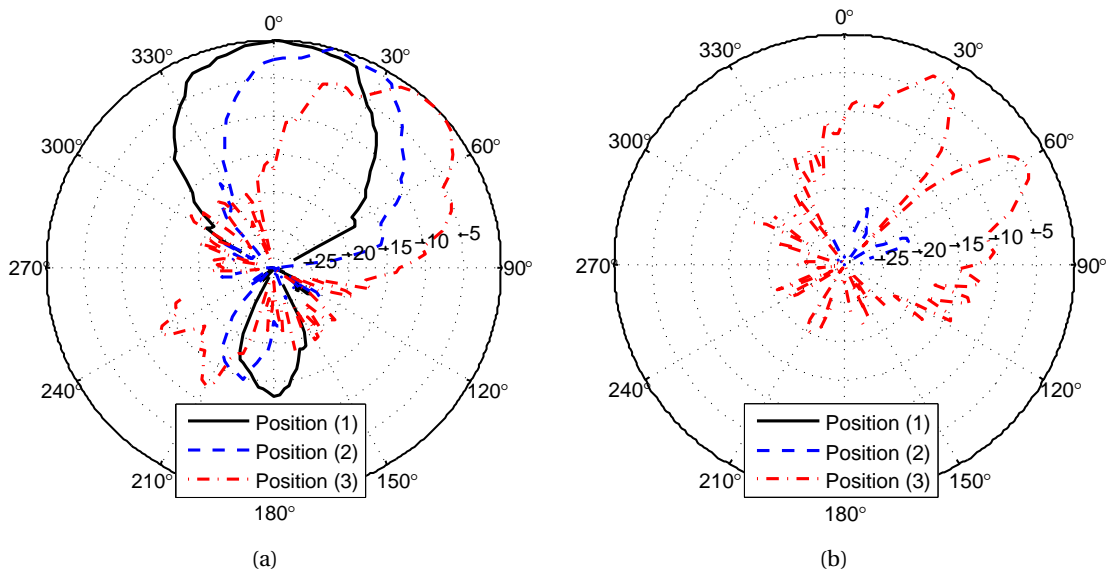


Fig. 4.23: (a) Co-polar and (b) X-polar components at 15 GHz of the H-plane normalized directivity for the different placements of a single SIW horn.

According to the previous discussion, the choice of 8 elements for the antenna array proved also to be an optimum number for systems placed on quadcopters or similar UAV with four rotors: Good performances are achieved yet minimizing the interaction with the platform.

4.6 Conclusions

The SIW technology is a very promising candidate to provide widespread commercial solutions. In order to achieve this goal, however, not only stand-alone SIW devices must be designed and tested but also complete RF systems. Most of complete SIW-based systems work with broadside radiating elements which cover a portion of a semi-sphere such as for radar or satellite communications.

In this chapter, the complete design, manufacturing and validation of an SIW-based DF system covering the azimuthal plane has been presented. The DF array is composed of 8 extremely low-profile SIW horn antennas as the one presented in Chapter 3. All SIW horns have been built in a single layer of substrate thus greatly reducing the manufacturing cost and time when compared to an array of standard horns. The RF electronics (MMICs) have been placed on another substrate and interconnected with the antennas through a robust and wideband transition. Therefore, the complete system uses commercial components, standard manufacturing processes and only requires 2 layers of substrate.

Practical considerations have been taken into account in order to choose the most appropriate RF and DC electronics. Common problems encountered in the implementation of these high frequency systems have been explained and solutions have been proposed and tested (need for a shielding structure, parasitic oscillations, etc.). All together resulted into a fully operational azimuth DF system working at the Ku-band.

In-line with possible future work, the interaction between the DF system and a quadcopter (as possible UAV platform to be mounted on) has been studied. It has been shown that the impact of the UAV on the antenna performances can be minimized as far as the array elements are not aligned with the main structural elements.

This chapter closes the design and implementation of a Ku-band DF system based on SIW horn antennas. This proves the viability at a system level of extending the working frequency range of these SIW antennas towards de Ku-band and below, i.e., the first objective of this PhD thesis. The second objective concerning the propagation of orthogonally polarized modes in a single substrate integrated guide is addressed in the following chapters.

5 Extended Substrate Integrated Waveguide (ESIW)

The Substrate Integrated Circuits (SICs) architecture can be used to design a broad range of hybrid planar/non-planar circuits and devices. A subfamily of SICs is the SIW (as explained in Section 2.1 and illustrated in Fig. 5.1(a)) which is typically used to carry TE_{m0} modes¹ since it exhibits similar performances to those of metallic Rectangular Waveguides (RWG) [29]. This is why this guide has been used in the previous chapters to create a vertically polarized H-plane SIW horn antenna based on the TE_{10} and TE_{30} modes. Other types of guides have been also proposed to carry vertically polarized modes: the Substrate Integrated Slab Waveguide (SISW) [108], the Substrate Integrated Image Guide (SIIG) [109], the Half-Mode SIW (HMSIW) [110], etc. Therefore, many H-plane SICs can be easily implemented using these guides.

In order to create E-plane SICs, thus dealing with TE_{0n} modes, conventional SIWs cannot be used since the longitudinal surface currents are subject to strong radiation due to the presence of the gaps between the metallized vias (see Fig. 5.1(a)). The most common integrated guide used to support TE_{0n} -like modes is the Substrate Integrated Non-Radiative Dielectric (SINRD) guide [31]. This guide is a substrate integrated version of the classical Non-Radiative Dielectric (NRD) guide [111] where the low permittivity region is created by drilling a periodic air-hole pattern (see Fig. 5.1(b)). This air-hole region has an effective permittivity ϵ_{rh} lower than ϵ_r such that the mode in this region is under cut-off and the energy is then confined within the central dielectric channel.

In an SINRD guide, the mode resembling the TE_{10} is the LSE_{10} mode and the one resembling the TE_{01} is the LSM_{11} mode (see Fig. 5.1). The expressions for the electric field distributions of TE/TM modes in a RWG and LSE/LSM modes in an SINRD are summarized in Appendix A. Different types of SINRD circuits (mainly based on the LSM_{11} mode) have been proposed such as filters, couplers and antennas [31, 112, 113]. Although this guide is already able to

¹Note that the sub-index m refers to the y -axis (parallel to the substrate plane) and the sub-index n to the z -axis (perpendicular to the substrate plane), being x the direction of propagation (see Figs. 5.1-5.2).

carry orthogonally polarized modes, its geometrical dimensions affect both LSE and LSM modes, being thus difficult to independently control them. For instance, increasing the width of the central dielectric channel not only decreases the cut-off frequency of the vertically polarized LSE_{10} mode, but also the one of the LSM_{11} mode. The latter is because more energy is more confined in the high permittivity channel and the decaying fields in the air-hole region become less relevant. Therefore, it is very challenging to design SINRD structures with good isolation and cross-coupling levels between these two modes.

Due to the previous drawbacks, even if the NRD guide is well-known since decades, practically no work has been reported in which LSE and LSM modes are simultaneously exploited. Only recently, a compact structure has been presented in [114] where similar modes are combined using an SIW and an iSINRD guide [115], although its performances are extremely narrow band ($< 1\%$). Other drawbacks of dielectric-based guides are the difficult implementation of efficient planar excitation schemes (specially for the LSM_{11} mode which may require additional structures to suppress spurious modes appearing at the feeding transition [116]) and the need for additional top and bottom metallic plates to cover the air-holes after the

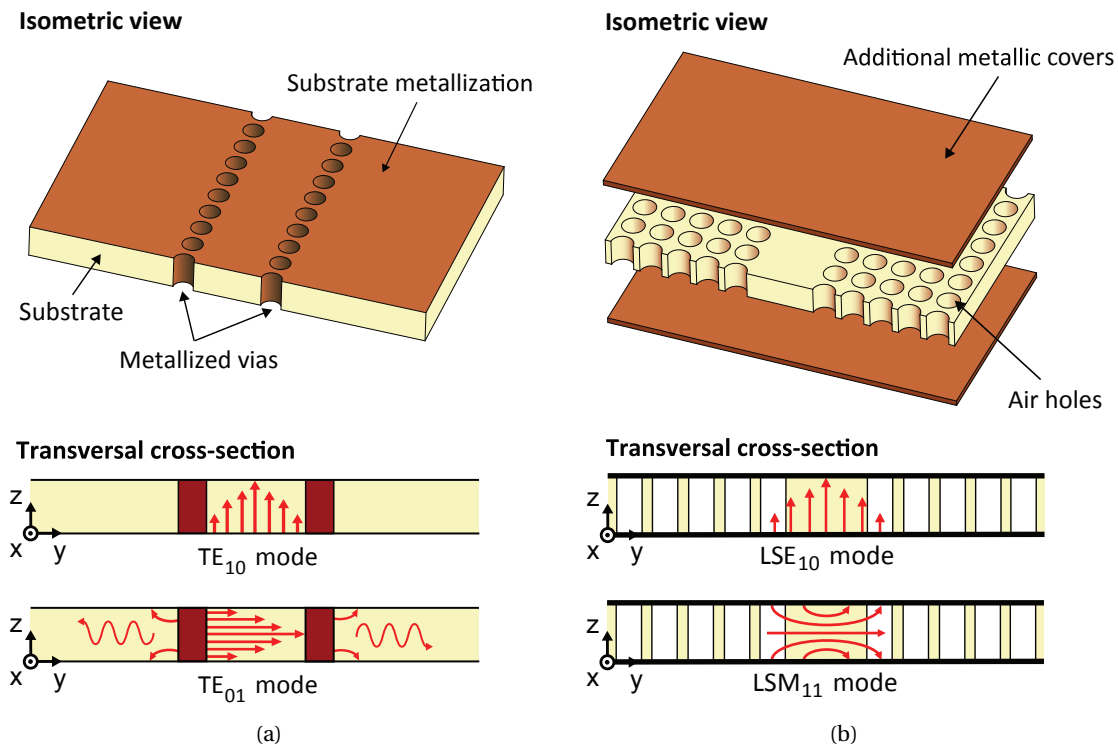


Fig. 5.1: (a) Substrate Integrated Waveguide (SIW) with the TE_{10} and TE_{01} modes and (b) Substrate Integrated Non-Radiative Dielectric (SINRD) guide with the LSE_{10} and LSM_{11} modes. Metal is represented in brown, dielectric substrate in beige and electric field lines in red.

drilling process. The latter problem has been addressed in [117], where they propose a PCB version of the SINRD guide based on the fact that the radiation loss due to the uncovered air-holes can be minimized by carefully choosing the guide and air-holes dimensions.

Aiming to develop robust dual-polarized SICs which alleviate the aforementioned drawbacks of SINRD guides, a new substrate integrated guide is here proposed and called Extended Substrate Integrated Waveguide (ESIW). The working principle of this guide is based on a combination of SIW and SINRD guides and its geometry is shown in Fig. 5.2. The two rows of metallized vias are the same as in a conventional SIW. The air-holes beyond the vias are used to contain the energy that would leak through the gaps between vias when modes having an electric field components along the y -direction are excited. Then, this guide becomes suitable to carry both TE_{m0} and TE_{0n} modes, quasi-independently control their propagation characteristics and can be manufactured in a simple and practical manner.

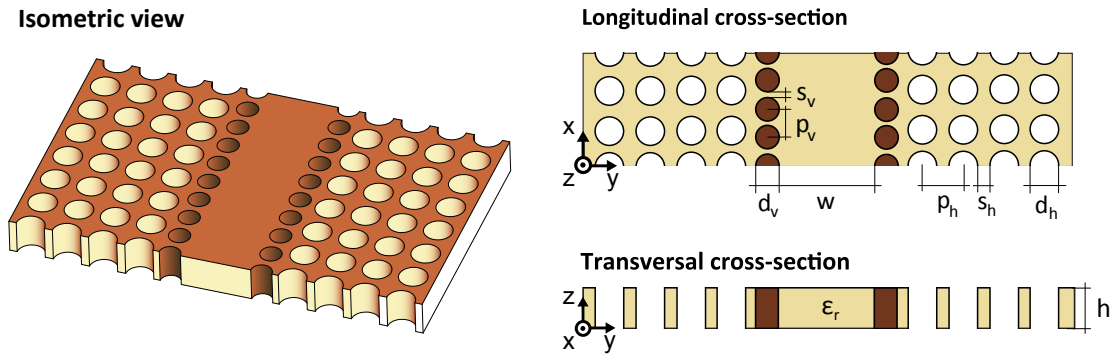


Fig. 5.2: Geometry of the proposed Extended Substrate Integrated Waveguide (ESIW).

The main properties of the ESIW are derived in Section 5.1, including the impact of the different geometrical parameters on the propagation characteristics of the TE_{01} mode. A new planar transition to efficiently excite this mode is also proposed in Section 5.2. Measurements of an ESIW prototype are presented in Section 5.3 validating the expected performances. It must be pointed out that the characteristics of the TE_{10} mode in the ESIW are not treated here because they are the same as in a conventional SIW. A complete and rigorous study of the TE_{10} mode properties in an SIW can be found in [118].

5.1 Analysis and Design of the ESIW

This section is devoted to study the propagation characteristics of the TE_{01} mode in the ESIW. First, the bandwidth is determined by finding its maximum frequency of operation (Section 5.1.1) and its cut-off frequency (Section 5.1.2). Several band-gap effects from which the ESIW might suffer are also studied in Section 5.1.3. Design rules are provided in order to maximize the operational bandwidth avoiding any band-gap effect within it. Finally, the ESIW radiation

losses and bandwidth are compared with other waveguides in Section 5.1.4.

5.1.1 Maximum Frequency of Operation

The maximum frequency of operation f_h of the TE_{01} mode is defined as the frequency beyond which the radiation leakage is no longer contained. This happens when the parallel plate mode in the air-holes region is no longer under cut-off and is able to propagate, as in the case of an SINRD guide. The value of f_h is then determined by the effective permittivity of the air-holes region ϵ_{rh} and the guide height h :

$$f_h = \frac{c}{2h\sqrt{\epsilon_{rh}}} \quad (5.1)$$

where c the speed of light in free space. The value of ϵ_{rh} can be approximated as [31]:

$$\epsilon_{rh} \simeq \epsilon_r \left(1 - \frac{A_{HOLES}}{A_{CELL}} \right) + \frac{A_{HOLES}}{A_{CELL}} \quad (5.2)$$

where A_{CELL} is the area of a unit cell in the air-holes region and A_{HOLES} the area of the air-holes in it. These areas depend on the pattern (rectangular, triangular, etc.), the hole periodicity p_h and the hole diameter d_h . The important quantity is the proportion of air-holes with respect to the total area. A more important proportion of air-holes (i.e., air) decreases the effective permittivity ϵ_{rh} which increases f_h and thereby the operational bandwidth. Although increasing this proportion might also increase the radiation losses (due to the lack of metallic covers), it is shown in Section 5.1.4 that these losses are negligible in practice.

5.1.2 Cut-off Frequency of the TE_{01} Mode

Transverse Equivalent Network

The propagation characteristics (and thus the cut-off frequency) of the TE_{01} mode in the ESIW can be determined by using the Transverse Equivalent Network (TEN) [119] representation of Fig. 5.3. In this case, the modes considered are TM^y modes (see Appendix A) with characteristic impedances Z_{TM1} and Z_{TM2} and transverse wavenumbers k_{y1} and k_{y2} , respectively. The width of the dielectric channel is w and the one of the air-holes region, w_h . The leakage in the air-holes region due to the lack of metallic covers has been neglected (this assumption is verified in Section 5.1.4).

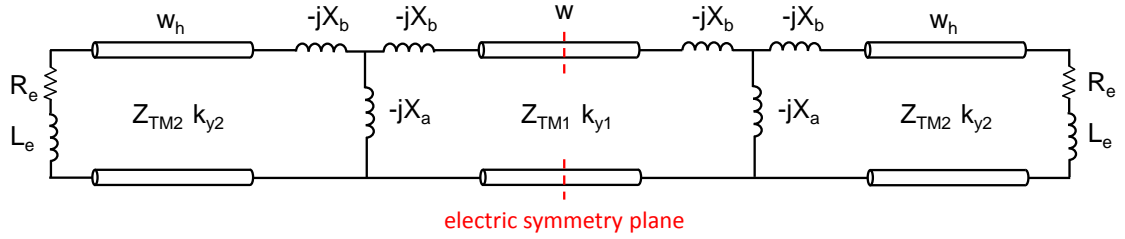
In the case of the TE_{01} mode, the metallic vias are parallel to the magnetic field so they can be treated as capacitive obstacles and modelled using the T-network equivalent circuit derived

by Lewin in [120]. The values for the normalized parallel X'_a and series X'_b impedances are:

$$X'_a = \frac{2p_v}{\pi k_{y1} d_v^2} \left(1 + \frac{7k_{y1}^2 d_v^2}{32} + \frac{k_{y1}^2 d_v^2}{8} \log\left(\frac{\pi d_v}{p_v}\right) - \frac{\pi^2 d_v^2}{12p_v^2} \right) \quad (5.3)$$

$$X'_b = \frac{\pi k_{y1} d_v^2}{8p_v} \left(1 + \frac{k_{y1}^2 d_v^2}{8} \log\left(\frac{\pi d_v}{p_v}\right) - \frac{3k_{y1}^2 d_v^2}{32} \right) \quad (5.4)$$

where p_v is the periodicity of the metallized vias and d_v their diameter.



$$k_{y1} = \sqrt{k_0^2 \varepsilon_r - k_x^2 - \left(\frac{\pi}{h}\right)^2} \quad Z_{TM1} = \frac{k_{y1}}{\omega \varepsilon_0 \varepsilon_r}$$

$$k_{y2} = \sqrt{k_0^2 \varepsilon_{rh} - k_x^2 - \left(\frac{\pi}{h}\right)^2} \quad Z_{TM1} = \frac{k_{y2}}{\omega \varepsilon_0 \varepsilon_{rh}}$$

Fig. 5.3: Transverse equivalent network representation of the ESIW with the TE_{01} mode.

The open-ended termination of the air-holes region can be modelled as an inductance in series with a resistance ($Z_e = R_e + jL_e$). When the mode is evanescent (below f_h), accurate values for Z_e can be obtained by following the procedure described in [121]. When the mode is propagating (above f_h), one can apply the approximated formula found in page 186 of reference [122].

Finally, by applying an electric symmetry plane condition for the TE_{01} mode, the complete Transverse Resonance Equation (TRE) can be written as:

$$\frac{1}{jZ_{TM1} \tan(k_{y1} \frac{w}{2}) - jX'_b Z_{TM1}} - \frac{1}{jX'_a Z_{TM1}} + \frac{1}{Z_{TM2} \left(\frac{Z_e + jZ_{TM2} \tan(k_{y2} w_h)}{Z_{TM2} + jZ_e \tan(k_{y2} w_h)} \right) - jX'_b Z_{TM1}} = 0 \quad (5.5)$$

which must be solved numerically tracking the correct solution of k_x in the complex plane. In order to compute the cut-off frequency f_c , Eq. (5.5) can be simplified assuming that the evanescent mode in the air-hole region is completely attenuated ($w_h \rightarrow \infty$). Then, the TRE becomes:

$$\tan\left(k_{y1} \frac{w}{2}\right) + \left(\frac{X'_a Z_{TM2} - jX'_a X'_b Z_{TM1}}{Z_{TM2} - j(X'_a + X'_b) Z_{TM1}} - X'_b \right) = 0. \quad (5.6)$$

As a remark on the TEN, note that the inductive cylinders in a conventional SIW with the TE_{10} mode can also be modelled using a T-network. In this case, they are inductive obstacles and the parallel arm impedance is the main term, while the impedances of the series arms are only second order corrections accounting for the exact geometry of the obstacle (cylindrical, rectangular, etc.) [120]. However, when dealing with capacitive obstacles, all terms are equally important in determining the behaviour of the obstacle. Actually, rectangular metallized vias provide considerably better performances than cylindrical ones. The drawback of rectangular vias is that, in general, they can only be drilled by laser micro-machining while circular ones can be realized by relatively simple PCB processing techniques.

Cut-off frequency analysis

The cut-off frequency f_c is accurately defined as the frequency at which the real and imaginary part of the TE_{01} wavenumber ($k_x = \beta_x - j\alpha_x$) are equal. The main parameters defining the value of f_c are the substrate thickness h , the permittivity ϵ_r , the metallic vias diameter d_v and the vias separation s_v . In SINRD guides, the value of ϵ_{rh} and the channel width w also play an important role in f_c , which usually narrows down the bandwidth. However, this influence is remarkably reduced in an ESIW since the energy is more confined in the central channel thanks to the metallized vias.

In order to illustrate this advantage, the cut-off frequency of an ESIW and an SINRD are plotted in Fig. 5.4 as a function of w and ϵ_{rh} . The guides are designed to work at the Ku-band with $\epsilon_{rh} = 9.56$, $h = 3.9$ mm, $d_v = 2$ mm and $s_v = 0.2$ mm. In addition, the results from the proposed TEN are compared with the ones from the Eigenmode solver of Ansys HFSS v14. It is shown that strong variations in the value of ϵ_{rh} or w slightly modifies the cut-off frequency of the ESIW (less than 2%) while they considerably affect the one of the SINRD guide (up to 10%).

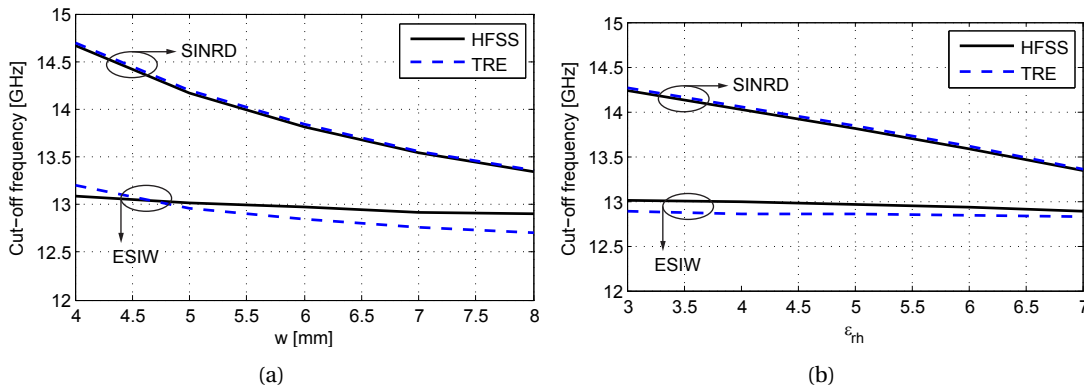


Fig. 5.4: Cut-off frequency f_c of the TE_{01} mode in an ESIW and of the LSM_{11} mode in an SINRD guide as a function of (a) w and (b) ϵ_{rh} . Parameters: $\epsilon_r = 9.56$, $h = 3.9$ mm, $d_v = 2$ mm and $s_v = 0.2$ mm.

The differences between the TEN and HFSS are mainly due to the higher order modes generated at the gap between vias s_v . As expected, the influence of these modes is higher as s_v increases and can deteriorate the ESIW performances until the point of being worse than the ones of an SINRD guide. The latter happens when the metallic vias acting as scatterers are much smaller than the cut-off wavelength λ_{gc} , i.e., $d_v = p_v - s_v \ll \lambda_{gc}$. This effect is shown in Fig. 5.5, where the value of f_c is plotted as a function of s_v and for different values of p_v . The two regions to be avoided when designing ESIWs are: (1) When the separation between vias s_v becomes too small to be properly manufactured (generally $s_v < 0.15$ mm) and (2) when the ESIW cut-off frequency becomes higher than the one of an SINRD guide.

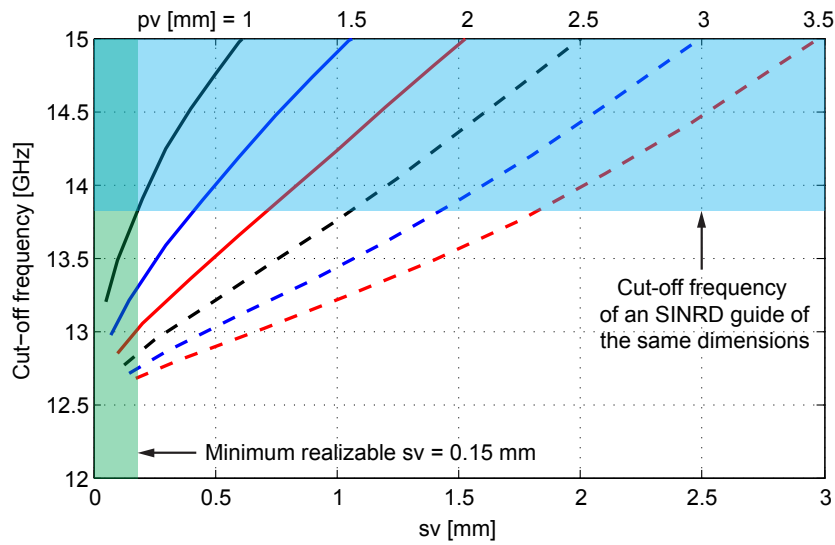


Fig. 5.5: Cut-off frequency f_c of the TE_{01} mode in an ESIW as a function of s_v and for different values of p_v (values obtain with the Ansys HFSS v14). Parameters: $\epsilon_r = 9.56$, $\epsilon_{rh} = 5$, $w = 6.1$ mm, $h = 3.9$ mm.

Although increasing the value of d_v seems to improve the ESIW performances, it might also introduce Electromagnetic Bandgaps (EBG) regions within the frequency range of interest. This important point is discussed in the following section.

5.1.3 Bandgap Effects

Due to the geometry of the ESIW, in particular the use of metallic capacitive obstacles, an EBG always appears. It starts at the theoretical cut-off frequency of the TE_{01} mode in an ideal Rectangular Waveguide (RWG) and is always present regardless of the type of material used or the size of the metallized vias/air-holes [31]. This phenomena is stronger as s_v increases or d_v decreases and might considerably affect the cut-off frequency f_c of the guide.

This bandgap cannot be predicted with the proposed TEN of Fig. 5.3 since higher order modes are not included in the Eqs. (5.3)-(5.4). For any value of s_v , d_v or p_v , the right propagation

curves can be obtained with a full-wave solver such as HFSS [123]. Nevertheless, when working inside the region of interest of Fig. 5.5 (white), the values for f_c obtained with the TEN are within a 3% error.

The aforementioned EBG can be seen in Fig. 5.6 where the phase constant β_x and attenuation constant α_x are plotted for $s_v = 0.4$ and $s_v = 1.2$ mm. As expected, the bandgap starts at the cut-off frequency of the ideal RWG (dashed-dotted red line) and the TEN model fails to predict the guide performances for a large separation between vias s_v (see Figs. 5.6(b) and (d)). Note that, as the frequency increases, the value of β_x tends to be the same as in a RWG since the vias diameter d_v is comparable with the guided wavelength λ_g . This is an important design-wise advantage and it is used in Chapter 6 to design a complex structure based on ESIWs.

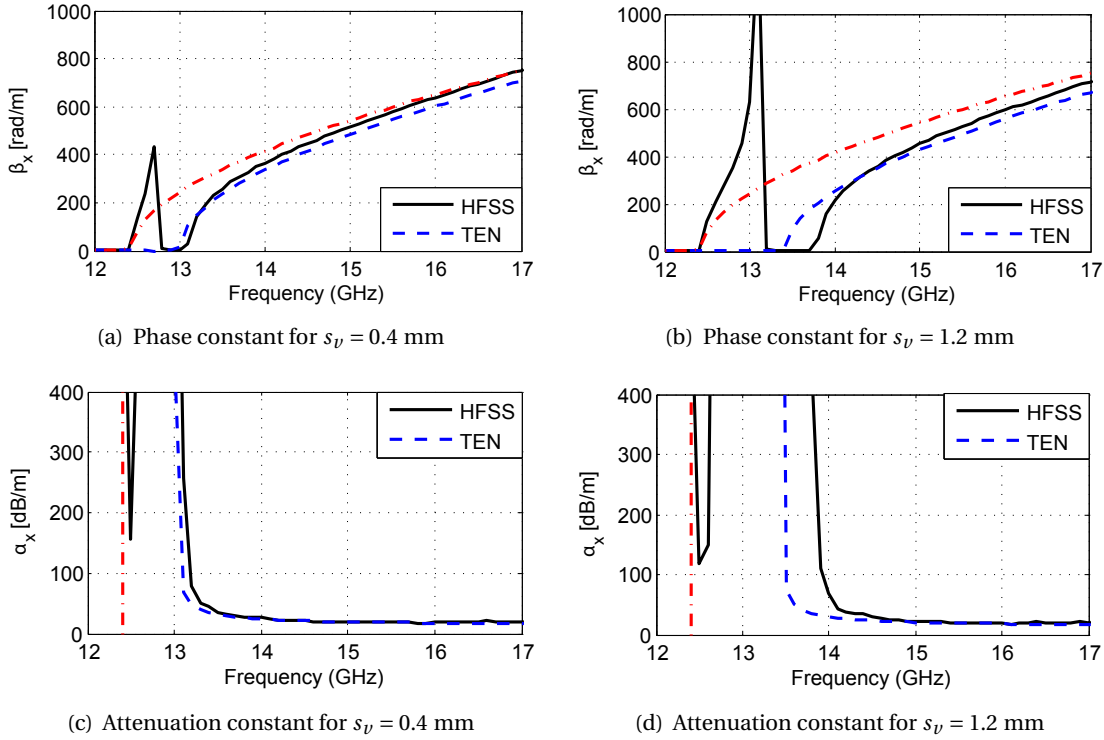


Fig. 5.6: Phase and attenuation constants of the TE_{01} mode in an ESIW for different values of s_v . The red dashed-dotted line corresponds to the ideal RWG. Parameters: $\epsilon_r = 9.56(1 + j0.0023)$, $\epsilon_{rh} = 5$, $h = 3.9$ mm, $w = 6.1$ mm, $p_v = 2.5$ mm

As in the case of any periodic structure, bandgaps in the ESIW also appear in accordance with the following condition:

$$p_v = n\pi/\beta_x, \text{ with } n \in \mathbb{Z}. \quad (5.7)$$

In general, the upper frequency limiting the TE_{01} mode bandwidth is the maximum frequency of operation f_h . Thus, the maximum value for the periodicity p_v can be chosen such that the

bandgap effect appears at f_h . By applying this condition in Eq. (5.7) one obtains:

$$p_v < \frac{\pi}{\sqrt{\epsilon_r \left(\frac{2\pi f_h}{c}\right)^2 - \left(\frac{\pi}{h}\right)^2}} = \frac{h}{\sqrt{\left(\frac{\epsilon_r}{\epsilon_{rh}}\right) - 1}} \quad (5.8)$$

where the propagation constant of an ideal RWG has been considered for β_x , which is a very good approximation at frequencies much higher than f_c (see Fig. 5.6).

While the minimum value of p_v for a proper behaviour of the ESIW has been found in the previous section, its maximum value can be now computed using Eq. (5.8). Importantly, this equation links the maximum bandwidth of a classical NRD (which depends on the permittivity ratio ϵ_r/ϵ_{rh}) with the periodic topology of the ESIW. One can see that while increasing ϵ_r/ϵ_{rh} increases f_h and thus the operational bandwidth, the highest possible value of p_v decreases which might lead to a non-desired region in Fig. 5.5.

As a numerical example, the ESIW of Fig. 5.6 has $f_h = 17.2$ GHz which implies a maximum value for p_v of 4.1 mm. In order to maximize the bandwidth, one would like to have only air in the air-hole region ($\epsilon_{rh} = 1$). However, in this case, p_v should be less than 1.33 mm being close to the top non-desirable region of Fig. 5.5 (meaning that the ESIW would offer similar performances as an SINRD guide).

5.1.4 Loss Mechanisms

Radiation Loss

The radiation losses α_{rad} of the TE₀₁ mode in the ESIW are due to the lack of top and bottom metallic covers. However, since the electric field is really confined in the central dielectric channel, these losses are much less than for the LSM₁₁ mode in an equivalent PCB-SINRD guide [117]. In the latter, the characteristics of the LSM₁₁ mode are strongly dependant on the air-holes region (as shown in Fig. 5.4) while, in an ESIW, the air-holes are only used to contain the energy that leaks through the gaps between vias.

The ESIW radiation losses for a different number of air-hole rows beyond the metallized vias are shown in Fig. 5.7(a). As in the previous examples, the substrate considered has a relative permittivity $\epsilon_r = 9.56$, a thickness $h = 3.9$ mm and the dielectric channel width $W = 6.1$ mm. The air-holes pattern used is rectangular with $d_h = 1.7$ mm and $s_h = 0.5$ mm, and the dimensions of the metallized vias are $d_v = 2$ mm and $s_v = 0.2$ mm. One can see that only 3 rows of air-holes are needed to guarantee a really low leakage ($\alpha_{rad} \simeq 0.15$ dB/m) over a 27% bandwidth (13.3 – 17.5 GHz), which can be neglected compared with the dielectric losses ($\alpha_d \simeq 18$ dB/m). The pic of losses appearing around 17.6 GHz corresponds to f_h .

The radiation losses of an ESIW, a PCB-SINRD and an SINRD guide are compared in Fig. 5.7(b). All guides have the same dimensions as in the previous case and, for a fair comparison, 4 rows of air-holes are considered for the SINRD guides and 1 row of vias and 3 rows of air-holes for the ESIW, i.e., all guides have the same footprint. As expected, the cut-off frequency of both SINRD guides is higher and the bandwidth narrower than for the ESIW. While the radiation losses of the SINRD are practically inexistant because of the additional metallic covers, the PCB version exhibits an average loss of $\alpha_{rad} \approx 0.8$ dB/m, five times higher than the ESIW one.

Dielectric and Conductor Loss

At the frequency range where we are characterizing the ESIW, i.e., the Ku-band, the main part of the losses are due to the dielectric substrate. This is also true in the case of standard SIWs or SINRD guides. At frequencies beyond the Ka-band, the conductor losses start to be considerable and the use of dielectric-based guides, such as the SINRD guide, might be then preferable.

The dielectric and conductor losses of an ESIW and an SINRD guide are shown in Fig. 5.8. The dimensions of the guides are the same as in the previous section. The substrate has a $\tan \delta = 0.0023$ and the copper a conductivity of $\sigma = 5 \times 10^7$ S/m. In this case, both guides present similar dielectric losses in the range of interest ($\alpha_d \approx 18$ dB/m) and, as expected, the ESIW conductor losses ($\alpha_c \approx 3$ dB/m) are higher than in an SINRD guide ($\alpha_c \approx 1.3$ dB/m). Nevertheless, the dielectric loss remains the dominant term accounting for more than 80% of the total losses.

Despite exhibiting slightly higher conductor losses, it has been proven that the ESIW offers a wider bandwidth, more control over the propagation characteristics of the TE_{01} mode and

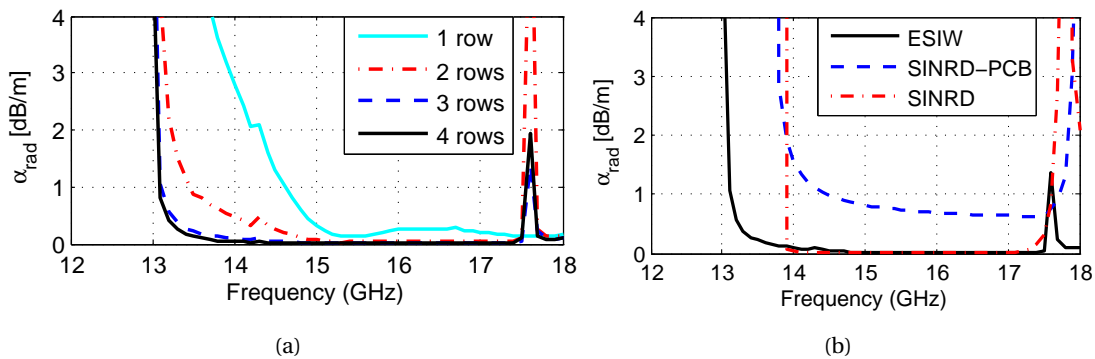


Fig. 5.7: (a) Radiation losses α_{rad} of the TE_{01} mode in an ESIW for different number of rows of air-holes beyond the metallized vias. (b) α_{rad} comparison between an ESIW, a PCB-SINRD and an SINRD of the same footprint.

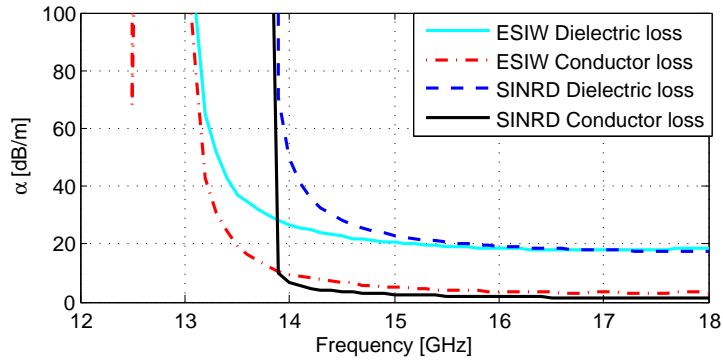


Fig. 5.8: Dielectric α_d and conductor α_c losses of an ESIW with the TE₀₁ mode and of an SINRD guide with the LSM₁₁ mode.

it is easier to manufacture than SINRD guides. Moreover, a compact excitation scheme for the TE₀₁ mode is proposed in the next section which, combined with the ESIW, allows one to suppress common spurious modes that appear in planar feeding transitions used to excite horizontally polarized modes.

5.2 Slotline Feeding for the TE₀₁ Mode

The ways of exciting the TE₁₀ mode in an ESIW are the same as in a conventional SIW, e.g., coaxial probes, MSL coupling, etc. [29]. However, the excitation of TE₀₁-like modes is more challenging. It has been mainly studied along with SINRD guides and two approaches are commonly used: feeding with a metallic rectangular waveguide [31, 117] or by MSL coupling [116, 124]. While the first one is bulky and complicated to manufacture, the MSL coupling generates undesired modes difficult to suppress. In addition, usually a high Insertion Loss (IL) of around 2 dB is obtained. To alleviate these problems, the slotline-based feeding structure represented in Fig. 5.9 is proposed. The possible use of a slotline to efficiently excite the TE₀₁ mode in SICs has been already mentioned [125, 126], but it has never been studied in detail or implemented in practice.

One option is to design a slotline in a thin substrate and then to sandwich it between two other thicker substrates that would create the ESIW [126]. However, this structure is mechanically weak and not likely to be integrated. As an alternative configuration, the proposed feeding scheme uses two substrates of different heights (h_1 and h_2) to create an ESIW of height h . A slotline line of width s_W is then placed on the thin substrate h_1 , defining thus a robust structure (see Fig. 5.9). In order to make it compatible with other circuits or electronic components, the slotline is in turn coupled to a MSL of width M_W placed on the other side of the h_1 substrate. The MSL-slotline coupling is done as explained in [127], using a MSL stub of length M_T and a slotline triangular stub of length s_T .

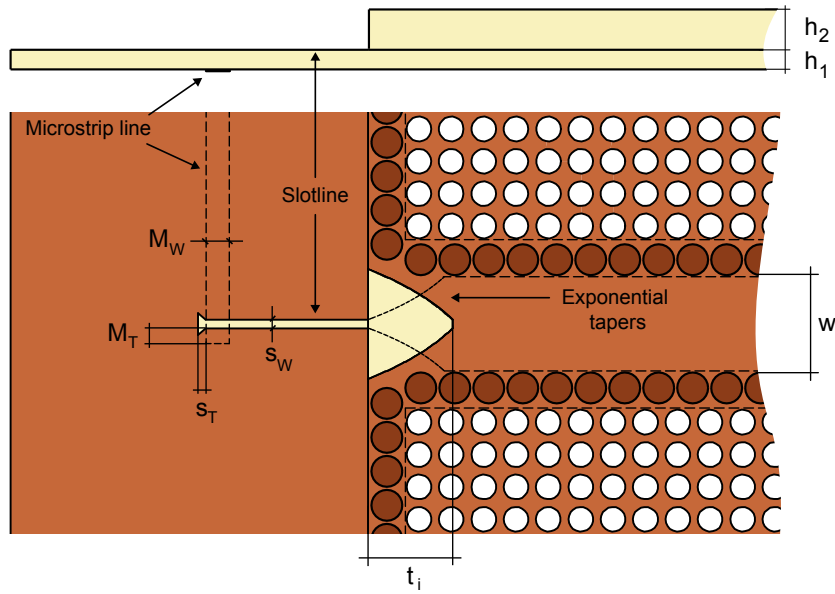


Fig. 5.9: Side and top view of an ESIW with the proposed slotline feeding structure to excite the TE_{01} mode. A MSL-slotline transition is also implemented to interconnect the whole structure with other circuits or electronic components.

Theoretically, the slotline should be placed at the middle of the guide to maximize the coupling between the slotline mode and the TE_{01} mode. To compensate for this asymmetry, the transition slotline-ESIW is designed using different exponential tapers: (1) at the top of the ESIW (top of the h_2 substrate) of length t_{top} , (2) at the bottom of the ESIW (bottom of the h_1 substrate) of length t_{bot} and (3) at the slotline part inside the ESIW of length t_{in} . All tapers have the same width w equal to the one of the ESIW.

A possible drawback of this slotline feeding is that, by symmetry, the TE_{20} mode might also be excited. In SINRD guides, this becomes a major problem since the characteristics of this mode cannot be altered independently from the ones of the LSM_{11} . An effective way to tackle this issue is to place mode suppressor structures after the transition [116]. While these structures are usually large, the own geometry of the ESIW can already be used to solve this problem. Indeed, by adjusting the distance between the two rows of metallic vias w , the TE_{20} cut-off frequency can be shifted out of the range of interest. Moreover, since the width w has a small effect on the TE_{01} mode (Fig. 5.4(a)), its value can be independently optimized to serve as mode suppressor and to maximize the slotline-ESIW coupling.

As example, let us design an ESIW working around $f_0 = 15$ GHz. To this end, two layers of Rogers TMM10 substrate with thickness $h_1 = 1.27$ mm and $h_2 = 2.54$ mm are considered. The dimensions of the ESIW are the same as in the previous sections. After a parametric study using full-wave simulations, the dimensions found to maximize the bandwidth of the slotline-ESIW transition are [mm]: $M_W = 1.3$, $M_T =$, $s_W = 10.56$, $s_T = 0.5$, $t_{top} = 5.25$, $t_{bot} = 5.5$, $t_{in} = 5.1$.

The S parameter of this configuration are shown in Fig. 5.10. Input port 1 corresponds to the slotline mode, output port 2 to the TE₀₁ mode and output port 3 to the TE₂₀ mode in the ESIW. The transition offers a 17% bandwidth (13.3 – 15.7 GHz) with $|S_{12}| > -1$ dB, $|S_{11}| < -17$ dB and a rejection of spurious modes $|S_{13}| < -28$ dB. As expected, after the cut-off frequency of the TE₂₀ mode (≈ 15.8 GHz), there is a strong coupling between this mode and the slotline mode ($|S_{13}| \approx -7$ dB).

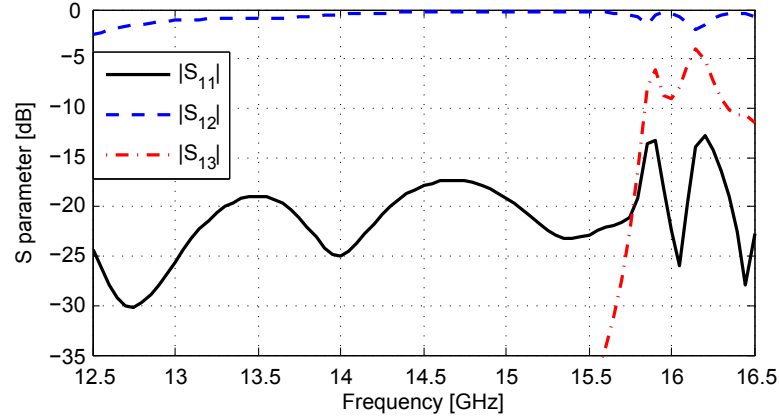


Fig. 5.10: S parameter of the slotline-ESIW transition using a Rogers TMM10 substrate. Port 2 and port 3 correspond to the TE₀₁ and TE₂₀ modes in the ESIW, respectively. Dielectric/conductor losses were not taken into account. The different dimensions are [mm]: $W = 6.1$, $d_v = 2$, $s_v = 0.2$, $d_h = 1.7$, $s_h = 0.5$, $h_1 = 1.27$, $h_2 = 2.54$, $M_W = 1.3$, $M_T = 1$, $s_W = 0.56$, $s_T = 0.5$, $t_{top} = 5.25$, $t_{bot} = 5.5$, $t_{in} = 5.1$.

These are really satisfactory performances compared with the current state of the art [31, 117] and for such a compact feeding. Nevertheless, as commonly encountered, the final bandwidth of this practical implementation is limited by the excitation scheme (17%) and not by the ESIW itself (26%).

5.3 ESIW Prototype and Measurements

A back-to-back MSL-slotline-ESIW transition was manufactured to validate the performances of the ESIW with the TE₀₁ mode and the slotline feeding (see Fig. 5.11). The prototype is designed to work at $f_0 = 15$ GHz and consists of a 37.6 mm long ESIW of the same dimensions as in Section 5.2. SMA connectors were used to characterize the structure, although the MSLs could be directly connected to other SICs or electronic components in practical applications.

The electric field distribution at the longitudinal cross-section of the ESIW is shown in Fig. 5.12. It can be seen that the TE₀₁ mode propagates well inside the ESIW and that the air-hole region effectively prevents the energy leakage. One can also see some spurious leakage due to the SMA-MSL transitions. A transition between a standard SMA and a relatively thick high permittivity substrate always present high IL.

The simulated and measured $|S_{11}|$ and $|S_{12}|$ parameters are plotted in Fig. 5.13. A 9.4% bandwidth (14.2 – 15.6 GHz) with $|S_{12}| > -4$ dB and $|S_{11}| < -12$ dB is achieved. In this frequency range, the simulated IL of the different transitions are: SMA-MSL ≈ 0.85 dB, MSL-slotline ≈ 0.25 dB, slotline-ESIW ≈ 0.45 dB; which makes a back-to-back IL of 3.1 dB. Adding the dielectric losses (≈ 0.9 dB), a prediction of -4 dB for the $|S_{12}|$ is obtained. This corresponds roughly to the measured values, thus proving the ESIW radiation loss to be negligible. A second prototype with the same dimensions but with an ESIW of 55.2 mm length was also manufactured. The difference between the $|S_{12}|$ of both prototypes is 0.3 dB (average difference across the frequency range of interest). This value is in accordance with the dielectric losses of a 55.2 – 37.6 = 17.6 mm long dielectric-filled RWG with the TE₀₁ mode, i.e., 0.29 dB.

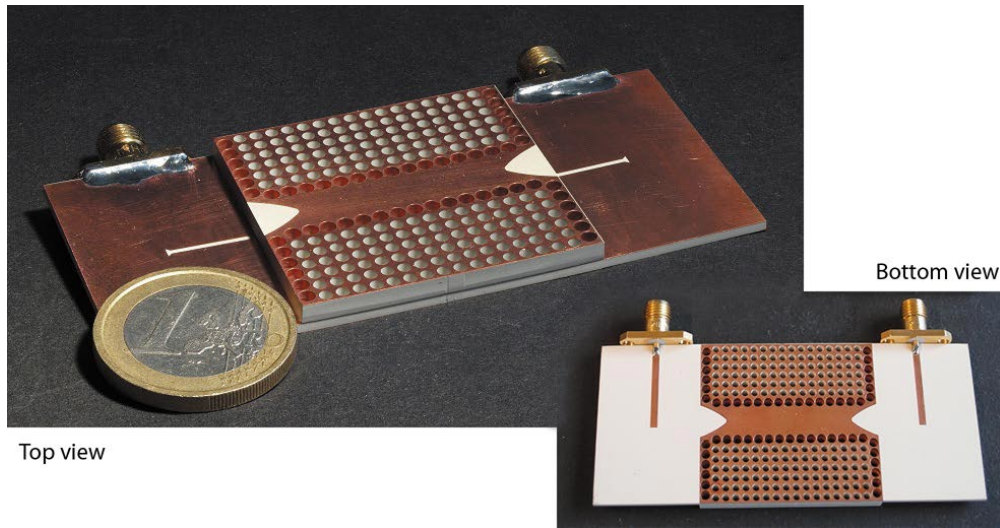


Fig. 5.11: Top and bottom view of the back-to-back MSL-slotline-ESIW transition of length 37.6 mm. The substrate used is Rogers TMM10 with thickness 1.27 and 2.54 mm.

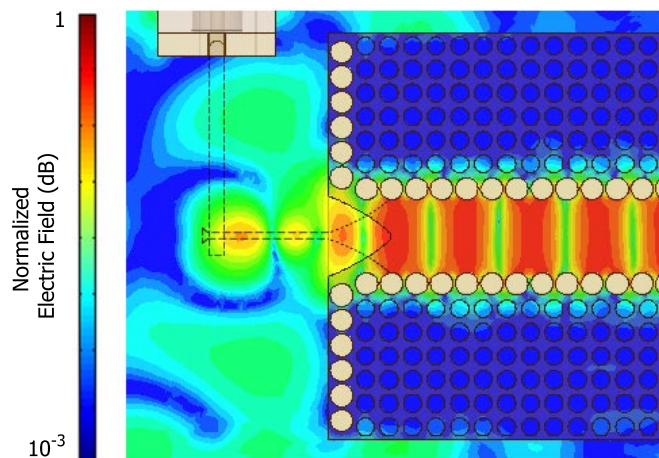


Fig. 5.12: Simulated electric field distribution at the longitudinal cross-section of the ESIW prototype.

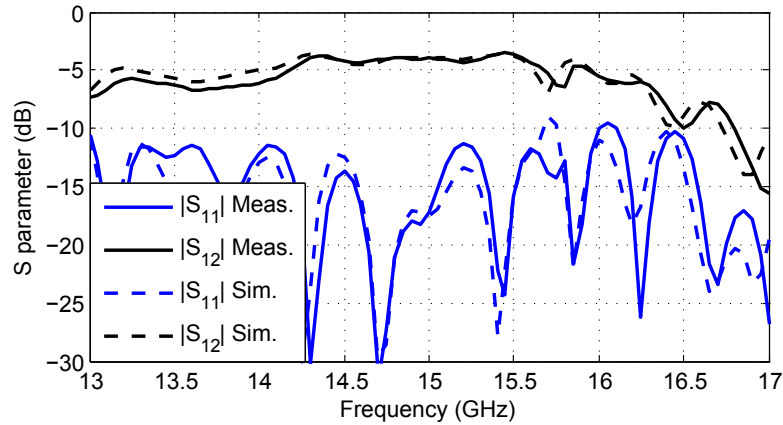


Fig. 5.13: Measured and simulated results of the back-to-back MSL-slotline-ESIW transition including the SMA connectors.

An additional purpose of these first ESIW prototypes was also to verify the properties of the Rogers TMM10 substrate. This substrate exhibits a strong anisotropic behaviour and the recommended design permittivity value of $\epsilon_r = 9.56$ [128] is not always suitable. This is particularly true in our case because the electric field in the ESIW has both parallel and perpendicular components within the substrate, corresponding to the TE_{01} and TE_{10} mode, respectively. One must then refer to the extended report issued by Rogers [129], where it is found that the permittivity value $\epsilon_r = 9.56$ is only valid when considering the perpendicular direction with respect to the substrate plane (z in Fig. 5.2) dealing thus with TE_{m0} -like modes. For the parallel directions (x and y), one should use a value of $\epsilon_r = 10.75$ which differs in more than a 10%. The really good agreement between simulations and measurements in Fig. 5.13 was obtained by including this anisotropic behaviour in the full-wave simulations.

5.4 Conclusions

In this chapter, an overview on the most common substrate integrated guides used to create H- and E-plane SICs has been presented. The lack of a substrate integrated guide able to support orthogonally polarized modes has been the motivation for the presented work. Hence, the Extended Substrate Integrated Waveguide (ESIW) topology has been proposed to simultaneously carry both TE_{m0} and TE_{0n} modes.

The propagation characteristics of the TE_{01} mode in the ESIW have been accurately studied, identifying the cut-off frequency, bandwidth, bandgap effects and loss mechanisms. Design rules have been provided in order to establish the minimum and maximum dimensions of the different geometrical parameters and their impact on the guide performances. Concerning the characteristics of the TE_{10} mode, they are exactly the same as in conventional SIWs.

As an important contribution, a planar excitation scheme for the TE_{01} has been also proposed. Most existing feeding transitions for horizontally polarized modes are not integrated, i.e., not PCB-based, and thus not directly compatible with other SICs. Few integrated solutions exists, but they suffer from high insertion losses and/or the presence of spurious modes. In order to alleviate these problems, a slotline based transition has been designed. Its unique geometry allows for a planar and robust excitation scheme as well as the suppression of common spurious modes.

A prototype of a back-to-back MSL-slotline-ESIW transition was manufactured, achieving a 9.4% bandwidth at 15 GHz for the TE_{01} mode with $|S_{11}| < -12$ dB and $|S_{12}| > -4$ dB (being an important part of the losses due to the transition to the SMA connector). These are perfectly satisfactory values compared with the current state of the art [31]. In addition, this prototype has been used to accurately characterize the anisotropic properties of the Rogers TMM10 substrate. This is an important point because the ESIW concept is used as cornerstone to construct a complete dual-polarized system in the next chapter.

6 Dual-Polarized System based on the ESIW

In the previous chapter, the characteristics and design rules to use ESIWs are provided. In the current chapter, this guide is used to create a fully integrated dual-polarized system. In particular, an Orthomode Transducer (OMT) and a dual-polarized horn antenna are designed and manufactured (see Fig. 6.1). The complete structure is composed of only 2 layers of substrate and compatible with standard PCB technology.

The design and optimization procedure for the substrate integrated OMT are detailed in Section 6.1. Compact and planar excitation schemes for the TE_{10} and TE_{01} modes are also proposed. Section 6.2 is devoted to study the matching and radiation performances of dual-polarized substrate integrated horn antennas. A design strategy to obtain an ESIW horn with similar performances for both polarizations is also proposed. Finally, a prototype of the complete structure is presented in Section 6.3 along with measurements.

6.1 Substrate Integrated Orthomode Transducer (OMT)

An OMT is a device that separates or combines two signals with orthogonal polarizations. OMTs are often used in satellite communications and radio astronomy transceivers in order to isolate the transmitting and receiving signals from a dual-polarized horn antenna [130–132]. A lot of high performance OMT designs can be found in the literature, mainly related with antenna feed chains for parabolic reflectors [133–135]. In addition, dual-polarization is also implemented in other applications to duplicate the link capacity using the same frequency bands [136].

The interest in OMT is recently growing towards more integrated solutions due to the increasing demand for capacity in modern communication systems. For instance, the advantages of using polarization diversity in terms of capacity and robustness in MIMO systems are discussed in [137, 138]. However, standard OMTs are built with metallic RWGs, which are bulky

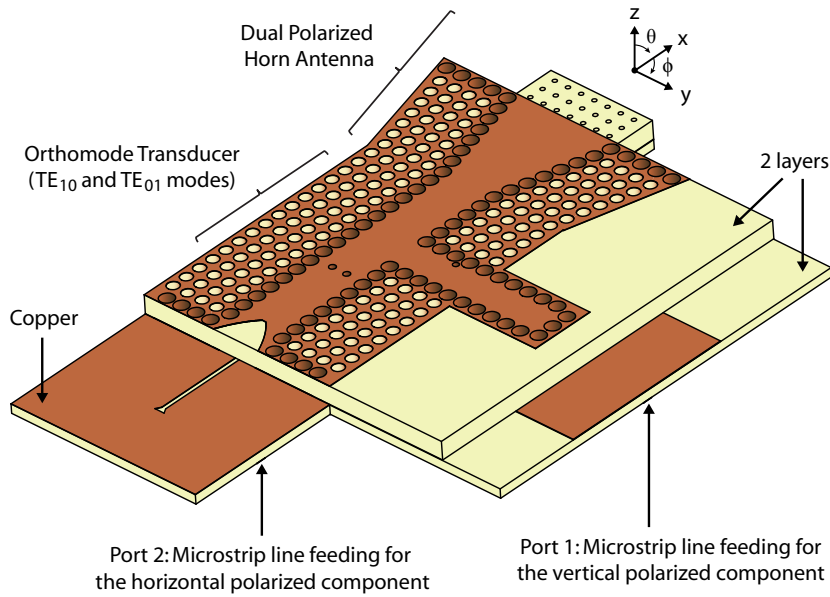


Fig. 6.1: Top isometric view of the complete dual-polarized system: horn antenna, orthomode transducer and feeding ports.

and require expensive machining. Several compact OMT designs have been also proposed, where the two polarizations in a waveguide/antenna are directly extracted using printed circuits [139, 140] or substrate integrated waveguides (SIW) [141–143]. Nevertheless, the main dual-polarized waveguide/antenna is not implemented in printed or SIW technology, the complete design remaining bulky and heavy.

The main purpose of this work is to conceive a complete dual-polarized system fully compatible with other substrate integrated devices. To this end, an asymmetric OMT design has been chosen, with both input ports on the same plane. Asymmetrical OMTs allow trading off RF performance (in terms of broadband operation and channel isolation) with the intrinsic manufacturing complexity of symmetric designs [141]. This is an important point since symmetric designs (such as the Bøifot [144] or Turnstile junctions [145]) would require a large multilayer structure loosing the main advantages of the SIW technology, namely compactness and ease of manufacturing.

The proposed OMT structure is shown in Fig. 6.2. It is designed to work at a central frequency $f_0 = 14.5$ GHz and is composed of only 2 layers of Rogers TMM10 substrate¹. The different thickness or height levels in this structure ($h_1 = 1.27$, $h_2 = 2.54$ and $h = h_1 + h_2 = 3.81$ mm) are efficiently employed to combine/split the TE_{10} (Port 1) and TE_{01} (Port 2) modes as well as to later create planar feeding transitions. Both substrates are finally combined to create an output

¹It is important to mention that the Rogers TMM10 substrate exhibits an important anisotropic behaviour such that $\epsilon_r^x = 10.75$, $\epsilon_r^y = 10.75$ and $\epsilon_r^z = 9.56$ [146]. As explained in Section 5.3, this effect is taken into account in all the presented full-wave simulations results.

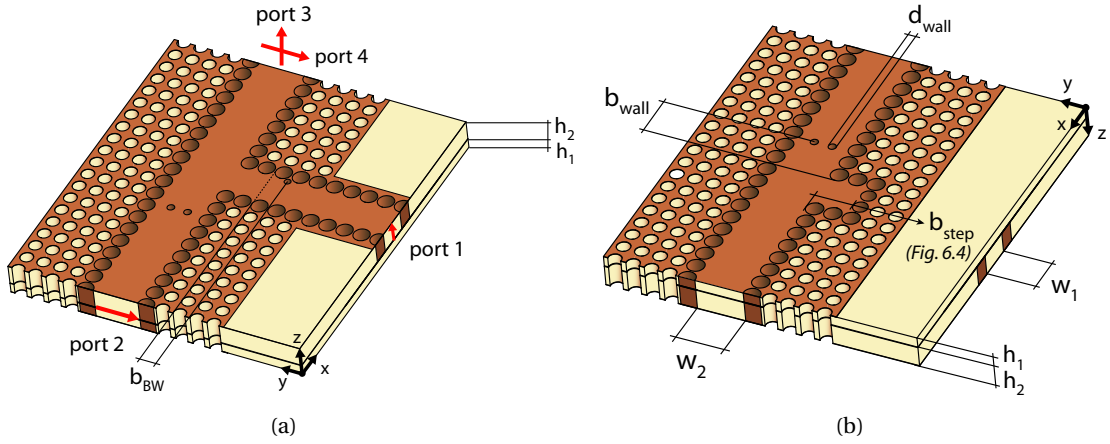


Fig. 6.2: (a) Top and (b) bottom isometric view of the proposed OMT with associated notations. Port 1 corresponds to the input TE_{10} mode, port 2 to the input TE_{01} mode and port 3 and 4 to the vertical and horizontal components in the output ESIW, respectively.

ESIW of height h with a vertical (Port 3) and a horizontal (Port 4) component orthogonal to each other.

According to the notations in Fig. 6.2(a), the following quantities are defined: transmission coefficients ($|S_{13}|$ and $|S_{24}|$), reflection coefficients ($|S_{11}|$ and $|S_{22}|$), isolation ($1/|S_{12}|$ and $1/|S_{34}|$) and cross-coupling ($|S_{14}|$ and $|S_{23}|$). The design strategies followed to optimize these figures of merit are explained in the next section.

6.1.1 OMT Design Strategy

First of all, the ESIW geometry should be chosen such that both TE_{10} and TE_{01} modes are above cut-off. On top of that, as explained in Section 5.1, it is also convenient from the design point of view to work far from the cut-off frequency. In this case, the propagation constant of the TE_{01} mode in an ESIW is practically the same as in a dielectric-filled RWG, allowing to conceive a preliminary OMT design using simulation models based on RWGs and hence much less time consuming.

Taking this into consideration, the dimensions chosen for the common ESIW in the OMT are [mm]: $w = 5.8$, $h = 3.81$, $d_v = 2$, $d_h = 1.7$ and $p_v = p_h = 2.2$. The simulated propagation constant β_x along this common ESIW is compared in Fig. 6.3 with the one of the ideal RWG. One can see that the value of β_x in the ESIW tends to the value of the RWG as frequency increases. Although the cut-off frequency of the RWG is 12 GHz and the one of the ESIW is 12.45 GHz, the difference in β_x at $f_0 = 14.5$ GHz is already less than 2%.

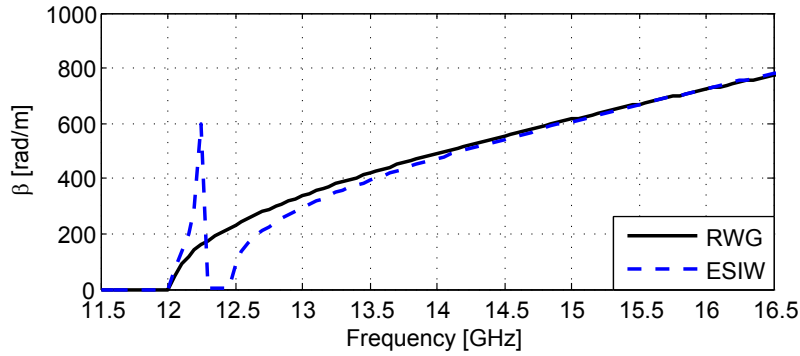


Fig. 6.3: Propagation constant β_x of the TE_{01} mode in a dielectric-filled RWG and in an ESIW using Rogers TMM10. Dimensions [mm]: $w = 5.8$, $h = 3.81$, $d_v = 2$, $d_h = 1.7$ and $p_v = p_h = 2.2$.

The next step is the choice of the strategy to properly guide and isolated both modes. In SIW technology, is easy to control vertically polarized modes since the metallized vias or posts act as inductive obstacles and strongly affect the propagation characteristics of these modes. On the contrary, horizontally polarized modes are difficult to control because the vias act as capacitive obstacles. Therefore, it is more convenient to excite the TE_{01} mode (port 2) in an ESIW directly connected to the OMT output (port 4), avoiding the need to further guide this mode (as shown in Fig. 6.2(a)).

The TE_{10} mode (port 1) is guided to the main ESIW of width w_2 through a perpendicular ESIW of width w_1 implemented only in the h_2 substrate. When these two guides are connected, an off-centered step w.r.t. the z axis is defined at a position b_{step} (see Fig. 6.2(b) and Fig. 6.4). The height $h_2 = 2.54$ mm is chosen such that the other mode cannot propagate in this perpendicular ESIW, which guarantees a good isolation between input ports, i.e., a high $1/|S_{12}|$. To finally guide the TE_{10} mode to the OMT output (port 3), two vertical posts of diameter d_{wall} are placed at a distance b_{wall} (see Fig. 6.2(b)).

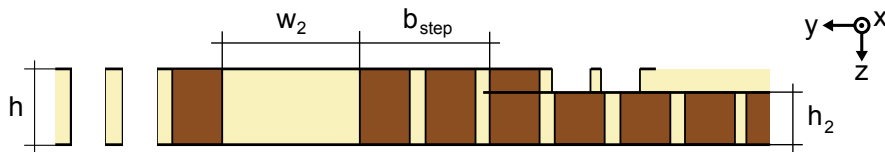


Fig. 6.4: Longitudinal view of the connection between the h ESIW and the h_2 ESIW with the step discontinuity.

The position of the step b_{step} is, in this design, the main parameter strongly affecting the TE_{01} mode since it is the only inductive discontinuity that this mode encounters. Thus, its position must be optimized to, at the same time, increase the transmission $|S_{24}|$ and reduce the reflection $|S_{22}|$. Once b_{step} is fixed, the distance b_{wall} is chosen to increase the transmission $|S_{13}|$ and reduce the reflection $|S_{11}|$.

Although the step or height change is needed to properly isolate the input ports, unwanted mode conversion takes place at it which degrades the cross-coupling. This phenomenon happens because the step is off-centered, i.e., the h_2 ESIW and the h ESIW are not aligned (as illustrated in Fig. 6.4). This could be solved by using 3 layers of substrate of thickness $h/3$ with the perpendicular ESIW implemented in the middle layer, thus making the interconnection between guides symmetric w.r.t. the z axis. However, it is desired to keep a 2-layer configuration to ease the manufacturing as well as to later create the feeding schemes in Section 6.1.2. In this case, the mode conversion can only be diminished by narrowing down w_1 in order to decrease the size of the step. Nevertheless, w_1 cannot be dramatically decreased since it defines the cut-off frequency of the TE_{10} mode, which calls for a trade-off.

Concerning the bandwidth of the OMT, the TE_{01} mode exhibits a wideband behaviour because it follows a direct path from the input port 2 to the output port 4. On the other hand, the TE_{10} mode is bended at the T-junction between guides and its bandwidth is determined by the positions of the two posts and the step. Thus, this mode will probably limit the overall OMT bandwidth. In order to enlarge it, an extra post of diameter d_{BW} is placed inside the perpendicular ESIW at a distance b_{BW} . This post introduces an inductance whose value is determined by d_{BW} and b_{BW} and is used to partially compensate the capacitance generated by the step [122]. This extra post could be placed at the T-junction, as typically done in H-plane junctions or power dividers [147, 148]. However, this implies a more complex design procedure since it also perturbs the other mode, creating the need to further retune the OMT dimensions.

After following the previous design steps along with parametric full-wave simulations, the chosen OMT dimensions are [mm]: $w_1 = 4.1$, $w_2 = 5.8$, $b_{step} = 4.5$, $b_{wall} = 5$, $b_{BW} = 2$, $d_{wall} = 0.9$, $d_{BW} = 0.8$. The simulated S parameters of this OMT design are plotted in Fig. 6.5. It exhibits a 8.3% bandwidth between 13.8 and 15 GHz with transmission > -1 dB, reflection < -10 dB, isolation > 25 dB and cross-coupling < -25 dB.

The electric field distribution for each mode at the central frequency $f_0 = 14.5$ GHz is also plotted in Fig. 6.6. One can see that the modes propagate as expected with a negligible leakage along the ESIWs. The feeding transitions to excite the TE_{10} mode at port 1 and the TE_{01} mode at port 2 are presented in the next section.

6.1.2 Excitation of the TE_{10} and TE_{01} Modes

The TE_{10} and TE_{01} modes are excited using microstrip lines (MSLs) in order to be compatible with other types of planar systems or electronic components. The MSLs for both modes are of width $M_W = 1$ mm and are placed on the same side of the h_1 substrate.

To excite the TE_{10} mode, a vertical transition between the MSL in the h_1 substrate and the

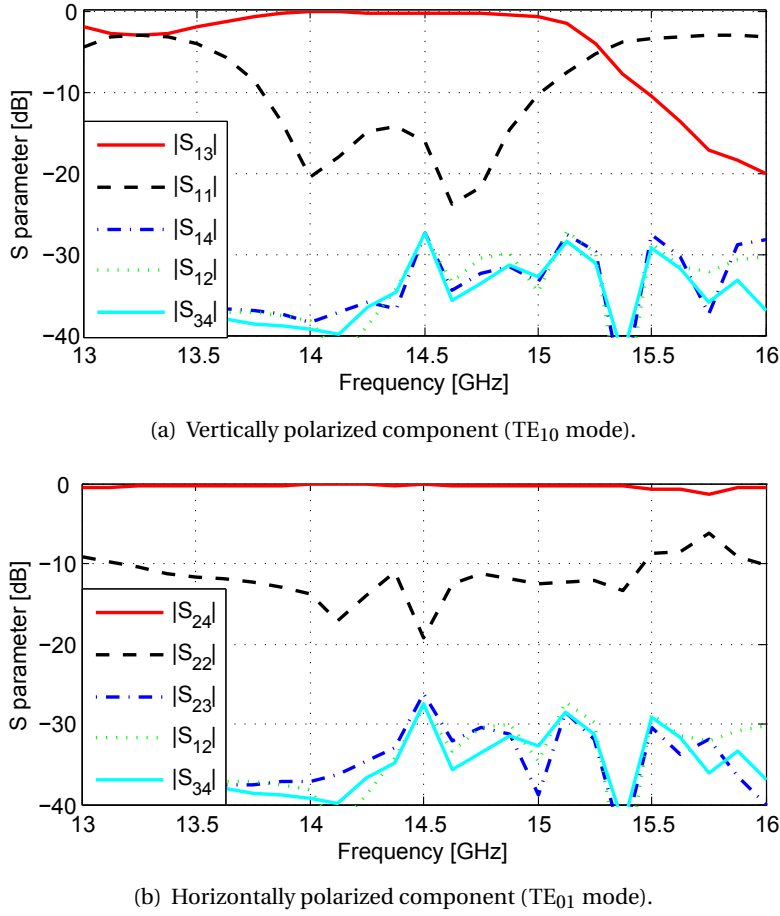


Fig. 6.5: Simulated S parameters of the OMT structure without feeding transitions. Dielectric and conductor losses have not been taken into account. The common ESIW is as in Fig. 6.3 and the rest of dimensions are [mm]: $w_1 = 4.1$, $w_2 = 5.8$, $b_{step} = 4.5$, $b_{wall} = 5$, $d_{wall} = 0.9$, $b_{BW} = 2$, $d_{BW} = 0.8$.

ESIW in the h_2 substrate is designed. As mentioned before, the height h_2 is such that only the TE₁₀ mode can propagate in this ESIW. Thus, standard SIW-MSL vertical transitions found in the literature can be implemented here. These transitions are mainly based on probe feeding [99, 101] and slot coupling [101, 102]. In our case, the slot coupling transition is chosen since it eases the assembling process and is more robust to possible misalignments. This transition is shown in Fig. 6.7 where g_W is the slot width, g_L the slot length and g_T the MSL extension beyond the slot. After an optimization process similar to the one in Section 4.1.1, an 11.4% bandwidth for this transition is obtained with the following dimensions [mm]: $g_W = 5.1$, $g_L = 1.3$, $g_T = 1.9$.

Concerning the TE₀₁ mode, the excitation scheme represented in Fig. 5.9 is used. Here, the MSL in the h_1 substrate is coupled to a slotline of width $s_W = 0.56$ mm located on the other side of the substrate, which then goes inside the final ESIW guide of height $h = h_1 + h_2$. The

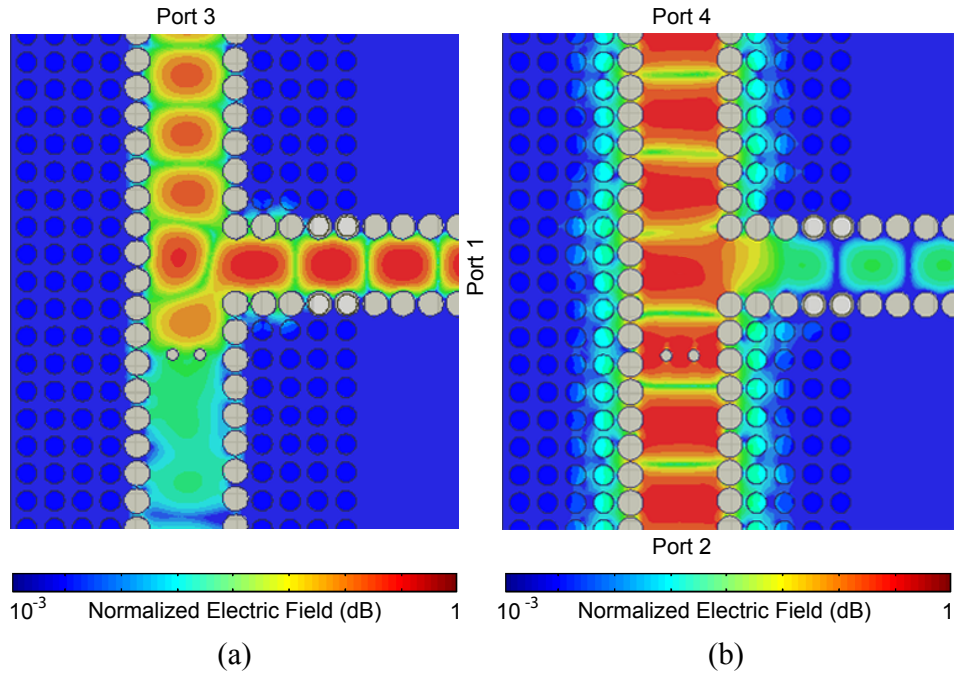


Fig. 6.6: Electric field distribution at $f_0 = 14.5$ GHz in the centre of the OMT from Fig.6.5. (a) TE_{10} mode and (b) TE_{01} mode.

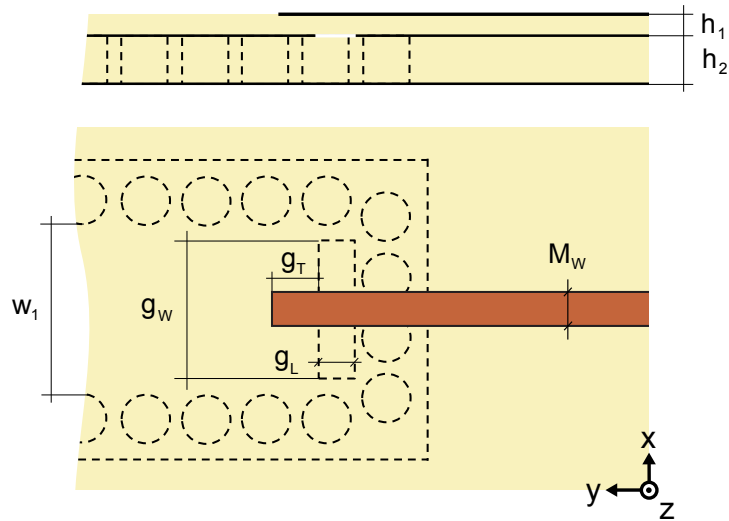


Fig. 6.7: Cross-section and top view of the slot coupling transition between a MSL in the h_1 substrate and an ESIW in the h_2 substrate used to excite the TE_{10} mode.

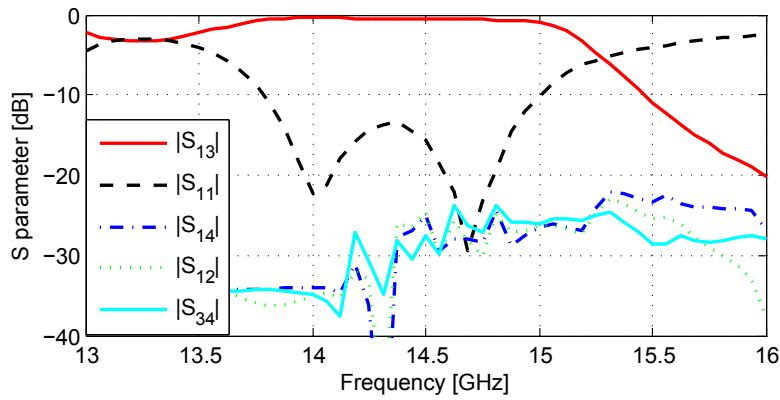
MSL-slotline coupling is done as explained in [127], using a MSL stub of length $M_T = 1.2$ mm and a slotline triangular stub of length $s_T = 0.7$ mm. The dimensions of the exponential tapers are $t_{top} = 4.6$ mm, $t_{bot} = 5$ mm, $t_{in} = 5.1$ mm and the bandwidth of the complete transition is 17.8%.

6.1.3 Complete OMT Performances

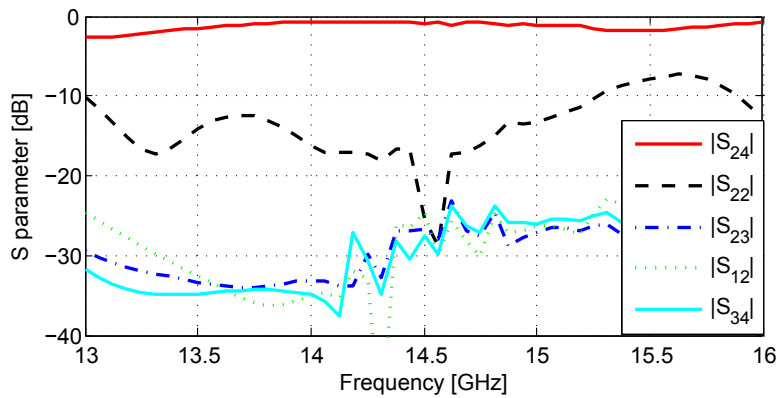
The simulated S parameters of the OMT of Section 6.1.1 with the previous feeding transitions are shown in Fig. 6.8. It can be seen that they are practically the same as the ones of the OMT alone. The performances are slightly worse in terms of isolation and cross-coupling but they still remain below -25 dB in the frequency range of interest (13.8 – 15 GHz).

The bandwidths of the different parts of the OMT are summarized in Tab. 6.1. One can see that the excitation schemes do not limit the overall 8.3% bandwidth, but the TE_{10} mode in the OMT does. Despite using an extra post to increase its bandwidth (see the two resonances in Fig. 6.5(a) or 6.8(a)), this one remains the limiting factor.

The different loss mechanisms have been simulated with HFSS and their values over the



(a) Vertically polarized component (TE_{10} mode).



(b) Horizontally polarized component (TE_{01} mode).

Fig. 6.8: Simulated S parameters of the OMT structure with feeding transitions. Dielectric and conductor losses have not been taken into account. The dimensions of the ESIW and OMT are the same as in Fig. 6.5. The dimensions of the feeding transitions are [mm]:

$$M_w = 1, g_w = 5.1, g_L = 1.3, g_T = 1.9, s_w = 0.56, s_T = 0.7, M_T = 1.2, t_{top} = 4.6, t_{bot} = 5, t_{in} = 5.1.$$

frequency band of interest (13.8-15 GHz) have been averaged and are presented in Tab. 6.2. The dielectric loss tangent of the Rogers TMM10 is $\tan \delta = 0.0023$ and the copper conductivity is $\sigma = 5 \times 10^7$ S/m. As expected at this frequency range, most part of the losses are due to the dielectric substrate ($\sim 82\%$), the conductor losses being five times lower. The ESIW leakage for both modes is negligible ($\sim 1\%$), as expected from Section 5.1.4. At much higher frequencies, where the conductor losses become the dominant term, SINRD guides might then be preferred, despite loosing the advantages provided by the ESIW topology.

The proposed ESIW OMT exhibits excellent performances for such a compact design. Although it is difficult to compare with previous work (since it is the first time that a dual-polarized substrate integrated guide is used), a similar asymmetric and compact OMT is proposed in [143]. The latter offers similar performances in terms of reflection, isolation and cross-coupling, but in a much narrower bandwidth (3.3%) than the proposed design (8.6%). The OMT size is also reduced in a 30% thanks to the use of a high permittivity substrate, but at a cost of doubling the dielectric losses.

It must be pointed out that different orthogonal modes have been already simultaneously used in a single SIWs, mainly to achieve multichannel data transmission (e.g., the TE_{10} and the TE_{20} modes in [149]). Nevertheless, this is the first time that two modes with orthogonal polarizations, the TE_{10} and TE_{01} , are combined in a substrate integrated structure.

This concludes the design and excitation of a substrate integrated OMT. In the next section, a dual-polarized ESIW horn antenna is designed and fed by this OMT.

OMT part	Bandwidth [%]
OMT for the TE_{10} mode	8.3
Feeding of the TE_{10} mode	11.4
OMT for the TE_{01}	14.2
Feeding of the TE_{01} mode	17.8

Tab. 6.1: Bandwidth of the different parts of the complete OMT.

Loss Mechanisms	TE_{10} Losses [dB]	TE_{01} Losses [dB]
Dielectric	0.790	0.910
Conductor	0.160	0.190
Radiation	0.003	0.014

Tab. 6.2: Mean value of the different loss mechanisms between 13.8 - 15 GHz of the OMT including the feeding transitions.

6.2 Dual-Polarized Substrate Integrated Horn Antenna

The previous OMT allows one to generate the two orthogonal TE_{10} and TE_{01} modes in a single ESIW. A horn antenna can then be created by flaring the cross-section of this ESIW until the edge of the substrate. In the case of the TE_{10} mode, the dimensions parallel to the H-field are flared while the perpendicular ones are kept constant, defining an H-plane horn antenna. Analogously, an E-plane horn antenna is obtained when considering the TE_{01} mode. Thus, a dual-polarized horn antenna with focusing capabilities in the XY plane is created (see Fig. 6.1).

In the next sections, the characteristics of the horn antenna created by each mode are studied. A design procedure to obtain a good matching for both modes at the same frequency band is also proposed.

6.2.1 The H-plane Horn Antenna

It is well known that H-plane SIW horn antennas usually suffer from a strong mismatch between the horn aperture and the air, due to the dielectric loading ϵ_r and the reduced substrate thickness h (as explained in detail in Section 3.1). The output guide of the previous OMT has a relative permittivity w.r.t. the z axis of $\epsilon_r^z = 9.56$ and a height $h = 3.81\text{mm} \simeq \lambda_0/5$. Hence, an H-plane horn implemented with this ESIW exhibits a strong capacitive behaviour. The aperture impedance of a H-plane horn with an aperture width $a > h$ can be represented as a resistance in parallel with a capacitance (Chapter 4 in [122]). In this case, the aperture resistance and capacitance of such H-plane horn at $f_0 = 14.5$ GHz are plotted in Fig. 6.9, as a function of a and for several h . It can be seen that the resistance values are high (in the range of $k\Omega$) and, contrary to an air-filled horn, the capacitance increases as both aperture dimensions a and h increase.

Since $h > \lambda_0/6$, this mismatch can be significantly reduced by extending the substrate layer at the horn aperture in order to act as a dielectric lens. After placing a rectangular lens at the horn aperture, the aperture impedance as a function of the length of the lens L is plotted in Fig. 6.10. As expected, the lens can be seen as an impedance transformer with a periodic behaviour with respect to L . This allows one to compensate the strong capacitance behaviour of the horn as well as to reduce the aperture resistance.

Concerning the radiation performances, thin H-plane horn antennas radiate similarly to a slot in an infinite ground plane, presenting thus low values of Front-to-Back Ratio (FTBR) (see Section 3.1). In this case, since $h \simeq \lambda_0/5$, the lens extension also helps to focus the radiation frontwards increasing the directivity and FTBR in both XY and XZ planes.

An alternative solution to improve the matching and FTBR would be as well the printed

transition of Chapter 3. Indeed, this is probably the only feasible option for horns with $h < \lambda_0/6$. However, this printed transition would act as an inductive obstacle for the TE_{01} mode degrading the radiation of the E-plane horn. For this reason, a dielectric lens is a better option in the design of dual-polarized (or circular polarized) horn antennas. The characteristics of the E-plane horn antenna are discussed in the next section.

6.2.2 The E-plane Horn Antenna

Analogously to the previous case, the E-plane horn antenna exhibits a strong inductive behaviour [122]. The series inductance and resistance at the aperture are shown in Fig. 6.11. In contrast to the H-plane horn, the resistance is here much lower and the inductance remains fairly constant with respect to a .

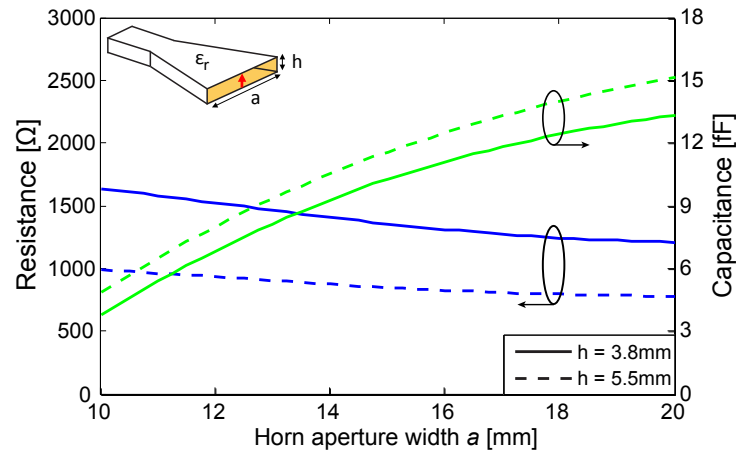


Fig. 6.9: Resistance and capacitance of the H-plane horn aperture at 14.5 GHz as a function of the aperture width a and for different values of the substrate thickness h . It has been assumed that the horn is long enough so that the phase error at the aperture is negligible.

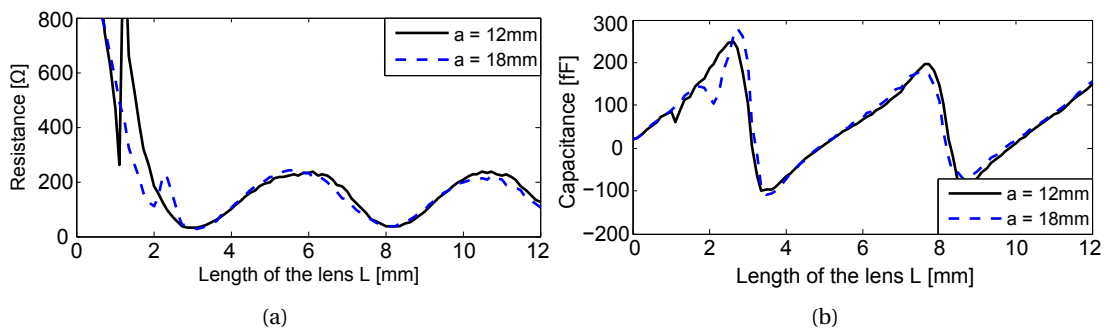


Fig. 6.10: Impedance of the H-plane horn aperture with a rectangular lens at 14.5 GHz: (a) resistance and (b) capacitance.

In order to reduce the high aperture inductance, a lens extensions can be also used. The aperture impedance of the E-plane horn with a rectangular lens is shown in Fig. 6.12, exhibiting a similar periodic behaviour as in the previous case. However, while the H-plane horn impedance is nearly independent of a , here a plays an important role since it is the dimension parallel to the E-field (see Fig. 6.12(a)). The value of a must be then chosen according to the E-plane horn matching as well as, of course, for the desired HPBW.

Concerning the radiation characteristics, thin E-plane horns radiate similarly to a dipole antenna with high values of FTBR. Thus, in order to avoid grating lobes, a should be less than $\lambda_0 (\simeq 20 \text{ mm})$. As in the previous case, the lens also helps to slightly improve the directivity.

Based on the characteristics and trends found for the H- and E-plane horns, a design strategy to match both horns at the same frequency band is presented in the next section.

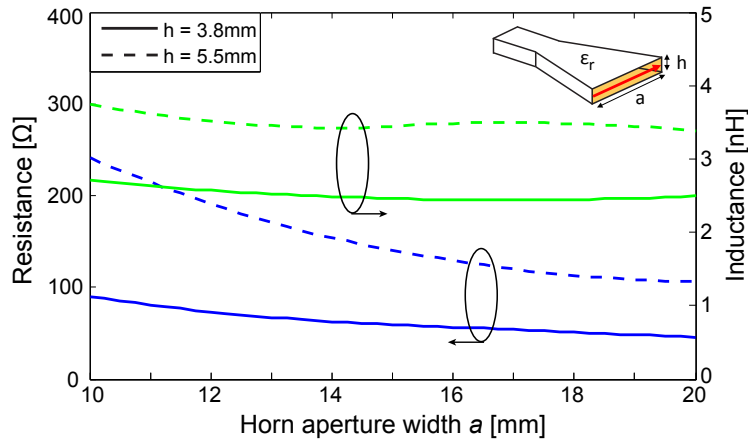


Fig. 6.11: Resistance and inductance of the E-plane horn aperture at 14.5 GHz as a function of the aperture width a and for different values of the substrate thickness h . It has been assumed that the horn is long enough so that the phase error at the aperture is negligible.

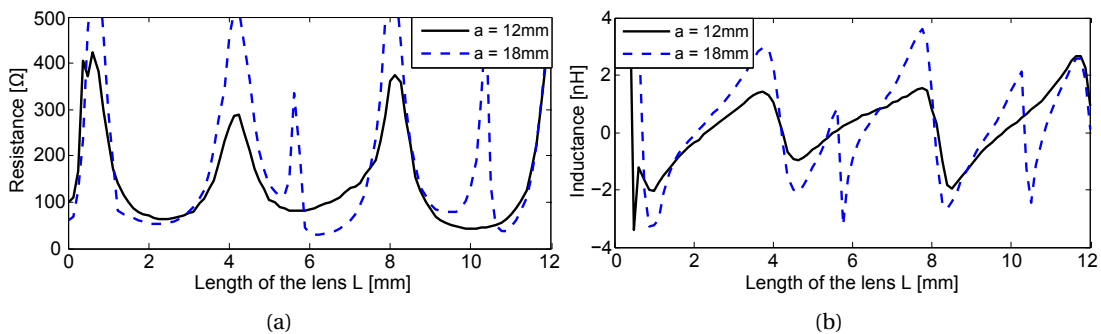


Fig. 6.12: Impedance of the E-plane horn aperture with a rectangular lens at 14.5 GHz: (a) resistance and (b) inductance.

6.2.3 Dual-Polarized Horn Antenna Design

In both lens-corrected horn antennas, the main parameter defining the resonant frequency is the length of the lens L . However, one can see from Fig. 6.10 and 6.12 that a different L is needed to match the H-plane ($L = 4.8$ mm) and the E-plane horn ($L = 4.2$ mm) at the same frequency f_0 . Thus, another degree of freedom in the design must be found to simultaneously match both horns. To do so, the equivalent relative permittivity of the lens ϵ_{rL} can be modified. This implies that not only its electrical length is different, but also the reflection at the horn aperture – lens interface. Then, one can optimize these two parameters (L and ϵ_{rL}) to match both horns at f_0 . In practice, the lens permittivity is changed by drilling air-holes of diameter d_L and periodicity p_L , which effectively reduces the substrate dielectric constant to a value of $\epsilon_{rL} < \epsilon_r$ (as in the design of the ESIW in Section 5.1).

The proposed dual-polarized ESIW horn antenna is shown in Fig. 6.13, where D is the horn length. Note that the last row of metallized vias at the horn aperture has been extended along y in order to create a reflector. Simulations showed an increase on the directivity of roughly 1 dB thanks to this small reflector.

After a parametric study, the values of $L = 5.7$ mm, $\epsilon_{rL} = 0.83 \cdot \epsilon_r$ and $a = 15.4$ mm were found to provide a reflection coefficient below -10 dB between 13.45 and 15.15 GHz (see Fig. 6.14) with a HPBW $\approx 50^\circ$ for both modes. In order to mimic this ϵ_{rL} , the diameter of the holes is $d_L = 0.7$ mm and its periodicity, $p_L = 2$ mm.

In the next section, a prototype of this dual-polarized ESIW horn antenna fed with the OMT of Section 6.1.3 is presented.

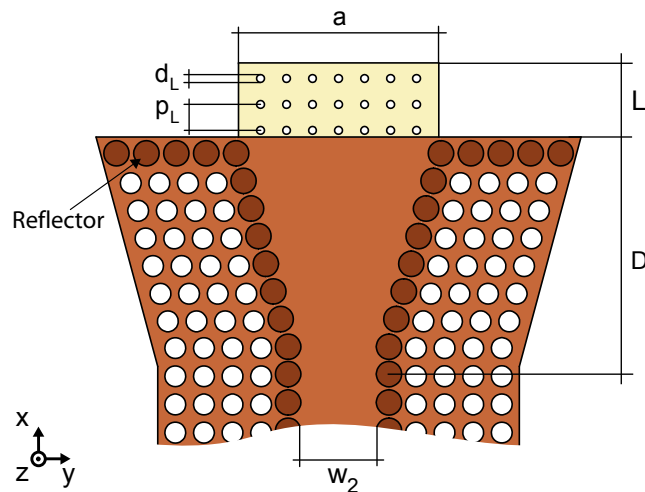


Fig. 6.13: Top view of the ESIW horn antenna with a rectangular dielectric lens extension with an air-hole pattern.

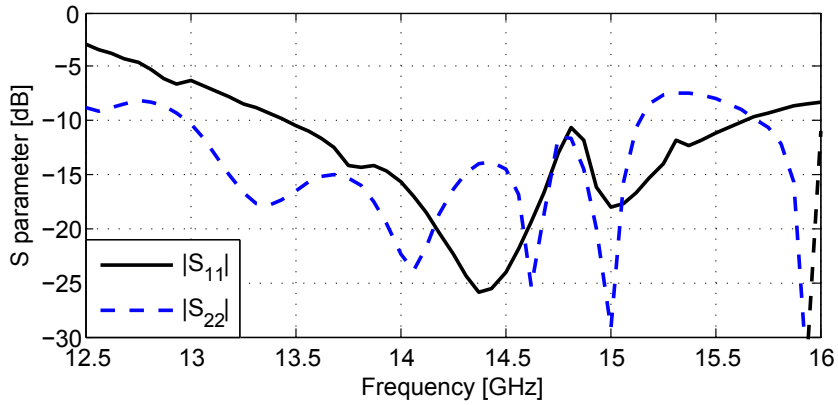


Fig. 6.14: Simulated S parameters of the dual-polarized ESIW horn from Fig. 6.13. Port 1 corresponds to TE_{10} mode and port 2 to the TE_{01} mode. The horn dimensions are [mm]:
 $h = 3.81, a = 15.4, D = 16.2, L = 5.7, d_L = 0.7, p_L = 2$.

6.3 Experimental Results

In order to validate the proposed concepts, a dual-polarized ESIW horn antenna has been manufactured (see Fig. 6.15). The dimensions of the OMT and the horn are the same as in Section 6.1.3 and 6.2.3, respectively. The overall size of the prototype is $81.9 \times 58.5 \times 3.9 \text{ mm}^3$ (or $3.9 \lambda_0 \times 2.8 \lambda_0 \times 0.2 \lambda_0$) and the connectors used are 23_SMA-50-0-2/111_NE.

Due to the high permittivity and thickness of the h_1 substrate, a strong capacitive effect was present at the SMA-MSL interface causing high insertion losses ($\approx 0.8 \text{ dB}$), as also mentioned in Section 5.3. In order to compensate for it, metallized vias were drilled near the MSL (see Fig. 6.15). Full-wave simulation showed a reduction of the insertion loss from 0.8 to 0.2 dB by using three vias of 1.2 mm of diameter. This solution would have also greatly reduced the insertion losses of the prototype in Fig. 5.11.

The simulated and measured S parameters of the prototype are plotted in Fig. 6.16. Port 1 corresponds to the H-plane horn created with the TE_{10} mode and port 2 to the E-plane horn created with the TE_{01} mode. Despite the anisotropy of the Rogers TMM10 substrate and the assembling process, simulations and measurements are in good agreement, which indicates a robust design. The measured $|S_{11}|$ and $|S_{22}|$ bandwidth at -10 dB is 8.6%, between 13.9 and 15.15 GHz. At this frequency range, the antenna also exhibits an excellent isolation between inputs ports higher than 28 dB.

The simulated and measured radiation patterns for several frequencies are shown in Fig. 6.18 for port 1 and in Fig. 6.19 for port 2. As expected, the E-plane horn (port 2) exhibits high values of FTBR ($\approx 15 \text{ dB}$) while the values for the other horn are lower ($\approx 7 \text{ dB}$) due to the reduced substrate thickness h . It can also be seen that the radiation patterns are broader at 15 GHz

than at lower frequencies. When using high permittivity dielectrics, the flare angle must be really small to minimize the phase error at the aperture [72]. In this case, the flare angle becomes too large at 15 GHz and higher order modes start to be excited. This is translated into a less uniform aperture field distribution and thus a broader radiation pattern. For the same reason, the cross-polarization levels are also higher at 15 GHz. Nevertheless, they remain always below -15 dB within the main beam.

Some differences in terms of small ripples and nulls are present between simulations and measurements, mainly in the XZ-plane for port 1. In this plane, the feeding cable affects the polarization of interest and must be placed so to minimize its effect. Nevertheless, the ripples are less than 3 dB within the main beam. The nulls appear in back directions and thus also out of the beamwidth of interest.

The realized gain at end-fire for both horns is shown in Fig. 6.17. Although the E-plane horn is more directive than the H-plane horn thanks to its higher FTBR (see Figs. 6.18-6.19), their realized gains are similar (between 4-5 dBi). This is because the mode corresponding to the E-plane horn (the TE_{01} mode) exhibits more losses in the OMT (see Tab. 6.2). In particular, the total efficiencies are around 80 % for the H-plane and 75 % for the E-plane horn.

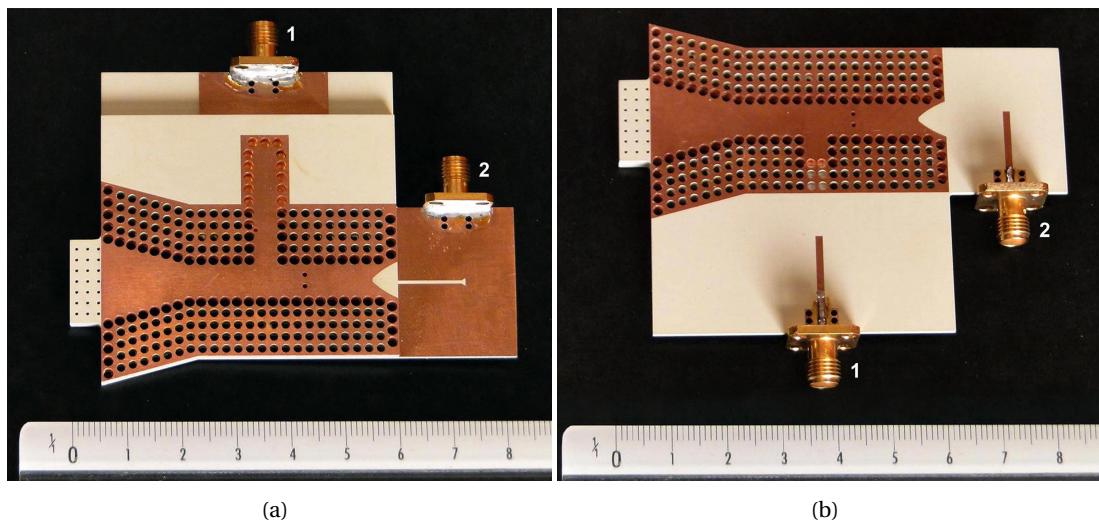
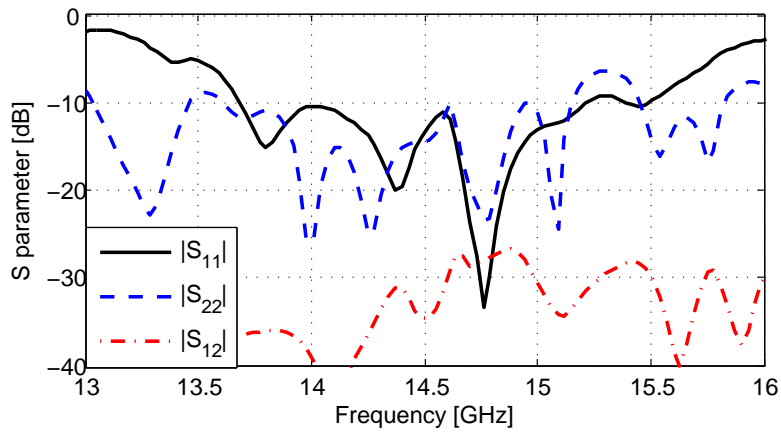
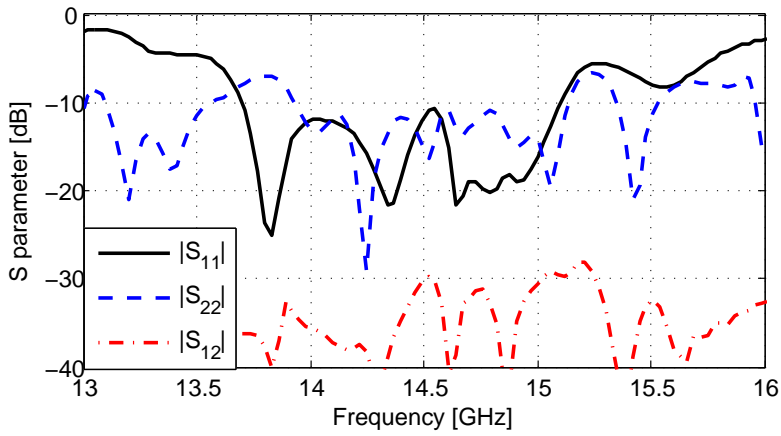


Fig. 6.15: (a) Top and (b) bottom view of the dual-polarized ESIW horn antenna prototype. The overall dimensions are $81.9 \times 58.5 \times 3.9$ mm³ (or $3.9 \lambda_0 \times 2.8 \lambda_0 \times 0.2 \lambda_0$).



(a)



(b)

Fig. 6.16: (a) Simulated and (b) measured S parameters of the ESIW horn prototype.

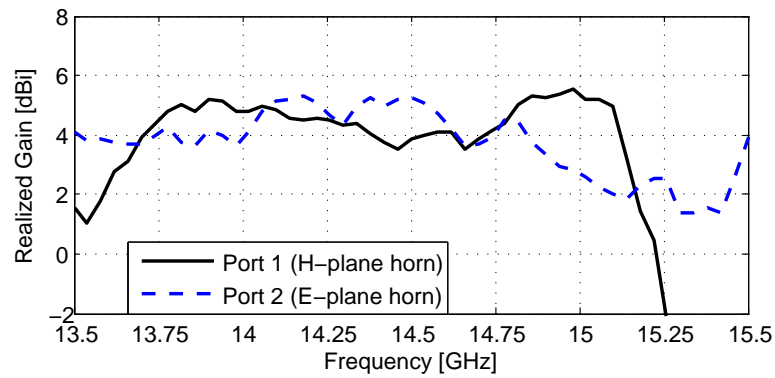


Fig. 6.17: Measured realized gain at end-fire vs. frequency for the two polarizations of the ESIW horn.

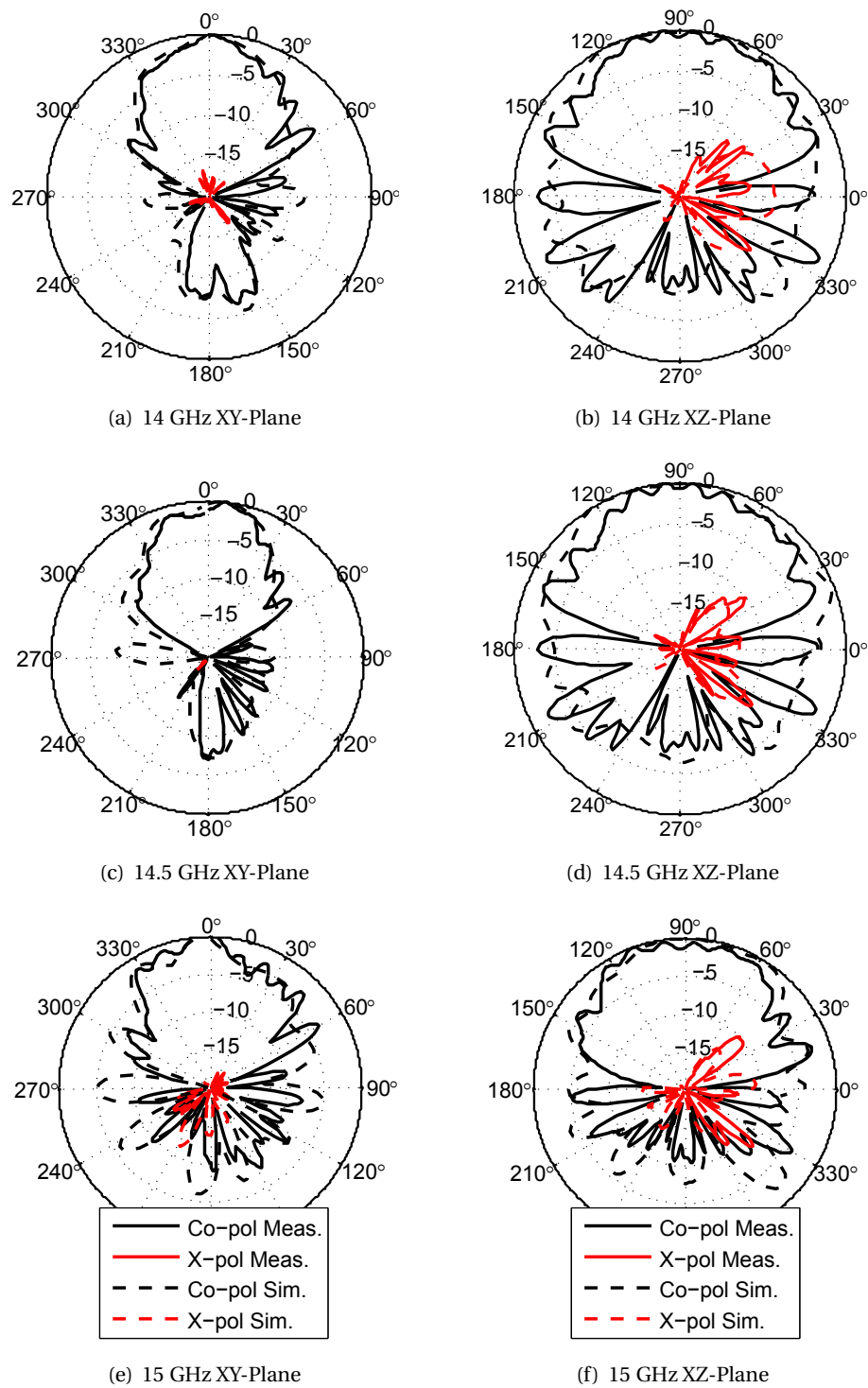


Fig. 6.18: Radiation patterns of the ESIW horn prototype corresponding to port 1 (H-plane horn) and for different frequencies. Measurements are in continuous lines and simulations in dashed lines.

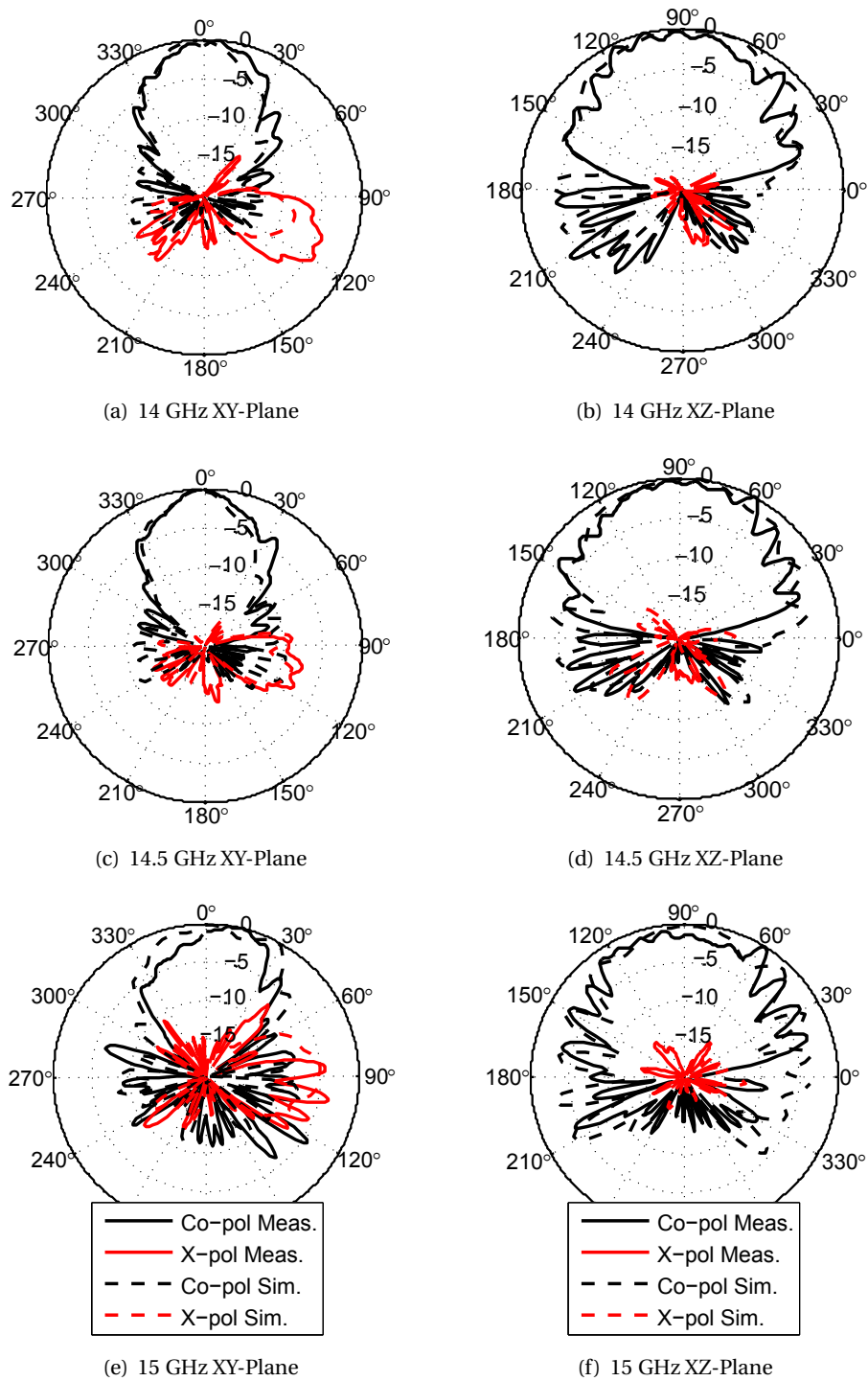


Fig. 6.19: Radiation patterns of the manufactured prototype corresponding to port 2 (E-plane horn) and for different frequencies. Measurements are in continuous lines and simulations in dashed lines.

6.4 Conclusions

A complete dual-polarized system implemented in substrate integrated technology has been presented. It comprises planar excitation schemes for both orthogonal TE_{10} and TE_{01} modes along with an OMT to combine them and to finally feed a dual-polarized horn antenna. The whole structure requires only 2 substrate layers and it is based on the ESIW concept.

A design strategy to easily optimize the proposed OMT structure has been explained along with the impact of the different geometrical parameters on its figures of merit (isolation, cross-coupling, etc.). The horn matching and radiation characteristics have been also studied in detail in order to design an ESIW horn with similar performances for both polarizations.

As a proof of concept, the complete structure has been fabricated using standard PCB processes. It exhibits an 8.6% bandwidth (13.9 – 15.15 GHz) with matching for both modes better than -10 dB and isolation between them higher than 28 dB. In the same frequency range, both modes exhibit similar end-fire gain (between 4-5 dBi) and a cross-polarization level below -15 dB within the main beam. The performances of the whole system are excellent for such a compact design, being the first time that a dual-polarized end-fire antenna is proposed in substrate integrated technology. Standard dual-polarized horns find room in many commercial applications and so could this planar and low-cost version.

The proposed design proves the viability of creating dual-polarized substrate integrated components, i.e., the second objective of this PhD thesis. This opens the door to new devices exploiting both polarizations as well as their use in applications requiring dual-polarized end-fire signals, such as for systems in need of cost-effective antenna packages. All together, this combined design becomes a promising approach to tackle the increasing demand for capacity in modern communication systems.

7 Conclusions and Perspectives

A very promising candidate to provide widespread commercial solutions for wireless systems at the Ku-band and beyond is the Substrate Integrated Waveguide (SIW) technology or, in general, the Substrate Integrated Circuit (SIC) architecture. Its most significant advantage is the possibility to integrate different types of components in the same substrate by using standard manufacturing processes, such as the PCB processing techniques.

Many antennas, passive and active components as well as complete RF systems have been manufactured and tested in SIW technology. However, the feasibility of implementing low-cost SIW devices is linked to the commercially available substrates and fabrication methods. These constraints typically limit (a) the frequency range of operation of certain SIW antennas and (b) the possibility of creating multimode structures dealing with orthogonal polarizations.

The aim of this thesis was to overcome these two limitations and thus to extend the scenarios of usage of the SIW technology. To this end, two research lines were established:

- A)** A new design for SIW horn antennas to extend their lowest frequency range of operation towards the Ku-band and below.
- B)** A new substrate integrated guide topology able to support orthogonally polarized modes and thus to create dual-polarized SICs.

These topics were studied in the framework of a research project awarded by armasuisse, whose main objective was to create an azimuth Direction Finding (DF) system for UAVs working at the Ku-band. After the statement of requirements of this system in Chapter 1, the SIW technology has been chosen in Chapter 2 as the best option to implement the DF antenna array thanks to its excellent characteristics in terms of low-profile, light weight and low-cost. Chapter 2 reviews the bases of the SIW technology and a detailed overview on the scenarios of usage and working frequency range of different SIW antennas is provided.

The latter review served to select the H-plane SIW horn antenna as the best option to construct the DF array. However, the design of these end-fire SIW antennas became really challenging because commercial substrates are electrically thin at the Ku-band. This triggered the first research line *A* of this thesis. Indeed, it has been shown how the performances of standard SIW horns strongly degrade as the substrate thickness is reduced. To overcome this limitation, a novel SIW horn design has been presented in Chapter 3. This new configuration targeted the improvement of both the matching and radiation performances of SIW horns, even when built in substrates thinner than a tenth of a wavelength. Importantly, the proposed design does not require any extra manufacturing processes with respect to a standard SIW horn keeping, therefore, the advantages of low-cost and single-layer PCB design. This novel SIW horn antenna has become one of the cornerstones of this PhD thesis and has been, not only referred, but even adopted by several other research groups [150–153].

In Chapter 4, a DF system based on an 8-element array of the previous SIW horns has been implemented. While the study of stand-alone SIW antennas (or other components) is important, the development of a complete RF system is a must to prove the reliability of the SIW technology for commercial applications. As first step towards a complete system, an efficient way to interconnect SIW horn antennas with commercial MMICs has been proposed. Detailed explanations concerning the electronic system design have been provided, also including solutions for common problems encountered in such high frequency systems (parasitic oscillations, shielding structure, etc.). All together resulted into a low-cost and low-profile azimuth DF system working at the Ku-band and closed the first research line *A* of this thesis.

In line with the foreseen future work, a preliminary study on the optimal placement of the DF system on an UAV platform has been presented at the end of Chapter 4. It has been shown that the system performances barely change provided that the antennas are not aligned with the UAV structural elements. As future work, the DF system could be flush-mounted in different UAVs and outdoor flying tests could be performed to assess the communication quality and mechanical stability. Although the functionality of the novel SIW horn design has been demonstrated for a simple DF operation, the concept is full of promises for more ambitious applications. In this context, future research lines would be the use of more complex electronics and communication algorithms to implement high-data rate transmission systems and/or inter-vehicle communications.

Concerning the second research line *B*, a new substrate integrated guide able to carry orthogonally polarized modes has been proposed in Chapter 5: the Extended Substrate Integrated Waveguide (ESIW). This guide combines the working principles of SIWs and SINRD guides to support the propagation of both TE_{m0} and TE_{0n} modes, while still being directly fabricated in PCB technology. As an important contribution along with the ESIW concept, a planar excitation scheme for the horizontally polarized TE_{01} mode has been also designed and validated.

The ESIW topology can be applied to known SIW antennas that would benefit from the presence of two orthogonally polarized modes. This is the case of the previously studied SIW horn antenna which, combined with the ESIW, becomes a dual-polarized substrate integrated horn, as has been presented in Chapter 6. In order to properly feed this horn with the two orthogonal TE_{10} and TE_{01} modes, a substrate integrated Orthomode Transducer (OMT) has been also designed. The whole structure is PCB-based and requires only 2 layers of substrate. This new concept holds promises not only for new devices taking advantage of both polarizations, but also for an increase of capacity (by using two orthogonal channels of information) and robustness (by using polarization diversity techniques) in communication systems.

Since this has been the first time that a robust dual-polarized guide in SIW technology have been proposed and validated, there is a broad range of future work lines ahead. The ESIW topology might find applications, for instance, in antenna feed chains or in the design of leaky-wave antennas. In the latter, one could use a single low-cost antenna to generate two independent beams and simultaneously cover different geographical areas. Other future work might concern the study of more complex OMTs which, by properly controlling the amplitude and phase difference between orthogonal modes, would serve to create circular polarized end-fire antennas. Standard dual or circular polarized horns find room in many applications and so could this planar and low-cost counterpart in SIW technology.

In the design of future devices, one should always keep in mind the manufacturing complexity. The SIW technology becomes really attractive when a complete structure can be directly fabricated in a PCB, such as the 8 SIW horns array in Chapter 4. Systems based on rectangular metallic waveguides are more costly but will generally offer higher performances and lower losses. Complex and time consuming SIW designs requiring a lot of layers and additional manufacturing processes may lose the fundamental advantages of this technology. Thus, an antenna engineer must have a global vision of the system in order to assess the most appropriate design and manufacturing technology.

In a nutshell, the overall combination of novel ideas and concepts proposed in this PhD thesis has served to extend the use of the SIW technology towards new scenarios. First, the possibility of building now SIW horn antennas in electrically thin substrates opens the door to their use at the Ku-band and below, where commercial applications are starting to be deployed. Secondly, the feasibility of creating dual-polarized substrate integrated systems hold promises to increase the capacity, robustness and compactness of modern communication systems.

A Comparison between TE and LSE/LSM Modes

In Rectangular Waveguides (RWGs), the set of modes that satisfy the boundary conditions is composed of the (TE^x and TM^x), the (TE^y and TM^y) or the (TE^z and TM^z) modes. In an empty or homogeneously filled RWG (such as the one in Fig. A.1(a)), the TE^x and TM^x modes can be used to express the different possible modes in the waveguide and have, respectively, zero electric and zero magnetic field component in the direction of propagation x . Usually, such modes are simply referred as TE and TM modes ¹.

Nevertheless, in some waveguide configurations such as partially filled RWG with dielectric slabs or Non-Radiative Dielectric (NRD) guides, TE^x and TM^x modes cannot satisfy the boundary conditions of the structure. In these configurations, the so-called Longitudinal Section Electric (LSE) and Longitudinal Section Magnetic (LSM) modes are considered. The appropriate set of LSE and LSM modes are defined based on a direction perpendicular to the material interface, which corresponds to the y -axis in the NRD guide shown in Fig. A.1(b). These modes have then zero y -components of the electric and magnetic field, respectively, and can be obtained using y -directed vector potentials (instead of the x -directed ones used for the TE^x and TM^x modes [154]). This is why these LSE and LSM modes are also alternatively called TE^y and TM^y modes, respectively.

Due to the different material interfaces, the field distributions of the LSE and LSM modes in an NRD guide are more complex than the ones of the TE and TM modes in a RWG and they present a dependence with respect to the propagation constant. Moreover, the expressions for the fields in the high permittivity ϵ_r channel are different from the ones in the low permittivity ϵ_{rh} region because, in the latter, the modes are under cut-off. An approach to derive the main characteristics of each mode in an NRD guide is to use the Transverse Resonance Method

¹Note that this notation differs from the commonly used one where the z -axis corresponds to the direction of propagation in the waveguide. This has been chosen to be coherent throughout the thesis because, in the final antenna system of Chapter 6, the z -axis corresponds to the broadside direction, i.e., the direction perpendicular to the substrate plane.

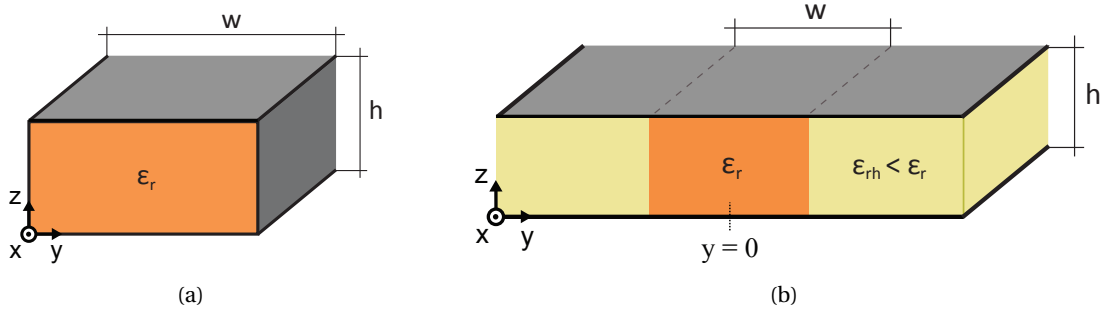


Fig. A.1: Isometric view of (a) dielectric-filled Rectangular Waveguide (RWG) and (b) Non-Radiative Dielectric (NRD) guide.

(TRM), as shown in Section 5.1. However, closed-form expressions for the different quantities, e.g., the propagation constant, usually cannot be found and numerical solutions are needed.

In the context of this thesis, it is important to determine which LSE and LSM modes are supported in NRD guides (or SINRD guides) and which similarities they share with other modes in RWGs (or SIWs). Hence, hybrid circuits combining both technologies could be created and even well-known strategies to excite certain modes in RWGs could be adopted in NRD guides. The expressions for the different components of the TE/TM modes in the dielectric-filled RWG of Fig. A.1(a) and for the LSE/LSM modes in the NRD guide of Fig. A.1(b) are presented in Tabs. A.1-A.2. These results are partly extracted or derived from [154, 155].

Quantity	TE _{mn}	TM _{mn}
$e_x(y,z) \propto$	0	$\frac{k_c^2}{\omega\mu_0\epsilon_0\epsilon_r} \sin\left(\frac{m\pi}{w}y\right) \sin\left(\frac{n\pi}{h}z\right)$
$e_y(y,z) \propto$	$\frac{1}{\epsilon_0\epsilon_r} \left(\frac{n\pi}{h}\right) \cos\left(\frac{m\pi}{w}y\right) \sin\left(\frac{n\pi}{h}z\right)$	$\left(\frac{n\pi}{h}\right) \frac{k_x}{\omega\mu_0\epsilon_0\epsilon_r} \cos\left(\frac{m\pi}{w}y\right) \sin\left(\frac{n\pi}{h}z\right)$
$e_z(y,z) \propto$	$\frac{1}{\epsilon_0\epsilon_r} \left(\frac{m\pi}{w}\right) \sin\left(\frac{m\pi}{w}y\right) \cos\left(\frac{n\pi}{h}z\right)$	$\left(\frac{m\pi}{w}\right) \frac{k_x}{\omega\mu_0\epsilon_0\epsilon_r} \sin\left(\frac{m\pi}{w}y\right) \cos\left(\frac{n\pi}{h}z\right)$
$h_x(y,z) \propto$	$\frac{k_c^2}{\omega\mu_0\epsilon_0\epsilon_r} \cos\left(\frac{m\pi}{w}y\right) \cos\left(\frac{n\pi}{h}z\right)$	0
$h_y(y,z) \propto$	$\left(\frac{m\pi}{w}\right) \frac{k_x}{\omega\mu_0\epsilon_0} \sin\left(\frac{m\pi}{w}y\right) \cos\left(\frac{n\pi}{h}z\right)$	$\frac{1}{\mu_0} \left(\frac{n\pi}{h}\right) \sin\left(\frac{m\pi}{w}y\right) \cos\left(\frac{n\pi}{h}z\right)$
$h_z(y,z) \propto$	$\left(\frac{n\pi}{h}\right) \frac{k_x}{\omega\mu_0\epsilon_0\epsilon_r} \cos\left(\frac{m\pi}{w}y\right) \sin\left(\frac{n\pi}{h}z\right)$	$\frac{1}{\mu_0} \left(\frac{m\pi}{w}\right) \cos\left(\frac{m\pi}{w}y\right) \sin\left(\frac{n\pi}{h}z\right)$

$$k_x = \sqrt{k_0^2\epsilon_r - \left(\frac{m\pi}{w}\right)^2 - \left(\frac{n\pi}{h}\right)^2}$$

$$k_c^2 = k_y^2 + k_z^2 = \left(\frac{m\pi}{w}\right)^2 + \left(\frac{n\pi}{h}\right)^2$$

Tab. A.1: TE and TM modes in the dielectric-filled RWG of Fig. A.1(a).

LSE_{mn} modes		
Quantity	$ y < w/2$	$ y > w/2$
$e_x(y,z) \propto$	$\frac{1}{\varepsilon_0 \varepsilon_r} \left(\frac{n\pi}{h} \right) \cos(k_{y1 m} y) \sin\left(\frac{n\pi}{h} z\right)$	$\frac{1}{\varepsilon_0 \varepsilon_r} \left(\frac{n\pi}{h} \right) \cos\left(k_{y1 m} \frac{w}{2}\right) \sin\left(\frac{n\pi}{h} z\right) e^{\alpha_{y2 m}(w/2- y)}$
$e_y(y,z) \propto$	0	0
$e_z(y,z) \propto$	$\frac{k_x}{\varepsilon_0 \varepsilon_r} \cos(k_{y1 m} y) \cos\left(\frac{n\pi}{h} z\right)$	$\frac{k_x}{\varepsilon_0 \varepsilon_r} \cos\left(k_{y1 m} \frac{w}{2}\right) \cos\left(\frac{n\pi}{h} z\right) e^{\alpha_{y2 m}(w/2- y)}$
$h_x(y,z) \propto$	$\frac{k_x k_{y1 m}}{\omega \mu_0 \varepsilon_0 \varepsilon_r} \sin(k_{y1 m} y) \cos\left(\frac{n\pi}{h} z\right)$	$\frac{k_x k_{y1 m}}{\omega \mu_0 \varepsilon_0 \varepsilon_r} \sin\left(k_{y1 m} \frac{w}{2}\right) \cos\left(\frac{n\pi}{h} z\right) e^{\alpha_{y2 m}(w/2- y)}$
$h_y(y,z) \propto$	$\frac{k_x^2 + \left(\frac{n\pi}{h}\right)^2}{\omega \mu_0 \varepsilon_0 \varepsilon_r} \cos(k_{y1 m} y) \cos\left(\frac{n\pi}{h} z\right)$	$\frac{k_x^2 + \left(\frac{n\pi}{h}\right)^2}{\omega \mu_0 \varepsilon_0 \varepsilon_r} \cos\left(k_{y1 m} \frac{w}{2}\right) \cos\left(\frac{n\pi}{h} z\right) e^{\alpha_{y2 m}(w/2- y)}$
$h_z(y,z) \propto$	$\frac{k_{y1 m}}{\omega \mu_0 \varepsilon_0 \varepsilon_r} \left(\frac{n\pi}{h} \right) \sin(k_{y1 m} y) \sin\left(\frac{n\pi}{h} z\right)$	$\frac{k_{y1 m}}{\omega \mu_0 \varepsilon_0 \varepsilon_r} \left(\frac{n\pi}{h} \right) \sin\left(k_{y1 m} \frac{w}{2}\right) \sin\left(\frac{n\pi}{h} z\right) e^{\alpha_{y2 m}(w/2- y)}$

LSM_{mn} modes		
Quantity	$ y < w/2$	$ y > w/2$
$e_x(y,z) \propto$	$\frac{k_x k_{y1 m}}{\omega \mu_0 \varepsilon_0 \varepsilon_r} \sin(k_{y1 m} y) \sin\left(\frac{n\pi}{h} z\right)$	$\frac{k_x k_{y1 m}}{\omega \mu_0 \varepsilon_0 \varepsilon_r} \sin\left(k_{y1 m} \frac{w}{2}\right) \sin\left(\frac{n\pi}{h} z\right) e^{\alpha_{y2 m}(w/2- y)}$
$e_y(y,z) \propto$	$\frac{k_x^2 + \left(\frac{n\pi}{h}\right)^2}{\omega \mu_0 \varepsilon_0 \varepsilon_r} \cos(k_{y1 m} y) \sin\left(\frac{n\pi}{h} z\right)$	$\frac{k_x^2 + \left(\frac{n\pi}{h}\right)^2}{\omega \mu_0 \varepsilon_0 \varepsilon_r} \cos\left(k_{y1 m} \frac{w}{2}\right) \sin\left(\frac{n\pi}{h} z\right) e^{\alpha_{y2 m}(w/2- y)}$
$e_z(y,z) \propto$	$\frac{k_{y1 m}}{\omega \mu_0 \varepsilon_0 \varepsilon_r} \left(\frac{n\pi}{h} \right) \sin(k_{y1 m} y) \cos\left(\frac{n\pi}{h} z\right)$	$\frac{k_{y1 m}}{\omega \mu_0 \varepsilon_0 \varepsilon_r} \left(\frac{n\pi}{h} \right) \sin\left(k_{y1 m} \frac{w}{2}\right) \cos\left(\frac{n\pi}{h} z\right) e^{\alpha_{y2 m}(w/2- y)}$
$h_x(y,z) \propto$	$\frac{1}{\mu_0} \left(\frac{n\pi}{h} \right) \cos(k_{y1 m} y) \cos\left(\frac{n\pi}{h} z\right)$	$\frac{1}{\mu_0} \left(\frac{n\pi}{h} \right) \cos\left(k_{y1 m} \frac{w}{2}\right) \cos\left(\frac{n\pi}{h} z\right) e^{\alpha_{y2 m}(w/2- y)}$
$h_y(y,z) \propto$	0	0
$h_z(y,z) \propto$	$\frac{k_x}{\mu_0} \cos(k_{y1 m} y) \sin\left(\frac{n\pi}{h} z\right)$	$\frac{k_x}{\mu_0} \cos\left(k_{y1 m} \frac{w}{2}\right) \sin\left(\frac{n\pi}{h} z\right) e^{\alpha_{y2 m}(w/2- y)}$

$$k_x = \sqrt{k_0^2 \varepsilon_r - k_{y1|m}^2 - \left(\frac{n\pi}{h}\right)^2} = \sqrt{k_0^2 \varepsilon_r h + \alpha_{y2|m}^2 - \left(\frac{n\pi}{h}\right)^2} \quad \alpha_{y2|m} = \sqrt{k_0^2 (\varepsilon_r - \varepsilon_{rh}) - k_{y1|m}^2}$$

Tab. A.2: LSE and LSM modes in the NRD guide of Fig. A.1(b).

The cross-section view of the electric field patterns for the first modes in a RWG and in an NRD guide are illustrated in Fig. A.2. Since the goal of this work is to create dual-polarized circuits, our attention is focused on modes having an electric field component mainly along the z -axis (e_z) or mainly along the y -axis (e_y), i.e., TE₁₀-like or TE₀₁-like modes, respectively.

In an NRD guide, the mode resembling the TE_{10} is the LSE_{10} mode. The main difference between the field distribution of these two modes is the dependence with the propagation constant exhibited by the LSE_{10} . The latter also has a higher cut-off frequency than the TE_{10} mode because the field is not only confined in the central ϵ_r channel but is also extended beyond it, in the lower permittivity region (see Fig. A.2(e)).

A TE_{01} -like mode can only be described by LSM modes because, by definition, LSE modes have zero electric field component along the y -axis, i.e., $e_y = 0$. It can be seen that the lowest order mode resembling the TE_{01} is the LSM_{11} , provided that the ratio w/h is sufficiently large (see Fig. A.2(g)): since this mode has both e_y and e_z components, the ratio w/h should be such that the e_y component is dominant with respect to e_z .

The detailed analysis provided in this appendix allows for a better understanding of the field distributions of the modes in different waveguide topologies. This is used in Chapter 5 to compare the performances of the substrate integrated versions of the guides of Fig. A.1, to propose a new substrate integrated guide topology able to support both TE_{10} and TE_{01} modes and to design a planar excitation scheme for the TE_{01} mode.

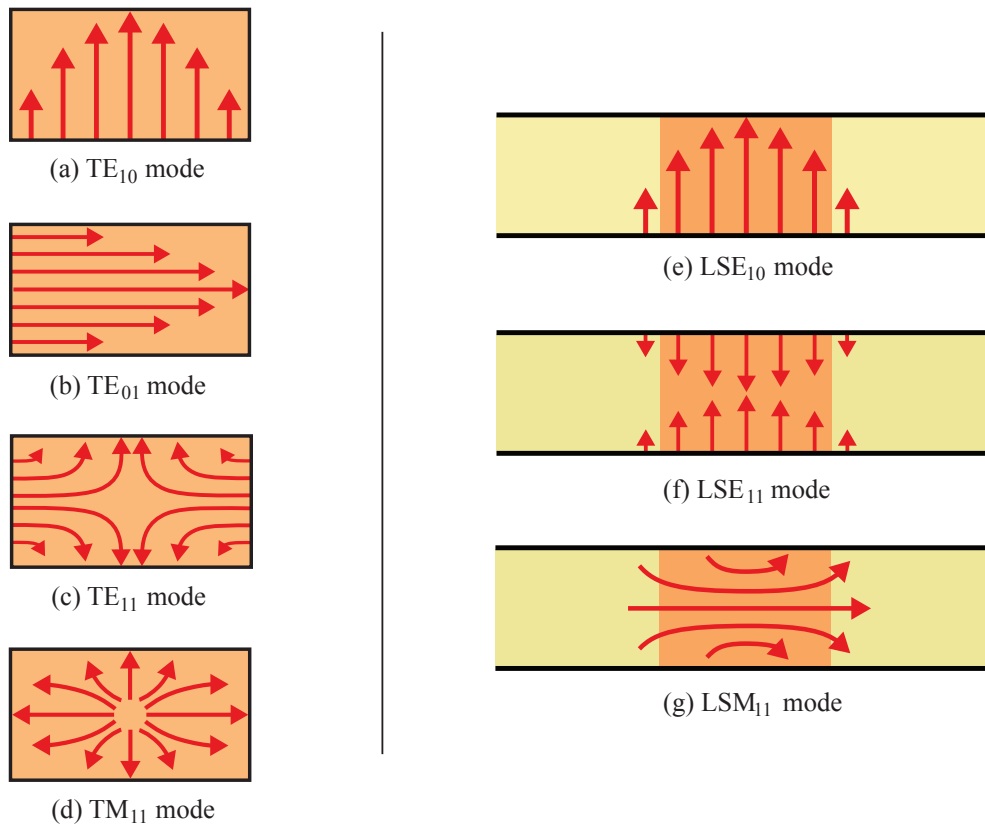


Fig. A.2: Cross-section view of the electric field patterns of the first modes in the RWG (a)-(d) and in the NRD guide (e)-(g). Electric field lines are sketched in red and it has been assumed that $w/h > 1$.

B Graphene-based Reconfigurable Leaky-Wave Antennas

In this appendix, the results of a collaboration with the Adaptive MicroNanoWave Systems - LEMA/Nanolab, mainly with Dr. Gómez-Díaz, are summarized. This work concerns the design of reconfigurable Leaky-Wave Antennas (LWA) at THz region using graphene and was disseminated in a conference paper [20] and two journal papers [21, 22].

B.1 Introduction

Graphene's unique electrical properties hold significant promises for the future implementation of integrated and reconfigurable (potentially all-graphene) terahertz transceivers and sensors. In this article, the term *terahertz* is used to define the frequency range between 300 GHz and 3 THz [156]. However, only few studies have considered the use of graphene in antenna applications. Initial works employed graphene as a component parasitic to radiation [157, 158], for instance as a switch element to choose among different states of a reconfigurable antenna. Then, the propagation of transverse-magnetic (TM) surface plasmon polaritons (SPPs) in graphene [159, 160] was exploited in [161] to propose patch antennas in the THz band. This study was the first to consider graphene an actual antenna linking free space waves to a lumped source/detector, as needed in most communication and sensing scenarios. Several works have further studied the capabilities of graphene in antenna design [162] and even the integration of graphene in beam steering reflectarrays [163].

On the other hand, different mechanisms have been proposed to excite SPPs in graphene structures, including the use of diffraction gratings [164, 165] or polaritonic crystals obtained by modulated graphene conductivity [166]. However, the applications of THz transceivers which include chemical and biological remote sensing, image scanning, pico-cellular and intrasatellite communications, or high resolution imaging and tomography [156, 167–169], require antennas with specific capabilities in terms of beamscanning and directivity.

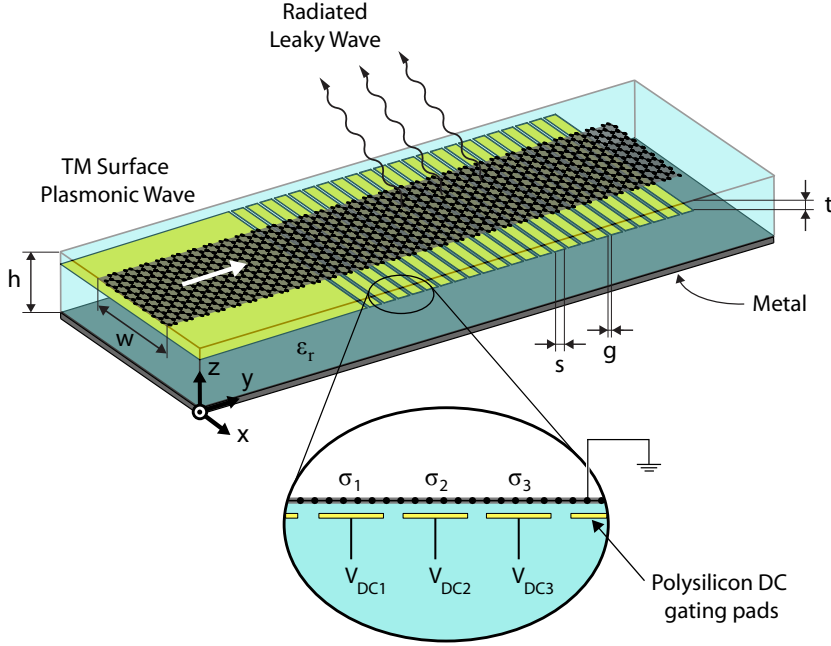


Fig. B.1: Proposed sinusoidally-modulated reactance graphene surface operating as a leaky wave antenna. The polysilicon pads (yellow) are used to modify the graphene conductivity σ_i as a function of the applied DC voltage V_{DCi} .

In this context, we propose the concept, analysis, and design of a graphene sinusoidally-modulated leaky-wave antenna (LWA) for electronic beamsteering in the THz band. The antenna is based on the principle of sinusoidally-modulated reactance surfaces to achieve leaky-wave radiation [170–172]. The proposed structure, shown in Fig. B.1, is composed of a graphene sheet transferred onto a back-metallized substrate and several polysilicon DC gating pads located beneath it. The graphene sheet supports the propagation of transverse-magnetic (TM) surface plasmon polaritons (SPPs) [160], which can be controlled via the voltages applied to the different pads (note that the graphene sheet is connected to the source ground). Indeed, as illustrated in the inset of Fig. B.1 and explained in more detail below, the application of a DC bias to the gating pads allows to control graphene’s complex conductivity [173]. This property is exploited to sinusoidally modulate the sheet surface reactance by applying adequate bias voltages to the different pads, thereby creating a leaky-wave mode [170–172].

Moreover, antenna radiation features such as pointing angle (θ_0) and leakage rate (α_{rad}) can be dynamically controlled by modifying the applied voltages, thus allowing electronic beamsteering at a fixed operating frequency. This simple and fully integrated antenna structure is designed and analyzed using leaky-wave antenna theory [174] and validated by full-wave simulations.

B.2 Tunability of Graphene Conductivity

Graphene is a two-dimensional material composed of carbon atoms bonded in hexagonal structure. Its surface conductivity can be modeled using the well-known Kubo formalism [175]. In the low terahertz band and at room temperatures, interband contributions of graphene conductivity can safely be neglected [176]. This allows one to describe graphene conductivity using only intraband contributions as

$$\sigma = -j \frac{q_e^2 K_B T}{\pi \hbar^2 (\omega - j2\Gamma)} \left[\frac{\mu_c}{K_B T} + 2 \ln \left(e^{-\frac{\mu_c}{K_B T}} + 1 \right) \right], \quad (\text{B.1})$$

where K_B is the Boltzmann's constant, \hbar is the reduced Planck constant, $-q_e$ is the electron charge, T is temperature, μ_c is graphene chemical potential, $\Gamma = 1/(2\tau)$ is the electron scattering rate, and τ is the electron relaxation time.

Graphene conductivity can be tuned by applying a transverse electric field via a DC biased gating structure (see Fig. B.1). Assuming non-chemically doped graphene (i.e., $V_{Dirac} = 0$ [173]), this field modifies the graphene carrier density n_s as

$$C_{ox} V_{DC} = q_e n_s, \quad (\text{B.2})$$

where $C_{ox} = \epsilon_r \epsilon_0 / t$ is the gate capacitance and V_{DC} is the applied DC bias field. Neglecting the quantum capacitance, i.e., assuming a relative thick gate oxide [177], the carrier density is related to graphene chemical potential μ_c as

$$n_s = \frac{2}{\pi \hbar^2 v_f^2} \int_0^\infty \epsilon [f_d(\epsilon - \mu_c) - f_d(\epsilon + \mu_c)] \partial \epsilon, \quad (\text{B.3})$$

where ϵ is energy, v_f is the Fermi velocity ($\sim 10^8$ cm/s in graphene), and f_d is the Fermi-Dirac distribution

$$f_d(\epsilon) = \left(e^{(\epsilon - |\mu_c|)/k_B T} + 1 \right)^{-1}. \quad (\text{B.4})$$

The chemical potential μ_c is accurately retrieved by numerically solving Eq. (B.3). Hence, we can see from Eq. (B.1) that the graphene conductivity σ or surface impedance $1/\sigma$ can be dynamically controlled by V_{DC} . This property can be used to create leaky-wave antennas with dynamic control as introduced in Section I and further detailed next.

B.3 Sinusoidally-Modulated Reactance Surfaces

Electromagnetic propagation along sinusoidally-modulated reactance surfaces was theoretically investigated in the 50s [170], but is still drawing significant interest as a powerful

way to control radiation properties [171, 178]. Surfaces with a dominant positive reactance impedance (such as graphene) allow the propagation of TM surface waves. If a modulation is then applied along the y axis, the modal surface reactance X_S can be expressed as:

$$X_S = X'_S \left[1 + M \sin \left(\frac{2\pi y}{p} \right) \right], \quad (\text{B.5})$$

where X'_S is the average surface reactance, M the modulation index and p the period of the sinusoid.

The interaction between surface waves and the reactance modulation produces a Bragg radiation effect thus creating leaky-wave radiation. The wavenumber k_y of the fundamental space harmonic along the impedance modulated graphene sheet can be written as [170]:

$$k_y = \beta_{spp} + \Delta\beta_{spp} - j(\alpha_{spp} + \alpha_{rad}), \quad (\text{B.6})$$

where β_{spp} is the propagation constant of the SPP on the unmodulated graphene sheet (i.e., with $M = 0$), $\Delta\beta_{spp}$ a small variation in β_{spp} due to the modulation, α_{spp} the attenuation constant due to losses and α_{rad} the attenuation constant due to energy leakage (leakage rate).

In this kind of periodic LWAs, the fundamental space harmonic is slow and usually the higher-order -1 space harmonic is used for radiation [170]. In this case, the pointing angle θ_0 of the radiated beam is approximated as [174]

$$\theta_0 = \arcsin \left(\frac{\beta_{-1}}{k_0} \right) \approx \arcsin \left(\frac{\beta_{spp}}{k_0} - \frac{\lambda_0}{p} \right), \quad (\text{B.7})$$

where β_{-1} is the propagation constant of the -1 space harmonic, λ_0 is a free space wavelength and $\Delta\beta_{spp}$ is assumed much smaller than β_{spp} [178]. Since the average surface reactance X'_S mainly determines β_{spp} and the modulation index M mainly determines α_{rad} , these LWAs allow for nearly independent control of the pointing angle and the beamwidth [171].

In the next Section, a graphene LWA based on this radiation principle is proposed taking into account realistic technological parameters for future implementation.

B.4 Periodically Modulated Graphene LWA

B.4.1 Proposed Structure

The proposed sinusoidally-modulated graphene LWA is shown in Fig. B.1. It consists of a graphene sheet transferred on a back-metallized substrate and several independent polysilicon DC gating pads beneath it. The surface impedance $Z_S = R_S + jX_S$ at the graphene position

($z = h$) determines the propagation characteristics of the SPPs, i.e., $k_{y,spp} = \beta_{spp} - j\alpha_{spp}$.

In an *unmodulated* graphene sheet, the dispersion relation of the SPPs can be computed by applying a transverse resonance equation (TRE) to the equivalent circuit shown in Fig. B.2 [179], where the width w of the graphene sheet is considered infinite. Then, by enforcing $Y_{UP} + Y_{DOWN} = 0$, where

$$Y_{UP} = \frac{\omega\epsilon_0}{\pm\sqrt{k_0^2 - k_{y,spp}^2}}, \quad (\text{B.8})$$

$$Y_{DOWN} = \sigma + \frac{\omega\epsilon_r\epsilon_0}{\pm\sqrt{\epsilon_r k_0^2 - k_{y,spp}^2}} \coth(\pm\sqrt{\epsilon_r k_0^2 - k_{y,spp}^2} h), \quad (\text{B.9})$$

the desired dispersion relation is obtained as

$$\frac{\omega\epsilon_0}{\pm\sqrt{k_0^2 - k_{y,spp}^2}} + \frac{\omega\epsilon_r\epsilon_0}{\pm\sqrt{\epsilon_r k_0^2 - k_{y,spp}^2}} \coth(\pm\sqrt{\epsilon_r k_0^2 - k_{y,spp}^2} h) = -\sigma. \quad (\text{B.10})$$

In the above expressions, ϵ_0 is the vacuum permittivity, ϵ_r is the dielectric permittivity, $k_0 = \omega/c$ is the free space wavenumber and h is the dielectric thickness. The surface impedance Z_S is then computed as $1/Y_{DOWN}$. It can be shown that the polysilicon pads can be safely neglected since they are extremely thin (~ 100 nm) and with a relative permittivity $\epsilon_r \simeq 3$ [180] similar to the one of the SiO_2 substrate used.

As explained in Section B.2, in order to modulate the surface impedance Z_S , the graphene conductivity σ is modified by applying adequate bias voltages V_{DC} to the different pads.

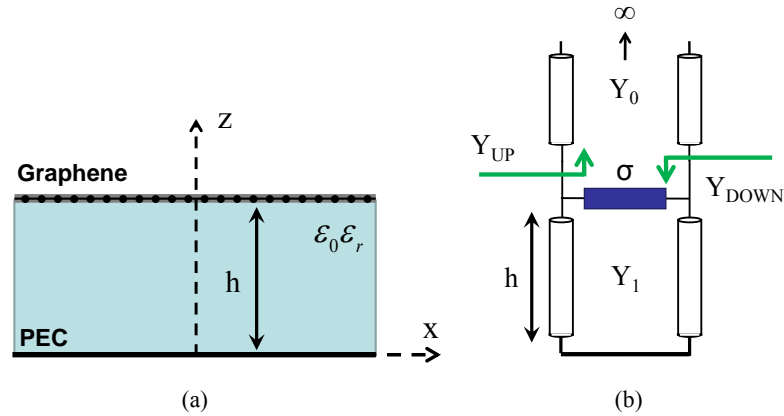


Fig. B.2: Schematic of graphene sheet transferred onto a back-metallized substrate (a) and its equivalent transverse network along the z -axis (b). The polysilicon pads have been neglected since they are extremely thin and with permittivity similar to the one of the SiO_2 substrate used.

This allows one to generate the desired periodic reactance modulation. Here, one modulation period p is sampled in N points according to the number of gating pads used, namely, $p = N(s + g)$, where s is the pad length and g the distance between pads (see Fig. B.3). The dimensions s and g should be chosen such that $g \ll s$ in order to guarantee a fairly constant perpendicular electrostatic field at the graphene section above each polysilicon pad. Therefore, p can be dynamically controlled according to the periodicity imposed by the different V_{DC} . Consequently, from Eq. (B.7), the proposed structure offers electronic beamsteering at a fixed frequency. This is a novel property absent when usual techniques such as the use of sub-wavelengths printed elements or dielectric slabs with variable thickness [171, 178, 181] are employed to implement sinusoidally-modulated LWA.

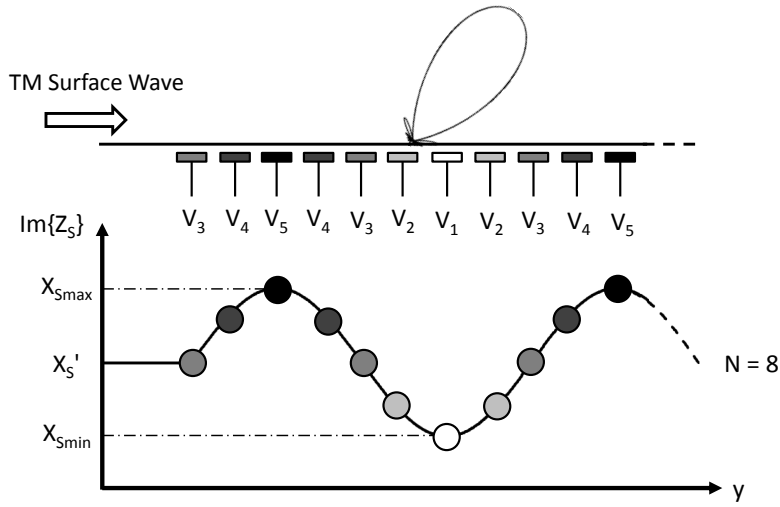


Fig. B.3: Schematic representation of the relationship between the DC bias voltage V_{DC} and graphene reactance X_S .

The impedance-modulated graphene sheet of Fig. B.1 may radiate towards both the upper and lower half-spaces depending on the substrate permittivity ϵ_r . The metallic plane is then used as a reflector and one should choose the substrate thickness h such that the main and the reflected beams add in phase. In addition, it is important to remark that, although SPPs on graphene sheets are confined into the layer [160], the presence of a metallic plane at a distance h from the graphene sheet might affect their propagation characteristics. This is particularly important when dealing with this type of LWA due to their high dispersive nature, where a small variation on β_{spp} can considerably tilt the pointing angle θ_0 . Here, this phenomenon is taken into account in the equivalent circuit of Fig. B.2 and is illustrated in the Section B.5.

B.4.2 Design Strategy

The design flow of the proposed graphene LWA must take into account the technological limitations of current graphene fabrication processes. Therefore, given the parameters of

a graphene sample (τ , T , t , V_{DC}), the substrate (ϵ_r), the frequency of operation f_0 and the pointing angle θ_0 , the design steps are the following:

1. Given θ_0 , the needed propagation constant of the -1 space harmonic β_{-1} is computed with Eq. (B.7).
2. Knowing the substrate and the graphene properties, the propagation constant β_{spp} of the SPPs is obtained. First, the available values of μ_c are found with Eqs. (B.2) and (B.3) as a function of t and the range of V_{DC} . Then, graphene conductivity σ is computed with Eq. (B.1) and, in turn, the wavenumber $k_{y,spp}$ of the SPPs with Eq. (B.10).
3. The required modulation period p is then computed as $p = 2\pi / (\beta_{spp} - \beta_{-1})$.
4. The next step is to find the possible values of the modulation index M that can be obtained with the graphene sample. First, the surface impedances $Z_S = R_S + jX_S$ are computed as a function of μ_c . Then, the desired range of reactances ($X_{S_{min}} - X_{S_{max}}$ in Fig. B.3) is chosen, thus defining the value of M .
5. The leakage factor α_{rad} can now be computed as described in [170].
6. If beamscanning around θ_0 is desired, the new periodicities around p are computed with (B.7). The dimensions of the gating pads s and g and the different values of N are chosen in order to synthesize the required periods.
7. Knowing the scanning range, the substrate thickness h is then chosen so that there is a constructive interference between the main and reflected beams in all the different angles.
8. Finally, the complex propagation constant k_y is determined by Eq. (B.6) and the radiation pattern of the LWA can be easily computed using standard techniques [174].

B.5 Design Example

In this example we consider a SiO_2 substrate of permittivity $\epsilon_r = 3.8$ [182]. We assume graphene with a relaxation time $\tau = 1$ ps, temperature $T = 300^\circ$ K and design the antenna for operation at $f_0 = 2$ THz. The value of τ was estimated from the measured impurity-limited DC graphene mobility on boron nitride [183] of $\mu \simeq 60000 \text{ cm}^2 / (\text{V s})$, which leads to $\tau = \mu E_F / (q_e v_f^2) \simeq 1.2$ ps for a Fermi level of $E_F = 0.2$ eV. Note that even higher mobilities have been observed in high quality suspended graphene [184].

The width w of the graphene strip is chosen to be electrically very large ($200 \mu\text{m}$) in order to support the propagation of SPPs with the same characteristics as in 2D infinite sheets thus allowing to use the simplified model of Fig. B.2.

The graphene chemical potential μ_c as a function of the DC bias voltage V_{DC} , computed using Eqs. (B.2) and (B.3), is shown in Fig. B.4 for different values of t . A distance $t = 20$ nm is chosen which offers values of μ_c until 0.8 eV using V_{DC} values below 45 V.

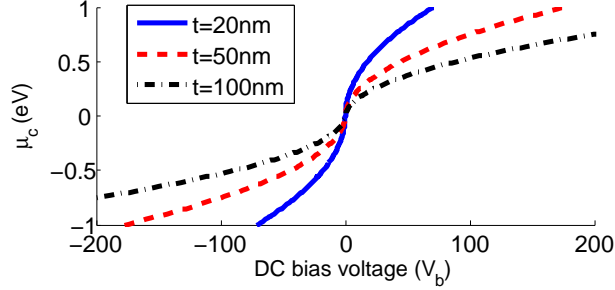


Fig. B.4: Graphene chemical potential μ_c as a function of the DC bias voltage V_{DC} . Parameters: $\tau = 1$ ps, $T = 300^\circ$ K, $f_0 = 2$ THz and $\epsilon_r = 3.8$.

The surface impedance Z_S is plotted in Fig. B.5 as a function of μ_c . It is observed that, while the graphene resistance R_S remains fairly constant, the reactance X_S can be considerably modified. Under these conditions, an average surface reactance $X'_S = 1302 \Omega/\square$ and a modulation index $M = 0.35$ are chosen. According to Fig. B.4 and B.5, this requires a range of chemical potentials between 0.3 and 0.8 eV, i.e., a range of DC voltages between 6.4 V and 45 V.

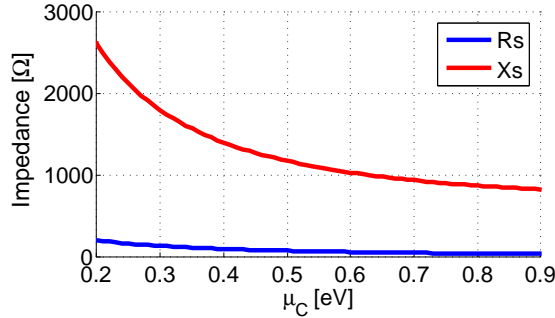


Fig. B.5: Surface resistance R_S and reactance X_S at the graphene sheet (position $z = h$ in Fig. B.2) as a function of the chemical potential μ_c . Parameters: $\tau = 1$ ps, $T = 300^\circ$ K, $f_0 = 2$ THz and $\epsilon_r = 3.8$.

The voltage V_{DC} needed for the desired X'_S is 13.5 V, i.e., $\mu_c = 0.436$ eV. This corresponds to $\beta_{spp}/k_0 = 3.59$ and $\alpha_{spp}/k_0 = 0.21$. In order to illustrate the effect of the metallic plane on the propagation of SPPs, β_{spp} and α_{spp} are plotted in Fig. B.6 as a function of h . The solid blue lines indicate the values obtained in the case of a graphene sheet on a semi-infinite substrate. It can be seen that for $h > 30 \mu\text{m}$ the effect of the metallic plane is negligible and thus the plasmon is indeed highly confined to the graphene layer.

Once β_{spp} is known, Eq. (B.7) allows determining that the -1 space harmonic is in the fast-wave radiation region for values of p comprised between 33 and 57 μm (see Fig. B.7). Depending on the size of the polysilicon pads, a different number of scanning beams can be obtained.

Although smaller pads offer the possibility to generate more beams, the complexity of the antenna also increases. As a trade-off, the dimensions of the pads are here chosen as $s = 4.8 \mu\text{m}$ and $g = 0.2 \mu\text{m}$, which satisfy $g \ll s$ and can be manufactured with current technology. This configuration can generate 4 different beams at -45.4 , -9.3 , 15.4 and 37.5° by varying N from 7 to 10 (see Fig. B.7). The radiation patterns obtained with LWA theory and full-wave simulations for these values of N are plotted in Fig. B.8.

In this case, a substrate thickness $h = 60 \mu\text{m}$ is chosen. A parametric study was performed to determine the optimum value of h so that there is a constructive interference between the main and reflected beams in all the different scanning angles. For the reader's convenience, a summary of the different parameters used in this design is presented in Tab. B.1.

Graphene			Substrate		Polysilicon pads		
τ	T	w	ϵ_r	h	t	s	g
1ps	300°K	200 μm	3.8	60 μm	20nm	4.8 μm	0.2 μm

Tab. B.1: Parameters used in the proposed GLWA design example.

In the scanning region, the proposed LWA presents a leakage factor $\alpha_{rad}/k_0 \approx 0.025$ and dissipation losses $\alpha_{spp}/k_0 \approx 0.21$. The effective length of the antenna for a 95% of dissipated power

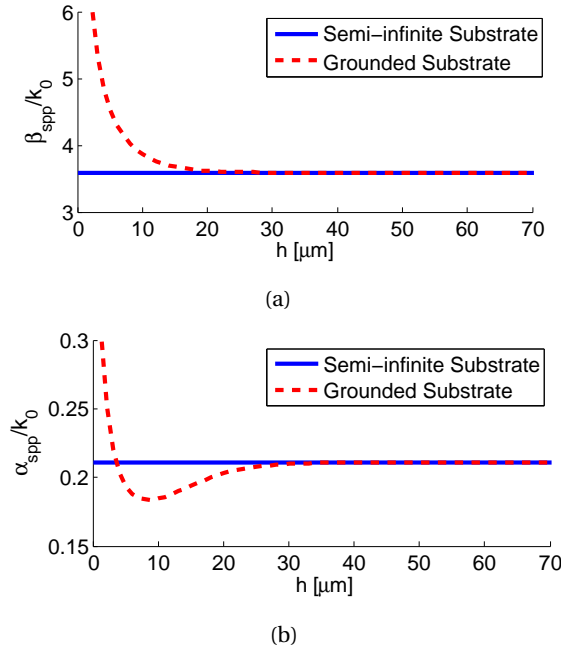


Fig. B.6: Normalized phase constant β_{spp}/k_0 (a) and dissipation losses α_{spp}/k_0 (b) of a SPP on the structure shown in Fig. B.2 as a function of the substrate thickness h . Parameters: $\tau = 1$ ps, $T = 300^\circ$ K, $f_0 = 2$ THz, $V_{DC} = 13.5$ V and $\epsilon_r = 3.8$.

is $L_e = 3/(2(\alpha_{rad} + \alpha_{spp}))$ [174]. The radiation efficiency η_{rad} of LWAs with non-negligible dissipation losses is given by [185]:

$$\eta_{rad} = \frac{\alpha_{rad}}{\alpha_{rad} + \alpha_{spp}} (1 - e^{-2(\alpha_{rad} + \alpha_{spp})L_e}). \quad (\text{B.11})$$

In our case, $L_e \approx \lambda_0$ and $\eta_{rad} \approx 11\%$. The radiation efficiency could be further increased by using a wider range of V_{DC} to achieve higher values of M , e.g., $M = 0.5$ leads to $\eta_{rad} \approx 19\%$.

B.6 Practical Considerations

This section briefly describe practical consideration related to the antenna's performance and fabrication.

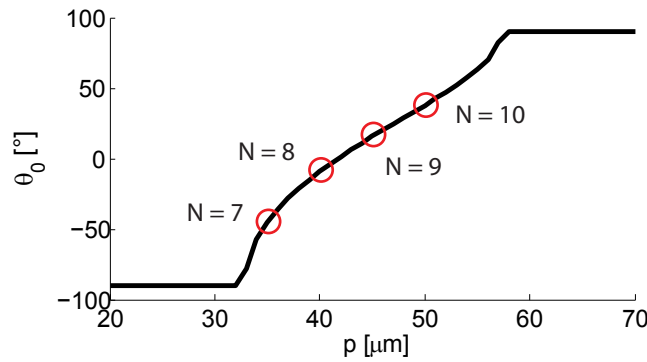


Fig. B.7: Pointing angle θ_0 as a function of the period p . N is the number of polysilicon pads used to define one modulation period p . Parameters: $\tau = 1$ ps, $V_{DC} = 13.5$ V, $T = 300^\circ$ K, $f_0 = 2$ THz, $\epsilon_r = 3.8$, $s = 4.8\mu\text{m}$ and $g = 0.2\mu\text{m}$.

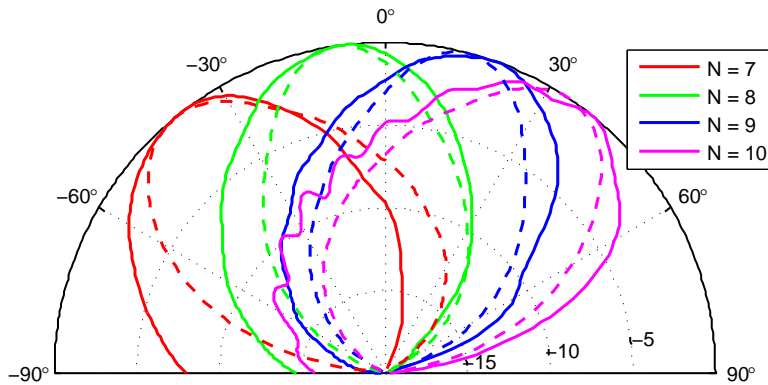


Fig. B.8: Radiation patterns (ZY plane) for different values of N . Solid lines are obtained with HFSS v14 and dashed lines with LWA theory [174]. Parameters: $\tau = 1$ ps, $T = 300^\circ$ K, $f_0 = 2$ THz, $V_{DC} = 6.5 - 45$ V, $\epsilon_r = 3.8$, $s = 4.8\mu\text{m}$ and $g = 0.2\mu\text{m}$.

First, the antenna directivity is increased when using lower permittivity substrates. Indeed, reducing ϵ_r reduces β_{spp} and α_{spp} and thus the effective length of the antenna is increased. For instance, using the same graphene sheet as in Section B.5 on a substrate with $\epsilon_r = 1.8$ implies $\beta_{spp}/k_0 = 2.23$, $\alpha_{spp}/k_0 \simeq 0.117$ and $\alpha_{rad}/k_0 \simeq 0.02$. Obviously, since β_{spp} is reduced, the values of p needed to scan with the -1 harmonic are larger. In this case, using pads of $s = 8.8\mu\text{m}$ and $g = 0.2\mu\text{m}$ and values of N between 6 and 9 generates the beams shown in Fig. B.9. The effective length of the antenna is now $1.74\lambda_0$ allowing for higher directive beams and a radiation efficiency around 15%. The drawback of this configuration is that low permittivity substrates are difficult to implement and a higher number of polysilicon pads is required.

Second, the radiation efficiency of the antenna always depends on the graphene quality, determined by the relaxation time τ . As τ increases, α_{spp} decreases and so do the losses. Measured values of $\tau = 1.0$ ps have been used in this work to obtain the radiation efficiencies. Note that, even though these values are not very high, they are within the state-of-the-art of THz antennas [156]. Moreover, most THz antennas do not include reconfiguration capabilities.

Third, the possible operation frequencies of the proposed structure are limited by graphene quality and the intrinsic behaviour of TM SPPs. On the one hand, the minimum operating frequency is within the low terahertz band ($\simeq 0.5$ THz) where graphene losses start to considerably increase and the surface reactance cannot be widely tuned by applying reduced DC voltages. On the other hand, the maximum operating frequency is predicted to be at few tenths of THz. At these frequencies, the plasmons are extremely confined at the graphene sheet and the dimensions of the polysilicon pads become really small to be implemented with current manufacturing processes. In addition, at very high frequencies (usually starting from 8 or 10 THz), the interband contributions of graphene conductivity are no longer negligible [176] and further theoretical studies would be necessary.

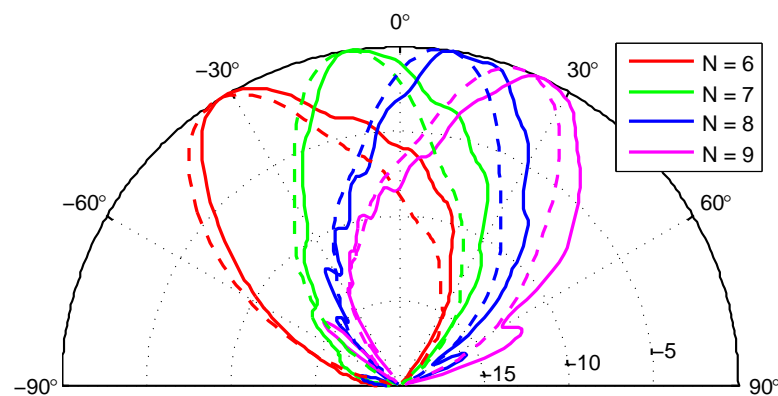


Fig. B.9: Radiation patterns (ZY plane) for different values of N . Solid lines are obtained with HFSS v14 and dashed lines with LWA theory [174]. Parameters: $\tau = 1$ ps, $T = 300^\circ$ K, $f_0 = 2$ THz, $V_{DC} = 6.5 - 45$ V, $\epsilon_r = 1.8$, $s = 8.8\mu\text{m}$ and $g = 0.2\mu\text{m}$.

It is also important to mention that the fringing electrostatic fields between consecutive polysilicon pads can be neglected and, therefore, they do not perturb the conductivity profile along the z -axis on graphene. First, it is shown in [186] that a finite-width gating pad imposes a *soft* boundary condition on the graphene sheet, leading to a smooth conductivity profile. Second, in order to provide a sinusoidal modulation of graphene's surface reactance, consecutive pads are DC biased with relatively similar voltages (as graphically illustrated in Fig. B.3) thus reducing even more the possible influence of the fringing fields.

Finally, it is worth mentioning that no power handling issues are foreseen in the proposed antenna structure. Similar mono-layer configurations have been studied and measured exhibiting really good performances in terms of thermal conductivity [187].

B.7 Conclusions

A graphene leaky-wave antenna which allows electronic beamsteering at a single frequency has been proposed. Its radiation principle is based on sinusoidally-modulated reactance surfaces which can be easily implemented using a graphene sheet thanks to its tunable characteristics when applying electric field biasing.

This novel antenna concept offers unprecedented performances at the THz band such as electronic control of several radiation characteristics preserving a radiation efficiency above 10%. The main limitations in its design are imposed by graphene properties (such as the relaxation time τ), the range of feasible voltages that can be applied to the gating pads, and the availability of substrates in the THz band.

The overall performances of this simple antenna structure are very promising for its integration in future all-graphene reconfigurable THz transceivers and sensors.

Bibliography

- [1] K. Gotsis, K. Siakavara, and J. Sahalos, "On the Direction of Arrival (DoA) Estimation for a Switched-Beam Antenna System Using Neural Networks," *IEEE Trans. Antennas Propag.*, vol. 57, no. 5, pp. 1399–1411, May 2009.
- [2] A. F. Molisch, *Wireless Communications*, 2nd ed. John Wiley & Sons Ltd., 2011, ch. 20.
- [3] Z. Chudy and L. Kachel, "Direction finding device with eight element circular antenna array," in *17th Int. Conf. Microw., Radar and Wireless Communications*, May 2008, pp. 1–4.
- [4] M. Jessup and S. Simpson, "Circular Dual-Polarised Wideband Arrays for Direction Finding," in *Institution of Engineering and Technology Seminar on Wideband, Multiband Antennas and Arrays for Defence or Civil Applications*, March 2008, pp. 61–80.
- [5] M. Sharawi, F. Sultan, and D. Aloï, "An 8-Element Printed V-Shaped Circular Antenna Array for Power-Based Vehicular Localization," *IEEE Antennas and Wireless Propag. Lett.*, vol. 11, pp. 1133–1136, 2012.
- [6] S. E. Lipsky, *Microwave Passive Direction Finding*. SciTech Publishing, 1987.
- [7] D. J. L. Volakis, Ed., *Antenna Engineering Handbook*. McGraw-Hill, 2007, ch. 47. Direction Finding Antennas and Systems.
- [8] "Swiss National Frequency Allocation Plan and Specific Assignments," Federal Department of the Environment Transport, Energy, and Communication DETEC, Tech. Rep., 2014.
- [9] M. Esquiús-Morote, B. Fuchs, and J. R. Mosig, "Analytical model of a printed transition for SIW antennas," in *Proc. 6th European Conf. Antennas and Propag. (EuCAP)*, March 2012, pp. 414–417.
- [10] M. Esquiús-Morote, B. Fuchs, J.-F. Zürcher, and J. R. Mosig, "A Printed Transition for Matching Improvement of SIW Horn Antennas," *IEEE Trans. Antennas Propag.*, vol. 61, no. 4, pp. 1923–1930, 2013.
- [11] M. Esquiús-Morote, B. Fuchs, and J. R. Mosig, "A new type of printed Ku-band SIW horn antenna with enhanced performances," in *Proc. 17th Int. Symp. Antennas Propag. (ISAP)*, Nov. 2012, pp. 223–226.

- [12] —, “Enhancing the Performances of H-plane SIW Horn Antennas,” in *Proc. 7th European Conf. Antennas and Propag. (EuCAP)*, April 2013, pp. 2869–2872.
- [13] M. Esquiús-Morote, B. Fuchs, J.-F. Zürcher, and J. R. Mosig, “Novel Thin and Compact H-Plane SIW Horn Antenna,” *IEEE Trans. Antennas Propag.*, vol. 61, no. 6, pp. 2911–2920, 2013.
- [14] —, “Low-profile SIW Horn Antenna Array with Interconnection to MMICs,” in *Proc. 8th German Microwave Conference (GeMiC)*, March 2014, pp. 1–3.
- [15] —, “Low-profile Direction Finding System with SIW Horn Antennas for Vehicular Applications,” in *Proc. IEEE Antennas Propag. Society Int. Symp. (APSURSI)*, July 2014.
- [16] —, “Low-profile Direction Finding System at the Ku-band using SIW Horn Antennas,” *Microwave Journal*, 2014.
- [17] —, “Extended SIW for TE_{m0} and TE_{0n} Modes and Slotline Excitation of the TE_{01} Mode,” *IEEE Microw. Wireless Comp. Lett.*, vol. 23, no. 8, pp. 412–414, 2013.
- [18] M. Esquiús-Morote, M. Mattes, and J. R. Mosig, “Orthomode Transducer for Dual Polarized Substrate Integrated Circuits and Antennas,” in *Proc. 8th European Conf. Antennas and Propag. (EuCAP)*, April 2014.
- [19] —, “Orthomode Transducer and Dual-Polarized Horn Antenna in Substrate Integrated Technology,” *IEEE Trans. Antennas Propag.*, vol. 62, no. 10, 2014.
- [20] J. Perruisseau-Carrier, M. Tamagnone, J. S. Gómez-Díaz, M. Esquiús-Morote, and J. R. Mosig, “Resonant and leaky-wave reconfigurable antennas based on graphene plasmonics,” in *Proc. IEEE Antennas Propag. Society Int. Symp. (APSURSI)*, July 2013, pp. 136–137.
- [21] J. S. Gómez-Díaz, M. Esquiús-Morote, and J. Perruisseau-Carrier, “Plane wave excitation-detection of non-resonant plasmons along finite-width graphene strips,” *Opt. Express*, vol. 21, pp. 24 856–24 872, Oct. 2013.
- [22] M. Esquiús-Morote, J. S. Gómez-Díaz, and J. Perruisseau-Carrier, “Sinusoidally-Modulated Graphene Leaky-Wave Antenna for Electronic Beamscanning at THz,” *IEEE Trans. THz Sci. Technol.*, vol. 4, no. 1, pp. 116–122, Jan. 2014.
- [23] K. Wu, “Integration and interconnect techniques of planar and non-planar structures for microwave and millimeter-wave circuits - current status and future trend,” in *Asia-Pacific Microw. Conf. (APMC)*, vol. 2, Dec. 2001, pp. 411–416.
- [24] Z.-C. Hao, W. Hong, J.-X. Chen, X.-P. Chen, and K. Wu, “Compact super-wide bandpass substrate integrated waveguide (SIW) filters,” *IEEE Trans. Microw. Theory Tech.*, vol. 53, no. 9, pp. 2968–2977, Sept. 2005.
- [25] X. Chen, W. Hong, T. Cui, J. Chen, and K. Wu, “Substrate integrated waveguide (SIW) linear phase filter,” *IEEE Microw. Wireless Components Lett.*, vol. 15, no. 11, pp. 787–789, Nov. 2005.

- [26] W. Feng, W. Che, and K. Deng, "Compact Planar Magic-T Using E-Plane Substrate Integrated Waveguide (SIW) Power Divider and Slotline Transition," *IEEE Microw. Wireless Components Lett.*, vol. 20, no. 6, pp. 331–333, June 2010.
- [27] F. Giuppi, A. Georgiadis, A. Collado, M. Bozzi, and L. Perregrini, "Tunable SIW cavity backed active antenna oscillator," *Electron. Lett.*, vol. 46, no. 15, pp. 1053–1055, 2010.
- [28] K. Wu, D. Deslandes, and Y. Cassivi, "The substrate integrated circuits -a new concept for high-frequency electronics and optoelectronics," in *Proc. 6th Int. Conf. on Telecom. in Modern Satellite, Cable and Broadcasting Service.*, vol. 1, Oct. 2003.
- [29] M. Bozzi, A. Georgiadis, and K. Wu, "Review of substrate-integrated waveguide circuits and antennas," *IET Microw., Antennas Propag.*, vol. 5, no. 8, pp. 909–920, June 2011.
- [30] D. Deslandes and K. Wu, "Integrated microstrip and rectangular waveguide in planar form," *IEEE Microw. Wireless Comp.Lett.*, vol. 11, no. 2, pp. 68–70, Feb. 2001.
- [31] Y. Cassivi and K. Wu, "Substrate integrated circuits concept applied to the nonradiative dielectric guide," *IEE Proc. Microw., Antennas and Propag.*, pp. 424–433, Dec. 2005.
- [32] Z. Li and K. Wu, "24-GHz Frequency-Modulation Continuous-Wave Radar Front-End System-on-Substrate," *IEEE Trans. Microw. Theory Tech.*, vol. 56, no. 2, pp. 278–285, Feb. 2008.
- [33] Z.-Y. Zhang, Y. R. Wei, and K. Wu, "Broadband Millimeter-Wave Single Balanced Mixer and Its Applications to Substrate Integrated Wireless Systems," *IEEE Trans. Microw. Theory Tech.*, vol. 60, no. 3, pp. 660–669, March 2012.
- [34] K. K. Samanta, D. Stephens, and I. Robertson, "Design and performance of a 60-GHz multi-chip module receiver employing substrate integrated waveguides," *IET Microw., Antennas Propag.*, vol. 1, no. 5, pp. 961–967, Oct. 2007.
- [35] Z.-Y. Zhang, Y. R. Wei, and K. Wu, "60 GHz transceiver architectures deploying substrate integrated circuits (SICs) technique," in *European Wireless Technology Conf. (EuWIT)*, Sept. 2010, pp. 33–36.
- [36] J. Chen, W. Hong, Z. Hao, P. Yan, X. Zhu, J. Zhou, P. Chen, and K. Wu, "Development of a single board microwave sub-system based on substrate integrated waveguide (SIW) technology," in *IEEE MTT-S Int. Microw. Symp. Digest*, June 2012, pp. 1–3.
- [37] S. Hu, Y.-Z. Xiong, B. Zhang, L. Wang, T.-G. Lim, M. Je, and M. Madhian, "A SiGe BiCMOS Transmitter/Receiver Chipset With On-Chip SIW Antennas for Terahertz Applications," *IEEE Journal of Solid-State Circuits*, vol. 47, no. 11, pp. 2654–2664, Nov. 2012.
- [38] B. Liu, W. Hong, Z. Kuai, X. Yin, G. Luo, J. Chen, H. Tang, and K. Wu, "Substrate Integrated Waveguide (SIW) Monopulse Slot Antenna Array," *IEEE Trans. Antennas Propag.*, vol. 57, no. 1, pp. 275–279, Jan. 2009.
- [39] Y.-J. Cheng, W. Hong, and K. Wu, "94 GHz Substrate Integrated Monopulse Antenna Array," *IEEE Trans. Antennas Propag.*, vol. 60, no. 1, pp. 121–129, Jan 2012.

- [40] Y. J. Cheng, W. Hong, K. Wu, Z.-Q. Kuai, C. Yu, J. X. Chen, J. Zhou, and H.-J. Tang, "Substrate Integrated Waveguide (SIW) Rotman Lens and Its Ka-Band Multibeam Array Antenna Applications," *IEEE Trans. Antennas Propag.*, vol. 56, no. 8, pp. 2504–2513, Aug. 2008.
- [41] Y. J. Cheng, W. Hong, and K. Wu, "Millimeter-Wave Substrate Integrated Waveguide Multibeam Antenna Based on the Parabolic Reflector Principle," *IEEE Trans. Antennas Propag.*, vol. 56, no. 9, pp. 3055–3058, Sept 2008.
- [42] P. Chen, W. Hong, Z. Kuai, J. Xu, H. Wang, J. Chen, H. Tang, J. Zhou, and K. Wu, "A Multibeam Antenna Based on Substrate Integrated Waveguide Technology for MIMO Wireless Communications," *IEEE Trans. Antennas Propag.*, vol. 57, no. 6, pp. 1813–1821, June 2009.
- [43] Z. L. Li and K. Wu, "A new approach to integrated horn antenna," *Proc. Int. Symp. on Antenna Technology and Applied Electromagnetics*, pp. 535–538, June 2004.
- [44] W. Che, B. Fu, P. Yao, Y. L. Chow, and E. K. N. Yung, "A compact substrate integrated waveguide H-plane horn antenna with dielectric arc lens: Research Articles," *Int. J. RF Microw. Comput.-Aided Eng.*, vol. 17, pp. 473–479, Sept. 2007.
- [45] H. Wang, D.-G. Fang, B. Zhang, and W.-Q. Che, "Dielectric Loaded Substrate Integrated Waveguide (SIW) H-Plane Horn Antennas," *IEEE Trans. Antennas Propag.*, vol. 58, no. 3, pp. 640–647, March 2010.
- [46] M. Yousefbecki, A. A. Domenech, J. R. Mosig, and C. A. Fernandes, "Ku-band dielectric-loaded SIW horn for vertically-polarized multi-sector antennas," in *Proc. 6th European Conf. Antennas and Propag. (EuCAP)*, March 2012, pp. 2367–2371.
- [47] R. Suga, H. Nakano, Y. Hirachi, J. Hirokawa, and M. Ando, "Cost-Effective 60-GHz Antenna Package With End-Fire Radiation for Wireless File-Transfer System," *IEEE Trans. Microw. Theory Tech.*, vol. 58, no. 12, pp. 3989–3995, Dec. 2010.
- [48] —, "A Small Package With 46-dB Isolation Between Tx and Rx Antennas Suitable for 60-GHz WPAN Module," *IEEE Trans. Antennas Propag.*, vol. 60, no. 3, pp. 640–646, March 2012.
- [49] I. Flammia, B. Khani, and A. Stoehr, "Substrate integrated waveguide integration platform for 60 GHz indoor photonic transmitter," in *Proc. 8th German Microw. Conference (GeMIC)*, March 2014, pp. 1–4.
- [50] D. Deslandes and K. Wu, "Substrate Integrated Waveguide Leaky-Wave Antenna: Concept and Design Considerations," in *Proc. Asia Pacific Microw. Conf. (APMC)*, vol. 1, Dec. 2005.
- [51] M. Ettorre, R. Sauleau, and L. Le Coq, "Multi-Beam Multi-Layer Leaky-Wave SIW Pillbox Antenna for Millimeter-Wave Applications," *IEEE Trans. Antennas Propag.*, vol. 59, no. 4, pp. 1093–1100, April 2011.

-
- [52] F. Xu, K. Wu, and X. Zhang, "Periodic Leaky-Wave Antenna for Millimeter Wave Applications Based on Substrate Integrated Waveguide," *IEEE Trans. Antennas Propag.*, vol. 58, no. 2, pp. 340–347, Feb. 2010.
- [53] J. Liu, D. Jackson, and Y. Long, "Substrate Integrated Waveguide (SIW) Leaky-Wave Antenna With Transverse Slots," *IEEE Trans. Antennas Propag.*, vol. 60, no. 1, pp. 20–29, Jan. 2012.
- [54] A. Martinez-Ros, J. Gomez-Tornero, and G. Goussetis, "Planar Leaky-Wave Antenna With Flexible Control of the Complex Propagation Constant," *IEEE Trans. Antennas Propag.*, vol. 60, no. 3, pp. 1625–1630, March 2012.
- [55] G. Q. Luo, Z. F. Hu, Y. Liang, L. Y. Yu, and L.-L. Sun, "Development of Low Profile Cavity Backed Crossed Slot Antennas for Planar Integration," *IEEE Trans. Antennas Propag.*, vol. 57, no. 10, pp. 2972–2979, Oct. 2009.
- [56] M. Awida, S. Suleiman, and A. Fathy, "Substrate-Integrated Cavity-Backed Patch Arrays: A Low-Cost Approach for Bandwidth Enhancement," *IEEE Trans. Antennas Propag.*, vol. 59, no. 4, pp. 1155–1163, April 2011.
- [57] K. Gong, Z. N. Chen, X. Qing, P. Chen, and W. Hong, "Substrate Integrated Waveguide Cavity-Backed Wide Slot Antenna for 60-GHz Bands," *IEEE Trans. Antennas Propag.*, vol. 60, no. 12, pp. 6023–6026, Dec. 2012.
- [58] M. Awida, S. Suleiman, and A. Fathy, "Dual-polarized low-profile 16x4 SIW cavity-backed patch array for direct broadcast satellite applications," in *IEEE Radio and Wireless Symp. (RWS)*, Jan 2013, pp. 115–117.
- [59] Z.-C. Hao, W. Hong, J. Chen, X.-P. Chen, and K. Wu, "A novel feeding technique for antipodal linearly tapered slot antenna array," in *IEEE MTT-S Int. Microw. Symp. Digest*, June 2005, p. 3.
- [60] Y. J. Cheng and Y. Fan, "Millimeter-Wave Miniaturized Substrate Integrated Multibeam Antenna," *IEEE Trans. Antennas Propag.*, vol. 59, no. 12, pp. 4840–4844, Dec. 2011.
- [61] B. El Khatib, T. Djerafi, and K. Wu, "Three-Dimensional Architecture of Substrate Integrated Waveguide Feeder for Fermi Tapered Slot Antenna Array Applications," *IEEE Trans. Antennas Propag.*, vol. 60, no. 10, pp. 4610–4618, Oct 2012.
- [62] N. Jastram and D. Filipovic, "PCB-Based Prototyping of 3-D Micromachined RF Subsystems," *IEEE Trans. Antennas Propag.*, vol. 62, no. 1, pp. 420–429, Jan. 2014.
- [63] Z. Zhang, K. Wu, and N. Yang, "Broadband millimeter-wave quasi-Yagi antenna using Substrate Integrated Waveguide technique," in *IEEE Radio and Wireless Sym.*, Jan. 2008, pp. 671–674.
- [64] X. Y. Wu, L. Akhoondzadeh-Asl, Z. Wang, and P. Hall, "Novel Yagi-Uda antennas for on-body communication at 60GHz," in *Loughborough Antennas and Propag. Conf. (LAPC)*, Nov. 2010, pp. 153–156.

- [65] S. Yu, W. Hong, C. Yu, H. Tang, J. Chen, and Z. Kuai, "Integrated millimeter wave filter for Q-LINKPAN application," in *Proc. 6th European Conf. Antennas Propag. (EUCAP)*, March 2012, pp. 1333–1336.
- [66] A. Patrovsky and K. Wu, "94-GHz Planar Dielectric Rod Antenna With Substrate Integrated Image Guide (SIIG) Feeding," *IEEE Antennas Wireless Propag. Lett.*, vol. 5, no. 1, pp. 435–437, Dec. 2006.
- [67] —, "Active 60 GHz front-end with integrated dielectric antenna," *Electron. Lett.*, vol. 45, no. 15, pp. 765–766, July 2009.
- [68] N. Ghassemi and K. Wu, "Planar Dielectric Rod Antenna for Gigabyte Chip-to-Chip Communication," *IEEE Trans. Antennas Propag.*, vol. 60, no. 10, pp. 4924–4928, Oct. 2012.
- [69] T. Lambard, O. Lafond, M. Himdi, H. Jeuland, S. Bolioli, and L. Le Coq, "Ka-Band Phased Array Antenna for High-Data-Rate SATCOM," *IEEE Antennas and Wireless Propag. Lett.*, vol. 11, pp. 256–259, 2012.
- [70] M. Sharawi and D. Aloï, "Design of an 8-element switched mode circular antenna array for vehicular direction finding," in *IEEE 12th Annual Wireless and Microw. Technology Conf. (WAMICON)*, April 2011, pp. 1–4.
- [71] P.-C. Chiang, W.-J. Liao, Y.-T. Tu, and H.-C. Liu, "Implementation of direction-of-arrival estimation using rotman lens array antenna," in *Proc. URSI Int. Symp. on Electromagnetic Theory (EMTS)*, May 2013, pp. 855–858.
- [72] A. Olver, P. Clarricoats, A. Kishk, and L. Shafai, *Microwave Horns and Feeds*. IEE, 1994, ch. 9.5.8.
- [73] S. Podilchak, A. Freundorfer, and Y. Antar, "Planar antennas for far-field beam steering at end-fire using directive surface-wave launchers," in *ANTEM/URSI 13th Int. Symp. on Antenna Technology and Applied Electromagnetics and the Canadian Radio Science Meeting*, Feb. 2009, pp. 1–4.
- [74] S. Podilchak, A. P. Freundorfer, and Y. Antar, "Planar antenna for directive beam steering at end-fire using an array of surface-wave launchers," *Electron. Lett.*, vol. 45, no. 9, pp. 444–445, April 2009.
- [75] A. Kishk and L. Shafai, "The effect of various parameters of circular microstrip antennas on their radiation efficiency and the mode excitation," *IEEE Trans. Antennas Propag.*, vol. 34, no. 8, pp. 969–976, Aug. 1986.
- [76] R. Vaughan, "Two-port higher mode circular microstrip antennas," *IEEE Trans. Antennas Propag.*, vol. 36, no. 3, March 1988.
- [77] N. Llombart, A. Neto, G. Gerini, and P. de Maagt, "Planar circularly symmetric EBG structures for reducing surface waves in printed antennas," *IEEE Trans. Antennas Propag.*, vol. 53, no. 10, pp. 3210–3218, Oct 2005.

- [78] S. Podilchak, A. Freundorfer, and Y. Antar, "Planar surface-wave sources and metallic grating lenses for controlled guided-wave propagation," *IEEE Antennas Wireless Propag. Lett.*, vol. 8, pp. 371–374, 2009.
- [79] H. Hammad, Y. Antar, A. Freundorfer, and S. Mahmoud, "Uni-planar CPW-fed slot launchers for efficient TM₀ surface-wave excitation," *IEEE Trans. Microw. Theory Tech.*, vol. 51, no. 4, pp. 1234–1240, April 2003.
- [80] C. A. Balanis, *Antenna Theory – Analysis and Design*, 3rd ed. Wiley, 2005.
- [81] Z. Li, X.-P. Chen, and K. Wu, "A Surface Mountable Pyramidal Horn Antenna and Transition to Substrate Integrated Waveguide," in *Int. Symp. on Signals, Systems and Electronics*, Feb. 2007, pp. 607–610.
- [82] K. Yazdandoost and D. Gharpure, "Simple formula for calculation of the resonant frequency of a rectangular microstrip antenna," in *Proc. IEEE 5th Int. Symp. on Spread Spectrum Techniques and Applications*, vol. 2, Sept. 1998, pp. 604–605.
- [83] J.-S. Hong and M. Lancaster, *Microstrip filters for RF/microwave applications*. Wiley, 2001, ch. 8.2.
- [84] S. Bedair, "Characteristics of Some Asymmetrical Coupled Transmission Lines (Short Paper)," *IEEE Trans. Microw. Theory Tech.*, vol. 32, no. 1, pp. 108–110, Jan. 1984.
- [85] M. H. Bao, *Handbook of sensors and actuators*, 1st ed. University of Twente, 2000, vol. 8, p. 144.
- [86] A. Abbosh and M. Bialkowski, "Deriving characteristics of the slotline using the conformal mapping technique," in *17th Int. Conf. on Microw., Radar and Wireless Communications*, May 2008, pp. 1–4.
- [87] P. Benedek and P. Silvester, "Capacitance of Parallel Rectangular Plates Separated by a Dielectric Sheet," *IEEE Trans. Microw. Theory Tech.*, vol. 20, no. 8, pp. 504–510, Aug. 1972.
- [88] F. Ishihara and S. Iiguchi, "Equivalent characteristic impedance formula of waveguide and its applications," *Electronics and Communications in Japan (Part II: Electronics)*, vol. 75, pp. 54–66, 1992.
- [89] J. R. James and P. Hall, *Handbook of microstrip antenna 1*. IEE, 1989.
- [90] D. Deslandes, "Design equations for tapered microstrip-to-Substrate Integrated Waveguide transitions," in *IEEE MTT-S Int. Microw. Symp. Digest*, May 2010, pp. 704–707.
- [91] T.-S. Horng, S.-C. Wu, H.-Y. Yang, and N. Alexopoulos, "A generalized method for distinguishing between radiation and surface-wave losses in microstrip discontinuities," *IEEE Trans. Microw. Theory Tech.*, vol. 38, no. 12, pp. 1800–1807, Dec. 1990.
- [92] T. Bird, "Mode matching analysis of arrays of stepped rectangular horns and application to satellite antenna design," in *Proc. 7th Int. Conf. IEE Antennas Propag. (ICAP)*, vol. 2, April 1991, pp. 849–852.

- [93] A. Bhattacharyya and G. Goyette, "Step-horn antenna with high aperture efficiency and low cross-polarisation," *Electron. Lett.*, vol. 38, no. 24, pp. 1495–1496, Nov. 2002.
- [94] —, "A novel horn radiator with high aperture efficiency and low cross-polarization and applications in arrays and multibeam reflector antennas," *IEEE Trans. Antennas Propag.*, vol. 52, no. 11, pp. 2850–2859, Nov. 2004.
- [95] K. Song, Y. Fan, and Y. Zhang, "Eight-Way Substrate Integrated Waveguide Power Divider With Low Insertion Loss," *IEEE Trans. Microw. Theory Tech.*, vol. 56, no. 6, pp. 1473–1477, June 2008.
- [96] PLATH GmbH, "DFA 2440 DF Antenna," <http://www.plath.de/>.
- [97] SPX Corporation, "TCI Model 645 Compact DF Antenna," <http://www.spx.com/>.
- [98] Poynting Antennas, "DF-A0095 Wideband Portable DF Antenna," <http://www.poyntingdefence.com/>.
- [99] A. Suntives and R. Abhari, "Transition Structures for 3-D Integration of Substrate Integrated Waveguide Interconnects," *IEEE Microw. Wireless Comp. Lett.*, vol. 17, no. 10, pp. 697–699, Oct. 2007.
- [100] F. Bauer and W. Menzel, "A wideband transition from substrate integrated waveguide to differential microstrip lines in multilayer substrates," in *Proc. 40th European Microw. Conf. (EuMC)*, Sept. 2010, pp. 811–813.
- [101] V. Zhurbenko, *Passive Microwave Components and Antennas*. InTech, 2010, ch. 11.
- [102] S. Z. Zhang, Z. Y. Yu, and C. Li, "Elliptic function filters designed in LTCC," in *Proc. Asia Pacific Microw. Conf. (APMC)*, vol. 1, Dec. 2005, p. 3.
- [103] Hittite Microwave Corporation, "www.hittite.com."
- [104] P. Horowitz and W. Hill, *The Art Of Electronics*, 2nd ed. Cambridge University Press, 1989, ch. 13.
- [105] P. Dixon, "Cavity-Resonance Dampening," *IEEE Microw. Magazine*, vol. 84, no. 2, pp. 74–84, June 2005.
- [106] —, "Theory and application of RF/Microwave absorbers," Emerson & Cuming Microwave Products Tech Notes, Tech. Rep., 2012.
- [107] Emerson & Cuming Microwave Products, "www.eccosorb.com."
- [108] D. Deslandes, M. Bozzi, P. Arcioni, and K. Wu, "Substrate integrated slab waveguide (SISW) for wideband microwave applications," in *IEEE MTT-S Int. Microw. Symp. Digest*, vol. 2, June 2003, pp. 1103–1106 vol.2.
- [109] A. Patrovsky and K. Wu, "Substrate integrated image guide (SIIG)-a planar dielectric waveguide technology for millimeter-wave applications," *IEEE Trans. Microw. Theory Techn.*, vol. 54, no. 6, pp. 2872–2879, June 2006.

-
- [110] W. Hong, B. Liu, Y. Wang, Q. Lai, H. Tang, X.-X. Yin, Y.-D. Dong, Y. Zhang, and K. Wu, "Half Mode Substrate Integrated Waveguide: A New Guided Wave Structure for Microwave and Millimeter Wave Application," in *Proc. Joint 31st Int. Conf. Infrared Millimeter Waves and 14th Int. Conf. THz Electronics (IRMMW-THz)*, Sept. 2006, pp. 219–219.
- [111] T. Yoneyama and S. Nishida, "Nonradiative Dielectric Waveguide for Millimeter-Wave Integrated Circuits," *IEEE Trans. Microw. Theory Tech.*, vol. 29, no. 11, pp. 1188–1192, Nov. 1981.
- [112] N. Ghassemi and K. Wu, "Planar Dielectric Rod Antenna for Gigabyte Chip-to-Chip Communication," *IEEE Trans. Antennas Propag.*, vol. 60, no. 10, pp. 4924–4928, 2012.
- [113] P. Mondal and K. Wu, "A Leaky-Wave Antenna in Substrate Integrated Non-Radiative Dielectric (SINRD) Waveguide With Controllable Scanning Rate," *IEEE Trans. Antennas Propag.*, vol. 61, no. 4, pp. 2294–2297, 2013.
- [114] J. Attari, T. Djerafi, and K. Wu, "Planar orthogonal mode transducer based on orthogonal LSM₁₀ and TE₁₀ modal fields of co-layered image SINRD (iSINRD) and SIW guides," in *European Microw. Conf. (EuMC)*, Oct. 2013, pp. 597–600.
- [115] —, "Fast and accurate simulation of novel millimeter-wave circuits based on commercial software package," *IEEE Microwave Magazine*, vol. 14, no. 2, pp. 106–111, March 2013.
- [116] J. Tang, D. Deslandes, and K. Wu, "Suppression of spurious modes for performance enhancement of hybrid planar/NRD-guide integrated circuits," *IEE Proc. Microw., Antennas and Propag.*, vol. 150, no. 4, pp. 285–289, Aug. 2003.
- [117] F. Xu and K. Wu, "Substrate Integrated Nonradiative Dielectric Waveguide Structures Directly Fabricated on Printed Circuit Boards and Metallized Dielectric Layers," *IEEE Trans. Microw. Theory Tech.*, vol. 59, no. 12, pp. 3076–3086, Dec. 2011.
- [118] D. Deslandes and K. Wu, "Accurate modeling, wave mechanisms, and design considerations of a substrate integrated waveguide," *IEEE Trans. Microw. Theory Tech.*, vol. 54, no. 6, pp. 2516–2526, 2006.
- [119] T. Itoh, *Numerical Techniques for Microwave and Millimeter-Wave Passive Structures*. Wiley, 1989, ch. 11.
- [120] L. Lewin, *Theory of waveguides: Techniques of the solution of waveguide problems*. Newnes-Butterworths, 1975, ch. 5, p. 145.
- [121] A. Sanchez and A. Oliner, "A New Leaky Waveguide for Millimeter Waves Using Nonradiative Dielectric (NRD) Waveguide-Part I: Accurate Theory," *IEEE Trans. Microw. Theory Tech.*, vol. 35, no. 8, pp. 737–747, 1987.
- [122] N. Marcuvitz, *Waveguide Handbook*. Boston Technical Publishers, INC., 1964.
- [123] J. Attari, T. Djerafi, and K. Wu, "Fast and Accurate Simulation of Novel Millimeter-Wave Circuits Based on Commercial Software Package," *IEEE Microw. Magazine*, vol. 14, no. 2, pp. 106–111, 2013.

- [124] Y. Cassivi and K. Wu, "Substrate integrated nonradiative dielectric waveguide," *IEEE Microw. Wireless Comp. Lett.*, vol. 14, no. 3, pp. 89–91, 2004.
- [125] K. Wu, D. Deslandes, and Y. Cassivi, "The substrate integrated circuits - a new concept for high-frequency electronics and optoelectronics," in *Proc. 6th Int. Conf. TELSIKS*, vol. 1, Oct. 2003, pp. III–X.
- [126] N. Grigoropoulos, S. Tse, and P. Young, "Non-radiative perforated dielectric waveguide (NRPD) with integrated transition to slotline for millimetre-wave components," in *High Frequency Postgraduate Student Colloquium*, Sept. 2004, pp. 127 – 131.
- [127] B. Shuppert, "Microstrip/slotline transitions: modeling and experimental investigation," *IEEE Trans. Microw. Theory Techn.*, vol. 36, no. 8, pp. 1272–1282, 1988.
- [128] J. Coonrod, "High Frequency Materials: Product Selector Guide," Rogers Corp., Tech. Rep., 2013.
- [129] —, "General information of dielectric constants for circuit design using Rogers high frequency materials," Rogers Corp., Tech. Rep., 2011.
- [130] J. Uher, J. Bornemann, and U. Rosenberg, Eds., *Waveguide Components for Antenna Feed Systems: Theory and CAD*. Artech House, 1993.
- [131] O. Peverini, G. Virone, R. Tascone, and G. Addamo, *Advances in Satellite Communications*. INTECH, 2011, ch. Passive Microwave Feed-Chains for High-Capacity Satellite Communications Systems, *Advances in Satellite Communications*.
- [132] O. Peverini, G. Virone, G. Addamo, and R. Tascone, "Development of passive microwave antenna-feed systems for wide-band dual-polarisation receivers," *IET Microw., Antennas Propag.*, vol. 5, no. 8, pp. 1008–1015, June 2011.
- [133] O. Peverini, R. Tascone, G. Virone, A. Olivieri, and R. Orta, "Orthomode transducer for millimeter-wave correlation receivers," *IEEE Trans. Microw. Theory Techn.*, vol. 54, no. 5, pp. 2042–2049, May 2006.
- [134] R. Garcia, F. Mayol, J. Montero, and A. Culebras, "Circular polarization feed with dual-frequency OMT-based turnstile junction," *IEEE Antennas Propag. Magazine*, vol. 53, no. 1, pp. 226–236, Feb 2011.
- [135] D. Dousset, S. Claude, and K. Wu, "A Compact High-Performance Orthomode Transducer for the Atacama Large Millimeter Array (ALMA) Band 1 (31-45 GHz)," *IEEE Access*, vol. 1, pp. 480–487, 2013.
- [136] J. Ruiz-Cruz, J. R. Montejo-Garai, and J. Rebollar, "Optimal configurations for integrated antenna feeders with linear dual-polarisation and multiple frequency bands," *IET Microw., Antennas Propag.*, vol. 5, no. 8, pp. 1016–1022, 2011.
- [137] P.-Y. Qin, Y. Guo, and C.-H. Liang, "Effect of Antenna Polarization Diversity on MIMO System Capacity," *IEEE Antennas Wireless Propag. Lett.*, vol. 9, pp. 1092–1095, 2010.

-
- [138] A. Morshedi and M. Torlak, "Measured Comparison of Dual-Branch Signaling Over Space and Polarization Diversity," *IEEE Trans. Antennas Propag.*, vol. 59, no. 5, pp. 1678–1687, 2011.
- [139] P. K. Grimes, O. G. King, G. Yassin, and M. E. Jones, "Compact broadband planar orthomode transducer," *Electronics Lett.*, vol. 43, no. 21, pp. 1146–1147, 2007.
- [140] M. Morgan, J. R. Fisher, and T. Boyd, "Compact Orthomode Transducers Using Digital Polarization Synthesis," *IEEE Trans. Microw. Theory Techn.*, vol. 58, no. 12, pp. 3666–3676, 2010.
- [141] Y. Tao and Z.-X. Shen, "Design of Compact Orthomode Transducers," in *IEEE MTT-S Int. Microw. Workshop Series on the Art of Miniaturizing RF and Microw. Passive Components*, Dec. 2008, pp. 38–42.
- [142] Y. Tao and Z. Shen, "Design of broadband planar orthomode transducers using substrate integrated waveguide," in *Proc. Asia Pacific Microw. Conf. (APMC)*, Dec. 2008, pp. 1–4.
- [143] M. Mandal, K. Wu, and D. Deslandes, "A compact planar orthomode transducer," in *IEEE MTT-S Int. Microw. Symp. Digest*, June 2011, pp. 1–4.
- [144] A. Boifot, E. Lier, and T. Schaug-Pettersen, "Simple and broadband orthomode transducer (antenna feed)," *IEE Proc. H Microw., Antennas Propag.*, vol. 137, no. 6, pp. 396–400, Dec. 1990.
- [145] A. Navarrini and R. Plambeck, "A turnstile junction waveguide orthomode transducer," *IEEE Trans. Microw. Theory Techn.*, vol. 54, no. 1, pp. 272–277, Jan. 2006.
- [146] J. Coonrod, "General Information of Dielectric Constants for Circuit Design using Rogers High Frequency Materials," Rogers Corp., Tech. Rep., 2010.
- [147] J. Hirokawa, K. Sakurai, M. Ando, and N. Goto, "An analysis of a waveguide T-junction with an inductive post," *IEEE Trans. Microw. Theory Techn.*, vol. 39, no. 3, pp. 563–566, 1991.
- [148] S. Germain, D. Deslandes, and K. Wu, "Development of substrate integrated waveguide power dividers," in *Proc. IEEE Canadian Conf. on Electrical and Computer Engineering*, vol. 3, May 2003, pp. 1921–1924.
- [149] A. Suntives and R. Abhari, "Design and Application of Multimode Substrate Integrated Waveguides in Parallel Multichannel Signaling Systems," *IEEE Trans. Microw. Theory Techn.*, vol. 57, no. 6, pp. 1563–1571, 2009.
- [150] I. Flammia, B. Khani, and A. Stohr, "Substrate integrated waveguide antenna for 60 GHz Radio-over-Fiber transmitter," in *38th Int. Conf. Infrared, Millimeter and Terahertz Waves (IRMMW-THz)*, Sept. 2013, pp. 1–2.
- [151] T. Vaupel, "Efficient Characterization of Combined Microstrip/Substrate Integrated Waveguide Structures and Antennas in the MM-Wave Region," in *5th. COST VISTA Workshop*, Sept. 2013.

- [152] I. Flammia, B. Khani, and A. Stoehr, "Substrate Integrated Waveguide Integration Platform for 60 GHz Indoor Photonic Transmitter," in *Proc. 8th German Microwave Conference (GeMIC)*, March 2014, pp. 1–4.
- [153] S. Razafimahatratra, J. Sarrazin, A. Benlarbi-Delai, and P. D. Doncker, "Horn antenna design for BAN millimeter wave on-body communication," in *Proc. IEEE Antennas Propag. Society Int. Symp. (APSURSI)*, July 2014.
- [154] C. A. Balanis, *Advanced Engineering Electromagnetics*, 1st ed. Wiley, 1989, ch. 8.
- [155] G. Conciauro, M. Guglielmi, and R. Sorrentino, *Advance Modal Analysis*. John Wiley & Sons Ltd., 2000, ch. 1.
- [156] P. H. Siegel, "Terahertz technology," *IEEE Trans. Microw. Theory Techn.*, vol. 50, pp. 910–928, 2002.
- [157] M. Dragoman, A. A. Muller, D. Dragoman, F. Coccetti, and R. Plana, "Terahertz antenna based on graphene," *Journal of Applied Physics*, vol. 107, p. 104313, 2010.
- [158] Y. Huang, L. S. Wu, M. Tang, and J. Mao, "Design of a Beam Reconfigurable THz Antenna With Graphene-Based Switchable High-Impedance Surface," *IEEE Trans. on Nanotechnol.*, vol. 11, no. 4, pp. 836–842, 2012.
- [159] M. Jablan, H. Buljan, and M. Soljagic, "Plasmonics in graphene at infrared frequencies," *Physical review B*, vol. 80, p. 245435, 2009.
- [160] J. S. Gómez-Díaz and J. Perruisseau-Carrier, "Propagation of Hybrid transverse magnetic-transverse electric Plasmons on Magnetically-Biased Graphene Sheets," *Journal of Applied Physics*, vol. 112, p. 124906, 2012.
- [161] M. Tamagnone, J. S. Gómez-Díaz, J. R. Mosig, and J. Perruisseau-Carrier, "Reconfigurable thz plasmonic antenna concept using a graphene stack," *Applied Physics Lett.*, vol. 101, p. 214102, 2012.
- [162] R. Filter, M. Farhat, M. Steglich, R. Alaee, C. Rockstuhl, and F. Lederer, "Tunable Graphene Antennas for Selective Enhancement of THz-Emission," *Opt. Express*, vol. 21, pp. 3737–3745, 2013.
- [163] E. Carrasco and J. Perruisseau-Carrier, "Tunable graphene reflective cells for THz reflectarrays and generalized law of reflection," *Applied Physics Lett.*, vol. 102, pp. 104–103, 2013.
- [164] W. Gao, J. Shu, C. Qiu, and Q. Xu, "Excitation of plasmonic waves in graphene by guided-mode resonances," *ACS nano*, vol. 6, pp. 7806–7813, 2012.
- [165] N. M. Peres, Y. V. Bludox, A. Ferreira, and M. I. Vasilevskiy, "Exact solution for square-wave grating covered with graphene: Surface plasmon-polaritons in the THz range," *Arxiv preprint*, vol. 1211.6358v1, 2012.
- [166] Y. V. Bludox, A. Ferreira, N. M. Peres, and M. I. Vasilevskiy, "A primer on surface plasmon-polaritons in graphene," *Arxiv preprint*, vol. 1302.2317v1, 2013.

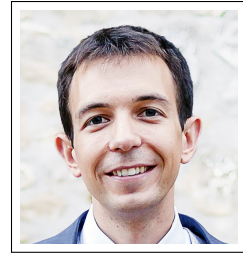
- [167] B. S. J. F. Federici, F. Huang, D. Gary, R. Barat, F. Oliveira, and D. Zimdars, "Thz imaging and sensing for security applications- explosives, weapons and drugs," *Semiconductor Science and Technology*, vol. 20, pp. 266–280, 2005.
- [168] A. Rogalski, "Infrared detectors: status and trends," *Progress in quantum electronics*, vol. 27, no. 2, pp. 59–210, 2003.
- [169] V. Lubecke, K. Mizuno, and G. Rebeiz, "Micromachining for terahertz applications," *IEEE Trans. Microw. Theory Tech.*, vol. 46, no. 11, pp. 1821–1831, 1998.
- [170] A. Oliner and A. Hessel, "Guided waves on sinusoidally-modulated reactance surfaces," *IRE Trans. Antennas Propag.*, vol. AP-7, pp. 201–208, 1959.
- [171] A. M. Patel and A. Grbic, "A Printed Leaky-Wave Antenna Based on a Sinusoidally-Modulated Reactance Surface," *IEEE Trans. Antennas Propag.*, vol. 59, no. 6, pp. 2087–2096, 2011.
- [172] S. Maci, G. Minatti, M. Casaletti, and M. Bosiljevac, "Metasurfing: Addressing Waves on Impenetrable Metasurfaces," *IEEE Antennas Wireless Propag. Lett.*, vol. 10, pp. 1499–1502, 2011.
- [173] K. Geim and K. S. Novoselov, "The rise of graphene," *Nature materials*, vol. 6, pp. 183–91, 2007.
- [174] A. A. Oliner and D. R. Jackson, "Leaky-wave antennas," in *Antenna Engineering Handbook*, 4th ed., J. L. Volakis, Ed. New York: McGraw-Hill, 2007.
- [175] V. P. Gusynin, S. G. Sharapov, and J. B. Carbotte, "On the universal ac optical background in graphene," *New J. Physics*, vol. 11, p. 095013, 2009.
- [176] G. W. Hanson, "Dyadic green's functions for an anisotropic non-local model of biased graphene," *IEEE Trans. Antennas Propag.*, vol. 56, no. 3, pp. 747–757, March 2008.
- [177] T. Fang, A. Konar, H. Xiang, and D. Jena, "Carrier statistics and quantum capacitance of graphene sheets and ribbons," *Appl. Phys. Lett.*, vol. 91, p. 092109, 2007.
- [178] G. Minatti, F. Caminita, M. Casaletti, and S. Maci, "Spiral Leaky-Wave Antennas Based on Modulated Surface Impedance," *IEEE Trans. Antennas Propag.*, vol. 59, no. 12, 2011.
- [179] T. Itoh, *Numerical Techniques for Microwave and Millimeter-Wave Passive Structures*. Wiley-Interscience, 1989.
- [180] R. J. Pryputniewicz, *MEMS SUMMiTV technology*. Worcester Polytechnic Institute, Worcester, MA, 2002.
- [181] B. H. Fong, J. S. Colburn, J. J. Ottusch, J. L. Visher, and D. F. Sievenpiper, "Scalar and Tensor Holographic Artificial Impedance Surfaces," *IEEE Trans. Antennas Propag.*, vol. 58, no. 10, pp. 3212–3221, 2010.
- [182] M. Naftaly and R. E. Miles, "Terahertz Time-Domain Spectroscopy for Material Characterization," *Proceedings of the IEEE*, vol. 95, no. 8, pp. 1658–1665, 2007.

- [183] C. R. Dean, A. F. Young, I. Meric, C. Lee, L. Wang, S. Sorgenfrei, K. Watanabe, T. Taniguchi, P. Kim, K. L. Shepard, and J. Hone, "Boron nitride substrates for high-quality graphene electronics," *Nature Nanotech.*, no. 5, pp. 722–726, 2010.
- [184] K. Bolotin, K. Sikes, Z. Jiang, M. Klima, G. Fudenberg, J. Hone, P. Kim, and H. Stormer, "Ultrahigh electron mobility in suspended graphene," *Solid State Communications*, vol. 146, pp. 351–355, March 2008.
- [185] J. L. Gómez-Tornero, G. Goussetis, and A. Álvarez-Melcón, "Correction of dielectric losses in practical leaky-wave antenna designs," *Journal of Electromagnetic Waves and Applications*, vol. 21, no. 8, pp. 1025–1036, 2007.
- [186] E. Forati and G. W. Hanson, "Soft-boundary graphene nanoribbon formed by a graphene sheet above a perturbed ground plane: conductivity profile and SPP modal current distribution," *J. Opt.*, vol. 15, p. 114006, 2013.
- [187] S. Ghosh, I. Calizo, D. Teweldebrhan, E. P. Pokatilov, D. L. Nika, A. A. Balandin, W. B. dn F. Miao, and C. N. Lau, "Extremely high thermal conductivity of graphene: Prospects for thermal management applications in nanoelectronic circuits," *Appl. Phys. Lett.*, vol. 92, p. 151911, 2008.

Marc Esquius Morote

*Telecommunication and Electrical
Engineer*

Av. du Tir-Fédéral 27, Ecublens
1024, Switzerland
☎ +41 (0)787059273
✉ mesquius@gmail.com
Nationality: Spanish
Date of birth: 28.11.1986



Education

- 08/2011 **PhD at the Laboratory of Electromagnetics and Acoustics (LEMA)**,
11/2014 *EPFL*, Lausanne, Switzerland.
- Design and manufacturing of planar and substrate integrated antennas and other microwave devices for widespread commercial solutions
 - Design of communication systems including high frequency electronics (MMICs, etc.)
 - Writing of technical proposals and projects involving AESA radars, wireless power transfer and several antenna systems for the European Space Agency (ESA)
- 09/2008 **Master degree in Electronic Engineering**, *UPC*, Barcelona, Spain.
03/2011 Microelectronic design, digital systems and power electronics.
Master thesis in IEEE 802.11s Mesh Networking.
- 09/2004 **Bachelor and Master degrees in Telecommunications Engineering**, *UPC*,
11/2010 Barcelona, Spain.
Communication theory, signal processing, electromagnetics and telematics.
Awarded as one of the ten best students of the promotion.
- 03/2010 **Master Thesis in Telecommunication Engineering**, *Tongji University*,
11/2010 Shanghai, People's Republic of China.
Research in Mobile Ad-hoc Networks (MANET) awarded with Distinction.
Chinese inter-cultural communication, history and culture lectures.

Professional experiences

- 09/2009 **Technician in antenna design**, *Urbiotica*, Barcelona, Spain.
02/2010 Design of antennas for sensor networks at 860 Mhz and 2.4 GHz.
- 01/2008 **Scholarship in antenna design**, *AntennaLab*, *UPC*, Barcelona, Spain.
01/2010 Research in different antenna topologies to be used in applications between 30 MHz and 3 GHz (direction finding, naval communications, etc.)
- 10/2008 **Vice-President for Public Relations**, *BEST (Board of European Students of
10/2009 Technology)*, Barcelona, Spain.
Volunteer work (Management, Education): organization of job fairs, educational courses and coordination of the promotion and marketing campaigns.
- 08/2008 **President and Chief Project Officer**, *AUCCOOP (Association of University
09/2009 Students for Cooperation)*, Barcelona, Spain.
Volunteer work (Telematics, Management): coordination of several cooperation projects with counterparts in South America.
- 05/2007 **Member of a cooperation project**, *UTEM*, (Universidad Tecnológica Metropol-
08/2007 litana del Estado de Chile), Chile.
Development of telecommunication networks to bring internet connectivity to rural schools in the south of Chile.

Professional Trainings and Courses

04/02/2013 **Antenna Project Management**, *École Polytechnique Fédérale de Lausanne*,
08/02/2013 EPFL, Lausanne, Switzerland.

Overview on the technical key steps of a project: how to clarify the requirements of a customer, make trade-offs, propose the best antenna system to fulfil the specifications, budget and timeframe estimations, etc.

12/03/2012 **Antennas for Space Applications**, *European Space Agency (ESA) Research*
16/03/2012 *Centre*, ESTEC, Noordwijk, Netherlands.

Overview of design approaches, constraints and technical solutions for space antenna systems in the applications of Telecommunication, Earth Observation and Science.

Languages

Catalan **Native language**

Spanish **Native language**

English **Full professional proficiency** *level C2 (according to the CEFR)*

French **Full professional proficiency** *level C1 (according to the CEFR)*

German **Intermediate proficiency** *level B2 (according to the CEFR)*

Chinese **Elementary proficiency** *level A1/A2 (according to the CEFR)*

Social skills and competences

Teamwork Wide experience in coordination and teamwork acquired as a member of different research teams and students' associations.

Mediating Oral presentations to industrial partners and in academic conferences were common skills activities during my research period. Public speeches and promotion events were also the main tasks as Vice-President for PR in BEST.

Intercultural Experience at working in multicultural environments at European, South American skills and Asiatic level.

Organizational skills and competences

- Experience in planning, organizing and evaluating projects between different countries dealing with both universities and companies.
- Experience in organizing and promoting job fairs, engineering competitions and educational events at European level.

Computer skills and competences

- Fully competent in full-wave electromagnetic solvers Ansys HFSS and CST Microwave Studio.
- Knowledge of programming languages C++, Matlab, VHDL.
- Strong background in computer systems, hardware and software.

Hobbies

- Oil painting (8 years of lectures) and graphic design (fully competent in Adobe Photoshop and Illustrator).
- Travelling, cultural experiences, hiking, cycling, tennis playing.

List of Publications

Refereed Journal Papers

- [J01] **M. Esquiús-Morote**, B. Fuchs, J.-F. Zürcher and J. R. Mosig, "A Printed Transition for Matching Improvement of SIW Horn Antennas", *IEEE Trans. Antennas Propag.*, vol. 61, no. 4, pp. 1923-1930, April 2013.
- [J02] **M. Esquiús-Morote**, B. Fuchs, J.-F. Zürcher and J. R. Mosig, "Novel Thin and Compact H-Plane SIW Horn Antenna", *IEEE Trans. Antennas Propag.*, vol. 61, no. 6, pp. 2911-2920, June 2013.
- [J03] **M. Esquiús-Morote**, B. Fuchs, J.-F. Zürcher and J. R. Mosig, "Extended SIW for TE_{m0} and TE_{0n} Modes and Slotline Excitation for the TE_{01} Mode", *IEEE Microw. Wireless Compon. Lett.*, vol. 23, no. 8, pp. 412-414, Aug. 2013.
- [J04] J. S. Gómez-Díaz, **M. Esquiús-Morote** and J. Perruisseau-Carrier, "Plane wave excitation-detection of non-resonant plasmons along finite-width graphene strips", *Opt. Express*, vol. 21, pp. 24856-24872, Oct. 2013.
- [J05] **M. Esquiús-Morote**, J. S. Gómez-Díaz and J. Perruisseau-Carrier, "Sinusoidally-Modulated Graphene Leaky-Wave Antenna for Electronic Beamscanning at THz", *IEEE Trans. THz Sci. Technol.*, vol.4, no.1, pp.116-122, Jan. 2014.
- [J06] **M. Esquiús-Morote**, M. Mattes and J. R. Mosig, "Orthomode Transducer and Dual-Polarized Horn Antenna in Substrate Integrated Technology", *IEEE Trans. Antennas Propag.*, vol. 62, no. 10, pp.4935-4944, Oct. 2014.
- [J07] **M. Esquiús-Morote**, B. Fuchs, J.-F. Zürcher and J. R. Mosig, "Low-profile Direction Finding System at the Ku-band using SIW Horn Antennas", *Accepted to Microwave Journal*, 2014.

Refereed International Conference Papers

- [C01] **M. Esquiús-Morote**, B. Fuchs and J. R. Mosig, "Analytical model of a printed transition for SIW antennas", *Proc. 6th European Conf. Antennas Propag. (EuCAP)*, pp. 414-417, March 2012.
- [C02] **M. Esquiús-Morote**, B. Fuchs and J. R. Mosig, "A new type of printed Ku-band SIW horn antenna with enhanced performances", *Proc. 17th Int. Symp. Antennas Propag. (ISAP)*, pp. 223-226, Nov. 2012.
- [C03] **M. Esquiús-Morote**, B. Fuchs and J. R. Mosig, "Enhancing the Performances of H-plane SIW Horn Antennas", *Proc. 7th European Conf. Antennas Propag. (EuCAP)*, pp. 2869-2872, April 2013.
- [C04] J. Perruisseau-Carrier, M. Tamagnone, J. S. Gómez-Díaz, **M. Esquiús-Morote** and J. R. Mosig, "Resonant and Leaky-Wave Reconfigurable Antennas based on Graphene Plasmonics", *Proc. IEEE Antennas Propag. Society Int. Symp. (APSURSI)*, pp.136-137, July 2013.
- [C05] **M. Esquiús-Morote**, B. Fuchs, J.-F. Zürcher and J. R. Mosig, "Low-profile SIW Horn Antenna Array with Interconnection to MMICs", *Proc. 8th German Microwave Conference (GeMiC)*, pp. 1-3, March 2014.
- [C06] **M. Esquiús-Morote**, M. Mattes and J. R. Mosig, "Orthomode Transducer for Dual Polarized Substrate Integrated Circuits and Antennas", *Proc. 8th European Conf. Antennas Propag. (EuCAP)*, April 2014.
- [C07] M. García-Vigueras, **M. Esquiús-Morote**, J. Perruisseau-Carrier and J. R. Mosig, "Dual-mode Radiation From 1D Leaky-Wave Antennas", *Proc. 8th European Conf. Antennas Propag. (EuCAP)*, April 2014.
- [C08] **M. Esquiús-Morote**, B. Fuchs, J.-F. Zürcher and J. R. Mosig, "Low-profile Direction Finding System with SIW Horn Antennas for Vehicular Applications", *Proc. IEEE Antennas Propag. Society Int. Symp. (APSURSI)*, July 2014.

Technical Reports

- [T01] **M. Esquiús-Morote**, B. Fuchs, J.-F. Zürcher and J. R. Mosig, "Conformal multifunction antenna system - Progress Report First Year", LEMA-EPFL, Tech. Rep., Dec. 2011.
- [T02] E. Tiezzi, R. Torres-Sanchez, B. Fuchs, **M. Esquiús-Morote**, J. R. Mosig and S. Vaccaro, "Miniaturised Multi-function Antenna System", European Space Agency (ESA) - ESTEC, Tech. Proposal, July 2012.

- [T03] **M. Esquiús-Morote**, B. Fuchs, J.-F. Zürcher and J. R. Mosig, "Conformal multifunction antenna system - Progress Report Second Year", LEMA-EPFL, Tech. Rep., Sept. 2012.
- [T04] **M. Esquiús-Morote** and J. R. Mosig, "Conformal multifunction antenna system - Progress Report Third Year", LEMA-EPFL, Tech. Rep., Sept. 2013.
- [T05] A. von Bieren, S. Capdevila, **M. Esquiús-Morote**, J. R. Mosig and A. Macor, "Lightweight and costeffective antenna feed chains based on additive manufacturing", European Space Agency (ESA) - ESTEC, Tech. Proposal, March 2014.
- [T06] S. Capdevila, **M. Esquiús-Morote** and J. R. Mosig, "High Frequency Solar Rectennas (HIFSOR): design and proof-of-concept prototyping", LEMA-EPFL, Tech. Proposal, July 2014.
- [T07] **M. Esquiús-Morote** and J. R. Mosig, "Pre-study on Active Electronically Scanned Arrays (AESAs)", LEMA-EPFL, Tech. Proposal, Sept. 2014.